Modélisation à l'échelle atomique de l'évolution microstructurale dans les alliages Ni-Fe : Corrélation entre les propriétés magnétiques et structurales

Iryna Vernyhora

▶ **To cite this version:**

Iryna Vernyhora. Modélisation à l'échelle atomique de l'évolution microstructurale dans les alliages Ni-Fe : Corrélation entre les propriétés magnétiques et structurales. Physique [physics]. Université de Rouen, 2009. Français. NNT : . tel-00430789

HAL Id: tel-00430789

https://theses.hal.science/tel-00430789

Submitted on 9 Nov 2009

HAL is a multi-disciplinary open access archive for the deposit and dissemination of scientific research documents, whether they are published or not. The documents may come from teaching and research institutions in France or abroad, or from public or private research centers.

L'archive ouverte pluridisciplinaire **HAL**, est destinée au dépôt et à la diffusion de documents scientifiques de niveau recherche, publiés ou non, émanant des établissements d'enseignement et de recherche français ou étrangers, des laboratoires publics ou privés.

Université de Rouen

U.F.R. des Sciences et Techniques

École doctorale «SPMII»

THÈSE

Discipline : *Physique*

Spécialité : *Sciences des Matériaux*

présentée par

Iryna Vernyhora

pour obtenir le titre de

DOCTEUR DE L'UNIVERSITE DE ROUEN

Modélisation á l'échelle atomique de l'évolution microstructurale dans les alliages Ni-Fe : Corrélation entre les propriétés magnétiques et structurales

soutenue le 19 Octobre 2009 devant le jury composé de

P. Depondt	Maître de Conférences	Rapporteur
V. Lorman	Professeur	Rapporteur
O. Isnard	Professeur	Examinateur
I. A. Abrikosov	Professeur	Examinateur
H. Zapolsky	Professeur	Directeur
D. Ledue	Professeur	Directeur

Groupe de Physique des Matériaux, UMR CNRS 6634

Université de Rouen

Aknowledgements

First of all, I would like to thank to my thesis supervisors Héléna Zapolsky and Denis Ledue for accepting my candidature for this thesis and sharing their scientific experience. In particular, I would like to thank Héléna Zapolsky for giving me an introduction to the phenomena of phase transformations and for the valuable discussions during our research. I am very grateful to Denis Ledue for his help and introduction to the theory of magnetism and Monte Carlo simulations, for the numerous discussions on the subject of our study and corrections of the manuscript. Moreover, their help upon my arrival to France can not be overestimated and is very valuable for myself.

Also, I would like to thank to Renaud Patte for his excellent programming skills, his attention to the small things and good sense of humor.

I am very grateful to M. Philippe Depondt and Professor Vladimir Lorman for accepting to read the manuscript even in its "rare" version and for writing reports on the presented investigation. I want to thank to Professor Igor A. Abrikosov for accepting to be a part of jury and for providing the *ab initio* data calculated under his guidance. Without these data the part of the work would not have been accomplished. Also I would like to thank to Professor Olivier Isnard for being a part of jury and kindly accepting to read the manuscript.

I am grateful to the Director of the laboratory Groupe des Phisyque des Matériaux (GPM) Didier Blavette for giving me an opportunity to work on this thesis in the favorable conditions with all necessary materials. I would like to thank to all the members of GPM laboratory for the reception and in particular the members of the ER3M group to which I have belonged during these 3 years. I appreciate sincerely M. Pierre Emmanuel Berche for kindly sharing his office with me.

I would like to thank the facility of CRIHAN and its members for giving an opportunity to use their calculation resources which was exceptionally important for this work.

I want to thank to other Ph. D. students for sharing good moments and introducing to the local life. I want to express my special thanks to Viktor, Elena and Slava for their good humor, friendship and ability to have good words when needed. Finally, I am very grateful to my friends and my family. I can not express all my gratitude to my mother, my sister and my husband for keeping me motivated, for their encouragement and patience.

CONTENT

General introduction

Ordering in alloys has been extensively studied for many years, and especially for materials which are of great technological importance. Numerous experimental and theoretical investigations have been performed in order to understand the structural ordering and the underlying processes. For magnetic alloys, atomic ordering is accompanied by a magnetic ordering and the interplay between these two kinds of ordering has to be investigated. Indeed, the magnetic properties are sensitive to the heat treatment and, therefore, to the structure changes. Also, magnetic annealing can induce directional atomic ordering and influence the structure of the alloy. Hence, the variety of physical properties which appear as a consequence of the mutual influence of the two types of order leads to the extensive use of these alloys in the industrial applications and, thus, favors both theoretical and experimental investigations. From a theoretical point of view, the modeling of such alloys is more complicated and quite a few investigations have been performed. However, in principle, the thermodynamic description can be used for the prediction of phase diagrams, i.e. the analysis of phase transitions (order, temperatures) and domains of coexistence of the different phases. The ageing processes can be studied by means of kinetic investigations. In particular, such studies allow to investigate the precipitation and phase separation processes, the shape and volume fraction of the precipitates, etc. The latter is very important for the industrial applications, for example for the material development, due to the precipitation hardening mechanism.

One of the striking examples of the magnetic alloys are the Ni-Fe alloys which have been studied for approximately 100 years but still are interesting from the theoretical point of view. These alloys exhibit different physical properties depending on the composition. The Fe-rich alloys present a phenomenon of anomalous thermal expansion which is essential, for example, for the precision instruments. The Ni-rich alloys have attractive magnetic properties which are essential for the signal transmitting and recording devices. In the presented study we have investigated the Ni-rich alloys, and, in particular, Permalloys. The phase diagram of these alloys predicts a stable Ni_3Fe ($L1_2$-type) phase over wide temperature and concentration ranges. $Ni_{1-x}Fe_x$ alloys (x is the Fe concentration) are ferromagnetics and exhibit a 2^{nd} order paramagnetic↔ferromagnetic transition. Then, at lower temperature these alloys undergo a 1^{st} order transition from the disordered fcc phase to the ordered $L1_2$ structure. The state of order of the alloy influences the magnetic properties and *vice versa*. The assumption of an antiferromagnetic Fe-Fe coupling between nearest neighbors [58-62] helps to understand the influence of magnetism on the chemical ordering in a wide concentration range. This hypothesis

has been widely used for the alloy description [40,44-46,50-51,64, etc.]. Therefore, as the alloy orders ferromagnetically, the number of nearest Fe-Fe pairs should be reduced which induces atomic rearrangements and stabilizes the $L1_2$ ordered structure. The precipitation of the ordered phase takes place at relatively low temperatures ($<780K$) which makes ordering a slow process due to the slowing down of diffusion. In most experiments the equilibrium ordered state has not been achieved. During the annealing and ageing of the materials, the formation of spherical precipitates [130] which grew till the domain sizes with lowering the temperature was observed. The combined action of the magnetic and chemical interactions should be considered during the investigation of these alloys. Thus, the goal of this work was to investigate mutual influence of magnetic and atomic orderings and, more precisely, to understand their effect on the thermodynamic properties (phase transition) and on the kinetics of the precipitation in the system.

When experimental investigation of the alloys is complicated by the slow diffusion processes and the examination of the low temperature ordered phases becomes unreachable, the theoretical modeling becomes a very useful tool. Moreover, the power of today's supercomputers allows sophisticated modeling. The simulations allow modeling of the comparatively large systems until the late stages of evolution which cannot be realized in the real experiments. Also, the great advantage of the simulations is the possibility to vary the parameters of the model (mainly the interaction parameters) and, consequently to study the influence of the different energy terms on considered phenomena. Then, a comparison with the experimental data permits to obtain a magnitude order of the different energy terms. Moreover, when the macroscopic experimental behavior is reproduced (for example, thermal variation of a thermodynamic quantity), numerical simulations enable to propose a microscopic scenario which is sometimes very difficult (or too expensive) to observe by experiments. In our study we have used Monte Carlo and mean-field methods for the thermodynamic investigation and construction of the phase diagram of the Ni-rich Ni-Fe alloys. The kinetic behavior was studied only using mean-field approach. The thermodynamic properties and the morphology of simulated microstructures were compared to the experimental data when possible. The main advantage of the Monte Carlo method is taking into account the short range correlations, i.e. the local fluctuations, unlike the mean field technique. On the other hand, it is large time consuming, that is why we have chosen to investigate the precipitation kinetics using the mean field method combined with the Önsager microscopic kinetic equation.

The presented thesis consists of 4 chapters. In the first chapter, we present a description of the Ni-Fe alloys and Permalloys, in particular. The ordering temperatures and the structural changes upon ordering alloys are recalled. In this chapter we also discuss the magnetic properties

of Ni-Fe alloys such as: magnetic moments of Ni and Fe and their alloys, magnetization and Curie temperatures. The main features of Permalloys which are important for the technical applications (permeability, magnetostriction and magnetic anisotropy) are shortly reviewed at the end of the chapter.

The 2nd chapter is devoted to the Monte Carlo simulations. The theoretical basis is briefly presented as well as the algorithm which has been used. The total Hamiltonian which includes both chemical and magnetic interactions and the method of calculation of thermodynamic quantities (internal energy, specific heat, magnetization, zero-field magnetic susceptibility and chemical order parameters) are given.

In the 3rd chapter a short review of the theory of ordering phenomenon is presented. In the framework of the mean-field approach, the Hamiltonian and the Helmholtz free energy are formulated. Thermodynamic mean-field model is followed by the discussion of the alloy kinetics. The nucleation, growth and coarsening regimes are discussed and the Lifshitz-Slyozov-Wagner (LSW) theory is reminded. For the calculation of the kinetic path in Ni-Fe system, the formalism of the Önsager-type microdiffusion equation is proposed.

The 4th chapter is devoted to the description of the obtained results – Monte Carlo and mean-field simulations. The Monte Carlo simulation results consist of the investigation of the $Ni_{1-x}Fe_x$ alloy near the stoichiometric Permalloy composition. The simulations were performed on stoichiometric (75% at. Ni) and non-stoichiometric alloys without external magnetic field. The results were compared with the experimental phase diagram. Also, the effect of the interaction parameters and the influence of the external magnetic field on the phase transitions have been investigated. Then, the mean-field description starts with the extensive description of the formulae and numerical results for the modeled ordering alloy with 2 magnetic atoms. The thermodynamic properties have been investigated and compared to the Monte-Carlo results. From the Helmholtz free energy curves, the phase coexistence intervals have been found and used for the following kinetic simulations. The coarsening of the ordered $L1_2$ phase and its characteristics have been investigated and compared with the predictions of the LSW theory. For both Monte Carlo and mean-field simulations, the obtained results have been compared with the experimental data when possible (the order of the transition, the temperature of the magnetic and chemical order transitions, the obtained crystal structure and morphology of the precipitated phases). For both types of simulations the magnetic and atomic ordering is considered and the importance of their combined action is discussed.

At the end of the manuscript the conclusions and perspectives are given.

Chapter 1

Ni-Fe alloys

1.1. Introduction

Ni-Fe alloys are widely used for industrial applications due to their properties. Anomalies of abnormal thermal expansion coefficient in *Invar* alloys (Fe_3Ni) have lead to their use in metrology and geodesy, in precision metallurgy, microelectronics, television, etc. *El'Invars* (FeNi) are used for the applications where high elasticity is important (for example in chronometry), they are also used for the power transmission devices. *Permalloys* ($FeNi_3$) are soft magnetic materials and are widely used in the electronics and engineering (for transformers transmitting the weak signals of communication apparatus, for reading heads (in computers), etc.). Properties of these alloys can be improved by addition of other elements (Cr, Mo, Al, C, etc) [2,9-11].

The experimentally obtained phase diagram of Ni-Fe alloys (Fig. 1.1) shows regions where different alloys are formed. Due to the slow diffusion processes in these alloys the equilibrium is reached very slowly and, therefore, it is hard to obtain experimentally the low temperature part of the diagram.

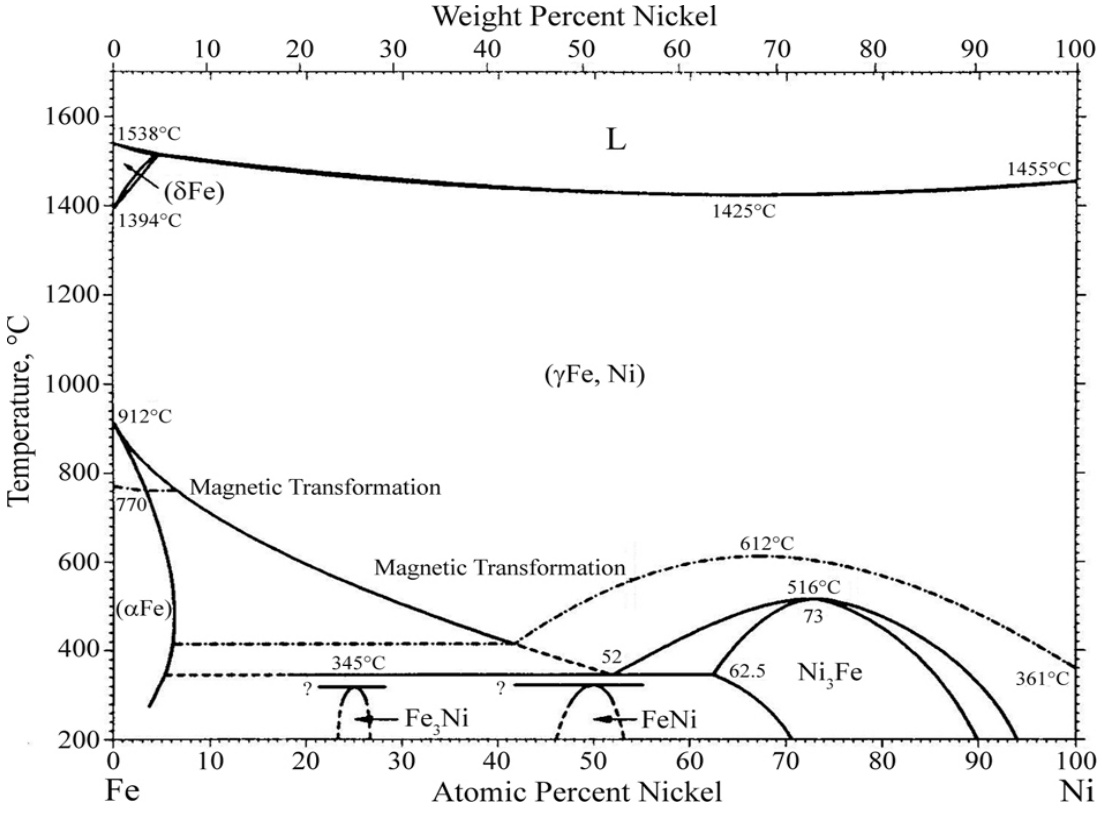

Figure 1.1. Experimental phase diagram [1]

From this diagram it follows that Permalloy alloys (around 75% at. Ni) form a stable structure over a wide temperature and concentration ranges. When the temperature, *T*, is decreased, the alloy exhibits two sequential phase transitions (magnetic and structural,

respectively). To understand this behavior of Ni-Fe system (and Permalloy, in particular) it is necessary at the beginning to consider in details the constituent elements and their properties.

1.2. Pure Ni and Fe

Ni and Fe are closely situated in the Mendeleev periodic table of elements and have almost identical electronic structure. Both elements are ferromagnetic, and their alloys also exhibit ferromagnetic behavior. Some of the properties of the Ni and Fe are presented in Table 1.1 [2-3].

	Fe	**Ni**
Electronic structure	$[Ar]3d^6 4s^2$	$[Ar]3d^8 4s^2$
Atomic number	26	28
Atom radius (Å)	1.27	1.25
Crystalline lattice structure	α, β, δ – bcc (A2) γ – fcc (A1)	γ - fcc (A1)
Lattice parameter (Å) for γ – fcc phase	3.6468 (at 900 °C)	3.5243 (at 20 °C)
Self diffusion coefficient (m^2/s) for γ – fcc phase	2.19×10^{-15}	1.749×10^{-21}
Fusion point (°C, *K*)	1535, 1808	1453, 1726
Thermal dilatation at 20 °C (10^{-6}/°C) for γ - phase	12	13
Magnetic state	Ferromagnetic (αFe) ; Antiferromagnetic (γFe)	Ferromagnetic
Curie temperature (°C, *K*)	(bcc αFe) 770, 1043	350, 623
Neel temperature (°C, *K*)	(fcc γFe) -203, 70	—
Magnetic moment per atom (μ_B)	2.2	0.6

Table 1.1. Pure Fe and Ni elements and their properties

Both Fe and Ni belong to the group of 3*d*-transition elements, therefore pure elements and their alloys also exhibit properties of this group, which is characterized by the incomplete 3*d* and complete 4*s* electronic shells. The overlap of the outer electronic shells and their rearrangement leads to the practically full delocalization of outer electrons [5-8]. The analysis of the electronic structure of *d*-metals indicates an enhanced density of electronic states near the Fermi level (Fig. 1.2).

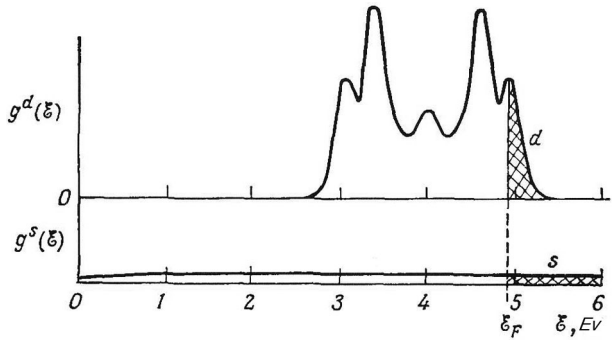

Figure 1.2. Illustration of the contribution of *d*- and *s*- bands to the density of states of transition metals

Various properties of transition metals appear due to their electronic structure (strong cohesion, high electro-resistivity, appearance of magnetism and different chemical properties). The magnetic order appears due to the dominance of exchange coupling which is stipulated by the active influence of the conduction electrons upon the system of uncompensated magnetic moments of former *d*-electrons [5].

1.3. Fe-Ni alloys

Fe alloys could be divided in 3 groups: steels, cast iron and precision materials (including soft-magnetic and strong-magnetic materials). The properties of the materials are defined by the structure and phase composition, which are subject to the type of treatment – deformation, thermal treatment, etc.

Ni alloys are also of great interest from the technological and industrial point of view. They present valuable anti-corrosion, mechanical, magnetic and electric properties. When Ni is alloyed with Fe, Cr, Cu, Mo, it forms a substitutional solid solution with a fcc lattice over a wide concentration range, which gives them high plasticity. The hardening of such alloys is originated from the precipitation.

1.3.1. Close review of the phase diagram. Permalloy alloys

As seen from the phase diagram, at low temperatures the following structures are formed from a disordered solid solution: Ni_3Fe, NiFe, $NiFe_3$. The existence of stable (or metastable) NiFe and $NiFe_3$ was proposed after the study of meteorites and diffraction experiments on Invar alloys. Due to the similarity of the electronic structure and lattice parameters of Fe and Ni, it is observed [2-3,9-11]:

- high fusion temperatures and small solidification intervals;

- wide concentration region with fcc (γ) structure, which transforms into a bcc (α) structure starting from 27% at. Ni (when the concentration of electrons per atom does not allow the existence of Ni compact structure).

The fcc structure in the whole region where Ni > 27% presents great advantages:

- possibility of rolling till small thickness (d ~ 10 μm);
- fragility does not appear at low temperatures (the Invar effect);
- possibility of thermal treatment for all temperatures without changing the phase; such treatments are useful for developing recrystallization structures and special magnetic properties.

For the whole region with Ni > 27% the fcc phase is stable and at low temperature the ferromagnetic and chemical order is observed.

Ni_3Fe alloys are of great interest due to their structural and magnetic properties. As was previously mentioned, they belong to the soft-magnetic materials and are widely used in the industrial applications. Soft magnetic materials are easily magnetized till saturation by weak fields; they exhibit narrow hysteresis loops and low coercive fields, small magnetic losses, high initial and maximum magnetic permeabilities. Permalloy alloys have very small magnetocrystalline anisotropy and magnetostriction.

To reach better magnetic properties, the soft magnetic materials (Permalloys, in particular) should undergo thermal treatments which increase their chemical purity and change their long-range and short-range atomic order. Alloying Ni_3Fe with Mo, Cr, Cu, Co, Mn, Si also improves its properties [3]. For example, Co is added to Permalloys to increase their magnetization and improve their susceptibility to magnetic field treatment. Mo and Cu are added to improve soft magnetic properties and, in particular, Supermalloy ($Ni_{79}Fe_{16}Mo_5$) has the highest permeability among the other soft magnetic materials.

1.3.2. Structural properties

It was mentioned above that in fcc Ni-Fe alloys the order-disorder transformation is observed. As a result, from a disordered fcc solid solution (*A*1-type), the substitutional superstructures Cu_3Au ($L1_2$-type) and CuAu*I* ($L1_0$-type) are formed (Fig. 1.1 and Fig. 1.3).

(a) (b)

Figure 1.3. Distribution of Ni and Fe atoms on the sites of a fcc lattice for perfect atomic LRO substitutional superstructures:
(a) Ni_3Fe and Fe_3Ni (Cu_3Au-$L1_2$-type) (●,○ – Fe(Ni) and Ni(Fe) atoms)
(b) NiFe (CuAu*I*–$L1_0$-type) (●,○ – Fe and Ni atoms)

From the phase diagram it is seen that the order-disorder transformation from fcc to $L1_2$ structure takes place over a wide composition range, from 50 % to 80 % at. Ni. The decrease of the lattice parameter of the 75 % at. Ni alloy which occurs on the formation of the ordered ($L1_2$ - type) structure is about 2×10^{-3} Å [12]. The formation of order is extremely sluggish and takes place in the temperature range 767*K* to 773*K*, so highly disordered condition can be retained, for example, at 300*K* by rapidly cooling from above 773*K*. The ordered state of the alloy for a wide concentration range may be obtained by annealing for some time at a steady temperature below the temperature of order-disorder transition, T_K, or by cooling at a fixed rate (sufficiently small) (for example from just above to well below T_K). The alloy exhibits thermal 'hysteresis' as the order-disorder transition in Ni_3Fe is of 1st order type. This kinetic behavior makes Ni_3Fe alloy attractive for measuring physical properties as a function of temperature for both ordered and various metastable disordered conditions, and to compare the effects of configurational order on the magnetic properties [13].

Experimental evidence of ordering and formation of the ordered structure can be obtained by means of diffraction techniques (X-ray or thermal neutrons [15-21]), electrical resistivity and specific heat measurements [12-14]. Also, ordering can be exhibited during the magnetic measurements, such as Mossbauer spectroscopy [22-26].

Diffraction experiments are often used for the investigation of the short-range order in the alloys (above the order-disorder transition). A small change of the lattice parameter upon ordering and near equality of X-ray and neutron scattering factors for Ni and Fe should be taken into account during these experiments.

	T_K (K)
Shull&Wilkinson [21]	763
Cranshaw [25]	776
Orehotsky&Souza&Pinheiro [14]	820
Koolie&Brooks [13]	773
Wakelin&Yates [12]	771
Ferjani&Bley&Calvayrac [17]	*disorder*: 776 *order*: 785

Table 1.2. Experimentally obtained order-disorder transition temperatures, T_K, for Ni_3Fe

The order-disorder transition temperature can be defined using resistivity curves, it is the temperature at which the resistivity curve for slowly cooled alloy begins to diverge from the rapidly cooled curve (Fig. 1.4a). In the vicinity of 75 % at. Ni there is a maximum decrease in the resistivity (Fig. 1.4b).

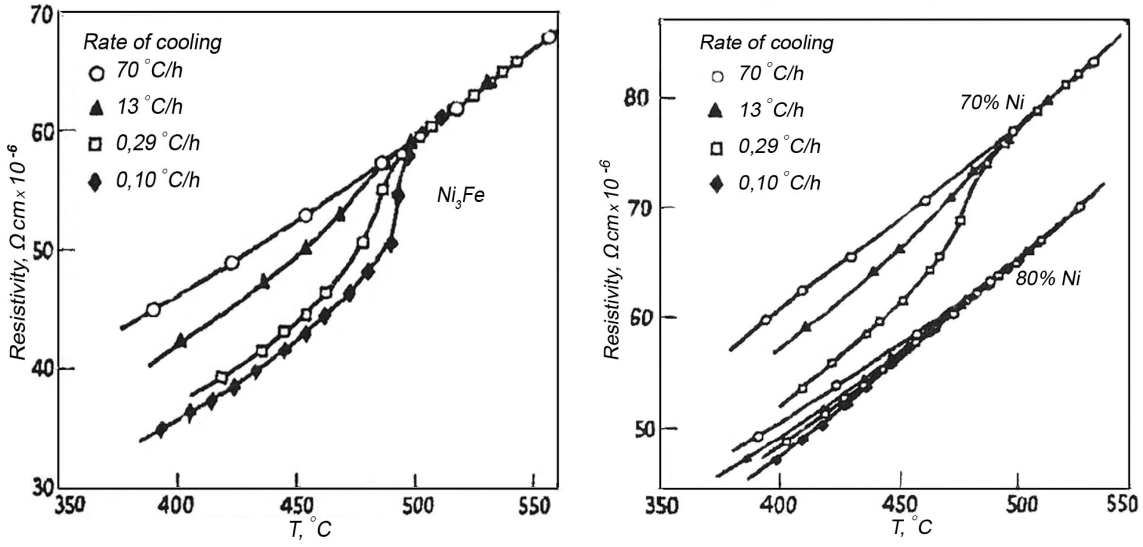

(a) (b)

Figure 1.4. Thermal variation of the resistivity [12]:

(a) Ni_3Fe

(b) Alloys containing 70% and 80 % at. Ni

Calorimetric measurements ensure the influence of the configurational order on the magnetic properties and, in particular, the Curie temperature, T_C, (Fig. 1.5). It is seen that if the system is trapped in the metastable state (which could happen if the heating rate was not slow enough, S_{BW} = 0.60; 0.66, S_{BW} – is the Bragg-Williams parameter), this would affect the T_C

value, so the influence of the heating rate on T_C is indirect. The higher the state of order of the system, the higher the Curie temperature.

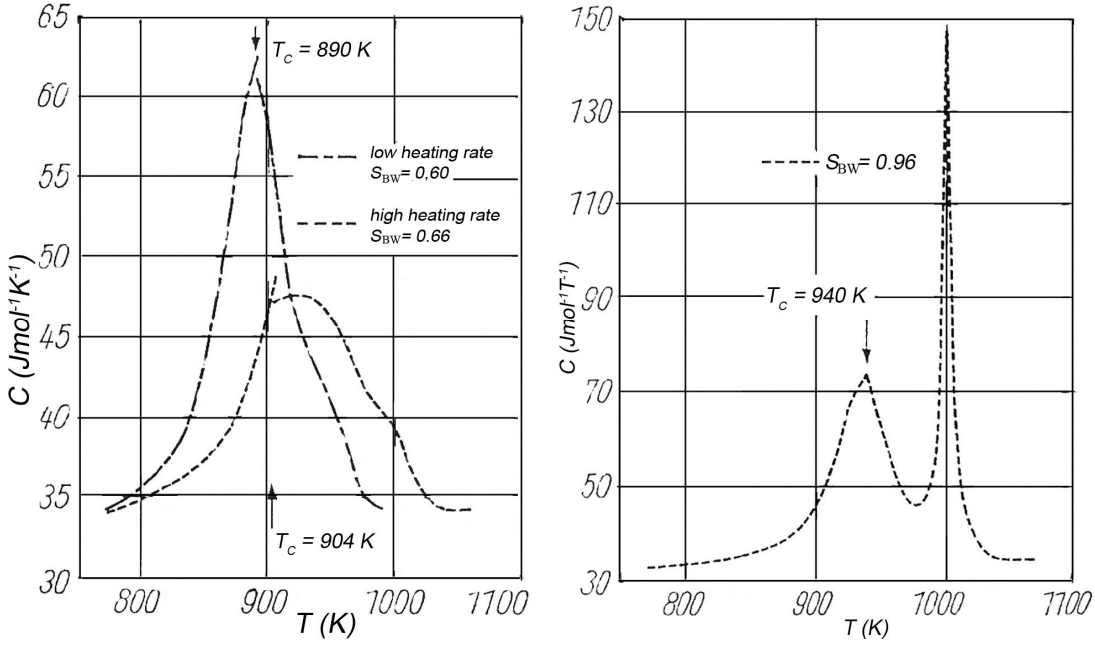

(a) (b)

Figure 1.5. Heat capacity curves for states having different Bragg-Williams long-range order parameter S [13]:
(a) S_{BW} = 0.60 (T_C = 890*K*) and S_{BW} = 0.66 (T_C = 904*K*)
(b) S_{BW} = 0.96 (T_C = 940*K*)

1.3.3. Magnetic properties

1.3.3.1. Magnetic moment distribution and spontaneous magnetization

The concentration dependence of the average magnetic moment per atom can be written in the following form:

$$\overline{\mu}(c_{Fe}) = c_{Fe}\mu_{Fe} + c_{Ni}\mu_{Ni} = c_{Fe}\mu_{Fe} + (1-c_{Fe})\mu_{Ni}\,, \tag{1.1}$$

where $c_{Fe} = \frac{N_{Fe}}{N}$ is the relative Fe atomic concentration $(N = N_{Fe} + N_{Ni})$, and μ_{Fe}, μ_{Ni} are the atomic magnetic moments of Fe and Ni, respectively.

Fig. 1.6 shows that, from 50 to 100% at. Ni, the value of $\overline{\mu}$ varies almost linearly with the alloy composition which means that μ_{Fe} and μ_{Ni} do not depend on c_{Fe}. Consequently, the atomic magnetic moments μ_{Fe} and μ_{Ni}, can be taken as constant and chosen from the experimentally observed values [54-57].

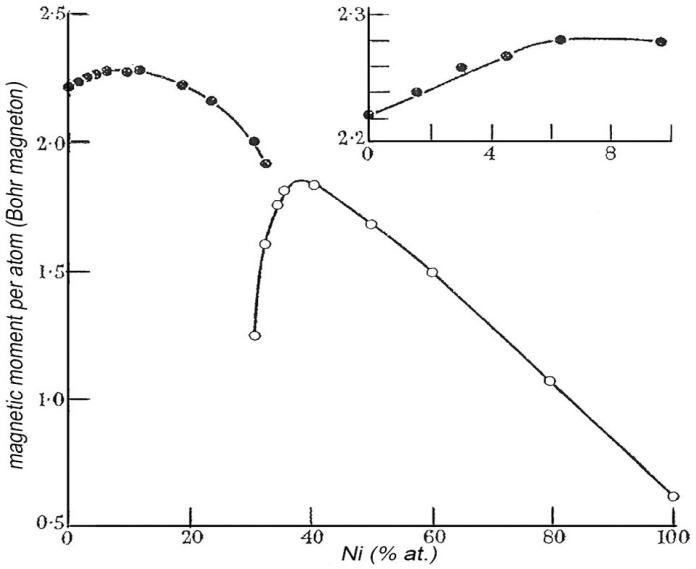

Figure 1.6. Variation of the magnetic moment per atom for bcc (●) and fcc (○) Ni-Fe alloys [57]

From Fig. 1.6 it is also seen that with increasing Fe content (while approaching Invar region) the average magnetic moment first starts to decline from the linearity and then decreases (for γ-fcc phase). This phenomenon has a fundamental meaning for the interpretation of the physical properties of Invar alloys and is connected to the dependence of the atomic magnetic moment of Fe, μ_{Fe}, on the local environment which changes with concentration. Several approaches were proposed to explain the Invar phenomenon (2-γ state approach [58], itinerant electron model, etc.). One of the explanations of such behavior is the experimental observation of antiferromagnetic nearest-neighbor Fe-Fe interactions [59-62], and with increasing Fe content antiferromagnetic interactions start to become dominant.

The plot of reduced spontaneous magnetization is presented in Fig. 1.7.

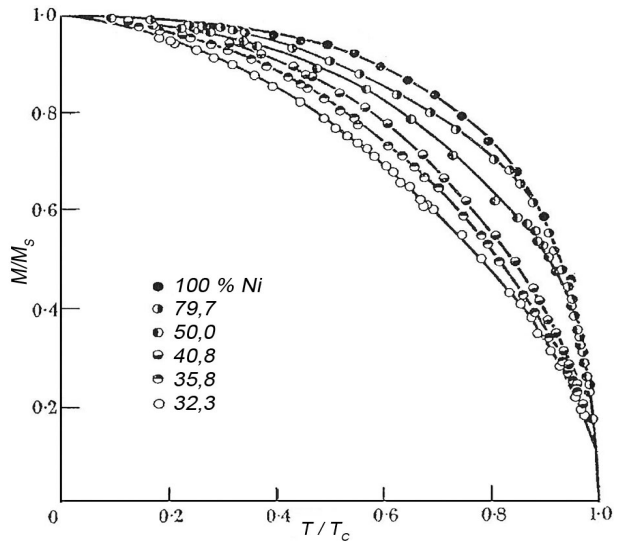

Figure 1.7. Reduced magnetization versus reduced temperature [57]

Fig. 1.7 shows that the law of corresponding states is not obeyed, i.e. the behavior of magnetization for different Fe-content does not follow the same universal curve when approaching the transition point T_C [63]. The magnetization at given temperature increases with the increase of Ni concentration.

	μ_{Fe} (μ_B)	μ_{Ni} (μ_B)
Wakelin&Yates [12]	2.62	0.6
Cable&Wallan (for ordered sample) [53] (neutron diffuse-scattering experiments)	3.10	0.68
Shull&Wilkinson [21] (neutron diffraction experiments)	2.97 (±0.15)	0.62 (±0.05)
Low&Collins [55] (neutron-diffuse-scattering experiments)	2.8 (±0.2)	0.6
Wohlfarth [4]	2.8	0.616

Table 1.3. Experimentally obtained atomic magnetic moments for Ni_3Fe

1.3.3.2. Curie temperature

The Curie temperature, T_C, is the paramagnetic↔ferromagnetic transition temperature (this transition is known to be 2nd order). It is hard to precise T_C due to the "smearing" of the transition and the transition temperature is obtained by extrapolating the $\boldsymbol{M}_S(T)$ (spontaneous magnetization) curve till the intersection with the temperature axis. It can also be located using heat capacity and electrical resistivity measurements which exhibit anomalies in the vicinity of the Curie temperature.

The concentration dependence of the Curie temperature in γ-fcc Fe-Ni alloys exhibits a maximum in the vicinity of 30% at. Fe (Fig. 1.8). All the experimental data are in good agreement for $c_{Fe} \leq 60\%$. Near the Invar region there are some discrepancies in the experimental data for T_C (it is supposed to decrease down to $0K$ as c_{Fe} increases). In this region the definition of T_C is complicated from one side by the smeared paramagnetic↔ferromagnetic transition and, from the other side, by the structural γ↔α transformation, which does not allow reaching c_{Fe} at which Curie temperature should become zero.

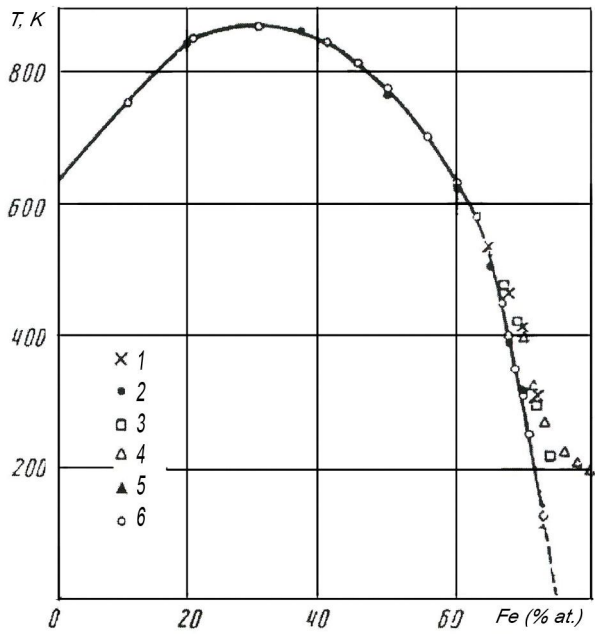

Figure 1.8. Curie temperature versus Fe-concentration [64]

× – [68]; ● – [57]; □ – [66]; Δ - [67];

▲ – [65]; ○ – [64]

The values of T_C are influenced by the state of order of the alloy as was shown in Fig. 1.5 [13]. T_C in the ordered state is approximately 100K [13,64] and about 200K higher than in the disordered state for Ni_3Fe and NiFe, respectively. Experimental values of T_C for Ni_3Fe are given in Table 1.4.

	T_C (K)	
	Ordered phase ($L1_2$)	Disordered phase (γ)
Menshikov&Yurchikov [64]		
a) experimental	943	840
b) theoretical	935	830
Koolie&Brooks [13], experimental	940	871
Wakelin&Yates [12], experimental	954	871
Orehotsky&Souza&Pinheiro [14], experimental		860
Van Deen&Van DerWoude [26], experimental		863±3

Table 1.4. Experimentally obtained Curie temperatures for Ni_3Fe

Consequently, from the theoretical point of view it is interesting to study the dependence of the Curie temperature on the state of order of the alloys. This question will be developed later (in Chapter 4).

1.3.3.3. Permeability, Magnetic anisotropy and Magnetostriction in Ni_3Fe alloys

It was mentioned above that the distinctive features of Permalloy alloys are connected to their high permeability, magnetic anisotropy constants and magnetostriction, low coercive force and rectangular shape of the hysteresis loop [3,9-11,69].

On the Fig 1.9 the permeability curves have maximum at about 79% at. Ni and are markedly influenced by the heat treatment; they are enhanced by the rapid cooling and magnetic anneal (which also changes the form of hysteresis loop). Noted permeability maxima lies between the compositions with zeros of polycrystalline magnetostriction (K_1) and lattice anisotropy (λ_{111}).

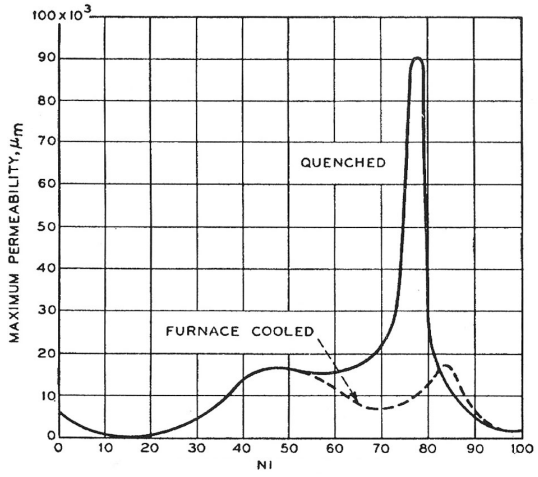

(a)

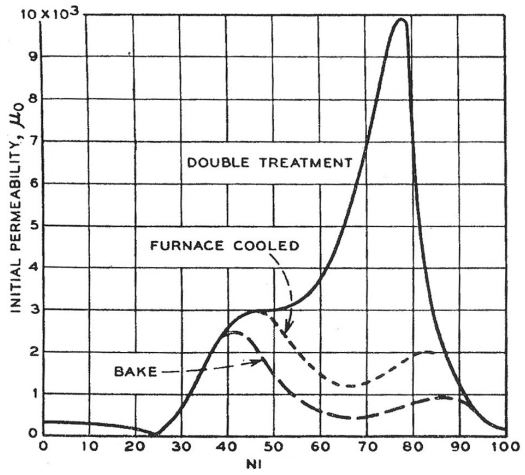

(b)

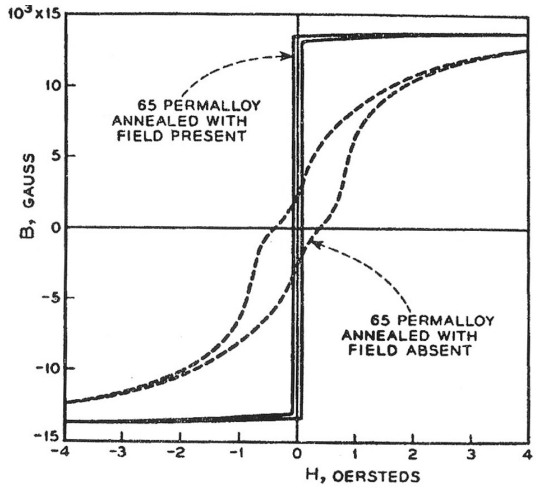

(c)

Figure 1.9. Ni-concentration dependences of [10]:

(a) Maximum permeability

(b) Initial permeability

(c) Hysteresis loop (induction versus applied field)

Heat treatment also influences the magnetic anisotropy constants which have lower (more negative) values for the slowly cooled alloys. In a range of composition near Ni_3Fe a deep minimum occurs (Fig 1.10a).

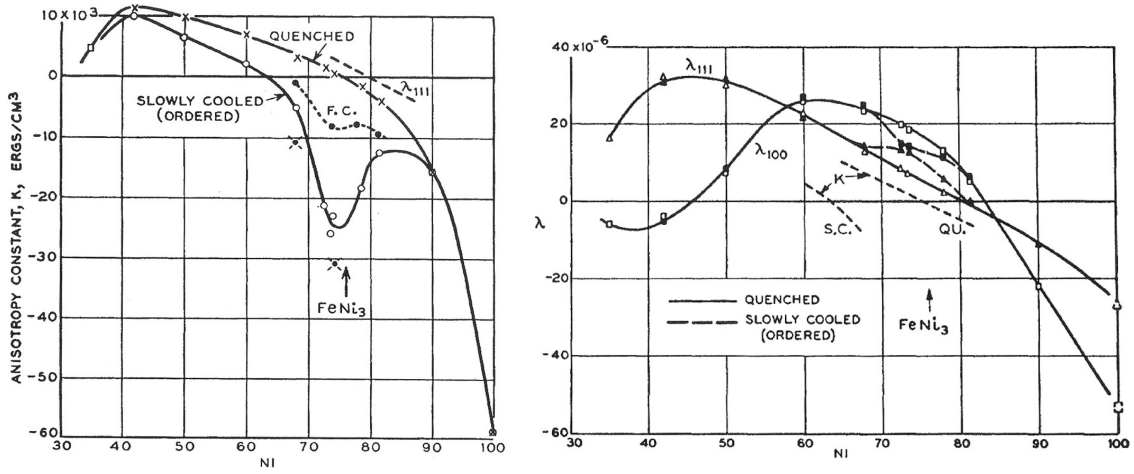

(a) (b)

Figure 1.10. Ni concentration dependences of [11]:

(a) Anisotropy constant

(b) Magnetostriction

To explain the behavior of the magnetic anisotropy constants in Ni-Fe alloys, in Ref. [11] authors proposed 4 types of anisotropy: magnetocrystalline, magnetostrictive, thermomagnetic, and slip-induced. *Magnetocrystalline* anisotropy is present when one of the crystallographic directions is magnetically preferred. The presence of elastic stress in a ferromagnetic sample results in *magnetostrictive* anisotropy (in permalloys the magnetostriction constants λ_{111} and λ_{100} are functions mainly of the composition and not sensitive to heat treatment). *Thermomagnetic* anisotropy is obtained by annealing alloys below the Curie temperature T_C , the principal mechanism is thought to be "directional ordering", a preferential alignment of atom pair parallel to the local magnetization direction. The mechanism, which is called *slip-induced* directional order, is closely related to that, obtained by magnetic annealing.

Magnetostriction varies with heat treatment in a narrow composition range that was observed for anisotropy, namely, from 68 to 81% at. Ni (Fig. 1.10b). The ordered alloys are more isotropic than the disordered alloys, and at about 73% at. Ni λ_{100} and λ_{111} are almost equal.

Finally, it is possible to mention that the reduction of anisotropy to zero does not lead to high permeabilities unless the magnetostriction also approaches zero. However, disappearance of the magnetostriction in the direction of easy magnetization can cause high permeability even though the anisotropy is not zero.

1.4 Theoretical approaches to the description of the Ni-Fe alloys

Besides experimental investigations, theoretical studies have been devoted to the Ni-Fe alloys. Both Ni- and Fe-rich parts of the phase diagram have been explored. Different approaches have been applied to model these alloys. Among others, it is necessary to mention numerical simulations (Monte Carlo [40-41,44-46] and cluster variation [47-49] methods), mean-field [42-44,50-51] and ab initio [27-39] calculations.

Monte Carlo simulations have been widely applied to the investigation of the phase diagrams of alloys [73-74,98-100] and Ni-Fe alloys in particular [40-41,44-46]. Taylor *et al*. [44] have performed MC simulations for the Ni-rich alloys using Ising Hamiltonian for both chemical and magnetic subsystems. Nearest-neighbor magnetic interaction between Fe atoms has been considered as antiferromagnetic, the interaction parameters within next nearest neighbors were also examined and the obtained results have been compared to the experimental phase diagram and magnetization curves [12,57]. Dang *et al*. [40] have used the same model with only nearest neighbor interactions. In this work the influence of the magnetic interactions on the chemical order (and order-disorder transition, in particular) has been evidenced from the behavior of the internal energy and order parameters (magnetization and chemical order parameters). It should be noted that the specific heat and the magnetic susceptibility have not been investigated. Their work is restricted to the stoichiometric NiFe, Ni_3Fe and $NiFe_3$ alloys only. However, the Ising model is not well suitable to model soft magnetic materials because its critical exponents are different from those of Ni [4,70-72]. In particular, it overestimates the magnetization just below T_C in comparison with the classical Heisenberg model. In Ref. [45] Taylor *et al*. have attempted to investigate Ni-Fe alloys by using the Heisenberg model for the spin system. In their study the magnetic and chemical interactions are limited to the nearest neighbors. The compositional dependence (in the Ni-rich region) of the transition temperatures has been simulated and compared to that obtained by the Ising model [44]. It should be mentioned that no thermal variation of the thermodynamic quantities are presented and the separate description of the magnetic and chemical subsystems has not been performed. Therefore, it is hard to conclude about the mutual influence of the two types of order, and in particular, about the effect of the magnetic ordering on the chemical one in the framework of the Heisenberg model. In this work it has been underlined that the Heisenberg model better reproduces the diffraction data on the chemical short-range order. Finally, let us note that in these previously discussed works [40,44-45] the influence of an external magnetic field has not been studied.

By means of Monte Carlo method, in particular its linearized inverse version [46], the interaction parameters for Ni_3Fe alloys were extracted from experimental data and it was also

shown that interactions till 4th coordination shell can explain short-range order at given temperature.

Another widely used simulation technique is the cluster variation method [47-49,106-108]. In Ref. [47] Lawrence and Rossiter have implemented in their simulations the concentration dependent interaction parameters and have obtained a coherent phase diagram of the Ni-Fe system. The concentration variation of the interaction parameters in Ni-Fe was also discussed in [49] where authors have underlined the influence of the interactions in the 3rd and 4th coordination shells on the transition temperatures. In Ref. [48] the phenomenological investigation of Ni-Fe was performed and stability of $L1_0$ phase was predicted. In this work the cluster variation method was combined with Lennard-Jones type potentials. In spite of their effort to describe the phase diagram of the Ni-Fe system, the mutual influence of magnetic and chemical orderings has not been well understood. It should be mentioned that in Refs. [106-108] the influence of both interactions on the phase diagram was underlined.

For the investigation of the phase diagram of the alloys the mean-field approximation has been also applied. In this approach the description of the ordering phenomena is mainly based on the Bragg-Williams approximation [88-90]. This approach has been applied also to the description of the ferromagnetic alloys [50-51,53,102-104]. The internal energy term is usually evaluated using Ising- and Heisenberg-type Hamiltonians for chemical and magnetic interactions, respectively. The formulation of the magnetic entropy term is usually complicated [135-136] and was neglected in most of models. In [50-51] the explicit form of the magnetic entropy has been presented and the obtained results for Ni-Fe alloy were compared with the experimental data and other simulations. In general, the mutual influence of both magnetic and chemical subsystems was noticed for ferromagnetic systems in [53,102-104-98], where the obtained thermodynamic quantities have justified the importance of both magnetic and chemical interactions. Rancourt *et al*. [42-43] have presented a cluster-method mean field theory for the disordered magnetic alloy which has been applied to Ni-Fe alloys in a wide composition region. The concentration dependencies of the magnetic moment, Curie temperature and susceptibility were calculated in the framework of the given approximation.

A key point of modeling of the alloys is the choice of the interaction parameters (chemical and magnetic) and the value of the magnetic moments. This is usually done by fitting the diffusion scattering data, magnetic measurements, etc. In most of models, these parameters are considered to be constant [40-42,44-45] and their concentration and temperature dependences are neglected. Indeed, such dependences should be considered. As have been shown by *ab initio* calculations (mainly for Invar alloys), the magnetic behavior of Ni-Fe alloys is closely connected to the dependence of the magnetic moments and interactions on the local

environment and studied volume [34,36-39]. In particular, it was found that for Fe-rich alloys antiferromagnetically aligned moments occur on Fe sites which have no or only one Ni neighbor. In [38] the atomic magnetic moments of Fe were defined as: 2.43μB for ferromagnetic orientation and (-)1.64μB for antiferromagnetic orientation. The appearance of antiferromagnetically aligned magnetic moments of Fe is supposed due to the locally frustrated exchange interaction parameters in Fe-Ni alloys [37]. In most of works, the antiferromagnetic coupling between nearest neighbor Fe atoms was considered. However, the hypothesis about ferromagnetic Fe-Fe interactions has been discussed [61-62] on the basis of some experimental observations. It is necessary to mention the works of Staunton et al. [27-28] in which the mean-field approach was combined with the first principles (spin polarized KKR-CPA) calculations to study of the Ni-rich part of the Ni-Fe phase diagram. The authors have remarked that chemical ordering in Ni-Fe systems is stipulated by the magnetic interactions. Also, the stability of the ordered structures in Ni-Fe alloys was studied in [30,35].

From all these investigations it is possible to conclude about the importance of the magnetic and chemical interactions in Ni-Fe systems. Due to the complexity of the theoretical description the ordering in this system, only qualitative agreement between experiments and theoretical results has been obtained. The goal of this thesis is to develop a model, which will take into account magnetic and chemical interactions simultaneously, in order to better understand the thermodynamic properties and kinetics in Permalloys.

Chapter 2

Model and Monte Carlo simulation technique

2.1. Model description

For the description of Permalloy (namely Ni_3Fe) systems, a model, based on the fcc lattice was used. For this lattice the coordination numbers for 1st and 2nd neighbors are $z_1 = 12$ and $z_2 = 6$, respectively. In the disordered state the Fe and Ni atoms are randomly distributed on the sites of the fcc lattice. The ordered structure corresponds to the $L1_2$-type superstructure shown in Fig. 2.1.

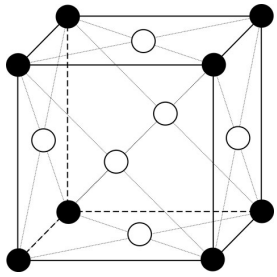

Figure 2.1. Distribution of Ni and Fe atoms on the sites of a fcc lattice for perfect $L1_2$-type superstructure (● – Fe atoms, ○ - Ni atoms)

Since the simulations are performed on finite-size lattices, the periodic boundary conditions were imposed to eliminate boundary effects and to reduce finite-size effects. Each vertex of the lattice is occupied by a Fe or Ni atom and holds a spin of a respective magnitude, s_{Fe} or s_{Ni}. We have considered the classical Heisenberg model in which each spin is described by a 3D vector $\vec{S} = (S_x, S_y, S_z)$ which can take all directions. The magnetic moment in this case will be defined as:

$$\vec{m} = -g\mu_B \vec{S},$$

where the Landé factor g is approximately equal to 2, and μ_B is the Bohr magneton.

The choice of the 3D Heisenberg model is reinforced by the similarity of its static critical exponents with those of pure Ni ($\alpha \approx -0.11$, $\beta \approx 0.36$ and $\gamma \approx 1.39$) [4,70-72].

2.1.1. Heisenberg Hamiltonian

The Heisenberg Hamiltonian of the system of interacting spins (atomic magnetic moments) can be defined in such a form [5-8]:

$$\mathcal{H}_{magn} = -\sum_{\langle ij \rangle} J_{ij} (\vec{S}_i \cdot \vec{S}_j) = -\sum_{\langle ij \rangle} J_{ij} (S_i^x S_j^x + S_i^y S_j^y + S_i^z S_j^z), \qquad (2.1)$$

where J_{ij} are the "exchange" parameters, $\vec{S}_i, \vec{S}_j$ are spin variables of atoms *i* and *j*, respectively, and the sum is taken over all interacting pairs. The "exchange" parameters J_{ij} are positive or negative for ferromagnetic and antiferromagnetic bonds, respectively.

Including the external field will transform the Hamiltonian to:

$$\mathcal{H}_{magn} = -\sum_{\langle ij \rangle} J_{ij}(\vec{S}_i \cdot \vec{S}_j) + \mu_B \vec{B} \sum_i g_i \vec{S}_i \,, \tag{2.2}$$

The second term represents the *Zeeman energy* which is caused by the external magnetic induction $\vec{B}$.

2.1.2. Hamiltonian of the chemical sub-system

It was previously discussed in Chapter 1, that Ni_3Fe system exhibits structural ordering. Thus, the total Hamiltonian will include a component which will describe chemical ordering. This term can be written in the Ising-type form:

$$\mathcal{H}_{chem} = -\sum_{\langle ij \rangle} \sum_{\alpha,\beta} V_{ij}^{\alpha\beta} \xi_i^{\alpha} \xi_j^{\beta} \tag{2.3}$$

where $\xi_i^{\alpha} = \begin{cases} 1, \text{ if site } i \text{ is occupied by an } \alpha\text{-atom} \\ 0, \text{ otherwise} \end{cases}$

(α, β) defines the type of atom, i.e. Fe or Ni and $V_{ij}^{\alpha\beta}$ is the pair-wise chemical interaction parameter.

2.1.3. Total Hamiltonian

In Ni_3Fe alloy magnetic order and structural order co-exist and experience mutual influence. Consequently, to describe correctly the properties of this alloy both sub-systems (spins and atoms) should be considered in the total Hamiltonian (including external magnetic field):

$$\begin{aligned} \mathcal{H}_{total} = \mathcal{H}_{magn} + \mathcal{H}_{chem} = &-\sum_{\langle ij \rangle} \sum_{\alpha\beta} J_{ij}^{\alpha\beta} (\vec{S}_i^{\alpha} \cdot \vec{S}_j^{\beta}) \xi_i^{\alpha} \xi_j^{\beta} - \sum_{\langle ij \rangle} \sum_{\alpha\beta} V_{ij}^{\alpha\beta} \xi_i^{\alpha} \xi_j^{\beta} \\ &+ \mu_B \vec{B} \sum_i \sum_{\alpha} g_i^{\alpha} \vec{S}_i^{\alpha} \xi_i^{\alpha} \end{aligned} \tag{2.4}$$

2.2. Monte Carlo technique

The Monte Carlo (MC) method can be used in many research areas, such as physical, chemical, mathematical, biological, economical problems and so on. A general definition of the MC method can be given as follows [73-75]:

The MC method is a method to estimate the parameters of a hypothetical population, based on a random sequence of numbers to construct a sample of the population, from which statistical estimates of the parameters can be obtained.

The key point of a problem is to define the Hamiltonian (without the kinetic energy term) and an appropriate statistical ensemble. Using associated distribution function and the partition function we should compute all the observables needed. So, the idea is to sample the main contributions to get an estimate for the observable.

2.2.1. Basic assumptions

The MC method is a stochastic simulation method which concept is based on the theory of Markov chain or Markov process. Markov process is the probabilistic analogue to classical mechanics. It is characterized by a lack of memory, i.e., the statistical properties of the immediate future are determined by the present, regardless of the past. The important property of a Markov chain is the existence of an invariant distribution of states.

Let us consider a sequence of states $\mathbf{x_0},...,\mathbf{x_n},\ldots$ of a system (this sequence is a sample of the phase space), the transition probabilities per unit time, $W(\mathbf{x},\mathbf{x'})$, from one state $\mathbf{x}$ of the system to a state $\mathbf{x'}$ are required to undergo certain restrictions in order to ensure that the states are distributed according to the equilibrium probability $\mathrm{P}(\mathbf{x})$:

i) Ergodicity – for all pairs (S,S′) of sets of phase points: there exists $\mathbf{x}\in\mathrm{S}$ and $\mathbf{x'}\in\mathrm{S'}$ such that $W(\mathbf{x},\mathbf{x'})\neq 0$;

ii) Positivity – for all $\mathbf{x}$, $\mathbf{x'}$: $W(\mathbf{x},\mathbf{x'})\geq 0$;

iii) Conservation – for all $\mathbf{x}$: $\sum_{\mathrm{x'}} W(\mathbf{x},\mathbf{x'})=1$;

iv) For all $\mathbf{x}$: $\sum_{x'} W(\mathbf{x},\mathbf{x'})\mathrm{P}(\mathbf{x'})=\mathrm{P}(\mathbf{x})$.

The condition for generating a stationary probability distribution during the process is:

$$\sum_{\mathrm{x'}} W(\mathbf{x},\mathbf{x'})P(\mathbf{x})=\sum_{\mathrm{x'}} W(\mathbf{x'},\mathbf{x})P(\mathbf{x'}) \tag{2.5}$$

Usually, one considers a more restrictive condition which is called the "detailed balance" condition:

$$\boxed{W(\mathbf{x},\mathbf{x'})\mathrm{P}(\mathbf{x})=W(\mathbf{x'},\mathbf{x})\mathrm{P}(\mathbf{x'})} \tag{2.6}$$

2.2.2. Monte Carlo method in the canonical ensemble

2.2.2.1. Metropolis algorithm

In the canonical ensemble [76-78] we can define the probability distribution at temperature T as:

$$P_T(\mathbf{x}) = \frac{\exp\left(-\mathcal{H}(\mathbf{x})/k_B T\right)}{Z^*(T)} = \frac{\exp\left(-\mathcal{H}(\mathbf{x})/k_B T\right)}{\sum_{\mathrm{x}} \exp\left(-\mathcal{H}(\mathbf{x})/k_B T\right)}, \tag{2.7}$$

where $\mathcal{H}(\mathbf{x})$ is the Hamiltonian of the system, k_B is the Boltzman constant and $Z^*(T)$ is the partition function at temperature T.

Combining Eq 2.7 with the "detailed balance" condition (Eq. 2.6) we obtain the ratio of the transition probabilities which depends only on the energy variation during the transition $\mathbf{x}\rightarrow\mathbf{x}'$:

$$W(\mathbf{x},\mathbf{x}')/W(\mathbf{x}',\mathbf{x}) = \exp(-[\mathcal{H}(\mathbf{x}') - \mathcal{H}(\mathbf{x})]/k_B T) = \exp(-\Delta\mathcal{H}/k_B T) \tag{2.8}$$

This equation doesn't specify the unique transition probability and many choices are possible. The *Metropolis MC method* is one of them. In this method [79], the transition probability W($\mathbf{x}$,$\mathbf{x}'$) per unit time is given by:

$$\boxed{W(\mathbf{x},\mathbf{x}') = \min\left\{1, \exp(-\Delta\mathcal{H}/k_B T)\right\}} \tag{2.9}$$

The Metropolis algorithm is defined as follows:

1) Specify an initial configuration $\mathbf{x_0}$
2) Choose randomly a new state $\mathbf{x}'$
3) Compute the energy variation associated to the transition: $\mathbf{x}\rightarrow\mathbf{x}'$
4) Compute the transition probability $W(\mathbf{x},\mathbf{x}') = \min\left\{1, \exp(-\Delta\mathcal{H}/k_B T)\right\}$
5) Generate a random number R$\in$[0,1]
6) If $W(\mathbf{x},\mathbf{x}') \geq R$ the transition $\mathbf{x}\rightarrow\mathbf{x}'$ is accepted,

   If $W(\mathbf{x},\mathbf{x}') < R$ the transition is rejected
7) Return to the step 2.

One MC step corresponds to the examination of each site of the system once.

In general, this algorithm guarantees that time averages are equal (within statistical errors) to the statistical mechanical averages which is called the ergodicity principle.

To study the behaviour of Ni_3Fe alloy we have distinguished 3 types of simulation:

1. *Simulations with Heisenberg Hamiltonian*

For the description of a magnetic system which consists of *N* interacting Heisenberg spins $\overrightarrow{S^i} = \left(S_x^i, S_y^i, S_z^i\right)$ we used the Hamiltonian defined by Eq. 2.1. Thus, each state of the system is defined as $\mathbf{x} = \left(\overrightarrow{S_1}, ..., \overrightarrow{S_i}, ...\overrightarrow{S_N}\right)$ and each new state $\mathbf{x}' = \left(\overrightarrow{S_1}, ..., \overrightarrow{S_i'}, ...\overrightarrow{S_N}\right)$ differs from the previous one by the change in the orientation of only one spin (single spin rotation algorithm): $W(\mathbf{x}, \mathbf{x}') = W\left(\overrightarrow{S_i}, \overrightarrow{S_i'}\right)$.

2. *Simulations with chemical Hamiltonian*

The system of *N* atoms is described by the configuration $\mathbf{x} = (\xi_1^\alpha, ..., \xi_i^\alpha, ..., \xi_k^{\alpha'}, ...\xi_N^\alpha)$, where α=(Ni or Fe) and α′≠α. The Hamiltonian corresponds to Eq. 2.3. Each new configuration is defined as $\mathbf{x}' = (\xi_1^\alpha, ..., \xi_i^{\alpha'}, ..., \xi_k^\alpha, ...\xi_N^\alpha)$, and differs from the previous state by the exchange of the atoms *i* and *k*: $W(\mathbf{x}, \mathbf{x}') = W\left(\left(\xi_i^\alpha, \xi_k^{\alpha'}\right); \left(\xi_i^{\alpha'}, \xi_k^\alpha\right)\right)$, α′≠α.

3. *Simulations with total Hamiltonian*

When the Hamiltonian includes both magnetic and chemical terms (Eq. 2.4) each state of the system is described by the atomic configuration and the direction of the spins, related to each atom, i.e. each configuration is described by a set of variables: $\mathbf{x} = \left(\left(\xi_1^\alpha, ..., \xi_i^\alpha, ..., \xi_k^{\alpha'}, ...\xi_N^\alpha\right); \left(\vec{S}_1^\alpha, ..., \vec{S}_i^\alpha, ..., \vec{S}_k^{\alpha'}, ..., \vec{S}_N^\alpha\right)\right)$. So, the new state of the system can differ from the previous by changes in both spin orientation and chemical configuration: $W(\mathbf{x}, \mathbf{x}') = W\left(\left(\xi_i^\alpha, \xi_k^{\alpha'}\right), \overrightarrow{S_i}; \left(\xi_i^{\alpha'}, \xi_k^\alpha\right), \overrightarrow{S_i'}\right)$. The combination of the previously described algorithms was implemented in a following way: **firstly, two atoms of different types are chosen and exchanged, then, a new orientation of their spins was proposed**.

2.2.2.2. Simulated annealing – Calculation of thermodynamic quantities

The algorithm of simulated annealing was proposed by S. Kirkpatrick *et al.* [80-81] and is used for optimization problems. In an annealing process the system, which is initially at high temperature and disordered, is slowly cooled so that the system is in thermodynamic equilibrium at any time. As cooling proceeds, the system becomes more ordered and approaches a "frozen" ground state at $T = 0K$. If the initial temperature of the system is too low or the cooling is not

sufficiently slow, the system may be frozen in a metastable state (i.e. trapped in a local minimum energy state).

At each temperature T, a large number of MC steps are performed in order to reduce statistical errors. The probability of transition to the new configuration decreases with the temperature (it is approximately 1 at high T in the disordered state and approaches 0 for low T when the system is almost ordered).

In the course of the annealing process it is possible to estimate the observables of the system. The technique of calculation is as follows. A certain number of MC steps, n_0, is used to reach equilibrium at temperature T. This period of time is the so called *equilibration time* (Fig. 2.2). The equilibration time is the time needed for the system to "forget" the initial configuration. This is because in the Markov chain the configurations generated one after another are correlated. To estimate n_0 it is possible to plot the graph of any observable (for example, internal energy) as a function of time and to note when the system reaches the equilibrium. "*Equilibrium*" means that the average probability of finding the system in any particular state **x** is proportional to the Boltzmann weight $e^{(-\mathcal{H}(\mathbf{x})/k_B T)}$. Thus, the averaging should be done over $(n-n_0)$ MC steps, where n is the total number of MC steps. A system in equilibrium spends the majority of its time in small subsets of states in which its properties take a narrow range of values.

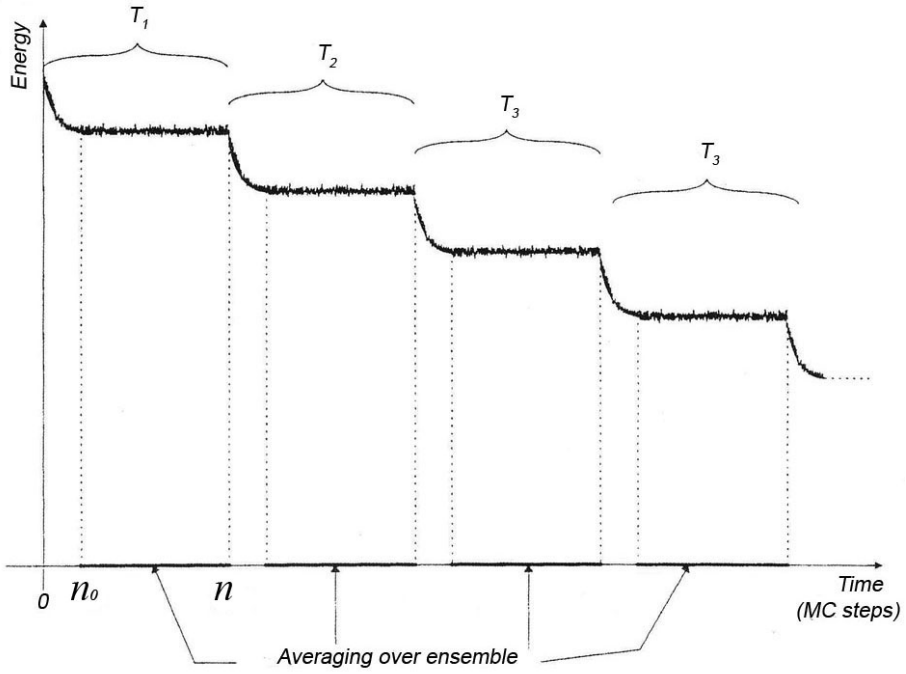

Figure 2.2. Schematic representation of the time variation of the energy during the simulated annealing

When the system has reached the equilibrium, the observables can be estimated (within statistical errors) by averaging over the MC steps:

$$\langle A \rangle_T \cong \frac{1}{n - n_0} \sum_{l=n_0+1}^{n} A(\mathbf{x}_l) \tag{2.10}$$

The thermodynamic quantities of our interest are: internal energy, magnetization, specific heat, susceptibility, long-range and short-range order parameters. Thus, taking into account Eq. 2.10, $\langle \ \rangle_T$ will denote time averaging and the calculation of these quantities can be done as follows.

- Internal energy $U(T)$ per spin (atom):

$$U(T) = \langle E \rangle_T = \frac{\langle \mathcal{H} \rangle_T}{N} \cong \frac{1}{(n - n_0)N} \sum_{l=n_0+1}^{n} \mathcal{H}(\mathbf{x}_l) \tag{2.11}$$

where N is the total number of spins (atoms).

- Specific heat $C(T)$ per spin (atom):

$$C(T) = \frac{\partial U(T)}{\partial T} = \frac{1}{N k_B T^2} \left(\langle \mathcal{H}^2 \rangle_T - \langle \mathcal{H} \rangle_T^2 \right) \tag{2.12}$$

During the evolution of the system it is interesting to measure its state of order, which can be defined using the order parameters, either long-range or short-range. In the ordered state they have non-zero values and in the fully disordered state they are equal to zero.

For the chemical ordering the long-range and the short-range order parameters can be defined as follows. The redistribution of the atoms in the lattice leads to a preferential occupation of certain "right" positions (appropriate for certain type of atom) in order to form an ordered structure (as was previously mentioned, for the Ni_3Fe alloy the random structure transforms into the ordered $L1_2$-type superstructure). In this way the order can be defined by the distribution of atoms on all sites (i.e. not only 1st coordination shell) of the lattice and therefore it is called *long-range order*.

- Long-range order parameter $\eta(T)$:

$$\eta(T) = \frac{1}{3} \left(4 \frac{\langle N_{Fe,A} \rangle_T}{N_{Fe}} - 1 \right), \tag{2.13}$$

where $N_{Fe,A}$ is the number of Fe atoms on A – sublattice (in Fig. 2.1 the whole set of Fe atoms forms the A-sublattice and the B-sublattice is formed by Ni atoms, respectively), N_{Fe} is the total number of Fe atoms. So, $\eta = 1$ in the ordered state, and $\eta = 0$ in the disordered state.

The state of order can be characterized in another way, considering how fully atoms of a certain kind (in the whole crystal) are surrounded by the atoms of another kind. In this way the order is defined by the local environment of the atoms and therefore it is called *short-range order*. It should be underlined that even in a disordered alloy where no long-range order is present, there still be short-range order (for example in disordered state above T_K). Short-range order shows the presence of correlations between atomic substitutions.

- Short-range order parameters

  SROP(T):

$$SROP(T) = \frac{1}{3}\left(4\left\langle Z_{NiFe}\right\rangle_T - 9\right), \tag{2.14}$$

where $\left\langle Z_{NiFe}\right\rangle_T$ is the average number of Ni-Fe bonds per atom. $SROP = 1$ in the ordered state (because for $L1_2$ $\left\langle Z_{NiFe}\right\rangle_T = 3$), and $SROP = 0$ in the disordered state (because $\left\langle Z_{NiFe}\right\rangle_T = \frac{9}{4}$).

Warren-Cowley parameter $\alpha_r(T)$:

$$\alpha_r(T) = 1 - \frac{p_{Ni-Fe,r}(T)}{c_{Ni}}, \tag{2.15}$$

where r is the number of the coordination shell and $p_{Ni-Fe,r}$ is the probability to find a Ni-Fe pair. In the disordered state $p_{Ni-Fe,r}$ is equal to the average concentration, c_{Ni} , and therefore $\alpha_r = 0$. For the $L1_2$-type superstructure α_r = -1/3 and 1, for the 1st and 2nd coordination shells, respectively. The negative values of α_r signify short-range ordering tendency in the studied system. This short-range order parameter is closely connected to the experimental results and its value can be obtained from scattering intensity [15-20,96].

For the ferromagnetic ordering, the reduced magnetization, $M(T)/M_{sat}$, characterizes the long-range order in the system and can be considered as a long-range magnetic order (LRMO) parameter.

- "Magnetization" $M(T)$ per spin:

$$M(T) = \left\langle m\right\rangle_T \cong \frac{1}{n-n_0}\sum_{l=n_0+1}^{n}\left(m_x^2(\mathbf{x}_l) + m_y^2(\mathbf{x}_l) + m_z^2(\mathbf{x}_l)\right)^{1/2} \tag{2.16a}$$

where $\vec{m}$ is defined by $\vec{m} = -\frac{1}{N}\sum_i g_i \vec{S}_i$ and represents the magnetic moment per atom (in μ_B units). The reduced magnetization $M(T)/M_{sat}$ is obtained by using

$$M_{sat} = \frac{1}{N}\left[N_{Fe} g_{Fe} s_{Fe} + N_{Ni} g_{Ni} s_{Ni}\right] \tag{2.16b}$$

- Magnetic susceptibility $\chi(T)$ per spin:

$$\chi(T) = \lim_{H \to 0} \frac{1}{\mu_0} \left.\frac{\partial M(T,H)}{\partial H}\right|_T = \frac{N}{k_B T}\left(\left\langle m^2 \right\rangle_T - \left\langle m \right\rangle_T^2\right), \tag{2.17}$$

where H represents the applied magnetic field.

2.2.3. Statistical and systematic errors

In MC simulations different kinds of errors and limitations can influence the numerical results. Firstly, we should mention truncation and round-off errors which arise due to the limited computer word length and hence limited precision for the numerical values. Although these errors are negligible, they should be indicated. Statistical and systematic errors appear due to the limited computer time.

Statistical errors occur because of the necessarily finite number of MC steps during the simulations [73-75, 82-83]. Also, an additional contribution to the statistical errors is present when investigating systems with configurational disorder [84]. Then, it is necessary to average the numerical results over a sufficient number of MC steps and also over several configurations in order to reduce these errors.

Systematic errors can be divided into those which arise from the finite size of systems (so called finite-size effects) and those which appear owing to the finite number of MC steps.

In order to reduce both statistical and systematic errors, large enough system size and number of MC steps (much longer than the correlation time) should be considered.

In this work we were not interested in a particular analysis of these errors, but in the final results the uncertainties are supposed to include them by performing several "identical" simulations.

2.2.4. Finite-size effects

Finite-size effects influence both 2nd and 1st order transitions and introduce systematic deviations from the macroscopic behavior.

A 2nd order phase transition is characterized by the continuous character of the entropy and the long-range order parameter at the transition. Due to this fact the transition is not accompanied by a latent heat, but at the transition point some singularities occur in the

derivatives of the mentioned quantities [77]. Consequently, in the thermodynamic limit the specific heat, $\left(C \propto \frac{\partial S}{\partial T} \right)$, and the susceptibility, $\left(\chi \propto \frac{\partial M}{\partial H} \right)$ either diverge or exhibit a jump at the transition. For finite systems the divergence is rounded and therefore a maximum appears [8,76-78].

In its turn, a 1st order-disorder transition is accompanied by a latent heat, i.e. the entropy and the long-range order parameter are discontinuous at the transition. These discontinuities result in δ-function singularities in the specific heat and the derivative of the long-range order parameter. Due to finite-size effects, they turn into finite peaks with finite width [81,86]. The location of these peaks depends on the measured quantity and system size. For both 1st and 2nd order transitions, the location of the maxima of the 2nd derivatives of the free energy (for example, specific heat and susceptibility) tends to the transition temperature in the thermodynamic limit.

Chapter 3

Mean-Field theory for thermodynamic and kinetic's studies

3.1. Atomic ordering of alloys

In the substitutional alloys the atoms can be either randomly distributed on the lattice sites (disordered alloy) or different sorts of atoms can preferentially occupy different lattice sites and form a periodic ordered structure. Such ordered structures are realized at sufficiently low temperatures. Let us remind that we define the temperature of *order-disorder phase transition* as T_K . This temperature is also called the Kurnakov temperature.

The degree of order in the alloy can be characterized by the long-range order and short-range order parameters. These parameters characterize the state of order and particularly the environment of each atom, as was previously defined in section 2.2.2.2. It should be underlined that even in disordered alloys where the long-range order parameter is equal to zero, there is still short-range order.

In general case, the transition from a disordered alloy to an ordered state can be 1st or 2nd order. The order of transition can be defined from the derivatives of the Helmholtz free energy F. At constant volume, V, and pressure, p, the Helmholtz free energy is:

$$F = U - TS\,, \tag{3.1}$$

where U – is the internal energy, T – is the temperature and S – is the entropy.

The *1st order transitions* are those that involve a latent heat. During such a transition, a system either absorbs or releases a fixed amount of energy. Because energy can not be instantaneously transferred between the system and its environment, 1st order transitions are associated with "mixed-phase regimes" in which some parts of the system have completed the transition and others have not. At the transition point $T = T_K$ the phase equilibrium is obtained, and $F^{(1)} = F^{(2)}$, where $F^{(1)}$ and $F^{(2)}$ are the free energies of the different phases (for example, ordered and disordered phases, gas and liquid phases, etc…).

The *2nd order transition* occurs when the 1st derivatives of F with respect to temperature and pressure are continuous but the 2nd derivatives exhibit a discontinuity or divergence. Consequently, the specific heat, the thermal expansion coefficient and the compressibility have a jump at the transition temperature. In this case the latent heat is absent due to the absence of an entropy jump. The 2nd order transition proceeds smoothly. The high temperature phase transforms itself into the new low temperature phase in a continuous manner.

As was mentioned earlier, in case of Ni_3Fe alloy, two phase transitions take place – the 2nd order magnetic phase transition from paramagnetic to ferromagnetic state and the 1st order phase transition from a disordered fcc to the ordered $L1_2$ phase.

3.2. Some approaches to the description of ordering.

To describe the order-disorder phase transitions several theories have been developed. It is possible to distinguish between thermodynamic and statistical approaches. The *first* one is based on the properties of crystal symmetry and some thermodynamic functions [77, 88 and references therein].

The *second* one, the statistical approach is based on some simplified model of alloy. The entropic term in Eq. 3.1 is connected to the definition of a statistical sum and this task becomes a main problem in these models. The statistical sum, Z, represents the number of atomic configurations in the alloy at a given temperature T, and some simplifications should be done for its calculation. The internal energy term in Eq. 3.1 is defined using assumptions about the nature of the interactions between the atoms (pair-wise, many-body, etc...).

It is necessary to refer to the mean-field approximation of Bragg and Williams, which does not include correlations between the atoms but only long-range order is under investigation; the interactions are thought to be pair-wised. In spite of these simplifications, this approach gives a qualitative agreement with experimental data, but to improve a quantitative agreement it is necessary to make some further assumptions. Later, the short-range order has been taken into account by Bethe, Peierls [90 and references therein], Kirkwood [93] and in the "quasi-chemical" method. The "cluster variation method" proposed by Kikuchi [84-85] is also widely used. In terms of this method some results of the previous theories can be obtained (it is by itself an appreciable improvement of "quasi-chemical" method).

The development of the experimental diffraction data led Cowley to the formulation of the theory which included the specified short-range order parameter [96-97] which is related to the intensity of diffusion scattering. The short-range order in this case can be calculated till n^{th} neighbors.

To investigate the order in alloys the computer simulation methods have been also extensively used (Monte Carlo methods [98-100], iteration method (used in "cluster variation method") [95], etc.).

3.3. Mean-field approximation.

In the present work, to describe the thermodynamics and kinetics in Ni-Fe alloys a mean-field approximation was used. To calculate the free energy, we can firstly define the occupation variable $\xi_\alpha(\mathbf{r})$ in a substitutional alloy:

$$\xi_\alpha(\mathbf{r}) = \begin{cases} 1, \text{ if site } (\mathbf{r}) \text{ is occupied by an } \alpha\text{-atom} \\ 0, \text{ otherwise} \end{cases} \tag{3.2}$$

where α – is the sort of atom and $\mathbf{r}$ – is the vector which defines the site in the crystal lattice. Each lattice site is occupied by an atom, therefore the variables $\xi_\alpha(\mathbf{r})$ are not independent:

$$\sum_\alpha \xi_\alpha(\mathbf{r}) = 1 \tag{3.3}$$

Using the model of pair-wise interactions, the Hamiltonian of this system can be defined as:

$$\mathcal{H} = \frac{1}{2}\sum_{\mathrm{r,r'}}\sum_{\alpha,\beta} V_{\alpha\beta}(\mathbf{r}-\mathbf{r}')\xi_\alpha(\mathbf{r})\xi_\beta(\mathbf{r}') \tag{3.4}$$

This Hamiltonian is similar to that defined in previous chapter (Eq. 2.3) and $V_{\alpha\beta}(\mathbf{r}-\mathbf{r}')$ represents the pair-wise interaction parameter between atoms α and β, which are placed at sites $\mathbf{r}$ and $\mathbf{r}'$. It should be noted that the sign in Eq. 3.4 is different from Eq. 2.3. The sign is included into the value of $V_{\alpha\beta}(\mathbf{r}-\mathbf{r}')$. From Eq. 3.4 the internal energy U can be written as:

$$\left\langle \mathcal{H} \right\rangle_T = U = \frac{1}{2}\sum_{\mathrm{r,r'}}\sum_{\alpha,\beta} V_{\alpha\beta}(\mathbf{r}-\mathbf{r}')\left\langle \xi_\alpha(\mathbf{r})\xi_\beta(\mathbf{r}') \right\rangle \tag{3.5}$$

In the framework of mean-field approximation the correlations are neglected and we can write:

$$\left\langle \xi_\alpha(\mathbf{r})\xi_\beta(\mathbf{r}') \right\rangle = \left\langle \xi_\alpha(\mathbf{r}) \right\rangle \left\langle \xi_\beta(\mathbf{r}') \right\rangle = p_\alpha(\mathbf{r})\, p_\beta(\mathbf{r}') \tag{3.6}$$

where $p_\alpha(\mathbf{r})$ ($p_\beta(\mathbf{r}')$) is the probability to find an atom of sort α (β) at the site $\mathbf{r}$ ($\mathbf{r}'$). Then, Eq. 3.5 can be rewritten in the next form:

$$U = \frac{1}{2}\sum_{\mathrm{r,r'}}\sum_{\alpha,\beta} V_{\alpha\beta}(\mathbf{r}-\mathbf{r}')\, p_\alpha(\mathbf{r})\, p_\beta(\mathbf{r}') \tag{3.7}$$

The following condition is satisfied:

$$\sum_\alpha p_\alpha(\mathbf{r}) = 1 \tag{3.8a}$$

Then, in case of binary A-B alloy we can replace:

$$\begin{aligned} p_\alpha(\mathbf{r}) &\to p(\mathbf{r}) \\ p_\beta(\mathbf{r}) &\to 1 - p(\mathbf{r}) \end{aligned} \tag{3.8b}$$

and the internal energy (Eq. 3.7.) will take the next form:

$$\boxed{U = \frac{1}{2}\sum_{\mathrm{r,r'}} w(\mathbf{r}-\mathbf{r}')\, p(\mathbf{r})\, p(\mathbf{r}')} \tag{3.9}$$

where $w(\mathbf{r}-\mathbf{r}')$ – is the *ordering ("mixing") energy* defined as:

$$\boxed{w(\mathbf{r}-\mathbf{r}') = V_{AA}(\mathbf{r}-\mathbf{r}') + V_{BB}(\mathbf{r}-\mathbf{r}') - 2V_{AB}(\mathbf{r}-\mathbf{r}')} \tag{3.10}$$

At high temperature when $w / k_B T << 1$ the minimum of the free energy corresponds to an ideal solution. In this case the atoms are randomly distributed on all crystal lattice sites [88-92].

At low temperatures when the value of the ordering energy, w, is much larger that the thermal energy $k_B T$ (i. e. $w / k_B T >> 1$) the minimum of the free energy can be attained if some ordered phase is formed. In this case the lowest energy corresponds to the configurations in which each atom is surrounded by the other kind of atoms.

The phase transition from disordered to ordered phase takes place at an intermediate temperature when $w / k_B T \approx 1$.

In the mean-field approximation the second term in Eq. 3.1 corresponds to the configurational entropy, which can be written as:

$$S = -k_B \sum_{\mathbf{r}} \sum_{\alpha} p_\alpha(\mathbf{r}) \ln p_\alpha(\mathbf{r}) .$$

Taking into account Eq. 3.8, for binary A-B alloy this equation can be rewritten in the following form:

$$\boxed{S = -k_B \sum_{\mathbf{r}} \left[p(\mathbf{r}) \ln p(\mathbf{r}) + (1 - p(\mathbf{r})) \ln(1 - p(\mathbf{r})) \right]} \qquad (3.11)$$

Substituting Eq. 3.7 and Eq. 3.11 into Eq. 3.1, the expression for free energy of the alloy will be obtained in the framework of mean-field approximation.

3.4. Static concentration waves approximation.

In a disordered state, all crystal lattice sites are occupied by the different kinds of atoms with the same probability which is equal to the atomic fractions c_α ($c_\alpha = \frac{N_\alpha}{N}$). In the ordered structures, there is a preferential occupation of some sites and, therefore, the occupation probability becomes dependent on the site **r**. This dependence subdivides the lattice into different sublattices. To describe this dependence, A. G. Khachaturyan has proposed a "static concentration waves" (SCW) method [91-92].

In the SCW method, the occupation probability $p(\mathbf{r})$ can be presented as:

$$p(\mathbf{r}) = c + \Delta(\mathbf{r}) , \qquad (3.12)$$

where c is the atomic fraction of the solute element and $\Delta(\mathbf{r})$ is the fluctuation of concentration due to the ordering. In general case, the fluctuation in the solid state has a periodic character and, therefore, it can be expanded in a Fourier series. Thus, Eq. 3.12 will have a form:

$$p(r) = c + \frac{1}{2} \sum_{s} \sum_{j_s} \left[Q(\mathbf{k}_{j_s}) e^{i\mathbf{k}_{j_s}\mathbf{r}} + Q^*(\mathbf{k}_{j_s}) e^{-i\mathbf{k}_{j_s}\mathbf{r}} \right] \qquad (3.13)$$

The summation is carried out over all vectors $\{\boldsymbol{j}_s\}$ of the star $\boldsymbol{s}$. The "*star*" $\boldsymbol{s}$ is defined as a set of wave vectors $\boldsymbol{k}_{js}$ that may be obtained from given wave vector by applying to it all operations of the symmetry group of the disordered solution. A static concentration wave is represented by $\exp(i\mathbf{k}_{j_s}\cdot\mathbf{r})$, $\boldsymbol{k}_{js}$ are non-zero wave vectors defined in the 1st Brillouin zone of the disordered alloy, $\mathbf{r}$ is a site vector of the lattice, j_s is the index, denoting the wave vectors of a star $\boldsymbol{s}$ in the 1st Brillouin zone. Static concentration wave amplitude $Q(\mathbf{k}_{j_s})$ can be written as:

$$Q(\mathbf{k}_{j_s}) = \eta_s \gamma_s(j_s),$$

where η_s are the long-range order parameters and $\gamma_s(\boldsymbol{j}_s)$ are coefficients which determine the symmetry of the occupation probabilities $p(\mathbf{r})$ (the symmetry of superstructure).

Therefore, Eq. 3.13 gives the transition from the description of the relevant atomic distribution in an ordered phase in terms of N occupation probabilities $p(\mathbf{r})$ to the description in terms of N amplitudes $Q(\mathbf{k}_{j_s})$.

The long-range order parameters η_s are proportional to the amplitudes of the static concentration waves. To avoid the ambiguity in the definition of η_s it is possible to postulate that in the ordered state when the occupation probabilities $p(\mathbf{r})$ are either 0 or 1 on all lattice sites, all the parameters η_s should be equal to 1. This condition also completely defines the values of constants $\gamma_s(\boldsymbol{j}_s)$. The amplitude of the concentration wave is proportional to the structure amplitude of this reflection.

The $L1_2$-type superstructure (Fig. 2.1) is generated by three wave vectors (001), (010) and (100). Using the SCW approach the occupation probability for this superstructure can be rewritten as:

$$p(\mathbf{r}) = c + \frac{\eta}{4}\left(e^{i2\pi\mathbf{a}_1^*\cdot\mathbf{r}} + e^{i2\pi\mathbf{a}_2^*\cdot\mathbf{r}} + e^{i2\pi\mathbf{a}_3^*\cdot\mathbf{r}}\right) \tag{3.14}$$

where $\mathbf{a}_1^*, \mathbf{a}_2^*, \mathbf{a}_3^*$ - are the unit reciprocal lattice vectors of the f.c.c. lattice, $|\mathbf{a}_1^*| = |\mathbf{a}_2^*| = |\mathbf{a}_3^*| = 1/a_{fcc}$ and a_{fcc} – is the lattice parameter. In the case of fcc lattice the occupation probabilities can take only following values:

$$\begin{cases} p_1 = c + \dfrac{3}{4}\eta \\ p_2 = c - \dfrac{1}{4}\eta \end{cases}$$

This definition of the probability $p(\mathbf{r})$ can be used to define the internal energy and entropy (Eqs. 3.9, 3.11) of a system [91-92,105,119-126]:

$$U_{at} = \frac{N}{2}\left\{\tilde{w}(\mathbf{k}_0)c^2 + \frac{3}{16}\eta^2\tilde{w}(\mathbf{k}_X)\right\},$$

$$S_{at}(\eta) = -\frac{Nk_B}{4}\left\{\begin{array}{l} 3\left(c-\frac{\eta}{4}\right)\ln\left(c-\frac{\eta}{4}\right)+3\left(1-c+\frac{\eta}{4}\right)\ln\left(1-c+\frac{\eta}{4}\right)+ \\ +\left(c+\frac{3}{4}\eta\right)\ln\left(c+\frac{3}{4}\eta\right)+\left(1-c-\frac{3}{4}\eta\right)\ln\left(1-c-\frac{3}{4}\eta\right) \end{array}\right\} \quad (3.15)$$

The sub-script "*at*" signifies that these equations consider only chemical interactions, i.e. atomic ordering. $\tilde{w}(\mathbf{k})$ represents the Fourier transform of the mixing energy:

$$\tilde{w}(\mathbf{k}) = \sum_{\mathbf{r}} w(\mathbf{r})\exp(-i\mathbf{kr}) \quad (3.16a)$$

where $\mathbf{k} = (k_x, k_y, k_z) = 2\pi(h\mathbf{a}_1^* + k\mathbf{a}_2^* + l\mathbf{a}_3^*)$. This Fourier transform can be rewritten in the following form [101]:

$$\tilde{w}(\mathbf{k}) = \sum_{\mathbf{r}} w(\mathbf{r})\exp\left(-i\mathbf{k}\cdot\mathbf{r}\right) = \sum_{s} w^{(s)}\phi^{(s)}(\mathbf{k}), \quad (3.16b)$$

where $w^{(s)}$ is the effective interaction for the shell *s* and for fcc lattices the *shell function* ϕ, for an arbitrary coordination shell, is given by a formula:

$$\phi^{(s)}(\mathbf{k}) = \frac{z^{(s)}}{6}\sum_{j=1}^{3}\cos\left(2\pi h_1 p_j^{(s)}\right)\left[\cos\left(2\pi h_2 p_{j+1}^{(s)}\right)\cos\left(2\pi h_3 p_{j+2}^{(s)}\right)+\cos\left(2\pi h_3 p_{j+1}^{(s)}\right)\cos\left(2\pi h_2 p_{j+2}^{(s)}\right)\right],$$

where $z^{(s)}$ is the number of lattice points in the coordination shell *s*, $p_j^{(s)}$ are integers and half-integers denoting the Cartesian coordinates of a point in a 1st octant of the shell *s*, h_i denotes Cartesian coordinates in the 1st Brillouin Zone.

Following this formula it is easy to calculate the terms $\tilde{w}(\mathbf{k}_0)$ and $\tilde{w}(\mathbf{k}_X)$ in Eq. 3.15 for the supersymmetrical points $\mathbf{k}_{X,0}$ of the fcc lattice in the reciprocal space with coordinates {100} and {000}, respectively. Thus, $\tilde{w}(\mathbf{k}_0)$ and $\tilde{w}(\mathbf{k}_X)$ are defined as:

$$\begin{aligned} \tilde{w}(\mathbf{k}_0) &= 12w(\mathbf{R}_1)+6w(\mathbf{R}_2)+24w(\mathbf{R}_3)+12w(\mathbf{R}_4)+\ldots \\ \tilde{w}(\mathbf{k}_X) &= -4w(\mathbf{R}_1)+6w(\mathbf{R}_2)-8w(\mathbf{R}_3)+12w(\mathbf{R}_4)+\ldots \end{aligned} \quad (3.17)$$

where $\mathbf{R}_i$ corresponds to the radius of the i^{th} coordination shell.

3.5. Molecular field approach

The concept of the mean-field can be also applied to the magnetic transitions. To explain the spontaneous magnetization of ferromagnets P. Weiss proposed a hypothesis about the existence of an internal *molecular field* $\boldsymbol{H}_{\text{mol}}$ which acts similarly to an external magnetic field $\boldsymbol{H}_{ext}$ in paramagnets and induces the parallel orientation of atomic magnetic moments at low

temperature without applied field. At high temperatures the magnetic order is destroyed due to the strong thermal fluctuations.

P. Weiss assumed that $\boldsymbol{H}_{mol}$ would be proportional to the magnetization [5-6,8]. Consequently, the total magnetic field is:

$$\mathbf{H} = \mathbf{H}_{ext} + \mathbf{H}_{mol} = \mathbf{H}_{ext} + \lambda \cdot \mathbf{M}\,, \tag{3.18}$$

where λ – is the constant of molecular field. As the molecular field approximation by itself is a mean-field approach, all the fluctuations (spatial and time) of the molecular field are neglected [6,8,76]. This leads to an overestimation of T_C and sometimes to wrong results, especially for 1D and 2D systems.

Using the molecular mean-field approach all the thermodynamic quantities can be calculated. For example, the magnetization of the ferromagnetic system per atom, M, for the arbitrary spin S can be written in the next form [78]:

$$M = Sg\mu_B B_J\left(\frac{Sg\mu_B}{k_B T}(H_{ext} + \lambda \cdot M)\right) = M_{Sat} B_S(x)\,, \tag{3.19}$$

where g is the Landé factor ($g_S \approx 2$, $g_L \approx 1$), $M_{Sat} = g\mu_B S$ is the saturation magnetization and $B_S(\ )$ is the Brillouin function [5-8], which is defined by the formula:

$$B_S(x) = \left(1+\frac{1}{2S}\right)coth\left(\left(1+\frac{1}{2S}\right)x\right) - \frac{1}{2S}coth\left(\frac{1}{2S}x\right), \tag{3.20}$$

$$x = \frac{Sg\mu_B H}{k_B T}.$$

In Fig. 3.1 the Brillouin function is plotted for different values of spin S.

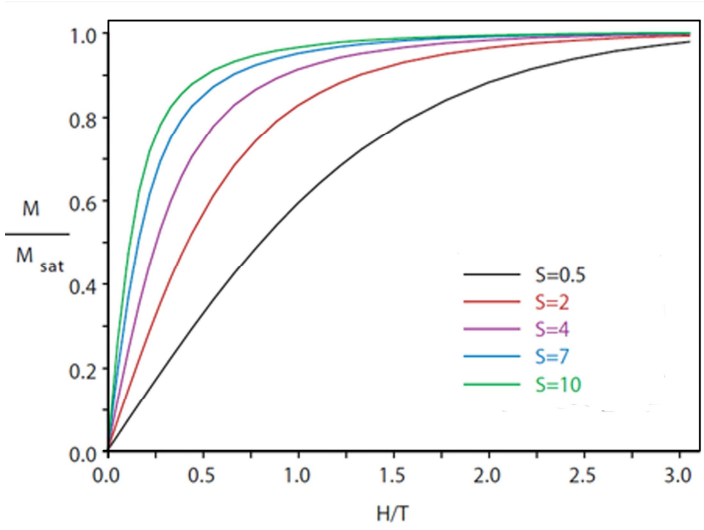

Figure 3.1. Brillouin function for different values of spin *S*

For the case when $S = ½$, the magnetization formula can be simplified:

$$M = \frac{g\mu_B}{2} th\left(\frac{g\mu_B}{2k_B T} \lambda \cdot M \right) \tag{3.21}$$

From Fig. 3.2 it is seen that in the temperature range (0; T_C) Eq. 3.21 describes quite well the experimentally observed data. As follows from this figure, there is a discontinuity of the second derivatives of the free energy at T_C (the second derivative with respect to the applied field is proportional to the first derivative of the magnetization).

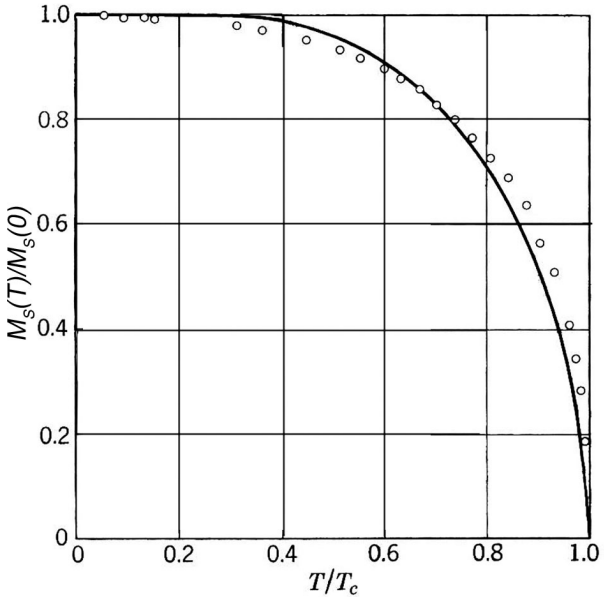

Figure 3.2. Saturation magnetization of Ni and theoretical (MFT) curve for *S* = ½ [2]

In general, the mean-field theory gives a reasonable agreement close to T_C only in 3D systems. At low temperatures, $T << T_C$, it gives rough approximation of the magnetization variation and does not predict spin waves [5-6,8].

It should be also mentioned that due to the fact that spin-correlations are neglected – the definition of the short-range order parameter is not included in the molecular field theory (so as in mean-field approximation). However, the experiments have shown that above T_C such short-range order exists [13]. To take into account this effect the microscopic theories have been developed [5], but we will further use the presented above approximation.

Using molecular-field approximation, the expression for the magnetic entropy can be evaluated. In case of an arbitrary quantum spin value S (integer or half-integer) and in the absence of external magnetic field, it gives a complicated self-consistent formula for the magnetic entropy:

$$S_{magn} = Nk_B \left\{ \ln sh\left(\frac{2S+1}{2S} y \right) - \ln sh\left(\frac{1}{2S} y \right) - yB_S(y) \right\}, \tag{3.22}$$

where $B_S(y)$ is a Brillouin function and y is defined as:

$$y = \frac{g\mu_B S}{k_B T} H = \left.\begin{cases} H = H_{ext} + H_{mol} \\ H_{ext} = 0; H_{mol} = \lambda \cdot M \end{cases}\right\} = \frac{g\mu_B S}{k_B T}(\lambda \cdot M)$$

The explicit derivation of Eq. 3.22 will be given in Appendix 5.2.1.

3.6. Precipitation processes in the alloys

A homogeneous non-stoichiometric solid solution is stable only at elevated temperatures. With a temperature decrease, the solid solution becomes unstable with respect to the thermal fluctuations and solute-rich clusters (precipitates) are formed. This is so called nucleation stage. After nucleation the particles of a new phase start to grow by absorption of solute elements from the matrix. Therefore, the solute concentration in the initial disordered matrix is lowered and precipitates continue to grow until the matrix concentration reaches its equilibrium value. After that, the coarsening stage is started. During this stage the free energy of a system is minimized by the reduction of the interface energy and it leads to the dissolution of small particles and the growth of larger ones. All these stages are described in more details below.

3.6.1 Nucleation and growth

It is generally known that after quenching the system is in metastable state. In the domain of nucleation to go to the equilibrium stable state the system should overcome an activation barrier and form the nuclei of a new phase. The formation of the nucleus of a new phase (for example, spherical precipitate) induces the increase in the free energy by the value of $4\pi\sigma R^2$, where R is the radius of a nucleus and σ is the interface energy per surface unit. At the same time, the change of the volume free energy is proportional to the volume of nucleus, $\frac{4}{3}\pi R^3$. Thus, when R is small, the volume free energy is smaller than the interfacial free energy and the formation of a nucleus is thermodynamically disadvantageous. Only starting from some critical radius, $R_C^{nucleus}$, the growth of a nucleus is accompanied by the reduction of the total free energy and the process can continue spontaneously. Therefore the formation of a nucleus of a new phase in the metastable state requires a fluctuation with some critical amplitude and size.

Let us suppose that after nucleation the stable nucleus is embedded into a still supersaturated matrix. The particle will then be surrounded by a concentration gradient which provides the driving force for a solute diffusion, and thus gives rise to its growth. The solute moves to the precipitate's boundary and matrix becomes depleted as shown in Fig. 3.3. The

region with a concentration gradient in the vicinity of precipitate is called the *depletion zone*. In general, it is assumed that in this zone there is a local thermodynamic equilibrium.

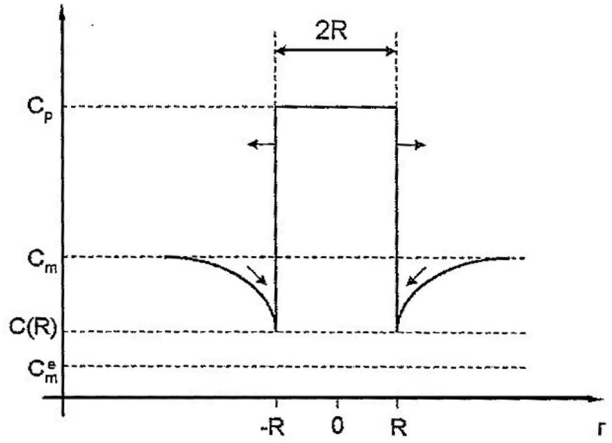

Figure 3.3. Schematic concentration profile of a precipitate with the radius *R*

The flux of atoms through the interface "matrix-precipitate" is described by the 1st Fick's law:

$$\vec{J} = -D\left(\frac{dC(r)}{dr}\right)\vec{u}_r, \tag{3.23}$$

where $C(r)$ is the concentration as a function of a radial variable r, $\vec{u}_r$ is the radial unit vector, and D is the diffusion coefficient, which is supposed here to be concentration independent.

Imposing the *mass balance condition* at the surface of the precipitate, the following expression for the infinitesimal volume variation is obtained:

$$\frac{d}{dt}\left(\frac{4\pi}{3}R^3\right) = -\vec{J}\cdot\vec{u}_r 4\pi R^2 \quad \Leftrightarrow \quad 4\pi R^2\frac{dR}{dt} = 4\pi R^2 D\left(\frac{dC(r)}{dr}\right) \tag{3.24}$$

Then, the *growth rate* of the precipitate will be:

$$\frac{dR}{dt} = D\left(\frac{dC(r)}{dr}\right) \tag{3. 25}$$

To obtain time dependence of the radius R it is necessary to solve the 2nd Fick's law for the concentration field $C(r)$ in the interval [R; +∞[. For the supersaturated matrix, where $\left(C_m - C_m^e\right)$ is very small (C_m and C_m^e are the concentration of solute in the matrix and concentration in equilibrium matrix, respectively), it is possible to suppose that $C(r)$ is time independent. Then, assuming quasi-stationary state it is sufficient to solve $\Delta C(r) = 0$, where Δ is Laplacian. The concentration gradient in the vicinity of precipitate's surface is equal to $\frac{1}{R}\frac{\left(C_m - C(R)\right)}{\left(C_p - C(R)\right)}$ and therefore:

$$\frac{dR}{dt} = \frac{\left(C_m - C(R)\right)}{\left(C_p - C(R)\right)} \frac{D}{R} \tag{3.26}$$

In Eq. 3.26 C_p is the equilibrium concentration in the precipitate (Fig. 3.3). To simplify the Eq. 3.26, it is possible to consider that the matrix concentration, C_m, is equal to the initial concentration C_0. The concentration in the depletion zone, $C(R)$, can be approximated by the matrix concentration at the end of precipitates' growth stage, C_m^e. Thus, the integration gives:

$$R = \left(2 \frac{C_0 - C_m^e}{C_p - C_m^e} \right)^{\frac{1}{2}} (Dt)^{\frac{1}{2}} \tag{3.27}$$

It should be mentioned that in general, the precipitates grow in different sizes and shapes. And when the precipitates volume fraction reaches its equilibrium value, small particles begin to disappear and larger ones grow – this stage corresponds to *coarsening*.

3.6.2. Coarsening

Following the stage of growth, the *coarsening* (or *Ostwald ripening* after the physical chemist W. Ostwald, who originally described this process qualitatively [109-110]) becomes a dominant diffusion process. In general, for the constant volume fraction of precipitates, an alloy with a large number of small precipitates has more interfaces than an alloy with a smaller number of large precipitates. The interfacial energy gives a positive contribution to the free energy of the system and during coarsening the morphology of the microstructure is governed by the reduction of this energy. The average radius of the precipitates increases. This occurs as a result of dissolution of small particles and growth of larger ones.

To proceed with the theory of coarsening it is necessary to consider the variation of the concentration $C(R)$ in the vicinity of the particle with radius R as a function of time t. The Gibbs-Thompson equation shows that the concentration $C(R)$ in the vicinity of a particle depends on the local curvature of the considered interface:

$$C(R) = C_m^e \exp\left(\frac{2\Omega_0 \sigma}{k_B T} \cdot \frac{1}{R} \right) \approx C_m^e \left(1 + \frac{2\Omega_0 \sigma}{k_B T} \cdot \frac{1}{R} \right), \tag{3.28}$$

where Ω_0 is a molar volume of a particle, σ is the interfacial energy between the precipitate and matrix, T is the absolute temperature. C_m^e is the equilibrium solute concentration at a plane interface in the matrix in equilibrium. $C(R)$ can be considered as the concentration at the surface of a spherical particle with radius R. The difference between C_m^e and $C(R)$ induces a diffusive flux of atoms from the smaller to the larger particles (due to the higher solubility of the small

precipitates). Thus, the average particle radius increases and the total number of particles decreases with time.

When $C(R)$ deduced from the Eq. 3.28 is substituted to the Eq. 3.26 it is seen that the growth rate dR/dT of a particle in a matrix with concentration C_m depends on the size of a particle. The solution of the equation $C = C_m$ gives a critical radius for coarsening, $R_C^{coarsening}$. Big particles with $R > R_C^{coarsening}$ for which $C < C_m$ will grow (faster when C is small), and small particles with $R < R_C^{coarsening}$ and $C > C_m$ will be dissolved in the matrix.

3.7. Lifshitz-Slyozov-Wagner (LSW) theory

A major advance in the theory of Ostwald ripening was made by Lifshitz and Slyozov [111] and, just after, by Wagner [112] (LSW). LSW developed a method for treating an ensemble of dilute coarsening particles, and were able to make quantitative predictions on the long-time behaviour of coarsening systems.

The assumption about infinite dilution in alloy allows description of the coarsening kinetiks without recourse to the details of the interparticle interactions. To treat the continuum problem, LSW made the critical assumption that a particle's coarsening rate is independent of its surroundings due to the small volume fraction considered. They also assumed that particles are spherically shaped and isolated from each other.

LSW theory is based on the Gibbs-Thompson equation (Eq. 3.28). For derivation of the theoretical results following equations should be introduced:

- a *mass conservation equation*:

$$\overline{C} = C_m + \left(C_p - C_m^e\right)\frac{4\pi}{3}\int_0^\infty R^3 f(R,t)dR\,, \tag{3.29}$$

where $\overline{C}$ is the average concentration of the alloy; $f(R,t)$ is the particle's size distribution function, C_m is the matrix concentration;

- a *continuity equation* describing the time evolution of a particle size distribution function:

$$\frac{\partial f(R,t)}{\partial t} + \frac{\partial}{\partial R}\left[f(R,t)\cdot\frac{dR}{dt}\right] = 0\,; \tag{3.30}$$

- a *kinetic equation* describing the growth or dissolution rate of an individual particle of a given size is given in Eq. 3.22. In the LSW theory this relation will have a form:

$$\frac{dR}{dt} = \frac{1}{R}\left[\frac{R}{\overline{R}} - 1\right], \tag{3.31}$$

where $\overline{R}$ is the average radius. As follows from this equation there is a critical radius $R_C^{coarsening}$ which depends on the matrix concentration C_m and influences the sign of $\frac{dR}{dt}$.

Substituting these equations into the Gibbs-Thompson relation (Eq. 3.28) leads to the asymptotic solution of a non-linear equation and thus to the results of the LSW theory:

1) the critical radius coincide with the average radius:

$$R_C(t) = \overline{R}(t) = \int_0^\infty R \cdot f(R,t) dR \,; \tag{3.32}$$

2) at latest stages of coarsening the cube of the average particle radius should vary linearly with time:

$$\overline{R}^3(t) - \overline{R}^3(0) = K \cdot t \,, \tag{3.33}$$

where $\overline{R}^3(0)$ is the average radius at the beginning of the coarsening, K describes the rate of coarsening (in general, it is dependent on the volume fraction). LSW obtained the following expression for K:

$$K = \frac{8 C_m^e \sigma D \Omega_0}{9\left(C_p - C_m^e\right) k_B T} \tag{3.34}$$

The rate of supersaturation of matrix $\left(C_m - C_m^e\right)$ decreases as $t^{-1/3}$ and the density of precipitates decreases as t^{-1};

3) an arbitrary distribution of particle radii when scaled by the average radius should assume a specific time-independent form (Fig. 3.4) [111-114]:

$$f(R,t) = \begin{cases} \dfrac{A}{\left(1 + \dfrac{t}{\tau_{D'}}\right)^{4/3}} \rho^2 h(\rho), & \text{if} \quad \rho = \dfrac{R}{\overline{R}} < \dfrac{3}{2} \\ 0, & \text{if} \quad \rho \geq \dfrac{3}{2} \end{cases} \tag{3.35}$$

where A – is a constant and $\tau_{D'}$ is a constant given by:

$$\tau_{D'} = \frac{9 k_B T \overline{R}^3(0)}{8 D \Omega_0 \sigma C_m^e},$$

and function $h(\rho)$ is defined as:

$$h(\rho) = \left(\frac{3}{3+\rho}\right)^{\frac{7}{3}} \left(\frac{3}{3-2\rho}\right)^{\frac{11}{3}} \exp\left(\frac{-2\rho}{3-2\rho}\right)$$

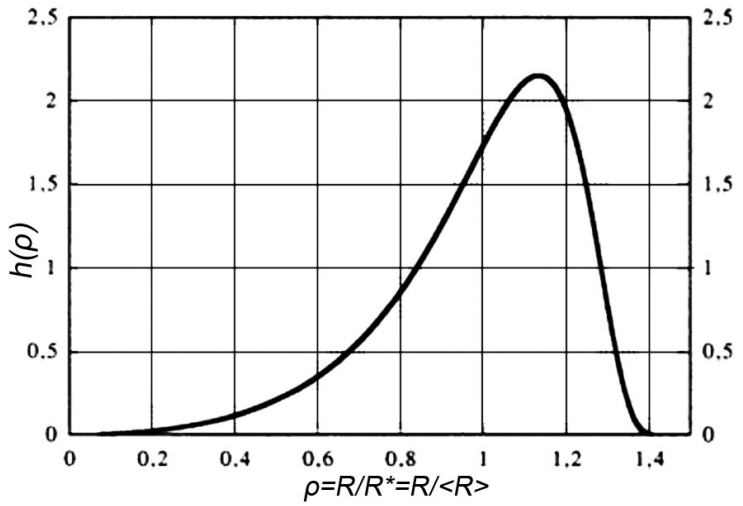

Figure 3.4. Normalized size distribution function after LSW [110]

Since the time-independent radii distribution predicted by LSW is usually not observed experimentally, modifications of the LSW theory were proposed [114 and references therein, 115-118]. It has been observed that the parameter K depends on the volume fraction and the LSW theory is valid for very small volume fraction of precipitates. The observed particle size distribution function is broadened and its peak is decreased if this dependence is considered.

3.8. Önsager microscopic diffusion equation

To describe the kinetics of phase transitions at the microscopic level the Önsager-type microscopic diffusion theory can be applied. This approach has been used for the investigation of the kinetic path and microstructure evolution during coarsening [119-124,126].

The Önsager-type microscopic diffusion equations were firstly proposed by Khachaturyan [91-92]:

$$\frac{dP_\alpha(\mathbf{r},t)}{dt} = \frac{1}{k_B T}\sum_{\beta=1}^{\nu}\sum_{\mathbf{r}'} L_{\alpha\beta}(\mathbf{r}-\mathbf{r}')\, c_\alpha c_\beta \left[\frac{\delta F}{\delta P_\beta(\mathbf{r}',t)}\right], \tag{3.36}$$

where $P_\alpha(\mathbf{r},t)$ (for α=1,2,…,ν) is the single-site occupation probability of an atom of sort α at the crystal lattice site $\mathbf{r}$ at time t; $L_{\alpha\beta}(\mathbf{r}-\mathbf{r}')$ is the Hermitian matrix of the kinetic Önsager coefficients, F is the Helmholtz free energy (it is defined in the Appendix 5.2.2), c_α is the atomic fraction of atoms of the kind α.

Due to the fact that the total number of atoms in the system is conserved, the conservation condition should be imposed:

$$\sum_{\mathbf{r}} L_{\alpha\beta}(\mathbf{r}) = 0 \tag{3.37}$$

For a binary A-B alloy it is possible to reduce the system of (ν-1) equations (Eq. 3.36) to one equation in terms of a probability $P(\mathbf{r})$ which was previously defined (Eq. 3.8):

$$\frac{dP(\mathbf{r},t)}{dt} = \frac{1}{k_B T}\sum_{\vec{r}'} L_{AB}(\mathbf{r}-\mathbf{r}')c(1-c)\left[\frac{\delta F}{\delta P(\mathbf{r}',t)}\right] \tag{3.38}$$

After regrouping constant terms this equation will be written in the form:

$$\frac{dP(\mathbf{r},t)}{dt} = \sum_{\mathbf{r}'} L(\mathbf{r}-\mathbf{r}')\left[\frac{\delta F}{\delta P(\mathbf{r}',t)}\right], \tag{3.39}$$

where $L(\mathbf{r}) = \dfrac{c(1-c)}{k_B T} L_{AB}(\mathbf{r})$.

The Fourier transform of this equation gives:

$$\frac{d\tilde{P}(\mathbf{k},t)}{dt} = \tilde{L}(\mathbf{k})\left\{\frac{\delta F}{\delta P(\mathbf{r},t)}\right\}_{\mathbf{k}}, \tag{3.40}$$

where $\tilde{P}(\mathbf{k},t), \tilde{L}(\mathbf{k}), \left\{\dfrac{\delta F}{\delta P(\mathbf{r},t)}\right\}_{\mathbf{k}}$ are the Fourier transforms of $P(\mathbf{r},t), L(\mathbf{r}), \dfrac{\delta F}{\delta P(\mathbf{r},t)}$, respectively.

The conservation condition in the reciprocal space becomes:

$$\tilde{L}(\mathbf{k}_0) = \tilde{L}(\mathbf{0}) = \sum_{\mathbf{r}} L(\mathbf{r}) = 0 \tag{3.41}$$

By assuming atomic jumps only between nearest neighbor sites and using the conservation condition, for fcc lattice the following equation for the Önsager kinetics coefficient can be written:

$$\tilde{L}(\mathbf{k}) = -4L_1\left[3 - \cos\pi h \cdot \cos\pi k - \cos\pi k \cdot \cos\pi l - \cos\pi l \cdot \cos\pi h\right] \tag{3.42}$$

The coefficient L_1 is connected to the diffusion coefficient D through the following relation:

$$L_1 = \frac{D}{a_{fcc}^2\left(\tilde{w}(\mathbf{k}_0) + \dfrac{k_B T}{c(1-c)}\right)}, \tag{3.43}$$

where $\tilde{w}(\mathbf{k}_0)$ is the Fourier transform of the ordering energy at **k=0**. The derivation of the presented relation can be found in [113, 121-124].

3.9. Application to the 2D-model

The numerical solution of the presented kinetics equations on a 3D lattice can be performed. However, this calculation will be large time consuming. That is why 2D simulations are performed for the investigation of the kinetic path in Ni-Fe alloys. A 2D projection of a respective 3D lattice is equivalent to assuming that the occupation probabilities do not depend on

the coordinate z along the [001] axis. In the presented work we investigate Ni_3Fe alloy and in the ordered $L1_2$ phase its 2D projection will have a form presented in Fig. 3.5.

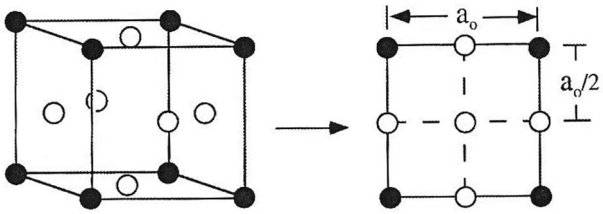

Figure 3.5. $L1_2$ unit cell and its 2D projection along [001] direction (● - Fe atoms, ○ - Ni atoms)

As it is seen, the 2D projection of a fcc lattice (in particular, $L1_2$ ordered cell) along the [001] direction is a square with a lattice parameter equal to $a_{2D} = a_{fcc}/2$. Therefore, a lattice vector **r** and the reciprocal vector **k** will be substituted as follows:

$$\begin{aligned} \mathbf{r}' &= x'\mathbf{b}_1 + y'\mathbf{b}_2 = \frac{x'}{2}\mathbf{a}_1 + \frac{y'}{2}\mathbf{a}_2 \\ \mathbf{k}' &= 2\pi\left(h'\mathbf{b}_1^* + k'\mathbf{b}_2^*\right) = 2\pi\left(2h'\mathbf{a}_1^* + 2k'\mathbf{a}_2^*\right) \end{aligned} \tag{3.44}$$

where $\mathbf{b}_1\left(\mathbf{b}_1^*\right), \mathbf{b}_2\left(\mathbf{b}_2^*\right), \mathbf{a}_1\left(\mathbf{a}_1^*\right), \mathbf{a}_2\left(\mathbf{a}_2^*\right)$ are unit cell vectors of the square lattice and a projected plane of the fcc lattice in the direct (reciprocal) space, respectively.

In this case the kinetic equations in the reciprocal space are obtained by substituting $(2h', 2k', 0)$ for (h, k, l) in calculation of "mixing" energy and Önsager coefficient (Eqs. 3.16 and 3.42, respectively):

$$\begin{aligned} \tilde{w}(\mathbf{k}') = 4w_1(\cos 2\pi h' \cdot \cos 2\pi k' + \cos 2\pi h' + \cos 2\pi k') + \\ 2w_2(\cos 4\pi h' + \cos 4\pi k' + 1) + \ldots \end{aligned} \tag{3.45}$$

and

$$\tilde{L}(\mathbf{k}') = -4L_1\left[3 - \cos 2\pi h' \cdot \cos 2\pi k' - \cos 2\pi k' - \cos 2\pi h'\right] \tag{3.46}$$

The solution of the kinetic equations was done by means of the explicit Euler technique.

3.10. Definition of the local order parameters in the kinetic simulation

The ordered structure can be described by the average concentration c and order parameters η_s, which are proportional to the amplitude of the concentration wave $\mathbf{k}_s$ (section 3.4). If the distribution $p(\mathbf{r})$ is known, it is possible to define the average parameters c and η_s by applying the Fourier transformation:

$$\eta_s = \frac{1}{N\gamma_s}\sum_{\mathbf{r}} p(\mathbf{r})\exp(-i\mathbf{k}_s\mathbf{r}),$$

where N is the total number of atoms in alloy and γ_s is the symmetry constant. The concentration is calculated by imposing $\mathbf{k}_0 = 0$ and $\gamma_0 = 1$, thus $\eta_s = c$. Such definition, in general, can give negative (complex) values.

The local order parameters $\eta_s(\mathbf{r})$ can be defined at each site $\mathbf{r}$ of the alloy. The formulation will be following.

$$\eta_s(\mathbf{r}) = \exp(-i\mathbf{k}_s\mathbf{r})\left(\mathrm{coef}_s(\mathbf{r}) \otimes p(\mathbf{r})\right),$$

where

$$\mathrm{coef}_s(\mathbf{r}) = \begin{cases} \dfrac{1}{N_B\gamma_s}\exp(-i\mathbf{k}_s\mathbf{r}), & \text{if } \mathbf{r} \in S_B \\ 0, & \text{otherwise} \end{cases}$$

The symbol $\otimes$ represents the discrete convolution operation. B is the box where the order parameters are defined. S_B is a ensemble of sites inside this box and N_B is the number of sites.

In case of Ni_3Fe alloy which has $L1_2$ structure in the ordered state, the presented expressions will be simplified. For 2D case, the box B corresponds to the $L1_2$ unit cell (Fig. 3.5). The $L1_2$ structure is generated by two wave vectors: $\mathbf{k}_{1x} = \dfrac{2\pi}{a_{2D}}\begin{pmatrix}\frac{1}{2} & 0\end{pmatrix}$ and $\mathbf{k}_{1y} = \dfrac{2\pi}{a_{2D}}\begin{pmatrix}0 & \frac{1}{2}\end{pmatrix}$, where a_{2D} is the 2D-lattice parameter. Thus, two corresponding local order parameters, η_{1x} and η_{1y}, can be defined. To each site the equilibrium coefficients can be prescribed: ½ to the facets, ¼ to the corners of a square and 1 to the center. Such coefficients are equal to the inverse of the number of atoms which are neighbors to the chosen site. In this case, the number of sites in the box N_B will be defined as $4\cdot\frac{1}{4} + 4\cdot\frac{1}{2} + 1 = 4$.

Therefore, the local order parameters can be defined as:

- $\eta_{1x}(\mathbf{r}) = \exp(-i\mathbf{k}_{1x}\mathbf{r})\left(\mathrm{coef}_{1x}(\mathbf{r}) \otimes p(\mathbf{r})\right)$,

where

$$\mathrm{coef}_{1x}(\mathbf{r}) = \begin{pmatrix} -\frac{1}{4} & +\frac{1}{2} & -\frac{1}{4} \\ -\frac{1}{2} & +1 & -\frac{1}{2} \\ -\frac{1}{4} & +\frac{1}{2} & -\frac{1}{4} \end{pmatrix}$$

- $\eta_{1y}(\mathbf{r}) = \exp(-i\mathbf{k}_{1y}\mathbf{r})\left(\mathrm{coef}_{1y}(\mathbf{r}) \otimes p(\mathbf{r})\right)$,

where $\mathrm{coef}_{1y}(\mathbf{r}) = \begin{pmatrix} -\frac{1}{4} & -\frac{1}{2} & -\frac{1}{4} \\ +\frac{1}{2} & +1 & +\frac{1}{2} \\ -\frac{1}{4} & -\frac{1}{2} & -\frac{1}{4} \end{pmatrix}$

- $c(\mathbf{r}) = \left(\mathrm{coef}_0(\mathbf{r}) \otimes p(\mathbf{r})\right)$,

where $\mathrm{coef}_0(\mathbf{r}) = \frac{1}{4}\begin{pmatrix} \frac{1}{4} & \frac{1}{2} & \frac{1}{4} \\ \frac{1}{2} & 1 & \frac{1}{2} \\ \frac{1}{4} & \frac{1}{2} & \frac{1}{4} \end{pmatrix}$

Chapter 4

Results

The purpose of this study is to investigate the magnetic and structural properties of Ni-Fe alloys in the concentration range of Permalloy series. As was mentioned earlier, the co-existence of magnetic and chemical ordering greatly influences the behavior of such alloys and, therefore, is of our most interest. The investigation is done by means of MC, mean-field thermodynamic calculations and Önsager kinetics simulations.

4.1. Monte Carlo simulation

As was previously mentioned in section 2.2.2.1, three types of simulations were performed, in order to distinguish the mutual influence of each subsystem – spin and atomic:

- Simulations with Heisenberg Hamiltonian – with magnetic interactions only;
- Simulations with chemical Hamiltonian – with chemical interactions only;
- Simulations with total Hamiltonian – with both magnetic and chemical interactions.

Firstly, we separated magnetic and chemical subsystems and made simulations in order to investigate separately magnetic and chemical ordering. These simulations are useful for comparison with experimental results and with simulations where both spin and atomic interactions are included. Obtained results make more visible the mutual influence of both types of ordering.

Simulations were done using different linear system sizes, L, (the total number of atoms in the fcc lattice is $N=4L^3$), numbers of MC steps per temperature and temperature steps (ΔT). All these parameters will be specified further for each type of simulation. Initial atomic configurations were chosen in two ways:

- disordered (atoms are randomly distributed);
- completely ordered (atoms are placed on the lattice sites according to the $L1_2$-type superstructure).

Stoichiometric and non-stoichiometric concentrations were considered, and results will be presented in the respective order.

The interaction parameters were taken in K, i.e. $W^{MC} = \frac{W}{k_B}$, where W is either chemical ($V_{\alpha\text{-}\beta}$) or magnetic ($J_{\alpha\text{-}\beta}$) interaction parameter. All units of calculated thermodynamic quantities are given taking into account this assumption.

4.1.1. Stoichiometric case (Ni_3Fe)

4.1.1.1 Simulations with magnetic interactions only

For the Hamiltonian which has a form of Eq. 2.1 it is necessary to choose the values of the spins s_{Fe} and s_{Ni}, and the "exchange" parameters J_{ij}. According to Ref. [4] (Table. 1.3), $\mu_{Fe} \approx 2.8\mu_B$ and $\mu_{Ni} \approx 0.616\mu_B$. So, using the formula $\mu_\alpha = -g\mu_B S_\alpha$ (α = Ni or Fe), where the Landé factor g is very close to 2 for both elements, we obtain $s_{Fe} \approx 1.4$ and $s_{Ni} \approx 0.308$. Three magnetic "exchange" parameters (only for the 1st coordination shell), J^{Ni-Ni}, J^{Ni-Fe} and J^{Fe-Fe} have to be defined. The value of J^{Ni-Ni} was chosen so that the model provides T_C of pure Ni ($\approx 623K$). Since the critical temperature of the Heisenberg model in the fcc lattice with nearest-neighbor interactions is $\frac{k_B T_C}{JS^2} \approx 3.16$ [70-72,85], the Ni-Ni interaction is given by $J^{Ni-Ni} \approx 2093K$. The Fe-Fe bond was chosen in order to model the antiferromagnetic γ-Fe with $T_N \approx 70K$ [4], that is $J^{Fe-Fe} = -80K$. The Ni-Fe interaction has been fitted in order to obtain the experimental value of T_C ($\approx 870K$) of the disordered phase at 75% at. Ni. A good agreement between our preliminary tests and the experimental T_C was obtained with $J^{Ni-Fe} = 1060K$. Due to the antiferromagnetic Fe-Fe interaction the system is frustrated, so at $0K$ one can expect that the stable magnetic configuration is no more collinear with Fe additions.

To reduce statistical errors in the simulations on the disordered alloy we average numerical data over few disordered chemical configurations. This was performed using a parallel version of the code.

We have compared simulations with different system sizes L = 10-20 (i.e. $4000 \le N \le 32000$), number of disordered configurations, (*nconf* = 1-200), and number of MC steps per temperature, ($n = 10^3 - 10^5$). Finally, reliable results have been obtained with a reasonable computational effort using the following parameters:

L	20 (N=32000)
n	50000
nconf	4 (for disordered alloy)
ΔT (K)	10

All numerical simulations were done without external magnetic field ($H = 0$). We will start with comparison of the magnetic properties of a random alloy (i.e. with disordered atomic configuration) with those of the perfect $L1_2$ structure.

1) Internal magnetic energy

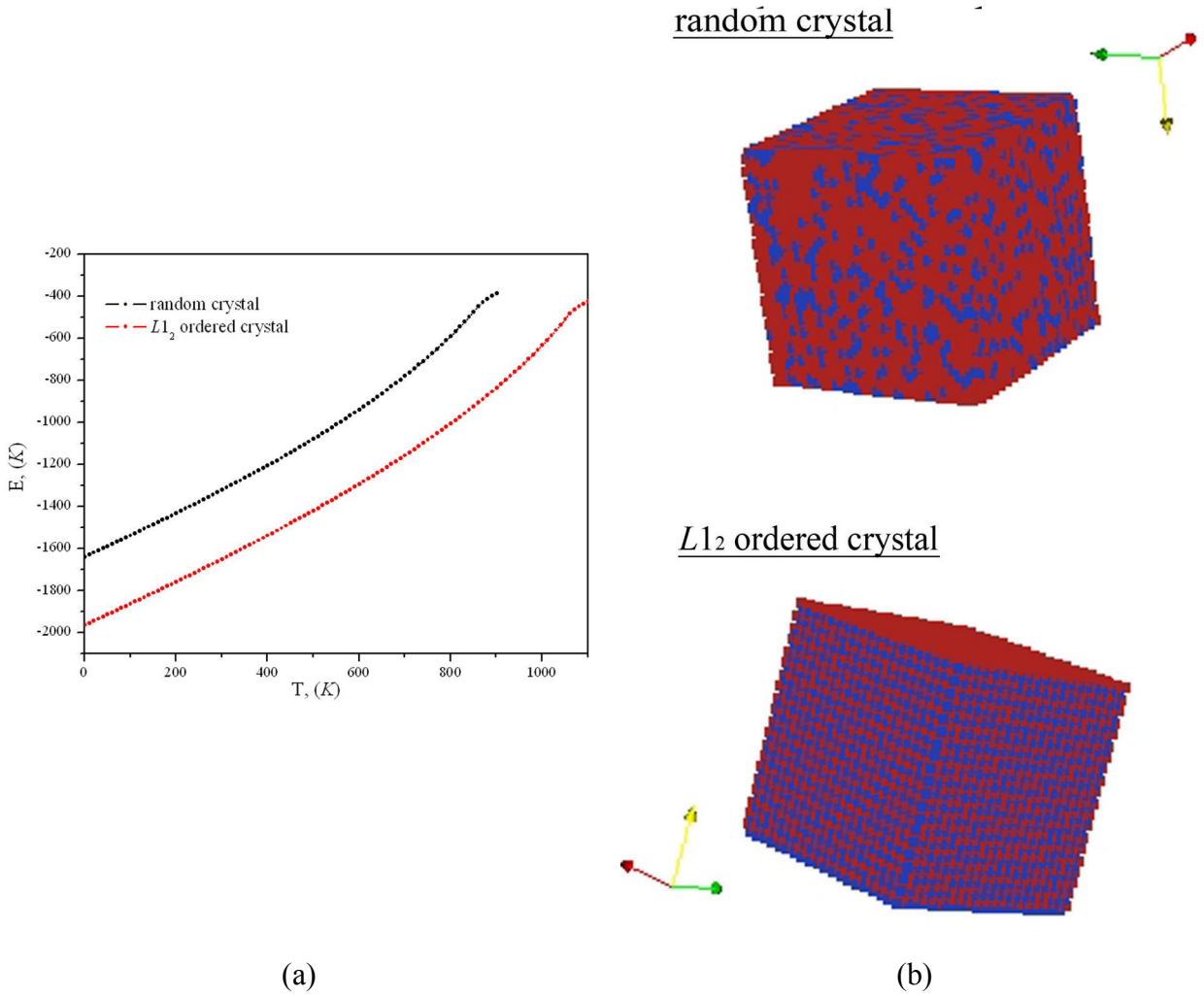

Figure 4.1.1. (a) Internal magnetic energy versus temperature
(b) Visualization of considered chemical configurations
Red and blue points represent Ni and Fe atoms, respectively

At 0*K* the system should be in its magnetic ground state, which is expected to be ferromagnetic, for this concentration. Using the formula:

$$E_{GS}^{magn} = -\left(Z_{Ni-Ni}J^{Ni-Ni}S_{Ni}^2 + Z_{Ni-Fe}J^{Ni-Fe}S_{Ni}S_{Fe} + Z_{Fe-Fe}J^{Fe-Fe}S_{Fe}^2\right), \qquad (4.1.1a)$$

where $Z_{\alpha-\beta}$ denotes the average number of α-β bonds per atom, we estimated the value of the ferromagnetic ground state energy per atom.

Also, we can estimate the lower limit for the magnetic energy, E_0^{magn}, which is not reachable due to frustration:

$$E_0^{magn} = -Z_{Ni-Ni}J^{Ni-Ni}S_{Ni}^2 - Z_{Ni-Fe}J^{Ni-Fe}S_{Ni}S_{Fe} + Z_{Fe-Fe}J^{Fe-Fe}S_{Fe}^2, \qquad (4.1.1b)$$

According to our numerical data for the random crystal, $Z_{Fe-Fe} \approx 0.37$; $Z_{Fe-Ni} \approx 2.25$ and $Z_{Ni-Ni} \approx 3.37$ per atom, so $E_{GS\_disordered}^{magn} \approx -1641.81K$ and $E_{0\_disordered}^{magn} \approx -1758.65K$. The

difference between these two values measures the degree of magnetic frustration which also can be defined as $Y = 1 - \frac{E^{magn}_{GS\_disordered}}{E^{magn}_{0\_disordered}} \approx 0.066$. From the energy plot (Fig. 4.1.1a) it is seen that the system is very close to the ferromagnetic ground state as $T \to 0K$ ($E^{magn}_{disordered} \approx -1640.68K$). When the chemical configuration is the $L1_2$ structure, there are no Fe-Fe bonds and consequently, no frustration and the ferromagnetic ground state energy is equal to the lower limit of the energy ($E^{magn}_{GS\_ordered} = E^{magn}_{0\_ordered} \approx -1966.85K$), which is seen in Fig. 4.1.1a.

2) Reduced magnetization (M_{tot}, M_{Fe} and M_{Ni})

As the reduced magnetization, $M / M_{Saturation}$, represents the long-range order parameter of the ferromagnetic system, we can estimate the transition temperature, T_C, from its temperature dependence. It is known that paramagnetic ↔ ferromagnetic transition is of 2nd order, so *M(T)* will go continuously to zero (Fig. 4.1.2).

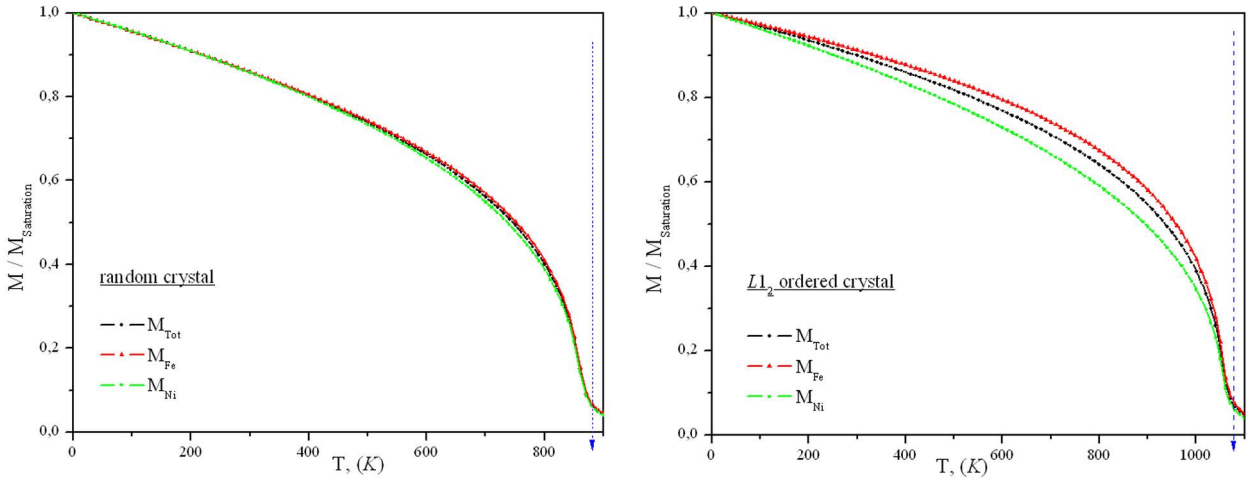

(a) (b)

Figure 4.1.2. Reduced magnetization versus temperature for:

(a) Random chemical configuration

(b) $L1_2$ ordered chemical configuration

In Fig. 4.1.2, $M_{Fe} / M^{Saturation}_{Fe}$ and $M_{Ni} / M^{Saturation}_{Ni}$ represent the reduced magnetization of Ni- and Fe-sublattices. The difference in the behavior of these quantities is noticeable and evidences the influence of the chemical order on the magnetic properties of the system. Indeed, as seen from Fig. 4.1.2a, when the crystal is disordered the magnetizations of Fe- and Ni-sublattices lie very close to each other. When the crystal is ordered (Fig. 4.1.2b) the difference between sublattice magnetizations is not negligible anymore (the Fe-sublattice magnetization is

larger than Ni-sublattice magnetization). From Fig. 4.1.2 it is seen that the magnetization above T_C still deviates from zero due to finite-size effects.

The Curie temperature (dashed line on the figures), T_C, also is influenced by the chemical order (Table 4.1.1).

	disordered	$L1_2$ *ordered*
T_C from $M(T)$, (K)	870±5	1070±5
T_C from $\chi(T)$, (K)	861±5	1061±5
T_C from $C(T)$, (K)	851±5	1051±5

Table 4.1.1. Curie temperature estimated from thermodynamic quantities

This has been shown experimentally during calorimetric measurements (Fig. 1.5) [13]. Ordered atomic configuration promotes higher T_C due to the absence of Fe-Fe pairs which makes easier reaching the ferromagnetic state, i.e. at higher temperatures.

In Fig. 4.1.3 the state of order is defined by the long-range order parameters: η for MC simulation and S_{BW} (Bragg-Williams parameter) for experimental results. From the two plots we can conclude that higher state of order promotes higher values of T_C. The possible difference in the obtained Curie temperatures and the experimental ones can be due to the interaction parameters considered in our simulations and, also, due to uncertainties in the experimental data.

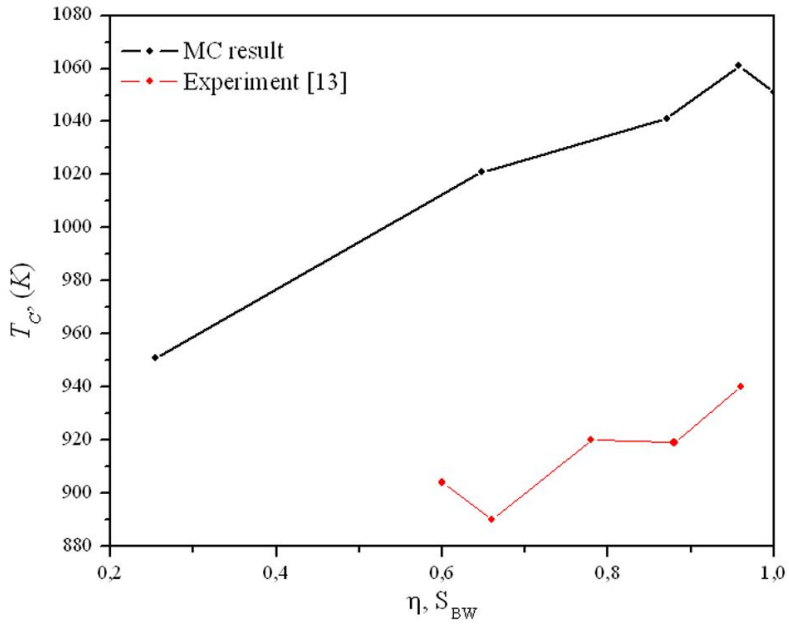

Figure 4.1.3. Comparison of the experimental [13] and simulated T_C for alloys with different state of order, i.e. chemical configuration

3) Susceptibility and specific heat

As was previously mentioned in section 2.2.4, in case of 2nd order transition the specific heat and susceptibility exhibit a maximum at the Curie temperature, T_C.

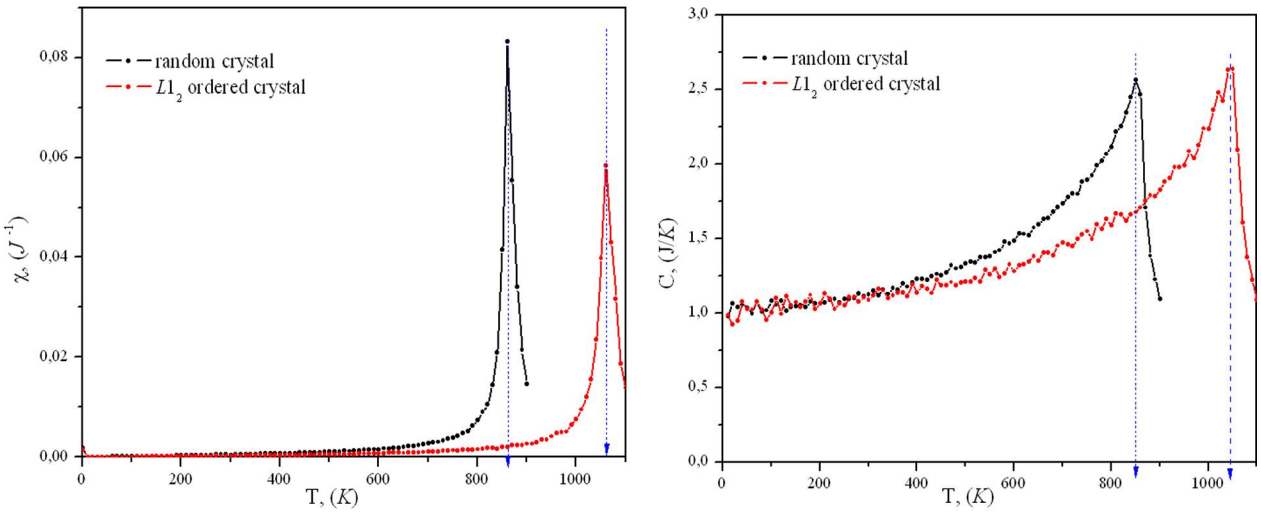

(a) (b)

Figure 4.1.4. Temperature dependence of:

(a) Zero-field magnetic susceptibility

(b) Specific heat

From Fig 4.1.4 we estimate T_C from the location of the maxima (dashed line) of C and χ. These estimates are reported in Table 4.1.1. As expected, $T_C^{disordered}$ agrees well with the experimental results from Table 1.4. All values are in reasonable agreement and possible discrepancies are due to finite-size effects [83]. Further for reason of convenience we will use the estimate obtained from the zero-field susceptibility because the behavior of the specific heat of the classical Heisenberg model is known to be cusp-like rather divergent at the phase transition [70].

It is interesting to visualize the orientations of the magnetic moments obtained by simulation. In Fig. 4.1.5 we will present such picture only for the lowest temperature $T = 1K$. For reasons of clarity, we will visualize only (001)* plane.

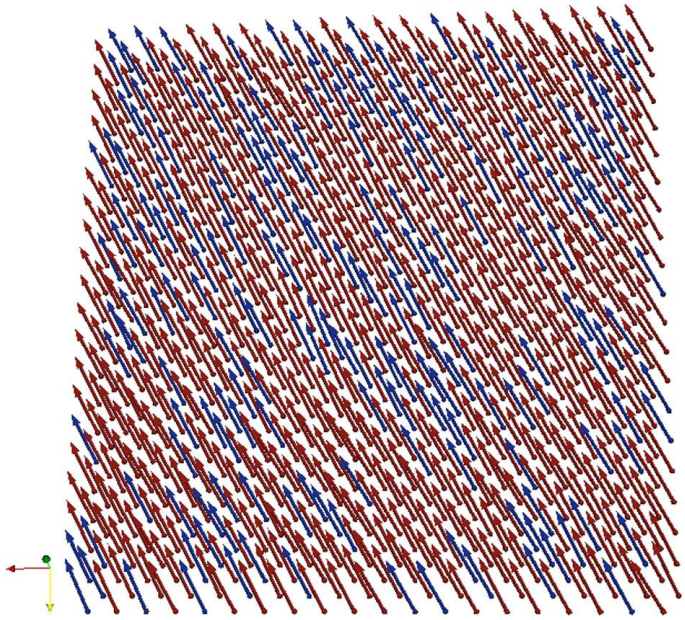

(a)

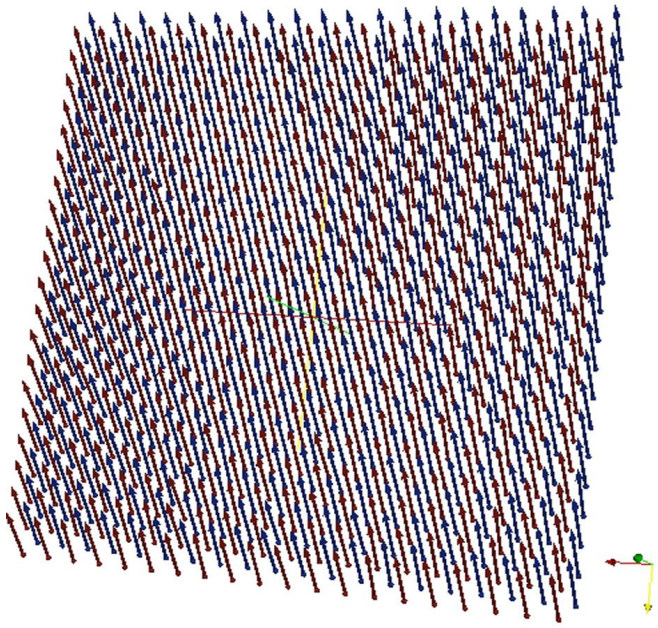

(b)

Figure 4.1.5. Visual representation of the magnetic moment orientations at $T = 1K$ for:

(a) Random chemical configuration

(b) $L1_2$ ordered chemical configuration

Ni and Fe moments are presented by red and blue arrows, respectively

Although, the ground state is ferromagnetic, it is seen that in the disordered crystal some magnetic moments still deviate from the average orientation. As was mentioned before, this happens due to magnetic frustration as a result of antiferromagnetic Fe-Fe bonds and also because the temperature is not exactly $0K$ but $1K$.

When simulations were performed on the ordered structure, all magnetic moments seem to be almost parallel to each other because there is no frustration.

Let us mention that the Curie temperature obtained for the $L1_2$–type ordered structure ($T_C^{ordered} \approx (1061 \pm 5)K$) is higher than experimental ones. But due to the fact that chemical ordering temperature, T_K, (Table 1.2.) is lower than magnetic transition temperature, the experimental T_C values can be underestimated because of atomic diffusion during the magnetic measurements at temperatures above T_K. Therefore the structure of the alloy does not correspond to the perfect $L1_2$ structure as in our simulation.

4.1.1.2. Simulations with chemical only interactions

The form of the Hamiltonian for the chemical subsystem was given in Eq. 2.3. In our simulation no vacancy or interstitial is present, and many-body interactions are neglected. The Hamiltonian is simplified to the form:

$$\mathcal{H}_{chem} = -\sum_{\langle ij \rangle}\sum_{\alpha,\beta} V_{ij}^{\alpha\beta}\xi_i^{\alpha}\xi_j^{\beta} = -\sum_{r}\left(Z_r^{Fe-Fe}V_r^{Fe-Fe} + Z_r^{Fe-Ni}V_r^{Fe-Ni} + Z_r^{Ni-Ni}V_r^{Ni-Ni}\right) \qquad (4.1.2)$$

where $Z_r^{\alpha\beta}, V_r^{\alpha\beta}$ are the number of (αβ) pairs and the pair-wise chemical interaction parameter in the r^{th} coordination shell, respectively.

In our simulations we have tested 2 sets of pair-wise chemical interactions, $V_r^{\alpha\beta}$. In the first case we have assumed only nearest-neighbor interactions (NN), i.e. only within the 1st coordination shell, and for the second case we have included also interactions between next-nearest neighbors (NNN).

We have also implemented simulations for different initial conditions:

- The initial configuration is a disordered state and the initial temperature satisfies $T_{init} > T_K$. The simulated annealing with a temperature step ΔT takes place until $T = 1K$ – *ordering case*.
- The initial configuration is a perfectly ordered state with $L1_2$ structure, the initial temperature is $T_{init} = 1K$ and the temperature is increased with a step ΔT until $T > T_K$ – *disordering case*.

We have tested different system sizes L = 10-20 (i.e. $4000 \le N \le 32000$), numbers of MC steps $n = 10^3$-10^4, temperature steps ΔT = 1-20K. To increase the accuracy in the vicinity of

the transition temperature we scaled the number of MC steps by a factor 5 or 10. Satisfactory results were obtained with the following parameters:

L	20 ($N = 32000$)
n	10 000
scale	10
$\Delta T\,(K)$	5

A. Nearest neighbor interactions (NN interactions)

We have chosen the values of pair-wise interaction parameters from Ref. [40]. The Ni-Ni bond, $V_1^{Ni-Ni} = 8590K$, is taken in order to correspond to measured cohesive energy of f.c.c. Ni, assuming the chemical bond energy is the dominant contribution. The Fe-Fe bond is taken to correspond to the cohesive energy of high-spin fcc Fe, $V_1^{Fe-Fe} = 8400K$. The Ni-Fe bond is equal to $V_1^{Ni-Fe} = 9200K$.

During our simulations we calculated the internal energy, the long-range and short-range order parameters, and the specific heat.

1) Internal energy

From the presented plot of the internal configurational energy (Fig. 4.1.6a) it is seen that the system undergoes a 1st order transition as expected. As usual for 1st order transitions, a thermal hysteresis is present. Such hysteretic behavior has been also observed experimentally [13,17,26].

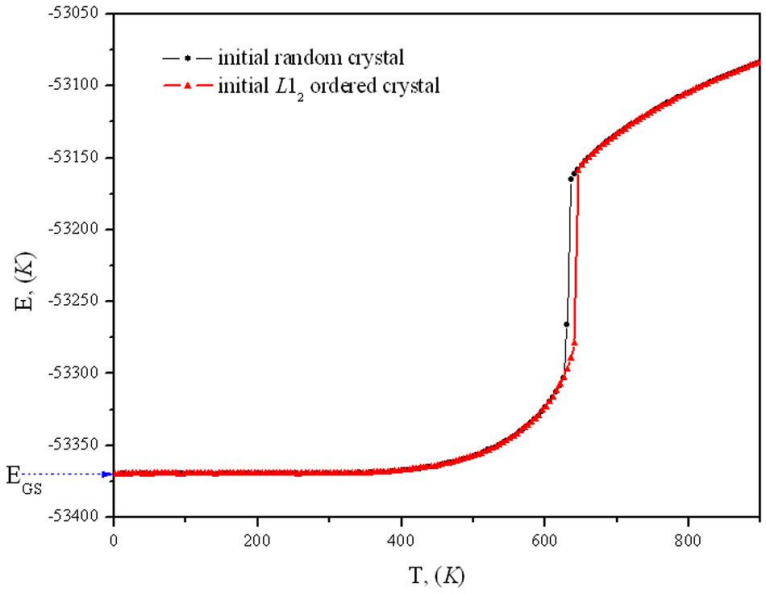

(a)

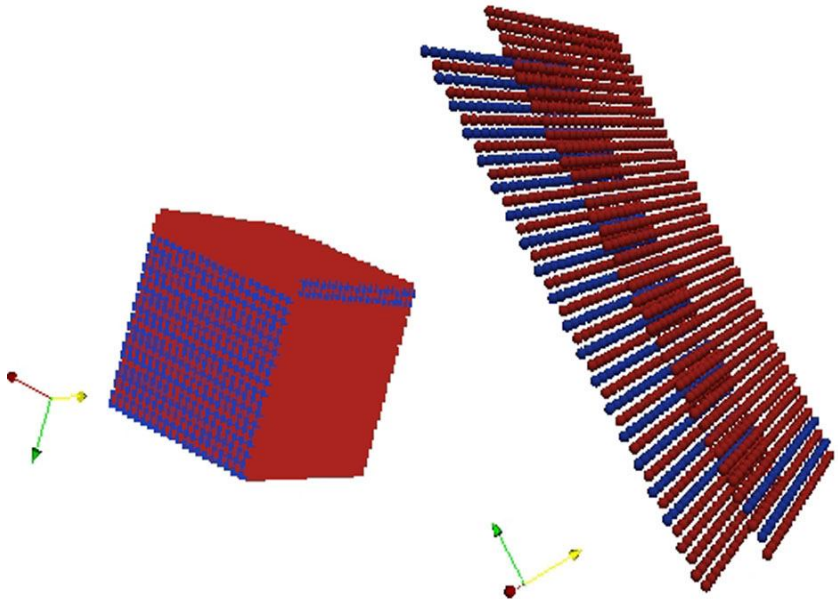

(b)

Figure 4.1.6. (a) Internal energy versus temperature

(b) Visualization of the chemical configuration obtained after annealing from $T_{init}>T_K$. Ni and Fe atoms are presented by red and blue points, respectively

On Fig 4.1.6b we have presented the visualization of the structure obtained at the end of the simulated annealing (at $1K$). It is seen that we obtain a structure which contains antiphase boundaries between ordered domains of $L1_2$-type. In general, $L1_2$ structure can be built with four translational variants and this induces the appearance of antiphase domains between these variants. The obtained picture can be explained by the use of only nearest neighbor interactions. Indeed, in this case, the antiphase domains do not make any cost in the internal energy. For the two simulations (starting from high temperature or from $T_{init} = 1K$) the energy at very low temperature is equal to the ground state energy per atom (Fig. 4.1.6a):

$$E_{GS}^{chem} = -3(V_1^{Ni-Ni} + V_1^{Ni-Fe}),$$

which is equal to $E_{GS}^{chem} = -53370K$.

2) Order parameters

When the state of the system changes abruptly it is expected that the order parameters (long-range and short-range) will exhibit a jump at the transition temperature, T_K.

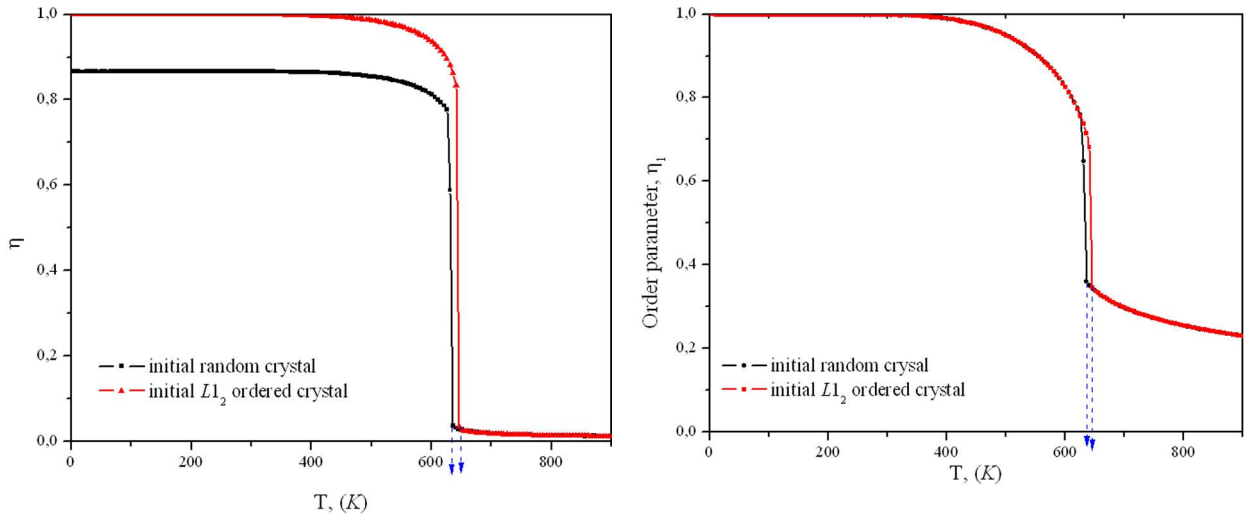

(a) (b)

Figure 4.1.7. Thermal variation of:

(a) Long-range order parameter η

(b) Order parameter η_1

We calculate the long-range order parameter, η, according to Eq. 2.13:

$$\eta(T) = \frac{1}{3}\left(4\frac{\left\langle N_{Fe,A} \right\rangle_T}{N_{Fe}} - 1 \right)$$

where $N_{Fe,A}$ is the number of Fe atoms on the A-sublattice. According to this formula, in the ordered state η = 1. But, as seen from Fig 4.1.7a, it is not true for the simulation starting from the random crystal at high temperature. This can be explained by the antiphase domains (Fig. 4.1.6b), so not all sites of the A-sublattice are occupied by Fe-atoms. To overcome this problem we have also calculated another "long"-range order parameter, η_1, according to the following formula:

$$\eta_1(T) = \frac{1}{2}\left(\frac{\left\langle N_{Fe,Ni=12} \right\rangle_T}{N_{Fe}} + \frac{\left\langle N_{Ni,\{Fe=4\,Ni=8\}} \right\rangle_T}{N_{Ni}} \right), \qquad (4.1.3)$$

where $N_{Fe,Ni=12}$ ($N_{Ni,\{Fe=4,Ni=8\}}$) is the number of Fe (Ni) atoms surrounded by exactly 12 Ni (4 Fe and 8 Ni) atoms in the 1st coordination shell. The obtained plots are given on Fig. 4.1.7b. However, since η_1 is not zero above T_K, we can not really say that this parameter defines long-range order. This parameter was used in order to define whether we have obtained $L1_2$-type superstructure at the lowest temperature or not.

The short-range order parameters defined by Eqs. 2.14-2.15 are plotted in Fig. 4.1.8.

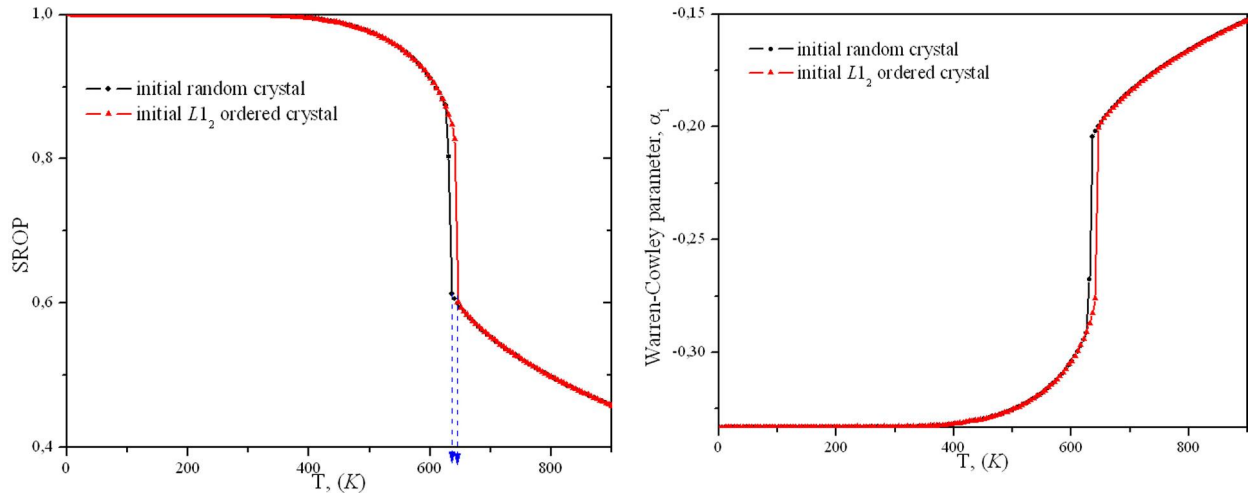

(a) (b)

Figure 4.1.8. Short-range order parameters versus temperature:

(a) SROP

(b) Warren-Cowley parameter, α_1

As expected, it is seen from Fig. 4.1.8a that above the transition temperature the SROP is not null. This fact signifies the presence of short-range order above T_K. Such conclusion is confirmed by experimental results [13].

We have also calculated the short-range Warren-Cowley parameter (Fig. 4.1.8b) in order to verify our numerical results. Negative values of α_1 ensure the ordering tendency in the studied system, and its value at low temperature, $\alpha_1 \approx -\frac{1}{3}$, confirms the formation of $L1_2$-type superstructure.

From the presented curves of the order parameters (η and η_1) we can estimate the values of the transition temperature, T_K, i.e. the lowest point of the jump (Table 4.1.2).

	ordering	*disordering*
T_K from $\eta(T)$, (K)	636.0±2.5	646.0±2.5
T_K from C(T), (K)	631.0±2.5	646.0±2.5

Table 4.1.2. Ordering temperatures, T_K, estimated from thermodynamic quantities

3) Specific heat per atom

In Fig 4.1.9 the temperature dependence of the specific heat, *C(T)*, is presented. As was mentioned in section 2.2.3, the δ-peak turns into a maximum of the specific heat due to finite size-effects. From the obtained plot we can locate the transition temperature by the peaks. In Table 4.1.2 we have listed estimated transition temperatures.

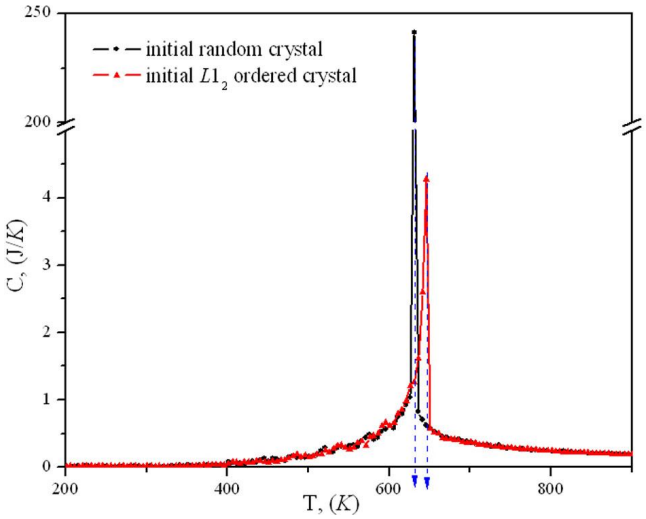

Figure 4.1.9. Temperature dependence of the specific heat, *C*(*T*)

The values of transition temperature obtained from order-parameter and specific heat curves are in complete agreement with each other.

From this simulation the order-disorder transition is underestimated in comparison with the experimental data. This is due to the choice of the interaction parameters. This estimation will be improved by taking into account magnetic interactions.

B. Interaction within 2 coordination shells (NNN interactions)

It is more realistic to consider interactions beyond the 1st coordination shell, so we have performed simulations including next-nearest-neighbor interactions. New pair-wise interaction parameters, $V^{\alpha\beta}_{r=\{1,2\}}$, were deduced from experimental data using mean-field theory. The definition of the ordering (or "*mixing*") energy, *w*, was given by Eq. 3.10. This parameter can be extracted from the experimental diffraction data [15-20] in the framework of the mean-filed approximation using the Krivoglaz-Clapp-Moss formula [105,133-134]:

$$I(\mathbf{k}) = \left|\varphi(\mathbf{k})\right|^2 \frac{c(1-c)}{1+c(1-c)\dfrac{\tilde{w}(\mathbf{k})}{k_B T}} \qquad (4.1.4)$$

where $I(\mathbf{k})$ is the diffuse intensity observed in the reciprocal space, $\varphi(\mathbf{k})$ is the effective atomic scattering factor depending on the difference f_A-f_B of the atomic scattering factors of A and B (for binary AB alloys) and on values of the static displacements, $\tilde{w}(\mathbf{k})$ is the Fourier transform of the "*mixing*" energy and *c* is the concentration.

Since MC simulations are performed in the real-space, it is necessary to recalculate the ordering energies (Eqs. 3.16-3.17). As we are interested in the calculation of parameters within 2 coordination shells, from Eq. 3.17 we will take the expressions only for 2 points in the reciprocal

space (Γ(000) and X(001)). After the calculation given in Appendix 5.1 we have obtained the following values of the interaction parameters:

$$\begin{aligned} V_1^{Fe-Fe} &= 5172.79K\ ; \quad V_1^{Ni-Fe} = 5665.44K\ ; \quad V_1^{Ni-Ni} = 5289.795K \\ V_2^{Fe-Fe} &= -2151.353K\ ; \quad V_2^{Ni-Fe} = -2356.244K\ ; \quad V_2^{Ni-Ni} = -2200.015K \end{aligned} \tag{4.1.5}$$

We have tested these values and compared our results with the previous ones (with only NN interactions ($L = 10$, $\Delta T = 10K$)). In Fig. 4.1.10 the plot of the specific heat is presented in order to compare the obtained transition temperatures.

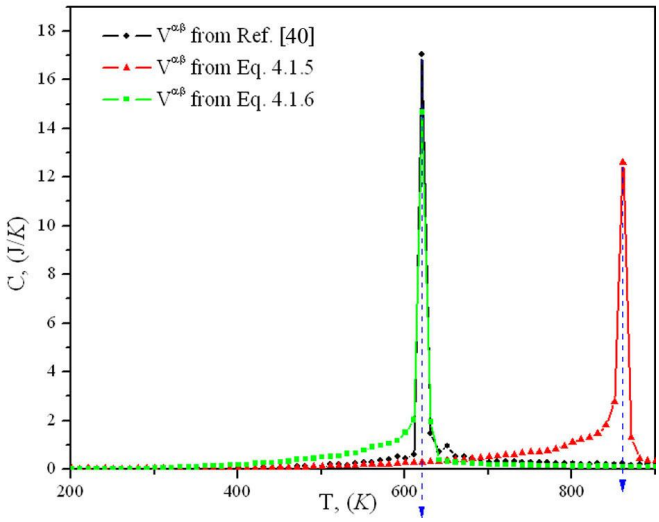

Figure 4.1.10. Temperature dependence of the specific heat, *C*(*T*)

It is seen that the transition temperature T_K is overestimated ($\approx (871.0 \pm 2.5)K$) in comparison with the previously determined T_K ($\approx (631.0 \pm 2.5)K$, see section *A*). In order to obtain the same transition temperature for both sets of $V_{r=\{1,2\}}^{\alpha\beta}$, we have rescaled the new pair-wise parameters (Eq. 4.1.5) by the ratio $\frac{871}{631} = 1.38$ and obtained:

$$\begin{aligned} V_1^{Fe-Fe} &= 3748.3986K\ ; \quad V_1^{Ni-Fe} = 4105.3913K\ ; \quad V_1^{Ni-Ni} = 3833.1848K \\ V_2^{Fe-Fe} &= -1558.9514K\ ; \quad V_2^{Ni-Fe} = -1707.4232K\ ; \quad V_2^{Ni-Ni} = -1594.2138K \end{aligned} \tag{4.1.6}$$

With these parameters T_K coincides with that obtained in section *A* (for chosen system size) (Fig. 4.1.10). Simulations with these newly defined $V_{r=\{1,2\}}^{\alpha\beta}$ were performed and the thermodynamic quantities (internal energy, long-range and short-range order parameters, and specific heat) are shown below. It should be noticed that thermal hysteresis is not visible, i.e. all plots for systems with different initial configurations and T_{init} exhibit the same T_K. Due to this fact, only the plots for $T_{init} > T_K$ will be presented in the following.

It should be noticed that the choice of the interaction parameters can be done arbitrarily but in accordance with the obtained ordering energies. We have tested different sets of $V_{r=\{1,2\}}^{\alpha\beta}$

and the results were identical if we kept the same w_1 and w_2.

1) Internal energy

With the new interactions within 2 coordination shells, the ground state energy per atom, E_{GS}^{chem}, for the $L1_2$ structure, is given by the formula:

$$E_{GS}^{chem} = -\left(3(V_1^{Ni-Ni} + V_1^{Ni-Fe}) + \frac{3}{4}V_2^{Fe-Fe} + \frac{9}{4}V_2^{Ni-Ni} \right),$$

where $V_{r=\{1,2\}}^{\alpha\beta}$ are defined in Eq. 4.1.6. Then, E_{GS}^{chem} is equal to -19059.5337K. As seen from Fig. 4.1.11a at very low temperature this value has been reached. The visualization of the final configuration confirms that there is no antiphase boundary anymore.

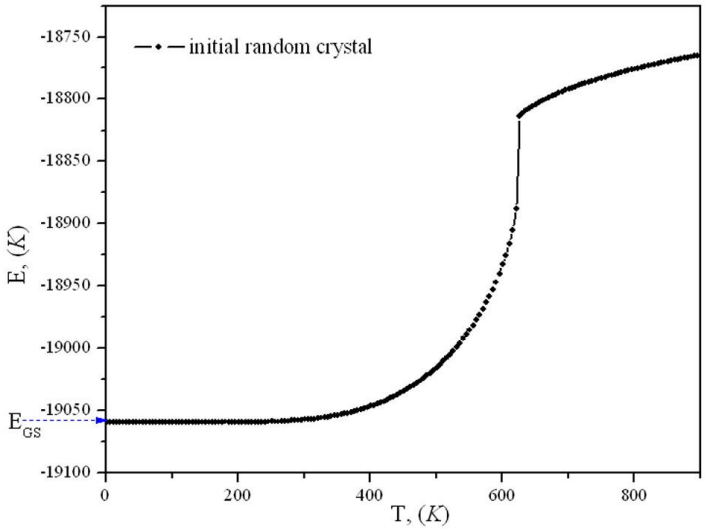

(a)

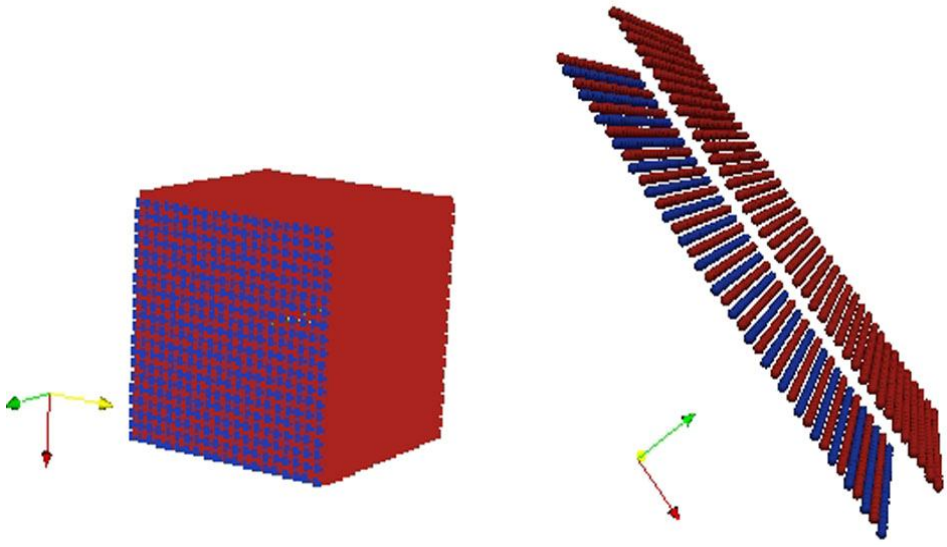

(b)

Figure 4.1.11. (a) Internal energy versus temperature
(b) Visualization of the obtained structure at 1*K*
Red and blue points represent Ni and Fe atoms, respectively

2) Order parameters

In Fig. 4.1.12a we have superimposed both the SROP and η. The long-range order parameter η at very low temperature is equal to 1 due to the perfect $L1_2$-type superstructure, so in this case it is not necessary to calculate the order parameter η_1 defined in Eq. 4.1.3. The Warren-Cowley parameter, α_1, is given only for the 1st coordination shell, and is equal to –0.33(3) at $1K$ which confirms the $L1_2$ ordering at low temperature.

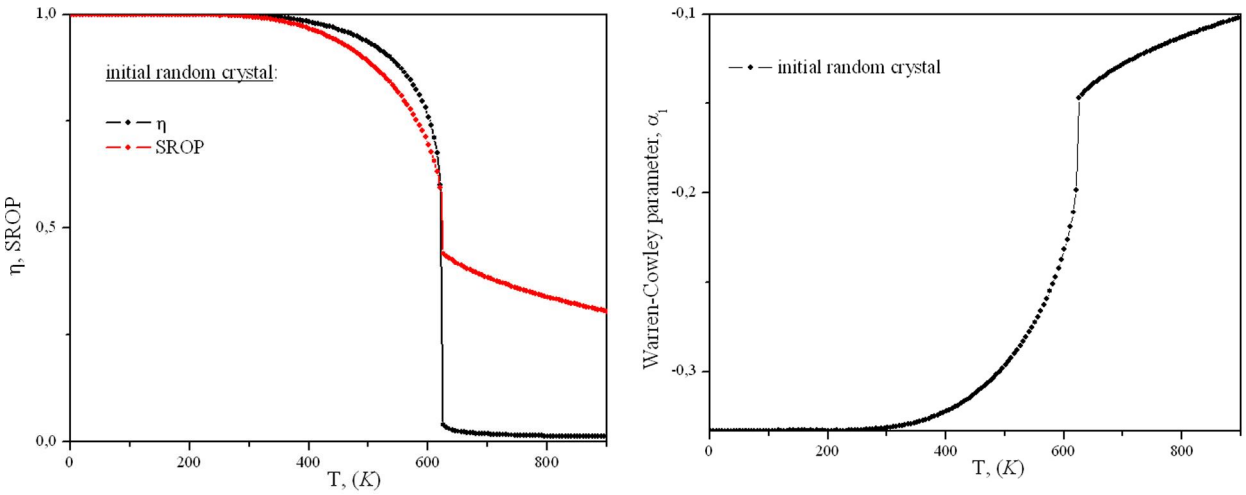

Figure 4.1.12. Temperature dependence of:

(a) Long-range, η, and short range, SROP, order parameters

(b) Warren-Cowley short-range order parameter, α_1

It is visible that above the order-disorder transition the short-range order is still present as it was mentioned in section *A*. The jump in η is less pronounced than in the case of only NN interactions (Fig. 4.1.7). This will be discussed later in section *C*.

3) Specific heat, *C*.

The specific heat plot is given below in Fig. 4.1.13. From the presented plot of the order parameters and the specific heat (Fig. 4.1.12-4.1.13, respectively) we have estimated the order-disorder phase transition temperature. These estimates (Table 4.1.3) agree with previously determined values of T_K.

T_K from $\eta(T)$, (K)	626.0±2.5
T_K from C(T), (K)	621.0±2.5

Table 4.1.3. Ordering temperatures, T_K, estimated from thermodynamic quantities (with NNN interactions)

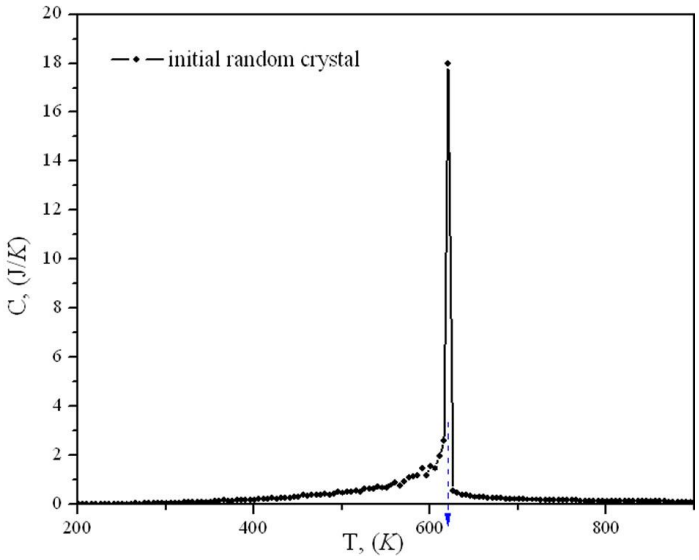

Figure 4.1.13. Temperature dependence of the specific heat, *C*(*T*)

C. Discussion

The obtained transition temperatures T_K are summarized in Table 4.1.4. $T_K^{ordering}$ is the transition temperature defined in simulation when the transition is approached from high temperature (*ordering case*) and $T_K^{disordering}$ when it is approached from low temperature (*disordering case*). In case of NNN interactions we were not able to distinguish between these two temperatures.

	NN interactions		**NNN interactions**
	$T_K^{ordering}$, (K)	$T_K^{disordering}$, (K)	T_K, (K)
from $\eta(T)$	636.0±2.5	646.0±2.5	626.0±2.5
from $C(T)$	631.0±2.5	646.0±2.5	621.0±2.5

Table 4.1.4. Comparison of different estimates of the transition temperature T_K

The estimates obtained in the simulations are self-consistent. It is important to notice the difference in the internal energy plots, corresponding to different sets of $V_{r=\{1,2\}}^{\alpha\beta}$ (Fig. 4.1.14a). It can be seen that the latent heat, L, corresponding to the energy jump, ΔE, at T_K, $\Delta E = L = T_K \cdot \Delta S$, has been reduced almost by a factor 2. When NNN interactions are neglected, the latent heat is equal to $L^{r=\{1\}} \approx 138K$, and when they are considered $L^{r=\{1,2\}} \approx 73.5K$. This means that taking into account NNN interactions softens the transition.

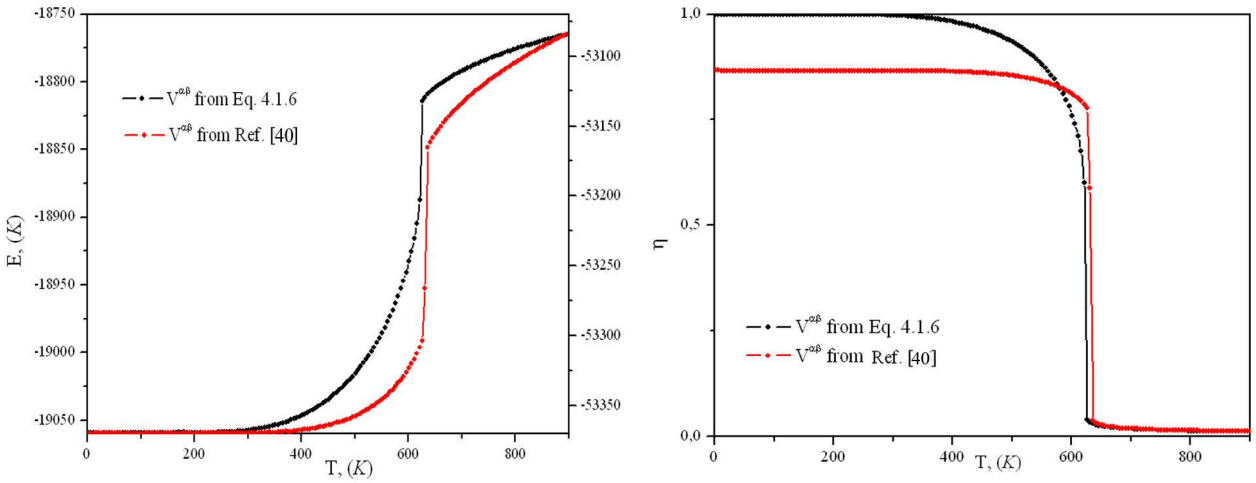

Figure 4.1.14 Comparison between the temperature dependencies of:

(a) Internal energy

(b) Long-range order parameter, η

For 2 sets of interaction parameters

Due to the softening of the transition [84,87], the hysteresis is less pronounced. Combined with a finite temperature step, this can explain that it is not visible in this case. One should note also that the long-range order parameter still exhibits a significant jump at the transition (Fig. 4.1.14b).

In the studied Ni_3Fe alloy the order-disorder transition is of 1st order. Above T_K short-range order still persists and consequently will be able to influence the magnetic order and, consequently, the Curie temperature. Thus, in order to adequately describe the alloy it is necessary to consider both types of interactions simultaneously.

4.1.1.3. Simulations with chemical and magnetic interactions

In sections 4.1.1.1-4.1.1.2 we have attempted to describe the Ni_3Fe system neglecting one of the interactions (chemical or magnetic, respectively). But taking into account properties of this system, experimentally observed features (Chapter 1) and presented above results it is necessary to mention that more realistic picture will be obtained if both magnetic and chemical interactions are included in the model. For this case the Hamiltonian of the system will have the form:

$$\mathcal{H}_{total} = \mathcal{H}_{magn} + \mathcal{H}_{chem} = -\sum_{\langle ij \rangle}\sum_{\alpha\beta} J_{ij}^{\alpha\beta}(\vec{S}_i^{\alpha}\cdot\vec{S}_j^{\beta})\xi_i^{\alpha}\xi_j^{\beta} - \sum_{\langle ij \rangle}\sum_{\alpha\beta} V_{ij}^{\alpha\beta}\xi_i^{\alpha}\xi_j^{\beta} \qquad (4.1.11)$$

All symbols correspond to those used for (Eq. 2.1) and (Eq. 4.1.2).

The algorithm, described in section 2.2.2.1 has been interpreted in a following way:

- Firstly, two atoms of different kind are exchanged and their spins are rotated;

- In case of rejection, only rotation of one of the two previously chosen spins is proposed.

Such algorithm was chosen in order to equilibrate the magnetic subsystem at low temperatures, because below T_K atomic jumps are rare ($\eta \approx 1$) and the chemical configuration is frozen whereas the magnetic moments still fluctuate ($M < M_{Sat}$).

Different initial conditions ($T_{init} > T_K$ and $T_{init} = 1K$) and sets of chemical interaction parameters, $V_{r=\{1,2\}}^{\alpha\beta}$, have been also implemented (as in case of only chemical interactions). After several tests, we have kept the following simulation parameters:

L	20 (N=32000)
n	10 000
scale	10
ΔT (K)	10

A. Nearest neighbor interactions (NN interactions)

The values of the magnetic "exchange" interactions, $J^{\alpha\beta}$, and chemical interactions, $V_1^{\alpha\beta}$ are those that were defined in sections 4.1.1.1 and 4.1.1.2*A*, respectively. The studied system should exhibit two phase transitions: a paramagnetic↔ferromagnetic 2nd order transition at T_C, and an order-disorder 1st order transition at $T_K < T_C$. Due to the mutual influence of magnetic and chemical order we can expect some new features in the plots of thermodynamic quantities. The following observables were measured: the internal energy (total, magnetic and chemical), the order parameters (magnetization (total, Fe- and Ni-sublattice) and the chemical long-range and short-range order parameters), the specific heat (magnetic and chemical) and the magnetic susceptibility.

1) Internal energy

In Fig. 4.1.15 we have presented thermal dependence of the magnetic, E_{MAGN}, chemical, E_{CHEM}, and total ($E_{\mathrm{TOTAL}} = E_{\mathrm{MAGN}} + E_{\mathrm{CHEM}}$) internal energies. As expected, a hysteresis appears in a narrow temperature interval ($\approx 20K$). At very low temperature T the system consists of ordered domains separated by antiphase boundaries (Fig 4.1.15a). From Fig. 4.1.15b, it is seen that both magnetic and atomic subsystems reach their ground state.

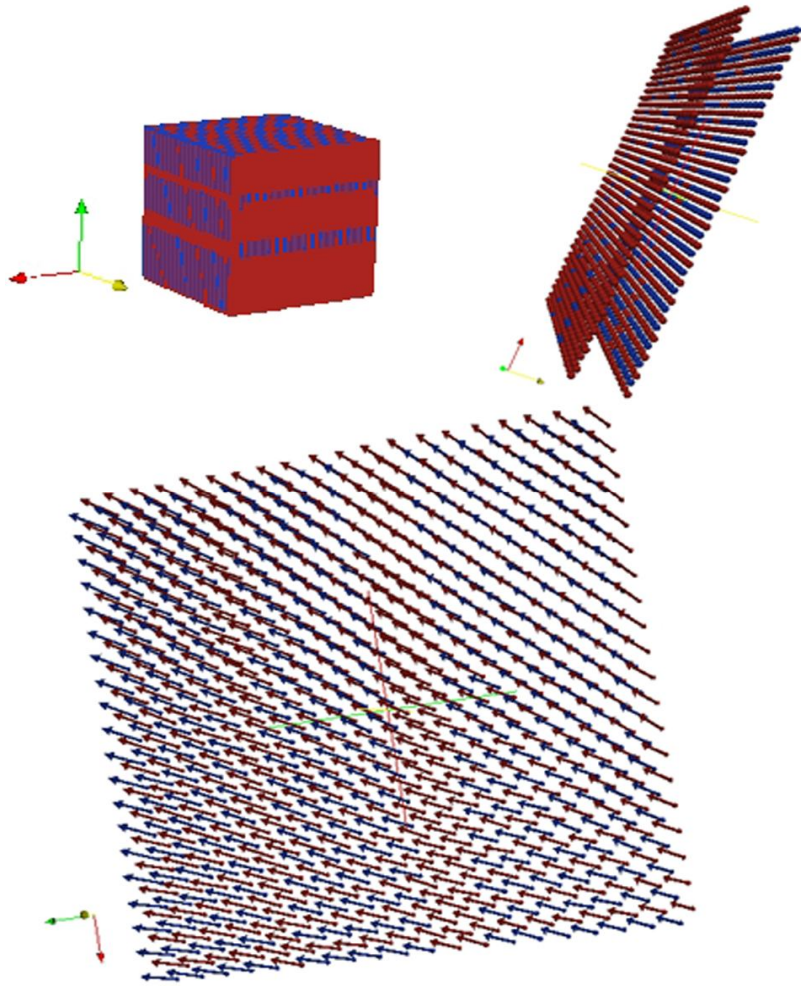

(a)

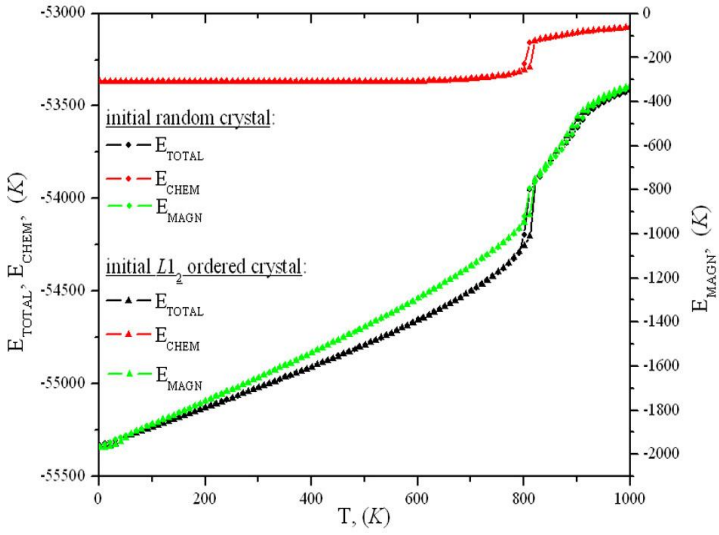

(b)

Figure 4.1.15. (a) Final structure visualization. Ni and Fe atoms are represented by red and blue points, respectively

(b) Internal energies (chemical, magnetic and total) versus temperature

Although the ground state magnetic energy $\left(E_{GS}^{magn} = -1966.85K\right)$ is much smaller than the ground state chemical energy $\left(E_{GS}^{chem} = -53370K\right)$, the magnetic contribution can not be neglected as usually done. Indeed, the magnetic energy variation during the annealing $\left(\Delta E_{\mathrm{MAGN}} \approx 1730K\right)$ is in fact larger than the variation of the chemical one $\left(\Delta E_{\mathrm{CHEM}} \approx 320K\right)$.

Furthermore, a new feature is visible from the presented curve of E_{MAGN} (Fig. 4.1.15b). It is seen that E_{MAGN} exhibits a jump at T_K. Such behavior can be explained as following: when the atomic configuration changes abruptly this should affect the magnetic configuration and, because the destruction of the $L1_2$ order above T_K increases the number of antiferromagnetic Fe-Fe pairs and, therefore, causes a reduction in the effective "exchange" (magnetic) interaction leading to an increase in E_{MAGN}. Obviously, the magnetization will exhibit similar feature.

2) Order parameters

As in the section 4.1.2*A*, we have calculated for the chemical sub-system long-range and short range order parameters. Here we have presented only the plots for the short-range order parameter, SROP, and "long"-range order parameter, η_1, (Fig. 4.1.16a). The thermal variations of the long-range order parameter, η, and of the Warren-Cowley parameter, α_1, are the same as have been already shown. The total reduced magnetization, $M / M_{Saturation}$, is also shown on the same plot.

Comparing with the plots obtained in section 4.1.1.1 (Fig. 4.1.2) it is possible to note the change in the behavior of the magnetization (total, Fe- and Ni-sublattices). From Fig. 4.1.16 it is seen that the magnetization exhibits a jump (the same as the internal magnetic energy) at T_K. When magnetic and chemical orders coexist ($T < T_K$), the magnetization slowly decreases and the destruction of the atomic order above T_K leads to a more rapid decrease (Fig. 4.1.16b). Below the transition point T_K, the magnetization behaves as for the $L1_2$ ordered system but above T_K the magnetization behaves similarly to the magnetization of a random chemical configuration. The Fe- and Ni sublattice magnetizations exhibit the same behavior (Fig. 4.1.16c). Below T_K the difference between their values is noticeable (as in Fig. 4.1.2b) and after transition both values approach the average total magnetization.

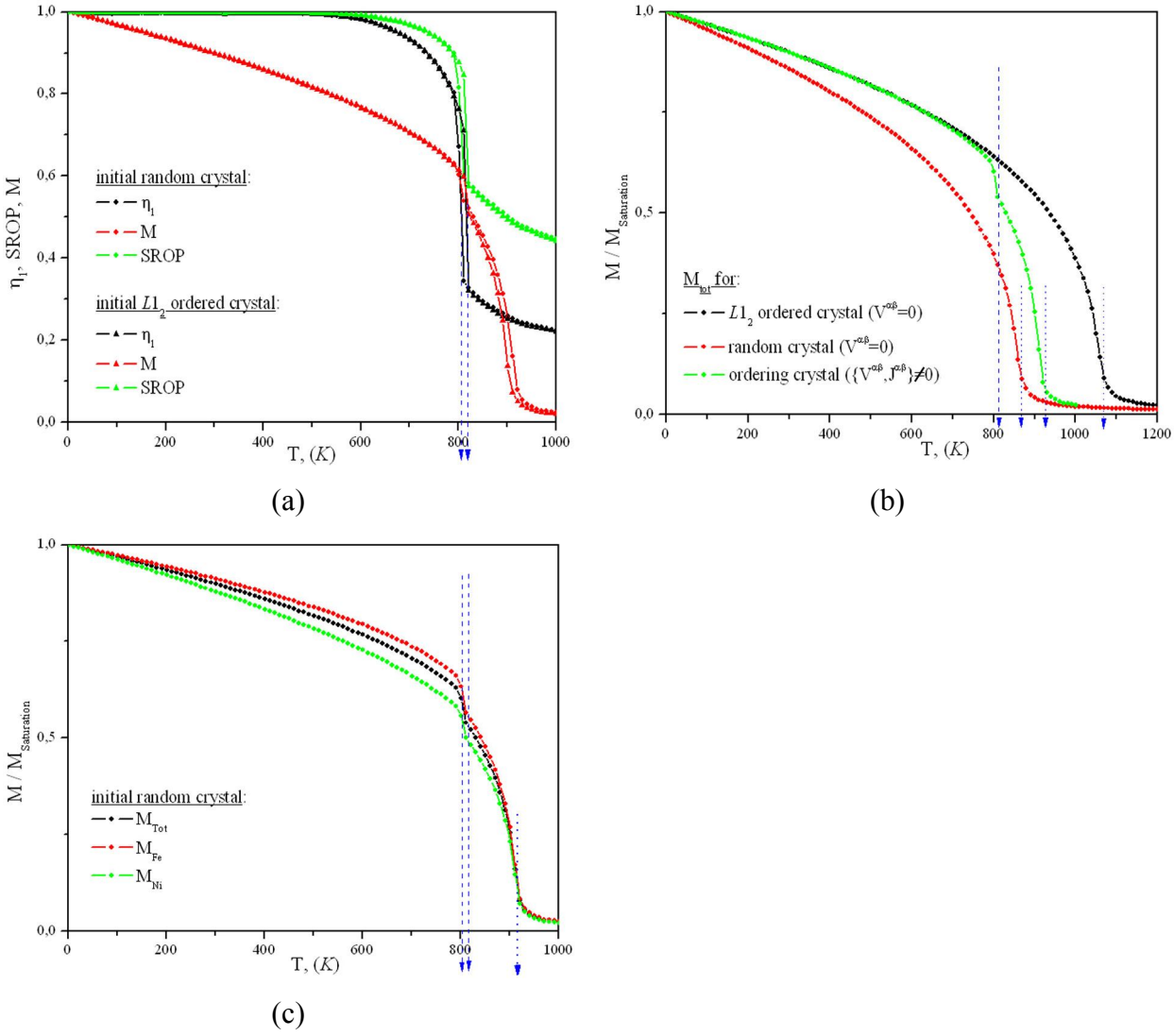

Figure 4.1.16. Thermal variation of:

(a) Order parameters η_1 and SROP, and reduced total magnetization M

(b) Reduced total magnetizations for crystal with different state of order

(c) Reduced magnetizations (total, Fe- and Ni-sublattices)

The existence of short-range chemical order above T_K leads to the increase of T_C in comparison with $T_C^{disordered}$ (Fig. 4.1.16b). Thus, the estimate of T_C is neither equal to $T_C^{disordered}(\approx 870K)$ nor to $T_C^{ordered}(\approx 1070K)$ but is somewhere in between. It is important to note that chemical short-range order still exists above T_C ($\mathrm{SROP}^{chem+magn}(T = 1001K) \approx 0.446$) and decreases slowly with the temperature. Thus, the simulated T_C corresponds to a chemically short-range ordered alloy. In this case, this short-range chemical order prevents the appearance of the Fe-Fe NN bonds and, therefore, it will influence the magnetic configuration. The short-range order parameter decreases faster when the magnetic interactions are not included. Also, magnetic short-range order interactions exist in the paramagnetic state and, consequently, are able to

influence chemical configuration of the alloy (which is also in the chemically short-range ordered state at high temperatures). At intermediate temperatures ($T_K < T < T_C$) also magnetic order enhances the values of the short-range order parameter ($\mathrm{SROP}^{chem+magn}(T = 851K) \approx 0.55$, and $\mathrm{SROP}^{chem}(T = 851K) \approx 0.48$).

According to the presented plots of the order parameters, the estimated transition temperatures (T_K – dashed line and T_C – dotted line) are given in Table 4.1.5.

	T_C, (K)	$T_K^{ordering}$, (K)	$T_K^{disordering}$, (K)
from $\eta(T)$	—	811±5	821±5
from $C_{\mathrm{CHEM}}(T)$	—	801±5	811±5
from M(T)	921±5	—	—
from $\chi(T)$ ($C_{\mathrm{MAGN}}(T)$)	911±5	—	—

Table 4.1.5. Estimated transition temperatures, T_C and T_K

From the configuration obtained in MC simulations at each temperature, it is possible to calculate the Fourier transformation and therefore to compute the diffraction patterns. For ordered structures at low temperature, the superstructure peaks should appear in addition to the structure ones. As known, for $L1_2$ structure the superstructure reflections correspond to (100) and equivalent positions. Such diffuse intensity patterns can be used for the definition of the short-range and long-range order parameters.

In Fig. 4.1.17(a-c) we have presented the result of the Fourier transformation of the configurations obtained from MC simulations. These MC simulations have been performed starting from the disordered crystal, i.e. $T_{init} > T_K$. These results correspond to the calculated diffuse intensities, I. The patterns above T_K (Fig. 4.1.17a) and T_C (Fig. 4.1.17b) can be compared to the diffuse intensity pattern of the random alloy (Fig. 4.1.17c).

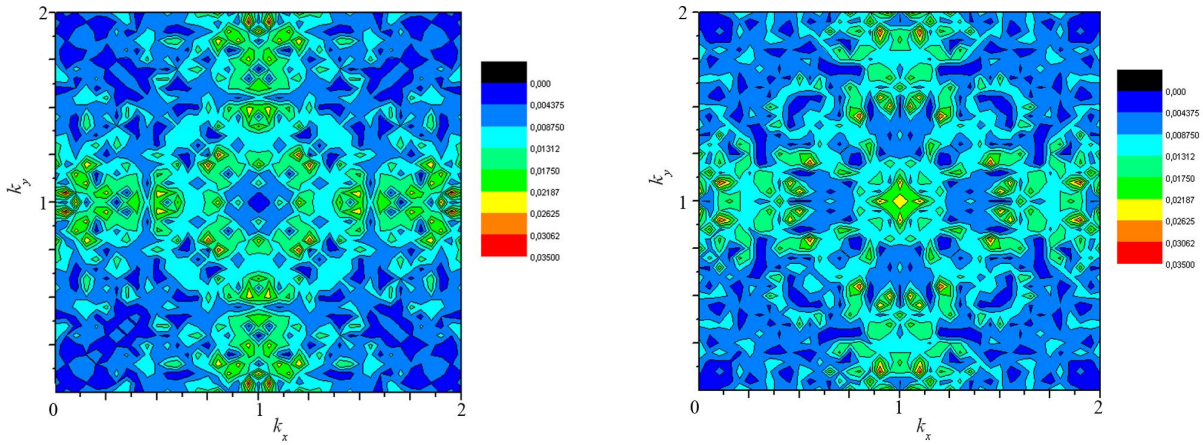

(a) (b)

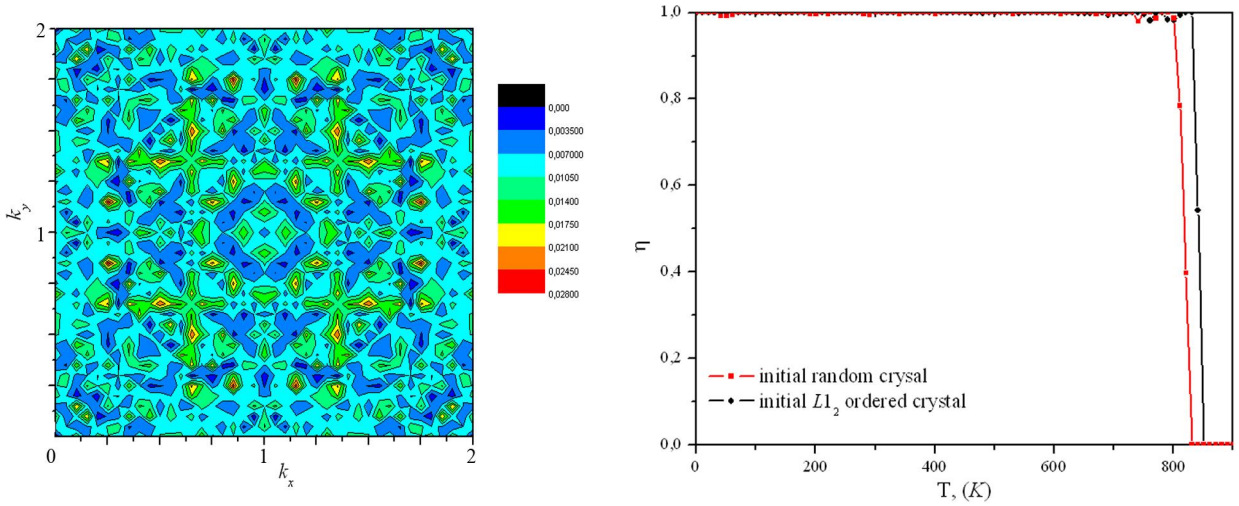

(c) (d)

Figure 4.1.17. Fourier transformation of different configurations:

(a)–(b) Diffuse intensities measured at $T = 881, 981K$, respectively

(c) Diffuse intensity of a random alloy

(d) Thermal variation of the long-range order parameter.

As seen, when the crystal is short-range ordered (at $T = 881K$ and $T = 981K$) we observe the increase of the intensity around the superstructure reflections. Using diffuse intensities we can also calculate the long-range order parameter by the following formula:

$$\eta^2 = \frac{I(100)}{I(200)}, \tag{4.1.4}$$

where $I(100)$ and $I(200)$ are the diffuse intensities at the superstructure and structure reflections, respectively. The result of this calculation is presented in Fig. 4.1.17d and can be compared with the long-range order parameter, calculated during simulations using Eq. 4.1.3 (Fig. 4.1.16a). The estimated transition temperatures are consistent within the errors.

3) Specific heat and susceptibility

The plots of the chemical specific heat C_{CHEM} (shown in Fig. 4.1.18a) look similar to the previously described simulations (Fig. 4.1.9) showing a maximum at T_K and a weak hysteresis.

The magnetic specific heat C_{MAGN} (Fig. 4.1.18a) and zero-field magnetic susceptibility χ (Fig. 4.1.18b) also have the expected shape (in comparison with Fig. 4.1.3) with a maximum corresponding to T_C. Moreover, there is one additional peak on both curves at TK, (this feature is clearly visible for the susceptibility curve obtained from the simulation in the ordering case with $T_{init} > T_K$). It can be explained by the influence of the atomic configuration on the magnetic ordering. As both internal magnetic energy and magnetization exhibit a jump at TK,

consequently a δ-peak (actually, a maximum due to finite size-effects) should be present on the plot of their derivatives, the magnetic specific heat and the susceptibility. The obtained transition temperatures are summarized in Table 4.1.5.

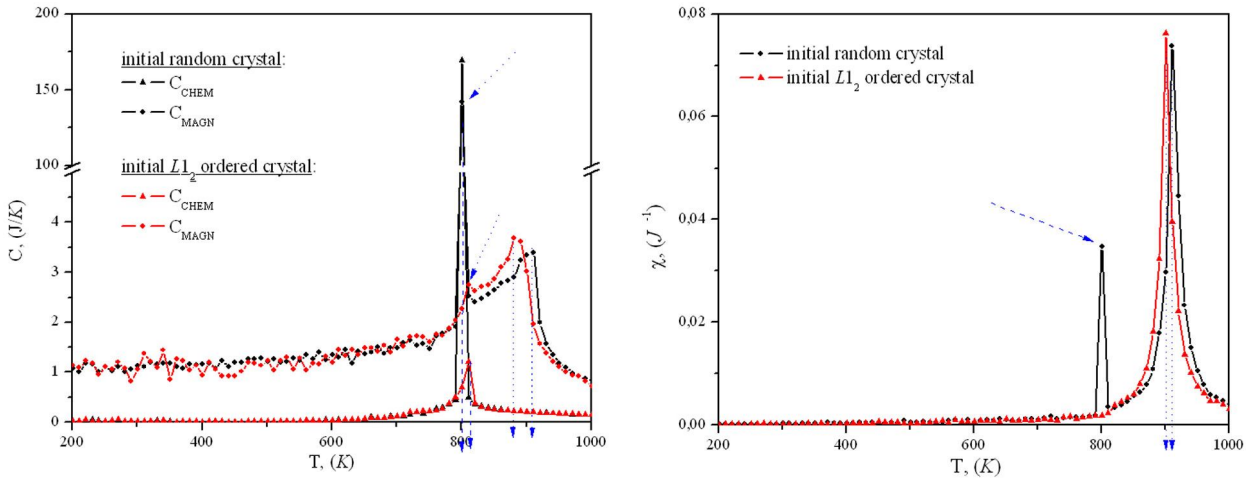

(a) (b)

Figure 4.1.18. Temperature dependences of:

(a) Specific heat (magnetic and chemical)

(b) Zero-field magnetic susceptibility

B. Interactions within 2 coordination shells (NNN interactions)

For these simulations the same values of the chemical pair-wise interactions, $V^{\alpha\beta}_{r=\{1,2\}}$, have been used (Eq. 4.1.6). Moreover, let us remind that taking into account NNN interactions allows reaching a perfectly ordered $L1_2$-type structure at very low temperature without antiphase boundaries.

1) Internal energy

As a result of this simulation, the crystal with a perfect $L1_2$-type superstructure has been obtained (Fig. 4.1.19a). The thermal variation of the total, magnetic and chemical energies are shown below in Fig. 4.1.19b. The curves look similar to those obtained in section *A*. The energy variation during the annealing, ΔE_{MAGN} (ΔE_{CHEM}), is about $1700K$ ($300K$). At the order-disorder transition, E_{MAGN} exhibits a jump (as expected and described earlier). Both E_{MAGN} and E_{CHEM} reach their ground state level at the end of the simulation, as expected.

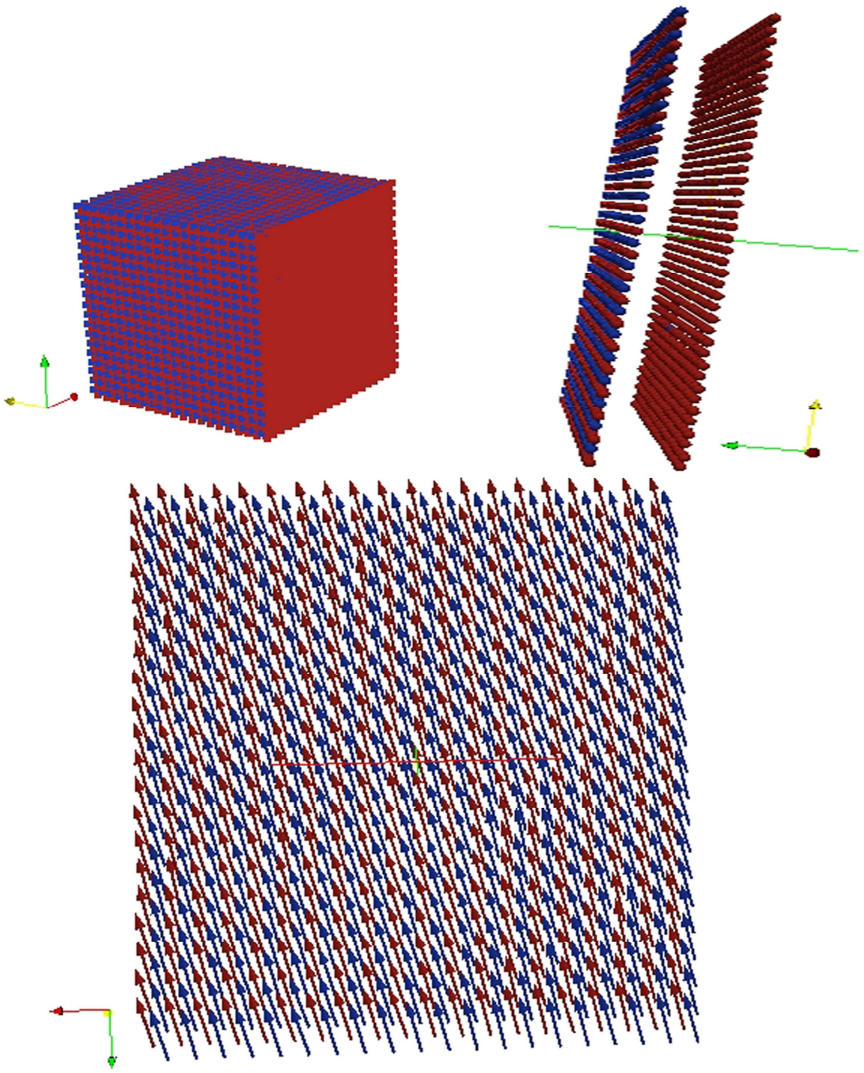

(a)

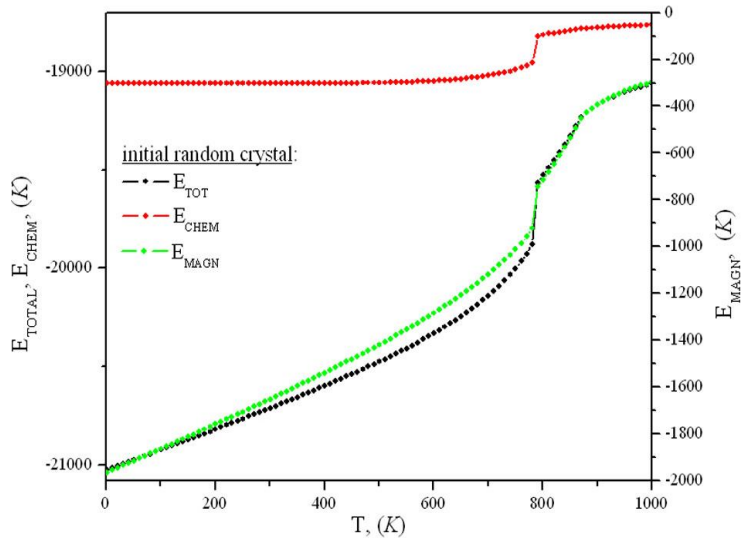

(b)

Figure 4.1.19. (a) Visualization of final configuration.

Red and blue points are Ni and Fe atoms

(b) Internal energy (chemical, magnetic and total) versus temperature

2) Order parameters

The thermal variation of the order parameters (long-range and short-range) are plotted in Fig. 4.1.20. The Warren-Cowley short-range order parameter, α_1, will not be shown here because it has the expected shape and have been discussed earlier in section 4.1.1.2. Due to the formation of a perfect ordered $L1_2$-type structure at very low temperature (Fig. 4.1.19a) it is possible to use the definition of the long-range chemical parameter η (Eq. 2.13).

As expected and described in the previous section *A*, the magnetization exhibits a jump at T_K connected with a formation (or destruction) of chemical order. Short-range chemical order is still present above T_K ($\mathrm{SROP}^{chem+magn}(T = 851K) \approx 0.39$) and even above T_C ($\mathrm{SROP}^{chem+magn}(T = 1001K) \approx 0.3$). The values of the SROP are lower than for NN interaction results (0.55 and 0.46, respectively, see Fig. 4.1.16a) and, therefore, can influence the value of T_C. The dashed and dotted lines in figure intersect the temperature axis at T_K and T_C, respectively (Table 4.1.6).

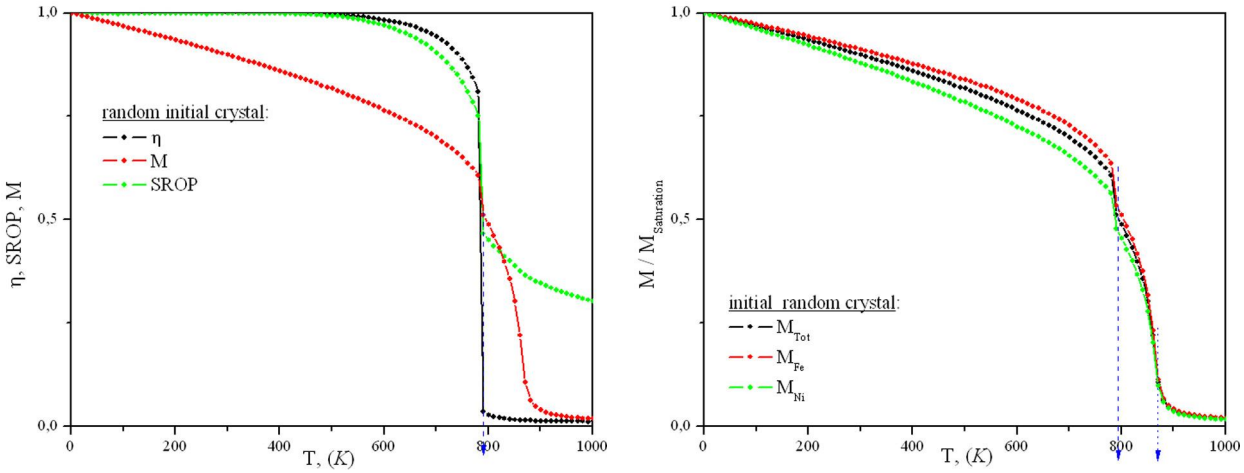

(a) (b)

Figure 4.1.20. Temperature dependence of:

(a) Order parameters η and SROP, reduced total magnetization M

(b) Reduced magnetizations (total, Fe- and Ni-sublattices)

	T_C, (*K*)	T_K , (*K*)
from $\eta(T)$	—	791±5
from $C_{\mathrm{CHEM}}(T)$	—	781±5
from M(*T*)	881±5	—
from $\chi(T)$ ($C_{\mathrm{MAGN}}(T)$)	871±5	—

Table 4.1.6. Estimated transition temperatures, T_C and T_K

3) Specific heat and susceptibility

The specific heat (C_{CHEM} and C_{MAGN}) and the zero-field magnetic susceptibility (Fig. 4.1.21) have the same shape as in section *A*. The estimated transition temperatures are listed in Table 4.1.6.

For reasons of clarity, only the curves for simulations in the ordering case with $T_{init} > T_K$ have been shown. It has to be noted that the additional peaks at T_K are not visible here because of the non zero temperature step ΔT (they are visible on the curves obtained with $T_{init} < T_K$).

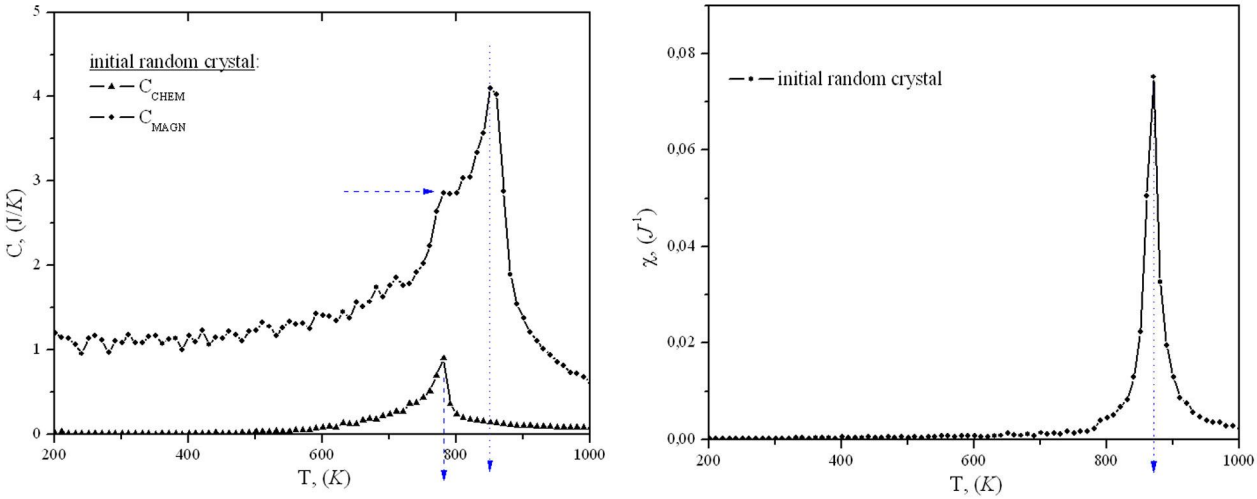

(a) (b)

Figure 4.1.21. Temperature dependence of:

(a) Specific heat (magnetic and chemical)

(b) Zero-field magnetic susceptibility

C. Discussion

The latent heat changes from $L^{r=\{1\}} \approx 160K$ when only NN interactions were considered, to $L^{r=\{1,2\}} \approx 135K$ when interactions were extended to NNN. The comparison of the latent heat is shown in Fig. 4.1.22 and Table 4.1.7.

	NN interactions	**NNN interactions**
	L, (*K*)	*L*, (*K*)
Chemical interactions ($J^{\alpha\beta} = 0$)	138	73.5
Chemical and magnetic interactions	160	135

Table 4.1.7. Comparison of the latent heat for simulations with NN and NNN interactions

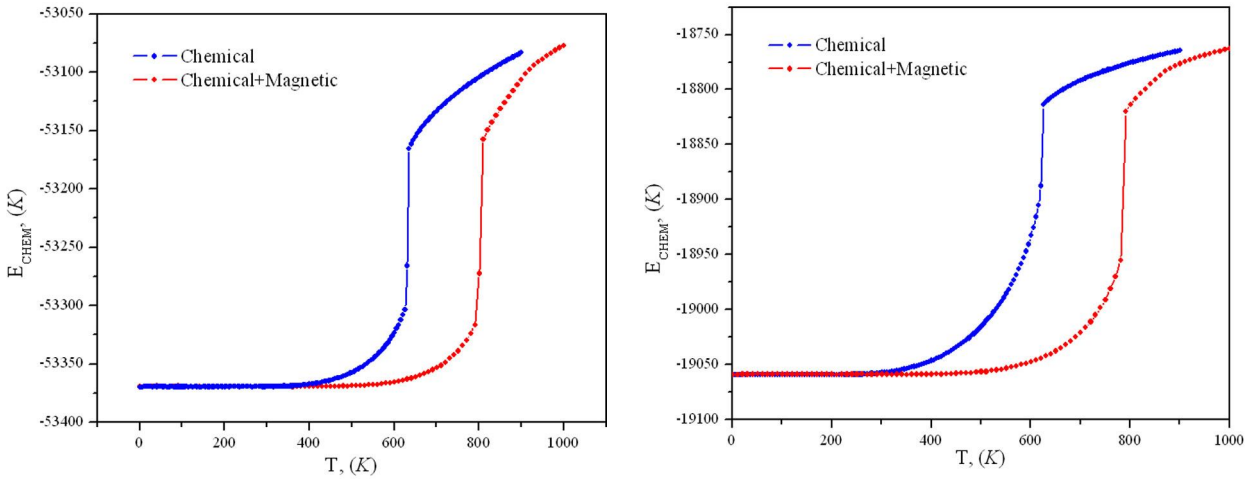

(a) (b)

Figure 4.1.22. Comparison of the thermal variation of the internal energy for:
(a) Simulations with NN interactions
(b) Simulations with NNN interactions

As seen from Fig. 4.1.22b and Table 4.1.7, the magnetic interactions have increased the values of the latent heat (as seen, in case of NNN interactions, the latent heat has increased by almost a factor 2).

The transition temperatures are slightly different for both cases and are given in Table 4.1.8. The difference in the values is attributed to the chemical short-range order, which is weaker in case of NNN interactions, as has been mentioned before in section *B*.

	NN interactions			**NNN interactions**	
	T_C, (K)	$T_K^{ordering}$, (K)	$T_K^{disordering}$, (K)	T_C, (K)	T_K, (K)
from $\eta(T)$	—	811±5	821±5	—	791±5
from $C(T)$	—	801±5	811±5	—	781±5
from M(T)	921±5	—	—	881±5	—
from $\chi(T)$ ($C(T)$)	911±5	—	—	871±5	—

Table 4.1.8. Comparison of the estimated transition temperatures, T_C and T_K, for simulations with NN and NNN interactions

4.1.1.4. Conclusion

In Fig. 4.1.23 we have given a comparison between chemical (η_1) and magnetic (M) order parameters for different types of simulations to make more evident the mutual influence of the two types of interactions.

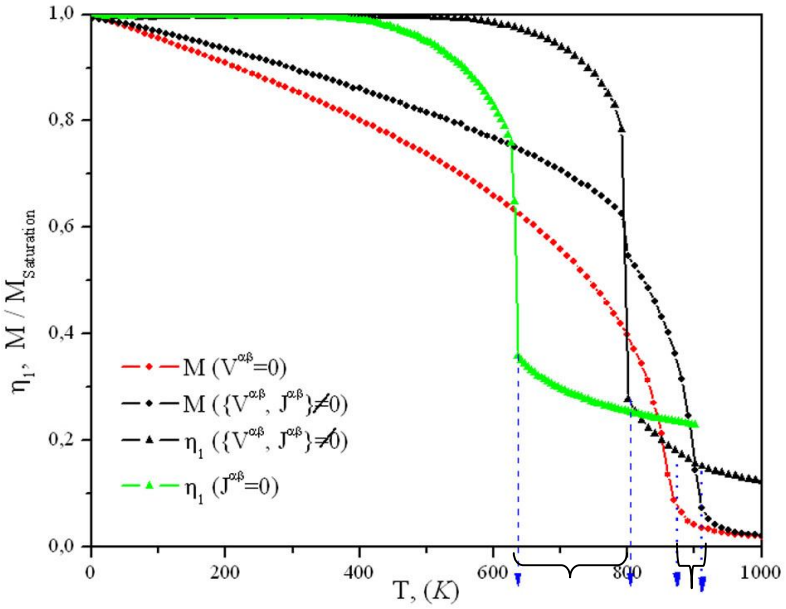

Figure 4.1.23. Comparison between order parameters for magnetic only, chemical only and simultaneous chemical and magnetic simulations (with NN interactions only)

Short-range chemical order (above T_K) obviously influences the magnetic behavior (because $T_K < T_C$) and, thus, the estimated Curie temperature T_C is higher than those determined from the simulations neglecting chemical ordering. Reciprocally, the magnetic order above T_K and T_C also influences atomic configuration.

To summarize the results it is interesting to compare our estimated transition temperatures for all three types of simulations with the experimental values (Table 4.1.9).

		T_C, (K) from $\chi(T)$		T_K, (K) from $\eta(T)$	
		disordered	$L1_2$ ordered	ordering	disordering
MC simulations (25% at. Fe)	Magnetic interactions ($V^{\alpha\beta} = 0$)	861±5	1061±5	-	-
	Chemical interactions ($J^{\alpha\beta} = 0$)	-	-	636±2.5	646±2.5
	Chemical and magnetic interactions	911±5		811±5	821±5
	Experiment (25% at.Fe) [12]	871	954	771	

Table 4.1.9. Comparison of the estimated transition temperatures with the experimental values (for simulation, only results with NN interactions are presented)

As seen from the table, the estimated Curie temperature from the simulation with magnetic and chemical interactions is slightly different from the experimentally obtained value.

The chemical short-range order could be responsible for the small deviation of estimated $T_C^{chem+magn}$ in comparison with experimental data on rapidly cooled alloy [12] which is supposed to be disordered. Besides that, the Curie temperature of the ordered alloy (in particular, the alloy was slowly cooled and considered to be ordered [12]) is also lower than estimated from the magnetic simulation on the $L1_2$ ordered crystal. This can be due to the fact, that during the measurements above T_K, the alloy may have already some "mixed" ordered/disordered structure due to the atomic diffusion processes. Such discrepancies in $T_C^{L1_2\,ordered}$ and $T_C^{\exp}$ have been discussed in section 4.1.1.1.

The obtained results can be compared to the results Dang *et al*. [40]. We should recall that the difference between our model and the model used in Ref. [40] consists in the application of the Heisenberg Hamiltonian to the magnetic subsystem. Therefore, the magnetic interactions have been also changed but the chemical interactions have been taken the same. The differences in the obtained transition temperatures are summarized in Table 4.1.10.

	$T_K^{chem+magn} - T_K^{chem}$	$T_C^{chem+magn} - T_C^{disordered}$
Our simulation	175	50
Rancourt *et al*. [40]	100	100

Table 4.1.10. Comparison of the obtained results with simulations of Dang *et al.* [40]

From the table it can be noticed that, in our simulations, the influence of the magnetic order on the Kurnakov transition temperature is more pronounced in comparison with Ref. [40]. Reciprocally, our estimate of the magnetic transition temperature is less influenced by the chemical order than in simulations of Dang *et al*. We can connect such discrepancies to the applied models for magnetic subsystems and their ability to adequately reproduce the spin fluctuations.

Finally, we can mention that although our model is quite simple, it is able to reproduce with a reasonable agreement the experimental values of T_K and T_C, i. e. $T_C - T_K \approx 100K$. (In Ref. [40], the authors have obtained $\approx 210K$.)

4.1.2. Non-stoichiometric case (NN interactions)

In the previous sections we have simulated the case of the Ni_3Fe alloy. Considering only NN interactions and using the same parameters (magnetic and chemical) as before we would like

to investigate the concentration effect on the transition temperatures and compare our results with the phase diagram.

In general, magnetic and chemical interaction parameters are concentration dependent. Also, temperature variations affect inter-atomic distances and so produce variations of the interaction parameters. In our model we have neglected these dependencies and postulated $V^{\alpha\beta} = const$ and $J^{\alpha\beta} = const$ in the studied concentration range, i.e. $c_{Fe} \in [0.15; 0.35]$. The concentration dependence of the Curie temperature T_C and of the order-disorder transition temperature T_K are presented in Fig. 4.1.24. On the presented plot the uncertainties have been taken equal to $\frac{\Delta T}{2}$. The experimentally obtained phase diagram is superimposed to give more evident comparison.

When both types of interactions are included in the simulations, the shapes of the concentration variation of T_C and T_K are in a good agreement with the experimental phase diagram, although our estimates of T_C and T_K are slightly higher than $T_C^{\exp}$ and $T_K^{\exp}$. The discrepancies can be explained by the simplicity of our model and also by the possible experimental errors (due to the difficulties in reaching stable ordered configuration).

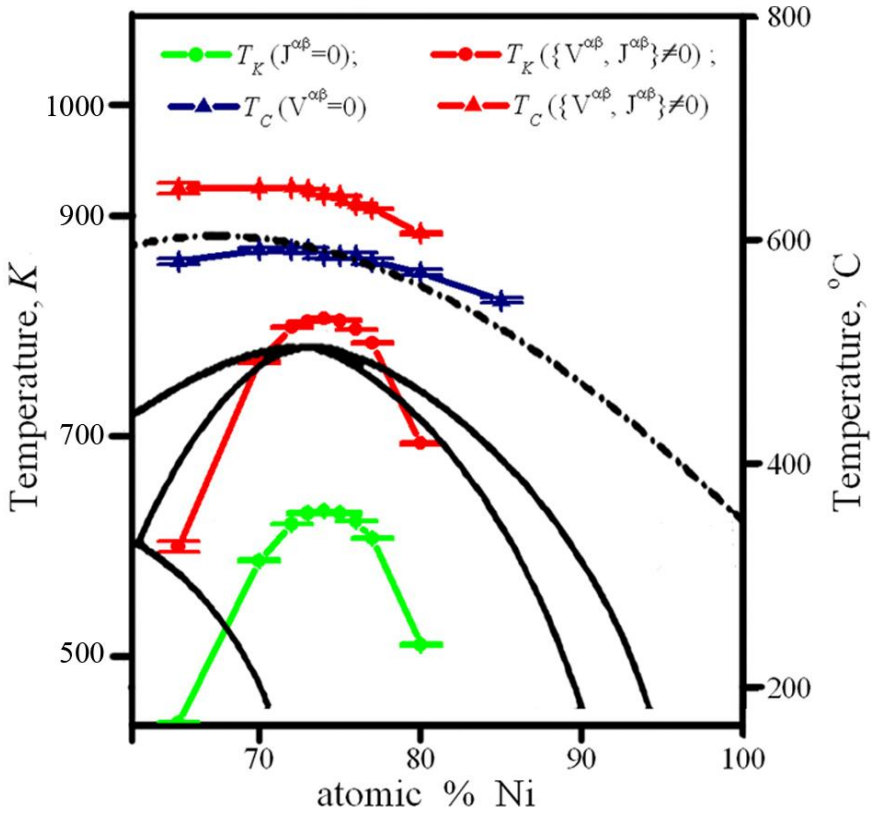

Figure 4.1.24. Comparison of the experimental phase diagram with simulated MC results (black continuous line – T_K, black dash-dotted line – T_C)

It is worth noting that magnetic interactions alone produce estimates of T_C close to the experimental data but the shape of the experimental curve is not well reproduced and T_C seems to be overestimated when c_{Ni} increases. This imperfection is eliminated when one considers chemical interactions. A better agreement in T_C would be probably obtained by considering magnetic interactions of smaller magnitude. The shapes of the two curves ($T_K^{chem}(c_{Fe})$ and $T_K^{chem+magn}(c_{Fe})$) are similar and seem to peak at $c_{Fe} \approx 0.26$. Theoretically, when magnetism of constituents is ignored, $T_K(c_{Fe})$ should be symmetrical with respect to $c_{Fe} = 0.25$ [88-90,100] due to the form of the chemical Hamiltonian. When magnetism is not neglected this maxima is shifted towards a higher value of c_{Fe} (≈ 0.26) because the form of the Hamiltonian is modified. This asymmetry has been previously shown for Ni-Fe and for other systems (for example, Fe-Co) [50-51,100-104,108].

Our model quite well reproduces the behavior of Ni_3Fe for concentrations close to stoichiometry. Let us mention that our numerical data are in reasonable agreement with experimental one only in the range $c_{Fe} \in [0.23; 0.3]$. With addition of either Ni or Fe we move to the regions of coexistence of several phases, i.e. $L1_2$+disordered and $L1_2$+$L1_0$. Therefore the discussion of the reliability of the model becomes more complex and our estimates of the transition temperatures become very approximate. For example we have faced such problem for $c_{Fe} = 0.15$ or 0.20.

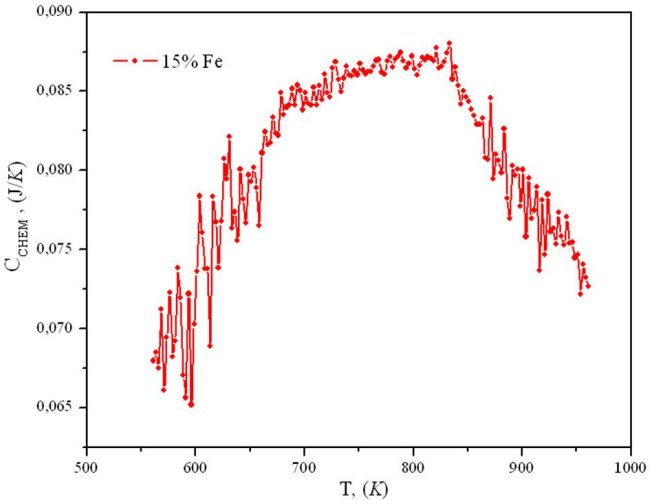

Figure 4.1.25. Temperature dependence of the chemical specific heat for $Ni_{85}Fe_{15}$

For such compositions the estimation of T_K is very rough, due to a broad peak in the chemical specific heat curves (Fig. 4.1.25), and a small magnitude of the jump in the long-range order parameter. We can refer this problem to the limitations that we have imposed before (constant values of interaction parameters, for example.). And we suspect that it will be possible

to overcome such difficulties and reproduce more closely the experimental phase diagram by removing these limitations.

It is also possible to compare the reduced total magnetization curves for different c_{Fe} (Fig. 4.1.26) with Fig. 1.7. Although, we have investigated only the Ni_3Fe region, it can be already seen that as the Fe-concentration is increased, the deviation of the curves from a universal one becomes more evident. Thus as was mentioned before, the law of corresponding states is not obeyed.

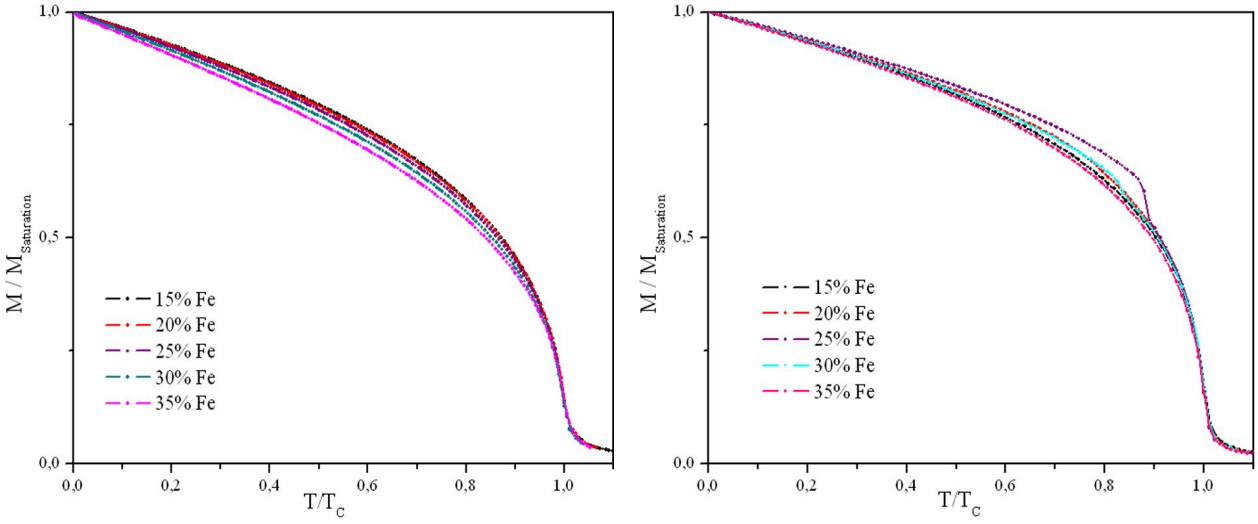

Figure 4.1.26. Temperature dependence of the reduced total magnetization for different c_{Fe} : (a) when $V^{\alpha\beta}=0$ and (b) when $V^{\alpha\beta}\neq 0$

In Fig. 4.1.26b it is seen that with changing the Fe-concentration from stoichiometry the jump in the magnetization is decreased and it is negligible already for c_{Fe} = 0.15 and 0.35. This is connected to the previously mentioned change in the value of the jump of the internal magnetic energy and the chemical long-range order.

4.1.3. Influence of an external magnetic field on T_K (NN interactions)

It is interesting to investigate the influence of an external magnetic field, **B**, on the chemical ordering process, since magnetic ordering influences chemical ordering. For this purpose we have chosen the stoichiometric Ni_3Fe alloy (25% at. Fe).

Due to the form of the Hamiltonian (Eq. 4.1.2), the orientation of the applied field should have no influence on the results. This has been checked by performing several simulations with different orientations.

The parameters of the simulations were taken the same as for previously presented simulations with both magnetic and chemical (only NN) interactions. To improve the estimation

of T_K, the temperature step was chosen equal to $\Delta T = 5K$. The magnitude of the external magnetic induction **B** was chosen in interval [0; 1500] *T*. Such high values are impossible to reach experimentally, but such strong fields were applied in order to make more visible the change in the ordering temperature T_K. The field dependence of the order-disorder transition temperature, T_K, is drawn in Fig. 4.1.27.

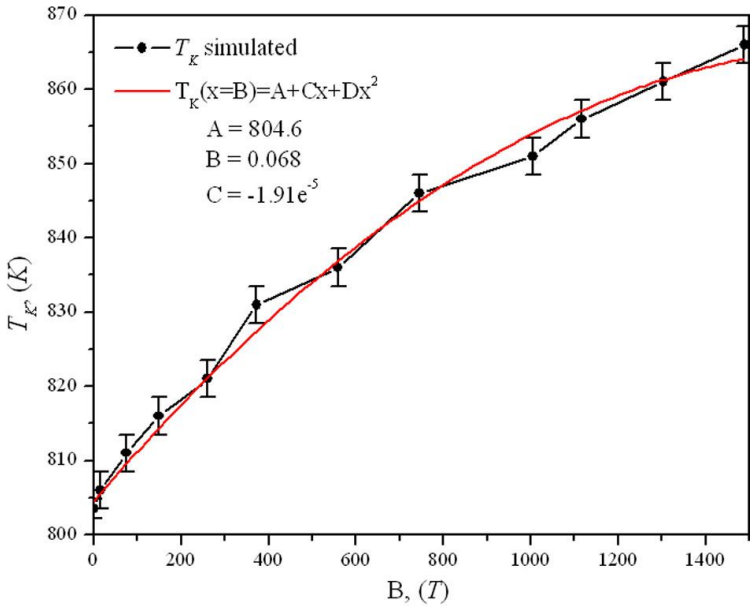

Figure 4.1.27. Order-disorder transition temperature (T_K) versus external magnetic field (black line)

The numerical results can be well fitted by the 2rd order polynom:

$$T_K(\mathrm{B}) = A + C \times \mathrm{B} + D \times \mathrm{B}^2; \qquad (4.1.7)$$

$$\text{with} \quad \begin{cases} A \approx 804.6 \ \ K \\ C \approx 0.068 \ \ K \cdot T^{-1} \\ D \approx -1.91 \cdot 10^{-5} \ \ K \cdot T^{-2} \end{cases} .$$

The external magnetic field increases the order-disorder transition temperature. This can be explained in a following way: as the field induces ferromagnetic alignment of the spins, it has the same effect as ferromagnetic interactions, i.e. it increases the order-disorder transition temperature, as seen previously (when results of only chemical and simultaneous chemical and magnetic simulations have been compared). Consequently, one should admit that an applied field could be used in principle in order to make easier the achieving of the equilibrium ordered state.

4.2. Mean-field and Önsager-kinetic simulation

The kinetics of the precipitation in Ni-Fe alloys was investigated using the Önsager-type microdiffusion equation (Eq. 3.40). The expression for the free energy was obtained by means of molecular field and mean-field approaches.

In this part we will present the results of simulation of the kinetics in Ni-Fe alloys and in particular, in the Ni-rich part of the phase diagram (Fig. 1.1) where the ordered $L1_2$ phase coexists with the disordered fcc γ phase. To evaluate the driving force of fcc→$L1_2$ transformation, it is necessary to fix the interaction parameters. That is why we will start this section with the discussion about the influence of the interaction parameters on the miscibility gap on phase diagram. Then, the results of the kinetic simulations, i.e. the microstructural evolution and different statistical characteristics of the precipitation process will be given. Also, the influence of magnetism on the alloy kinetics is investigated.

4.2.1. Calculation of the interaction parameters

To calculate the free energy of the Ni-Fe alloy it is necessary to define the interaction parameters. We will call "*paramagnetic*", the interaction parameters which does not include the magnetic contribution, i.e. represent only chemical interactions. Both paramagnetic (chemical) and magnetic interaction parameters should be defined.

The interaction parameters were defined within the Screened Generalized Perturbation Method (SGPM) [137]. They were determined within the framework of the Density Functional Theory (DFT) using the Exact Muffin-Tin Orbital Method (EMTO). For the exchange correlation function the local density approximation (LDA) was employed. The magnetic interactions were calculated using the Disordered Local Moments model (DLM) [127].

We have considered concentration independent interaction parameters which were calculated for $c_{Fe} = 0.25$. The values of the interaction parameters for the first 20 coordination shells in direct space (R-space) are given in Table 4.2.1, where **s** indicates the number of the coordination shell, **Z** is the coordination number for a given coordination shell, $w_{\mathrm{prm}}(\mathbf{r})$ is the value of paramagnetic "mixing" interactions and $J_{\mathrm{Fe\text{-}Fe}}(\mathbf{r})$, $J_{\mathrm{Ni\text{-}Fe}}(\mathbf{r})$ and $J_{\mathrm{Ni\text{-}Ni}}(\mathbf{r})$ are the magnetic interactions for Fe-Fe, Ni-Fe and Ni-Ni pairs, respectively. As can be seen from the table, in the data obtained from *ab initio* calculations the magnetic interactions between Fe-Fe pairs are positive for the first two coordination shells. This fact is opposite to the assumption about the antiferromagnetic interaction in the γ-Fe which was used in previously shown MC simulations, where it was considered that $J_{\mathrm{Fe\text{-}Fe}} < 0$ in the 1st coordination shell.

s	Z	p_1	p_2	p_3	$w_{prm}(\mathbf{r})$, [eV]	$J_{Fe\text{-}Fe}(\mathbf{r})$, [eV]	$J_{Ni\text{-}Fe}(\mathbf{r})$, [eV]	$J_{Ni\text{-}Ni}(\mathbf{r})$, [eV]
1	12	1	1	0	0,042982083	0,00766741	0,008289	0,001827
2	6	2	0	0	-0,007344411	0,00793427	0,000581	-0,00028
3	24	2	1	1	0,005460008	0,00091667	0,00114	0,000266
4	12	2	2	0	0,004634135	-0,00235316	-0,00062	-3,3E-05
5	24	3	1	0	0,001021796	0,00032723	0,000172	1,78E-05
6	8	2	2	2	-0,001311599	0,00079733	0,000119	-3,9E-05
7	48	3	1	2	0,00110343	-0,00050419	7,46E-06	5,09E-05
8	6	4	0	0	0,000306131	4,0019E-05	5,66E-05	1,18E-05
9	24	4	1	1	0,000190481	7,1834E-05	2,39E-05	2,05E-06
10	12	3	3	0	-0,00229938	0,00074559	-5,6E-05	-8,1E-05
11	24	4	2	0	0,000439467	-0,00021619	8,56E-06	1,63E-05
12	24	3	3	2	3,80962E-05	5,8792E-05	-6E-06	-1,1E-05
13	24	4	2	2	0,000238102	0,0001801	6,65E-05	5,23E-06
14	24	5	1	0	9,25194E-05	-3,6948E-05	1,1E-05	8,49E-06
15	48	4	3	1	-0,000103404	-0,00019392	-9,8E-05	-8,4E-06
16	48	5	2	1	2,17693E-05	5,3662E-05	6,3E-06	-5,1E-06
17	12	4	4	0	-0,000287082	0,00023024	0,000138	1,74E-05
18	24	4	3	3	-6,93896E-05	6,5096E-05	4,12E-06	-6E-06
19	24	5	3	0	3,67357E-05	-7,1893E-05	-2,2E-05	2,41E-06
20	6	6	0	0	-5,44232E-06	9,4299E-06	4,46E-06	8,24E-07

Table 4.2.1. ***Ab initio*** **chemical,** $w_{prm}(\mathbf{r})$**, and magnetic,** $J_{\alpha\text{-}\beta}(\mathbf{r})$**, interactions in R-space for the first 20 coordination shells**

In Fig. 4.2.1 the data from Table 4.2.1 is represented. As can be seen, the oscillating character of the interaction parameters is observed. It can be noticed that starting from the 6th coordination shell, the amplitude of these oscillations becomes less pronounced for both chemical and magnetic interactions. The decay of the magnetic interactions appears to be slower than that of the chemical one, and especially this is true for the Fe-Fe interaction, $J_{Fe\text{-}Fe}(\mathbf{r})$, which contribution is seen to be important until 13th coordination shell.

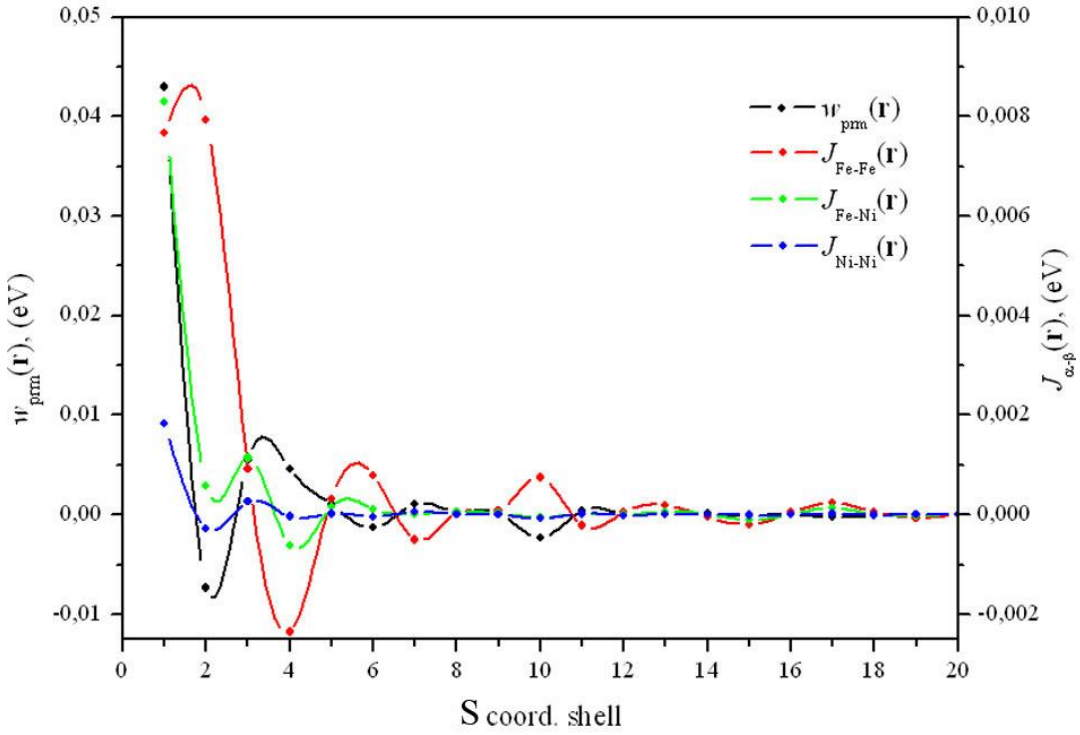

Figure 4.2.1. Chemical $w_{prm}(\mathbf{r})$, and magnetic, $J_{\alpha\text{-}\beta}(\mathbf{r})$, interaction parameters in R-space

To calculate the free energy in mean-field approximation, it is necessary to evaluate the interaction parameters in the reciprocal space (k-space). Using Eq. 3.16 the calculation of the interaction parameters in the reciprocal space can be performed. The result of this calculation is given in Fig. 4.2.2 and Table 4.2.2.

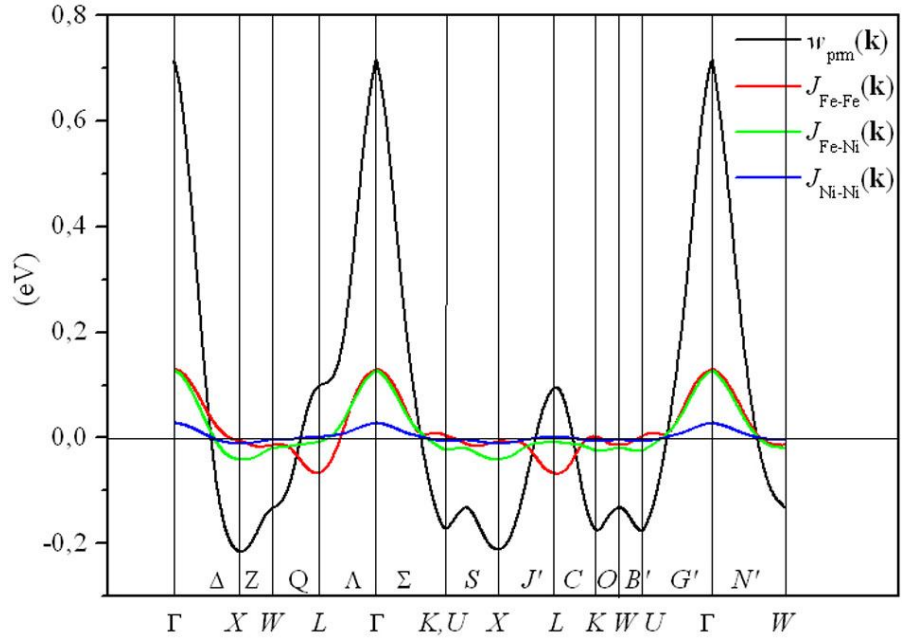

Figure 4.2.2. Fourier components of chemical, $w_{prm}(\mathbf{k})$, and magnetic, $J_{\alpha\text{-}\beta}(\mathbf{k})$, interaction parameters

It is known that stable $L1_2$-type superstructure is generated by wave vectors which correspond to the X-point of the reciprocal space. As seen from Fig. 4.2.2, the *ab initio* data reproduce quite well the $L1_2$ structure and give a minimum of $\tilde{w}_{prm}(\mathbf{k})$ at X-point. In Table 4.2.2 the values for some high-symmetry points are listed. These energetic parameters will be used further in our calculations.

k	$\tilde{w}_{prm}(\mathbf{k})$, **[eV]**	$\tilde{J}_{Fe-Fe}(\mathbf{k})$, **[eV]**	$\tilde{J}_{Fe-Ni}(\mathbf{k})$, **[eV]**	$\tilde{J}_{Ni-Ni}(\mathbf{k})$, **[eV]**
Γ (0 0 0)	0,715396	0,129901	0,127327	0,027874
X (1 0 0)	-0,21757	-0,006047	-0,041347	-0,011407
L (1/2 1/2 1/2)	0,103761	-0,060765	-0,008519	0,001605
W (1 1/2 0)	-0,132006	-0,014043	-0,019353	-0,004021

Table 4.2.2. ***Ab initio*** **chemical** $\tilde{w}_{prm}(\mathbf{k})$**, and magnetic,** $\tilde{J}_{\alpha-\beta}(\mathbf{k})$**, interactions in k-space**

4.2.2. Thermodynamic description of Ni-Fe alloys

In general case, the free energy of a system is $F = U - TS$. In case when studied system exhibits both atomic (chemical) and magnetic ordering, the presented expression should include both chemical and magnetic contributions:

$$F = F_{at} + F_{magn} = (U_{at} + U_{magn}) - T(S_{at} + S_{magn}) \tag{4.2.1}$$

Using mean-field approach and SCW approximation, for a binary A-B substitutianal alloy the U_{at} and S_{at} terms were defined from Eq. 3.15. The magnetic entropy S_{magn} for an arbitrary spin $\boldsymbol{S}$ is calculated by means of molecular mean-field approach and is given by Eq. 3.22. As the entropy is an additive quantity, for a system of 2 magnetic components (A and B) it is possible to write: $S_{magn} = S^{A}_{magn} + S^{B}_{magn}$. The internal magnetic energy U_{magn} is defined by a Heisenberg Hamiltonian (Eq. 2.1) which in case of magnetic alloy can be written in a following form:

$$H_{magn} = \frac{1}{2}\sum_{\alpha,\beta}\sum_{\mathbf{r},\mathbf{r}'} J_{\alpha\beta}(\mathbf{r}-\mathbf{r}')\xi_{\alpha}(\mathbf{r})\xi_{\beta}(\mathbf{r}')S_{\alpha}(\mathbf{r})S_{\beta}(\mathbf{r}'), \tag{4.2.2}$$

where $c_{\alpha}(\mathbf{r})$ $(c_{\beta}(\mathbf{r}'))$ is the occupation variable defined in (Eq. 3.2) and $S_{\alpha}(\mathbf{r})$ $(S_{\beta}(\mathbf{r}'))$ is the variable of spin of a sort α (β). Averaging of this Hamiltonian gives the internal magnetic energy U_{magn} (see Appendix 5.2.2 for the derivation of the formula):

$$U_{magn} = \frac{N}{2}\left\{\begin{array}{l} \tilde{J}_{Fe-Fe}(\mathbf{0})c_{Fe}^2\sigma_{Fe}^2 s_{Fe}^2 + \tilde{J}_{Ni-Ni}(\mathbf{0})(1-c_{Fe})^2\sigma_{Ni}^2 s_{Ni}^2 + 2\tilde{J}_{Fe-Ni}(\mathbf{0})c_{Fe}(1-c_{Fe})\sigma_{Fe}\sigma_{Ni}s_{Fe}s_{Ni} + \\ +\frac{3}{16}\eta^2\left(\tilde{J}_{Fe-Fe}(\mathbf{k}_X)\sigma_{Fe}^2 s_{Fe}^2 + \tilde{J}_{Ni-Ni}(\mathbf{k}_X)\sigma_{Ni}^2 s_{Ni}^2 - 2\tilde{J}_{Fe-Ni}(\mathbf{k}_X)\sigma_{Fe}\sigma_{Ni}s_{Fe}s_{Ni}\right) \end{array}\right\}, \tag{4.2.3}$$

where $\sigma_{Fe(Ni)}$ represents the reduced magnetization of the Fe (Ni) sublattice. Using the SCW method the free energy per atom of the $L1_2$ ordered phase can be obtained (see Appendix 5.2.2):

$$\frac{F}{N}=\frac{1}{2}\left\{\begin{array}{l}\tilde{w}_{prm}(\mathbf{0})c_{Fe}^2+\tilde{J}_{Fe-Fe}(\mathbf{0})c_{Fe}^2\sigma_{Fe}^2s_{Fe}^2+\tilde{J}_{Ni-Ni}(\mathbf{0})(1-c_{Fe})^2\sigma_{Ni}^2s_{Ni}^2+2\tilde{J}_{Fe-Ni}(\mathbf{0})c_{Fe}(1-c_{Fe})\sigma_{Fe}\sigma_{Ni}s_{Fe}s_{Ni}+\\ +\frac{3}{16}\eta^2\left[\tilde{w}_{prm}(\mathbf{k}_X)+\tilde{J}_{Fe-Fe}(\mathbf{k}_X)\sigma_{Fe}^2s_{Fe}^2+\tilde{J}_{Ni-Ni}(\mathbf{k}_X)\sigma_{Ni}^2s_{Ni}^2-2\tilde{J}_{Fe-Ni}(\mathbf{k}_X)\sigma_{Fe}\sigma_{Ni}s_{Fe}s_{Ni}\right]\end{array}\right\}+$$

$$+\frac{k_BT}{4}\left\{\begin{array}{l}3\left(c_{Fe}-\frac{\eta}{4}\right)\ln\left(c_{Fe}-\frac{\eta}{4}\right)+3\left(1-c_{Fe}+\frac{\eta}{4}\right)\ln\left(1-c_{Fe}+\frac{\eta}{4}\right)+\\ \left(c_{Fe}+\frac{3}{4}\eta\right)\ln\left(c_{Fe}+\frac{3}{4}\eta\right)+\left(1-c_{Fe}-\frac{3}{4}\eta\right)\ln\left(1-c_{Fe}-\frac{3}{4}\eta\right)\end{array}\right\}- \qquad (4.2.4)$$

$$-k_BT(1-c_{Fe})\left\{\ln sh\left(\frac{2s_{Ni}+1}{2s_{Ni}}y_{Ni}(\sigma_{Ni,Fe})\right)-\ln sh\left(\frac{1}{2s_{Ni}}y_{Ni}(\sigma_{Ni,Fe})\right)-s_{Ni}y_{Ni}(\sigma_{Ni,Fe})\right\}-$$

$$-k_BTc_{Fe}\left\{\ln sh\left(\frac{2s_{Fe}+1}{2s_{Fe}}y_{Fe}(\sigma_{Fe,Ni})\right)-\ln sh\left(\frac{1}{2s_{Fe}}y_{Fe}(\sigma_{Fe,Ni})\right)-s_{Fe}y_{Fe}(\sigma_{Fe,Ni})\right\}$$

The equilibrium values of the order parameters (η, σ_{Fe}, σ_{Ni}) can be deduced by the free energy minimization: $\frac{\partial F}{\partial \eta}=0$, $\frac{\partial F}{\partial \sigma_{Fe}}=0$ and $\frac{\partial F}{\partial \sigma_{Ni}}=0$.

For the system without magnetic interactions ($J^{\alpha\beta}=0$) this condition gives the following expression for the equilibrium long-range order parameter η_{eq}:

$$\boxed{\frac{\tilde{w}_{prm}(\mathbf{k}_X)}{k_BT}\eta_{eq}=\ln\frac{\left(c_{Fe}-\frac{\eta_{eq}}{4}\right)\left(1-c_{Fe}-\frac{3}{4}\eta_{eq}\right)}{\left(1-c_{Fe}+\frac{\eta_{eq}}{4}\right)\left(c_{Fe}+\frac{3}{4}\eta_{eq}\right)}}, \qquad (4.2.5a)$$

The jump of the order parameter $\Delta\eta$ at the 1st order phase transition and the temperature of the transition can be found from the conditions:

$$\boxed{\left\{\begin{array}{l}F_{disorder}^{(\eta=0)}=F_{order}^{(\eta=\eta_{eq})}\\ \left.\frac{\partial F}{\partial \eta}\right|_{\eta=\eta_{eq}}=0\end{array}\right.} \qquad (4.2.5b)$$

In general, the variation of the long-range order parameter η for 1st order phase transition exhibits a shape given in Fig. 4.2.3. In this figure, the *x*-axis represents the reduced temperature $\tau^*=\frac{k_BT}{w_{prm}}$. As seen from Fig. 4.2.3, the part $a-b$ on the curve represents equilibrium ordered states of the alloy, the part $b-c$ encloses the domain of coexistence of ordered and disordered phases, and $c-d$ corresponds to the maximum of the free energy F (Eq. 3.1 or Eq. 4.2.4) and therefore the states with such values of η can not exist.

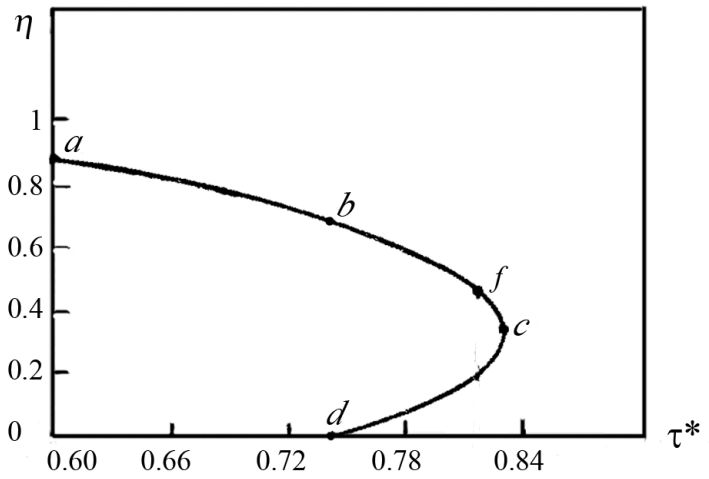

Figure 4.2.3. Thermal variation of the long-range order parameter η for 1st order phase transition

The ordering instability temperatures which are situated at points *b* and *c* will be called $T_K^{ordering}$ and $T_K^{disordering}$, respectively. Such notation is used for the comparison of estimated transition temperatures with MC results. Thus, $T_K^{ordering}$ is obtained when the simulation has started from the fully disordered state at high temperature and $T_K^{disordering}$ - when the alloy was fully ordered at low temperature at the beginning of the simulation. Indeed, the true transition temperature T_K is located between these two temperatures, at point *f*, and is found from Eq. 4.2.5b. Therefore, the interval $b - f - c$ corresponds to a two phases coexistence region. At the interval b - f the free energy of the ordered state exceeds the free energy of the disordered state ($\left|F_{order}^{(\eta=\eta_{eq})}\right| > \left|F_{disorder}^{(\eta=0)}\right|$) and the interval f - c corresponds to the opposite condition $\left|F_{order}^{(\eta=\eta_{eq})}\right| < \left|F_{disorder}^{(\eta=0)}\right|$.

Using the interaction parameters discussed in the previous section 4.2.1, it is possible to calculate the phase transition temperatures (both T_K and T_C). As a reference we have taken the concentration 27% at. Fe and compared obtained transition temperatures with those given by the experimental phase diagram (Table 4.2.3).

	Phase diagram	**Our calculation with *ab initio* data**
T_K, (*K*)	789	570
T_C, (*K*)	881	717

Table 4.2.3. T_K and T_C according to phase diagram and to *ab initio* data for c_{Fe} = 0.27

As seen, the transition temperatures obtained using *ab initio* interaction parameters are different from the phase diagram data. To fit our result to the experimental values of T_K and T_C, we have scaled the interaction parameters:

$\tilde{w}_{prm}^{new}(\mathbf{k}) = \alpha \cdot \tilde{w}_{prm}(\mathbf{k})$	$\alpha \approx 1.42418773...$
$\tilde{J}_{\alpha-\beta}^{new}(\mathbf{k}) = \gamma \cdot \tilde{J}_{\alpha-\beta}(\mathbf{k})$	$\gamma \approx 1.228731...$

The new interaction parameters after rescaling are reported in Table 4.2.4.

k	$\tilde{w}_{prm}(\mathbf{k})$, [eV]	$\tilde{J}_{Fe-Fe}(\mathbf{k})$, [eV]	$\tilde{J}_{Fe-Ni}(\mathbf{k})$, [eV]	$\tilde{J}_{Ni-Ni}(\mathbf{k})$, [eV]
Γ (0 0 0)	1,01886	0,15961339	0,156450632	0,034249648
X (1 0 0)	-0,30986	-0,00743013636	-0,0508043407	-0,0140161345
L (1/2 1/2 1/2)	0,14778	-0,0746638392	-0,0104675594	0,0019721133
W (1 1/2 0)	-0,188	-0,0172550694	-0,023779631	-0,00494072735

Table 4.2.4. Rescaled interaction parameters in k-space

This new data will be used in our further calculations. As the interaction parameters are considered to be independent of concentration and temperature, we can not expect a full agreement with the experimental phase diagram.

Using the new set of interaction parameters, the thermal variation of the long-range order parameter η can be calculated by Eq. 4.2.5. For the stoichiometric case (25% at. Fe) it is given in Fig. 4.2.4. This result can be compared to the literature data [89-90]. Also, we have provided results for $c_{Fe} = 0.25$ for future comparison with MC simulation results.

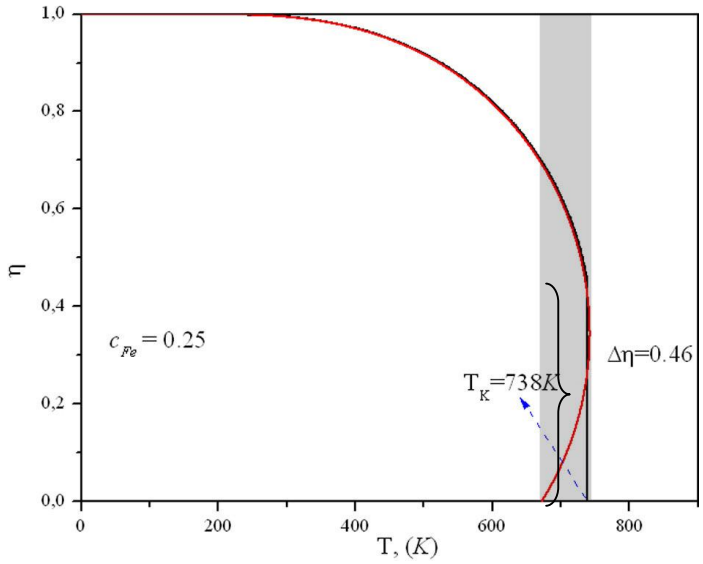

Figure 4.2.4. Thermal variation of the long-range order parameter η for $c_{Fe} = 0.25$ when magnetic interactions are neglected ($\tilde{J}_{\alpha-\beta}(\mathbf{k}) = 0$) (red line – analytical solution of Eq. 4.25, black line – numerical approximation)

As expected for a 1st order phase transitions, there is a domain of coexistence of high temperature disordered fcc phase and ordered $L1_2$ phase (shaded region on Fig. 4.2.4). The estimated order-disorder transition temperature, T_K^{order} (due to the simulation conditions), is equal to 738K and the long-range order parameter jump at order-disorder transition temperature is $\Delta\eta \approx 0.46$.

For chemically disordered system ($\eta = 0$) the variation of σ_{Fe} and σ_{Ni} with temperature can be calculated using Eq. 4.2.4 from the solution of the following system of equations:

$$\begin{cases} \sigma_{Ni} = B_{S_{Ni}}\left(-\frac{1}{k_B T}\left\{\tilde{J}_{Ni-Ni}(\mathbf{0})(1-c_{Fe})s_{Ni}^2\sigma_{Ni} + \tilde{J}_{Fe-Ni}(\mathbf{0})c_{Fe}s_{Ni}s_{Fe}\sigma_{Fe}\right\}\right) \\ \sigma_{Fe} = B_{S_{Fe}}\left(-\frac{1}{k_B T}\left\{\tilde{J}_{Fe-Fe}(\mathbf{0})c_{Fe}s_{Fe}^2\sigma_{Fe} + \tilde{J}_{Fe-Ni}(\mathbf{0})(1-c_{Fe})s_{Ni}s_{Fe}\sigma_{Ni}\right\}\right) \end{cases} \quad (4.2.6)$$

The magnetization curves are plotted in Fig. 4.2.5. From this plot it is seen that the Curie temperature is equal to 836K. If we compare this plot with the result of the Monte-Carlo simulation (Fig. 4.1.2) we will notice the difference in the Ni-sublattice magnetization. This can be explained by the difference in the values of the exchange parameters. As seen from Table 4.2.4, $\tilde{J}_{Ni-Ni}(\mathbf{k})$ has the smallest value (and, in particular, is much smaller that $\tilde{J}_{Fe-Fe}(\mathbf{k})$). The Curie temperature corresponds to $T_C^{disorder}$, i.e. to the Curie temperature defined for a fully disordered alloy.

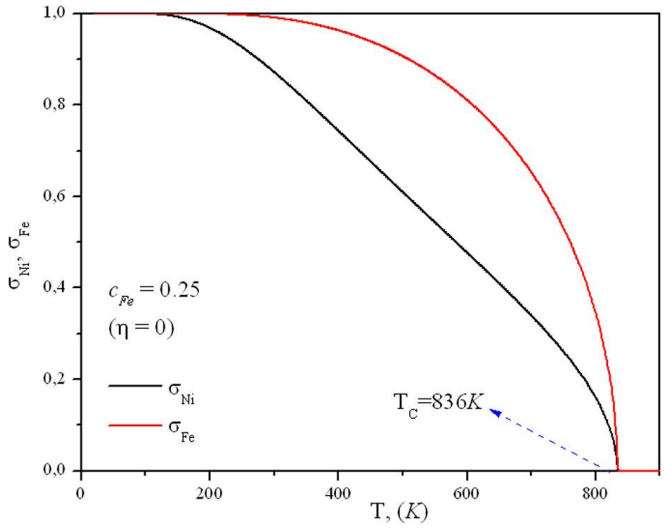

Figure 4.2.5. Temperature dependence of the reduced magnetizations of Fe- and Ni sublattices when η=0

When both magnetic and chemical interactions are considered, the minimization of free energy (Eq. 4.2.4) and search of the equilibrium order parameters (η, σ_{Fe}, σ_{Ni}) becomes more complex and is expressed through the following system of transcendental equations (see Appendix 5.2.3):

$$\begin{cases} \ln\dfrac{\left(c_{Fe}-\dfrac{\eta}{4}\right)\left(1-c_{Fe}-\dfrac{3}{4}\eta\right)}{\left(1-c_{Fe}+\dfrac{\eta}{4}\right)\left(c_{Fe}+\dfrac{3}{4}\eta\right)} = \dfrac{\eta}{k_BT}\left[\begin{array}{l}\tilde{W}(\mathbf{k}_X)+\\ +\tilde{J}_{Fe-Fe}(\mathbf{k}_X)s_{Fe}^2\sigma_{Fe}^2+\tilde{J}_{Ni-Ni}(\mathbf{k}_X)s_{Ni}^2\sigma_{Ni}^2-2\tilde{J}_{Ni-Fe}(\mathbf{k}_X)s_{Ni}s_{Fe}\sigma_{Ni}\sigma_{Fe}\end{array}\right] \\ \sigma_{Ni}=B_{S_{Ni}}\left(-\dfrac{1}{(1-c_{Fe})k_BT}\left\{\begin{array}{l}\tilde{J}_{Ni-Ni}(\mathbf{0})(1-c_{Fe})^2s_{Ni}^2\sigma_{Ni}+\tilde{J}_{Ni-Fe}(\mathbf{0})c_{Fe}(1-c_{Fe})s_{Ni}s_{Fe}\sigma_{Fe}+\\ +\dfrac{3}{16}\eta^2\left[\tilde{J}_{Ni-Ni}(\mathbf{k}_X)s_{Ni}^2\sigma_{Ni}-\tilde{J}_{Ni-Fe}(\mathbf{k}_X)s_{Ni}s_{Fe}\sigma_{Fe}\right]\end{array}\right\}\right) \\ \sigma_{Fe}=B_{S_{Fe}}\left(-\dfrac{1}{c_{Fe}k_BT}\left\{\begin{array}{l}\tilde{J}_{Fe-Fe}(\mathbf{0})c_{Fe}^2s_{Fe}^2\sigma_{Fe}+\tilde{J}_{Ni-Fe}(\mathbf{0})c_{Fe}(1-c_{Fe})s_{Ni}s_{Fe}\sigma_{Ni}+\\ +\dfrac{3}{16}\eta^2\left[\tilde{J}_{Fe-Fe}(\mathbf{k}_X)s_{Fe}^2\sigma_{Fe}-\tilde{J}_{Ni-Fe}(\mathbf{k}_X)s_{Ni}s_{Fe}\sigma_{Ni}\right]\end{array}\right\}\right) \end{cases} \quad (4.2.7)$$

To solve Eqs. 4.2.6-4.2.7 the modified globally converging Newton method [128] was applied. In Fig. 4.2.6 the equilibrium parameters obtained from the solution of Eq. 4.2.7 are presented. From Fig. 4.2.6 it is seen that chemical ordering influences the shape of the magnetization curves and at the order-disorder transition temperature they exhibit a jump. Similar behavior was also obtained in the previous MC simulations (Fig. 4.1.16). Magnetic transition takes place at the same temperature as in the case of solution of Eq. 4.2.6. This can be explained by the absence of the chemical order above T_K ($\eta = 0$ and short-range order is not considered in the mean-field approximation). In its turn, the magnetic ordering enhances the order-disorder transition temperature from 738K to 759K.

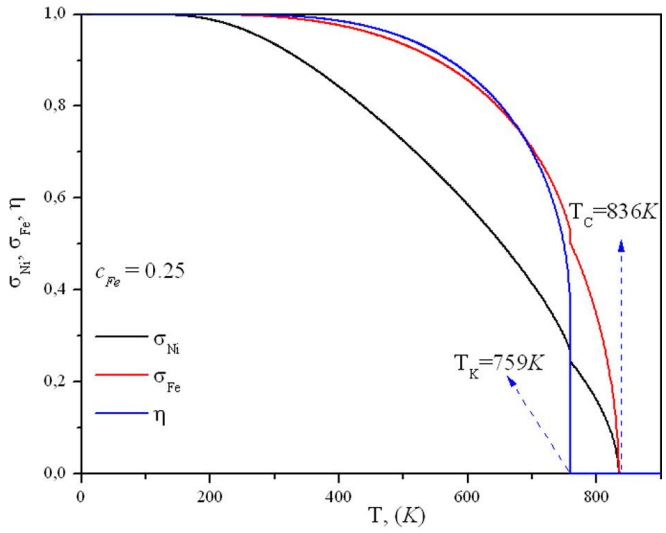

Figure 4.2.6. Temperature dependence of the long-range order parameter η, and reduced magnetizations of Fe- and Ni sublattices

Solving the system Eq. 4.2.7 for different concentrations it is possible to plot the concentration dependence of the free energy at given temperature. Using these curves for a number of temperatures it is possible to define the miscibility gap on the phase diagram and the concentrations of the disordered and ordered phases, $c_{Fe}^{disordered}$ and $c_{Fe}^{ordered}$. The results obtained using this procedure are presented in Fig. 4.2.7.

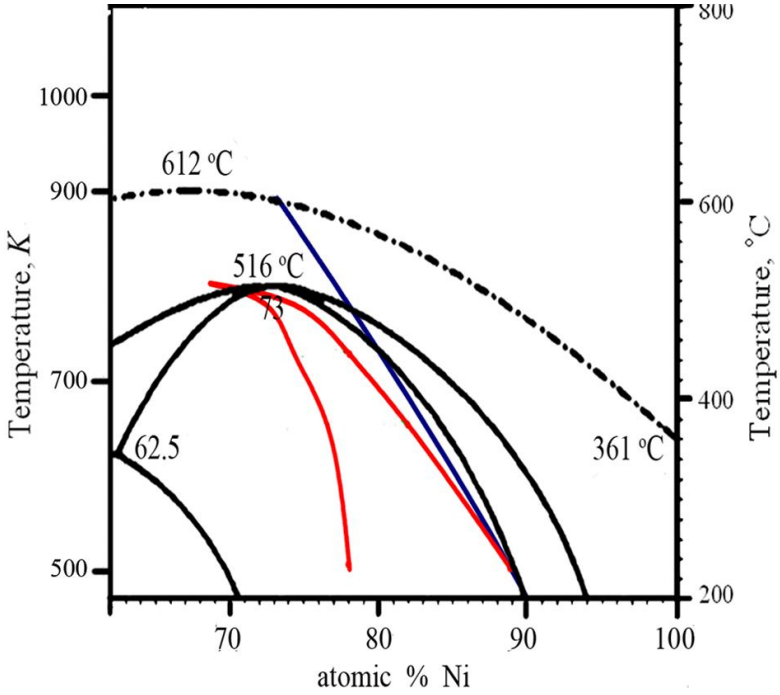

Figure 4.2.7. Ni-rich part of the experimental phase diagram (solid black line) in comparison with theoretically determined using *ab initio* data (solid blue line - T_C and solid red line – T_K)

As was mentioned above, the values of the interaction parameters were considered constant. Thus, the agreement with the experimental phase diagram is not enough satisfactory, as was expected. However, let us remark that our goal was to understand the influence of the magnetic interactions on the ordering kinetics at a given temperature. The difference between the calculated and the experimental phase diagrams induces only the difference in the volume fractions of coexisting phases.

Comparison with MC results

In this section the results obtained from the mean-field theory and those from MC simulations will be compared. In Fig. 4.2.8 the comparative plots for 3 types of simulations: including chemical, magnetic and both interactions are given. The transition temperatures obtained from each type of simulations, either by mean-field or MC method, are given in Table 4.2.5 in comparison with the experimental data.

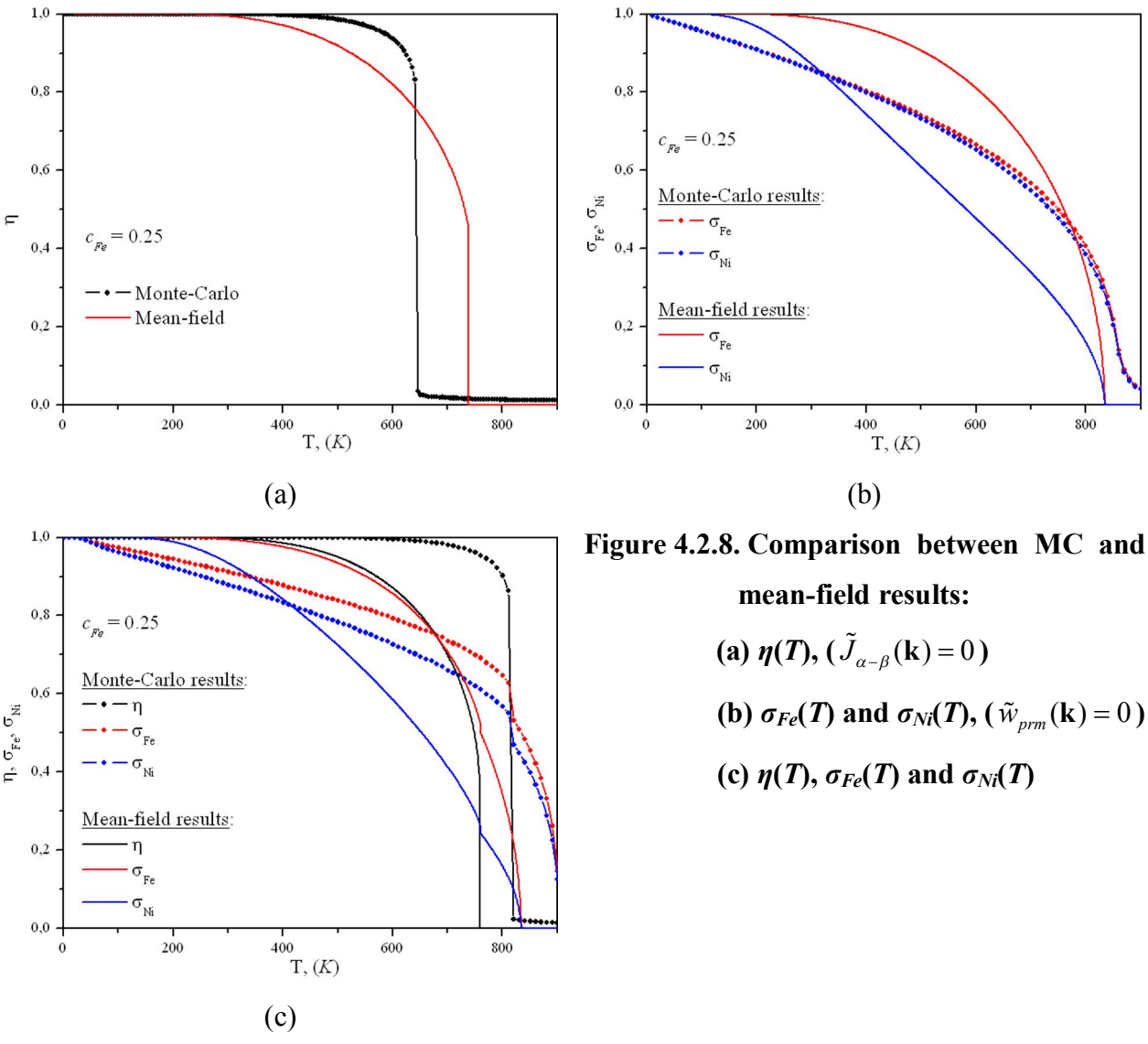

Figure 4.2.8. Comparison between MC and mean-field results:

(a) $\eta(T)$, ($\tilde{J}_{\alpha-\beta}(\mathbf{k}) = 0$)

(b) $\sigma_{Fe}(T)$ and $\sigma_{Ni}(T)$, ($\tilde{w}_{prm}(\mathbf{k}) = 0$)

(c) $\eta(T)$, $\sigma_{Fe}(T)$ and $\sigma_{Ni}(T)$

	$T_K^{disordering}$, (K)		$T_C^{disorder}$, (K)	
	chemical	*chemical+magnetic*	*magnetic*	*chemical+magnetic*
Monte-Carlo	646±2.5	821±5	861±5	911±5
Mean-field	738	759	836	
Experiment [12]	771		871	

Table 4.2.5. Comparison between MC, mean-field and experimental results for c_{Fe}=0.25

As can be seen from Fig. 4.2.8, the thermal variation of the different thermodynamic quantities is similar for both MC and mean-field simulations. However, the difference in the obtained transition temperatures was expected due to the interaction parameters. The order-disorder transition temperature obtained with mean-field simulation is closer to the experimental value. When magnetic interactions are not considered, in both simulations the Kurnakov temperature is lower than for simulations with magnetic interactions. The difference is more pronounced for MC simulations ($\approx 170K$) than for mean-field simulations ($\approx 20K$) due to the fact that in MC simulations the short-range order and fluctuations have been taken into account. Qualitatively the magnetization plots for both simulations are similar, they both exhibit a jump at the order-disorder transition and sub-lattice magnetizations seem to behave alike – the decay of Ni-sublattice magnetization is faster than for Fe-subllatice. As in Monte Carlo simulations the chemical short-range order is considered, the estimated Curie temperature is influenced by the chemical ordering. In mean-field calculation the short-range order interactions are neglected and, as a result, the unique value of T_C was obtained after solution of Eqs. 4.2.6-4.2.7 due to the absence of the chemical long-range order parameter.

4.2.3. Simulations of the kinetics in Ni-Fe alloy

It is well known that after quenching from high temperature the alloys are in metastable disordered state. In this section we will investigate the kinetic path in Ni-Fe alloy from the metastable disordered phase to a two-phase state where the $L1_2$ ordered phase coexists with the disordered fcc phase.

In Fig. 4.2.9 the Ni-rich part of phase diagram is given together with the marked alloy compositions (blue points) chosen for the simulation of the precipitation kinetics and phase coexistence intervals (red points) at the given temperatures.

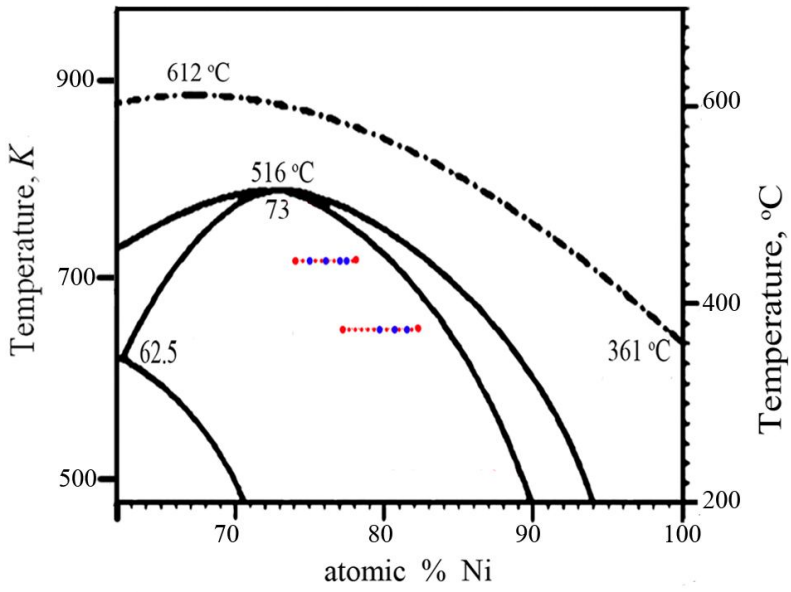

Figure 4.2.9. Ni-rich part of the experimental phase diagram (blue points – mean concentration of simulated alloys, red points – equilibrium concentrations of ordered and disordered phases for $T = 650K$ and $T = 716K$)

In order to proceed, we have chosen two isothermal sections on the phase diagram: at 650*K* and at 716*K*. The first one was chosen because the phase coexistence interval is quite wide, and the second – because we wanted to see the behavior of system close to the stoichiometric concentration for further comparisons with MC results. All simulations were performed on the lattice with 1024×1024 sites which is approximately equal to 190×190 nm^2. The initial configuration corresponds to the supersaturated matrix with 200 randomly distributed nuclei of ordered $L1_2$ phase. The concentration and the order parameter of the nuclei are equal to the respective equilibrium values at the chosen temperature. The Önsager equation was solved by the explicit Euler technique.

4.2.3.1. Relation between simulation and real time

As we are interested in the diffusion of the solutes in the matrix, the Önsager coefficient L_1 has to be related with the diffusion coefficient *D*. In our simulation for convenience the Önsager coefficient was fixed to a constant value $L_1^* = 1\ \text{meV}^{-1} \cdot \text{s}^{-1}$ and, therefore, the results of simulations are given in arbitrary time units t^*. However, it is possible to estimate a real time by using the diffusion coefficient of Fe in Ni. It was mentioned earlier in Chapter 3 that the Önsager coefficient is connected to the diffusion coefficient, *D* (Eq. 3.43):

$$L_1 = \frac{D}{a_{fcc}^2 \left(\tilde{w}(\mathbf{k_0}) + \dfrac{k_B T}{c(1-c)} \right)}$$

where $\tilde{w}(\mathbf{k}_0)$ is the Fourier transform of the interaction energy (paramagnetic or total) at $\mathbf{k} = \mathbf{0}$, a_{fcc} is the lattice parameter of a fcc solid solution ($a_{fcc}^{Ni_3Fe} = 3.5338$ Å) and c is the matrix concentration. The first term in the denominator is due to the interaction between solutes and second is the entropic term which corresponds to the Brownian motion of Fe atoms without interactions between them.

The diffusion coefficient can be calculated using the Arrhenius equation:

$$D = D_0 \exp(-\frac{E_A}{R \cdot T})$$

where D_0 is the frequency factor, E_A is the activation energy and R is the gas constant ($R = N_A k_B$). According to Ref. [129], $D_0 = 4.14 \times 10^{-4}$ m$^2 \cdot$s^{-1} and $E_A = 287.7 \times 10^3$ J$\cdot$mol^{-1}. Using this data the diffusion coefficient D for two chosen temperatures is presented in Table 4.2.6.

T, (*K*)	**D, (m^2·s^{-1})**
650	3.06817×10^{-27}
716	4.15896×10^{-25}

Table 4.2.6. Diffusion coefficients of Fe in Ni for the given temperatures

The Önsager coefficient (L_1) and real physical time ($t^{real} = \frac{L_1^*}{L_1} t^*$) for a given mean concentration are presented in Table 4.2.7 together with the calculated unit of the real time step ($t^* = t^{real}$).

***T*, (*K*)**	***magnetism***	c_{Fe}	***w*(0), (meV)**	L_1, (meV^{-1}·s^{-1})	t^{real}, (hours)
650	-	0.192	1018.86	1.78052×10^{-11}	1.56×10^7
	+		954.779094	1.8672×10^{-11}	1.49×10^7
	-	0.205	1018.86	1.80321×10^{-11}	1.54×10^7
	+		924.836451	1.93687×10^{-11}	1.43×10^7
716	-	0.23	1018.86	2.43589×10^{-9}	1.14×10^5
	+		942.564196	2.57985×10^{-9}	1.08×10^5
	-	0.24	1018.86	2.45406×10^{-9}	1.13×10^5
	+		926.939653	2.63235×10^{-9}	1.06×10^5

Table 4.2.7. Estimation of the real time associated with the kinetic simulations

It should be mentioned that the time of nucleation was disregarded due to the fact that the nuclei of the ordered phase were embedded in the initial matrix configuration. Therefore, the calculated physical time is underestimated and characterizes only regimes of growth and coarsening.

As we have investigated the kinetics at low temperatures, it was expected that the real time of physical ageing will be so long. From Table 4.2.7 we can conclude that the presence of magnetism accelerates the kinetic process. Also, the increase of the matrix concentration results in faster kinetics.

4.2.3.2. Simulations at 650*K*

Free energy of Ni_3Fe system was calculated using Eq. 4.2.4 with *ab initio* interaction parameters (Table. 4.2.4). The shape of the free energy at temperature 650*K* is presented in Fig. 4.2.10a. It is also seen that the magnetic interactions extend the domain of coexistence of the ordered and disordered phases. At 650*K* the concentrations of the disordered and ordered phases in ferromagnetic state are 0.18 and 0.23, respectively and in the paramagnetic state: 0.2 and 0.225. The concentration variation of the equilibrium order parameters in ferromagnetic and paramagnetic phases are plotted in Fig. 4.2.10b. From this plot it can be noticed that the magnetic interactions increase the critical concentration where the ordering structure appears.

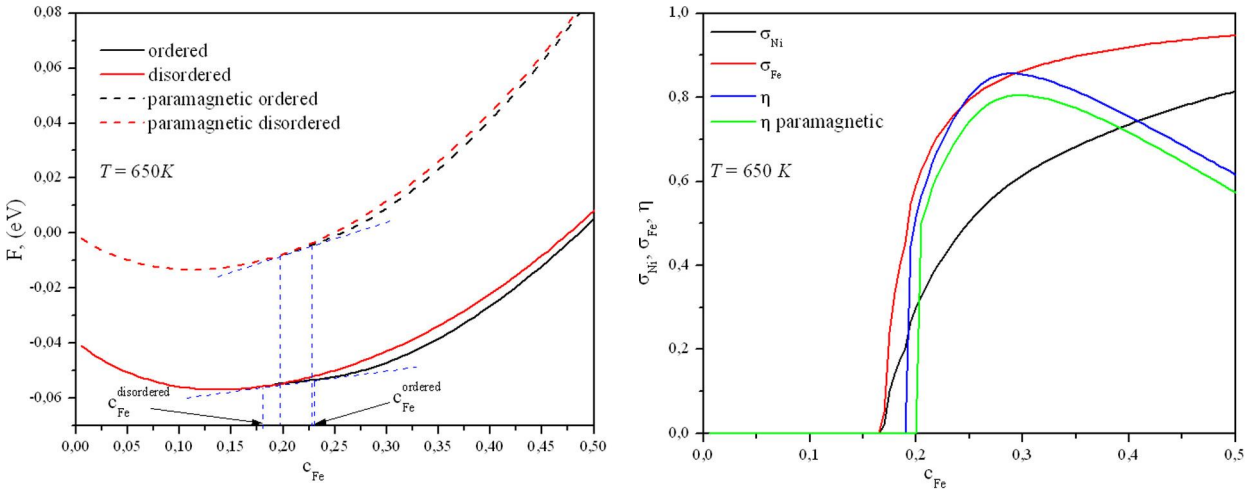

(a) (b)

Figure 4.2.10. Isothermal section at $T = 650K$ of:

(a) Free energy

(b) Equilibrium long-range order parameters

As seen, magnetic order appears at the concentration of 16% at. Fe. This value does not correspond to the value given by the phase diagram (Fig. 4.2.9). Indeed, according to it, the

magnetic order at this temperature appears already at 1% at. Fe and, also, pure Ni is ferromagnetic. These discrepancies should be due to the interaction parameters, used in this simulation. In fact, such behavior of the magnetization is expected, because as seen from Table 4.2.1, all three magnetic exchange interactions are ferromagnetic (in particular, $J_{Fe\text{-}Fe}$) and therefore increase of the Fe-concentration will result in the magnetization increase.

A. Simulation of the precipitation kinetics in Ni-Fe without magnetic interactions

For these simulations we have used only chemical interaction parameters from Table. 4.2.4. The algorithm of kinetic simulation will be described in details in Appendix 5.3. As the input data for simulation we will use the interaction parameters, extracted for 4 coordination shells in real space. This was done by the solution of the system (Eq. 4.2.8) which is obtained from Eq. 3.16 for points (Γ, X, L, W) of the reciprocal space.

$$\begin{cases} V(\Gamma) = 12w_1 + 6w_2 + 24w_3 + 12w_4 \\ V(X) = -4w_1 + 6w_2 - 8w_3 + 12w_4 \\ V(L) = -6w_2 + 12w_4 \\ V(W) = -4w_1 + 2w_2 + 8w_3 - 4w_4 \end{cases} \tag{4.2.8}$$

Thus, we will obtain the following values for the chemical interaction parameters:

	$w_{prm}(\mathbf{r})$, (meV)
1	58.865328
2	-10.45467
3	12.089796
4	7.0872625

Table 4.2.8. Chemical interaction parameters, $w_{prm}(\mathbf{r})$.

For this simulation we have chosen the concentration $c_{Fe} = 0.192$ which is inside domain of the coexistence of disordered and ordered phases. The microstructure evolution for this alloy is presented in Fig. 4.2.11. The time step for this and next simulations will be taken equal to $\Delta t = 1 \cdot 10^{-5}$.

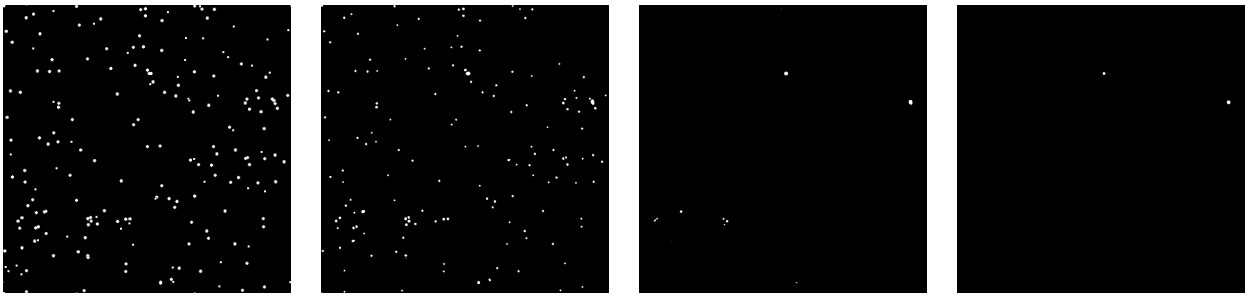

(a) (b) (c) (d)

Figure 4.2.11. Microstructure evolution for c_{Fe} = 0.192 at T = 650K when $J_{\alpha-\beta} = 0$ at time:

(a) $t^* = 0$ (a.u.)**; (b)** $t^* = 0.012$ (a.u.)**; (c)** $t^* = 0.03$ (a.u.)**; (d)** $t^* = 0.06$ (a.u.)

It is seen that initially embedded nuclei of the ordered phase (white color) are not stable and dissolve progressively in the disordered matrix (black color). At the time $t^* = 0.1$ (a.u.) no more precipitates are observed in the system. The time evolution of the volume fraction of the ordered phase is shown in Fig. 4.2.12. As can be seen, the precipitates volume fraction goes to 0 very fast. This fact shows that the ordered $L1_2$ phase is unstable at this temperature and concentration.

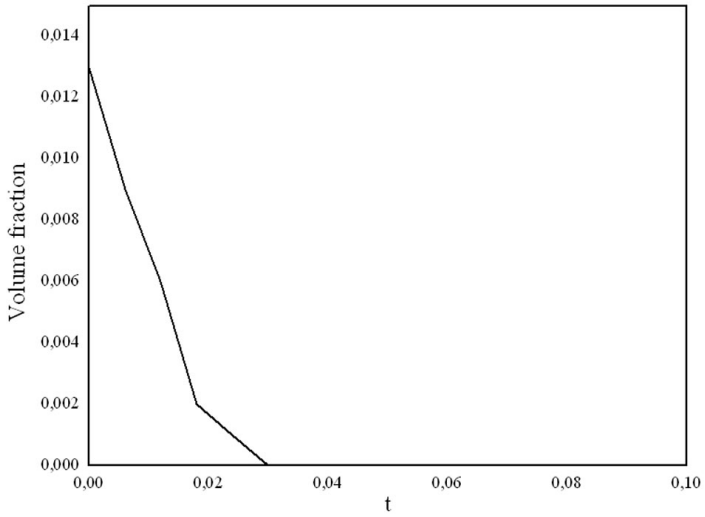

Figure 4.2.12. The time evolution of the volume fraction of the ordered phase (for c_{Fe} = 0.192 at T = 650K when $J_{\alpha-\beta} = 0$)

Other characteristic of the precipitation kinetics is the distribution of the size of precipitates. In Fig. 4.2.13 the size distribution obtained in our simulation at $t^* = 0.006$ (a.u.) is presented in comparison with the theoretical LSW distribution.

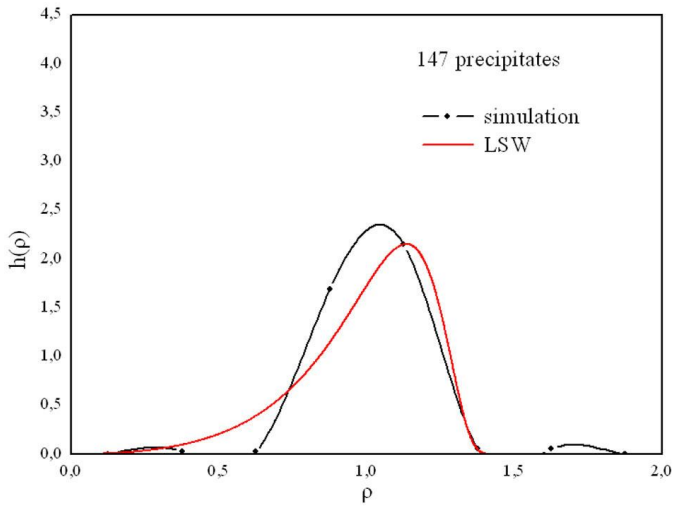

Fig. 4.2.13. The size distribution function at $t^* = 0.006$ (a.u.)

(c_{Fe} **= 0.192 at** T **= 650**K **when** $J_{\alpha-\beta} = 0$ **)**

The maximum of the distribution function obtained in our simulation is shifted from the theoretical one towards the smaller size of precipitates. The width of both distribution functions is comparable at the beginning of the simulation but the simulation curve is more symmetrical than the theoretical LSW curve. In general, the agreement with LSW is satisfactory due to the low volume fraction.

It should be also mentioned that as we introduce the ordered nuclei at the beginning of our simulation artificially, it can influence the shape of the distribution function.

B. Simulation of the precipitation kinetics in Ni-Fe with magnetic interactions

To include magnetic interactions we assumed that sublattice magnetizations (σ_{Ni}, σ_{Fe}) do not change during kinetic process and postulate their values at $c_{Fe} = 0.192$ as a constant. Thus, the formulation of the Önsager-type kinetic equation did not change from Eq. 3.39 and we included the magnetic contribution through the energetic term. The interaction term will change according to the following expression:

$$\tilde{w}_{total}(\mathbf{k}) = \tilde{w}_{prm}(\mathbf{k}) + \tilde{J}_{Fe-Fe}(\mathbf{k})\sigma_{Fe}^2 s_{Fe}^2 + \tilde{J}_{Ni-Ni}(\mathbf{k})\sigma_{Ni}^2 s_{Ni}^2 - 2\tilde{J}_{Fe-Ni}(\mathbf{k})\sigma_{Fe}\sigma_{Ni}s_{Fe}s_{Ni}, \quad (4.2.9)$$

where s_{Fe} and s_{Ni} are the spins of Fe and Ni, respectively. Using the equilibrium values of magnetization and data from Table 4.2.4, after solution of Eq. 4.2.8, the following interaction parameters, $w_{total}(\mathbf{r})$, were obtained (Table 4.2.9):

	w_{total} (**r**), (meV)
1	54.58669
2	-15,4978
3	12.37248
4	7.982156

Table 4.2.9. Total interaction parameters, w_{total}(r), for c_{Fe} = 0.192

For calculation we have used $\sigma_{Fe} = 0.50537957$ and $\sigma_{Ni} = 0.23716079$.

The simulation was done with the same conditions but at longer ageing times (till $t^* = 16$ (a.u.)). The statistical results were obtained by the averaging over two simulations with different initial precipitates sizes (r = 5 and r = 7).

In this simulation the ordered phase became stable and precipitates followed the stages of growth and coarsening. In Fig. 4.2.14 the microstructure evolution is shown.

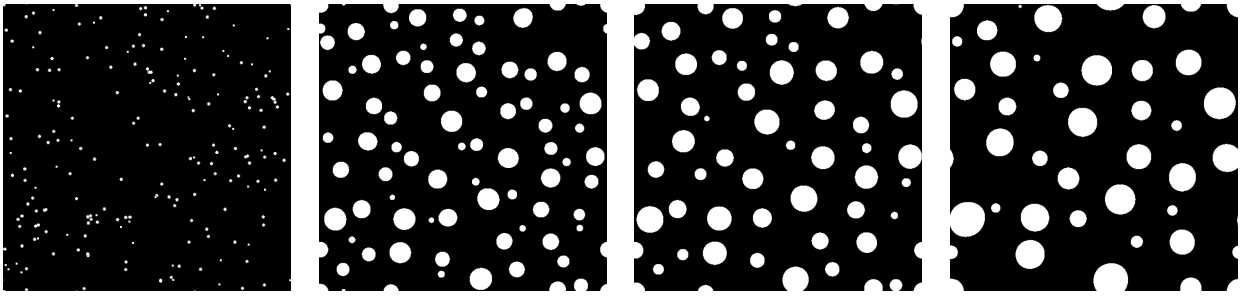

(a) (b) (c) (d)

Figure 4.2.14. Microstructure evolution for c_{Fe} = 0.192 at T = 650K at time:
(a) $t^* = 0$ (a.u.)**; (b)** $t^* = 4$ (a.u.)**; (c)** $t^* = 8$ (a.u.)**; (d)** $t^* = 16$ (a.u.)

From the presented picture it is seen that precipitates grow in the spherical form. At the time $t^* = 16$ (a.u.) the average radius is approximately 7 nm and is twice larger than the average radius at $t^* = 1$ (a.u.). As the lattice misfit between $L1_2$ and disordered phases is very small [12], the effect of elastic interactions is negligible and therefore can be excluded from further discussions. The growth stage at $t^* \approx 2$ (a.u.) is followed by the stage of coarsening and the volume fraction evolves towards the equilibrium value equal to 0.2 as can be seen from Fig. 4.2.15. From Fig. 4.2.15a we can also estimate the coarsening rate k (in arbitrary units): $k = 4380.5$. Unfortunately, we are not able to make a comparison with any experimental data. We can also conclude that the cubic law predicted by LSW theory is valid in this case.

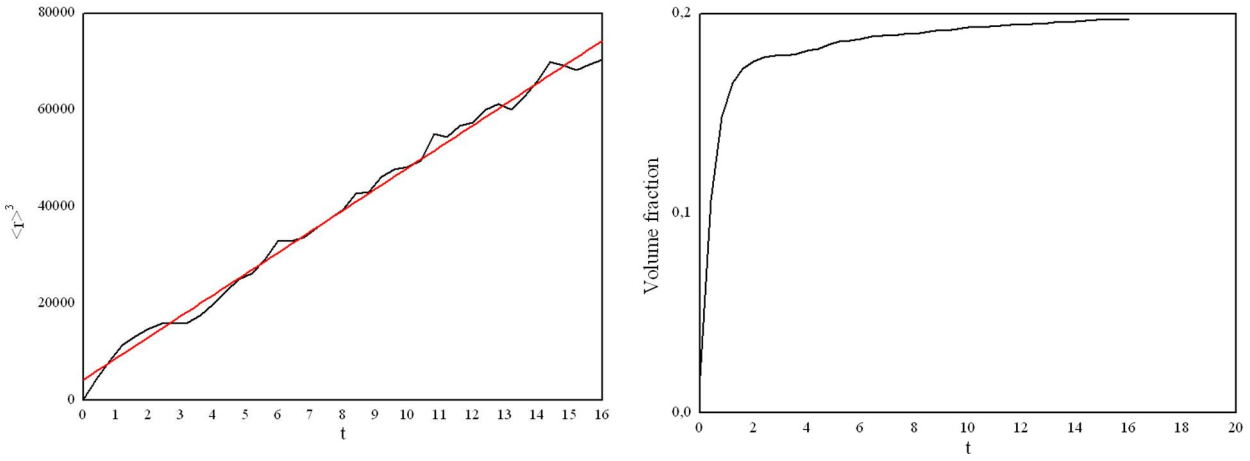

(a) (b)

Figure 4.2.15. The statistical characteristics for simulation for $c_{Fe} = 0.192$ at $T = 650K$:
(a) The cube of the average radius (black line) and its linear fit (red line)
(b) The volume fraction of the ordered phase

As can be noticed from Fig. 4.2.15b, the equilibrium constant volume fraction still has not been reached at the final time of the simulation. As can be seen from Fig. 4.2.16, the local concentration of the ordered precipitates c_{Fe} reached at the end of simulation approaches the value of 0.21 and, therefore, still has not reached the equilibrium concentration of the ordered phase which is equal to 0.23. We can attribute this to the fact, that in this simulation the magnetizations, which will obviously influence the results, have been considered constant while in mean-field calculation, from which the equilibrium concentration of the ordered phase was evaluated, the change of the magnetization with concentration and temperature was included.

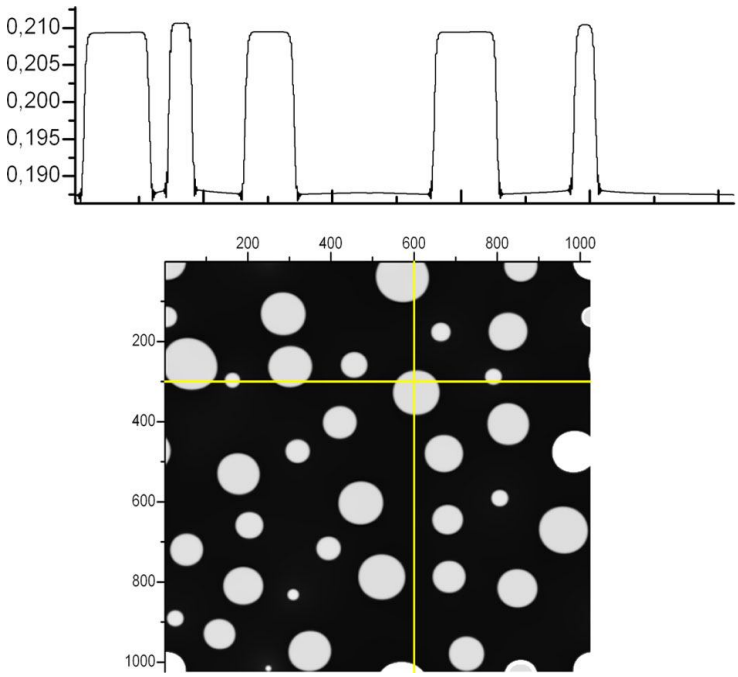

Figure 4.2.16. Microstructure and corresponding concentration profile
(at $t^* = 16$ (a.u.) for $c_{Fe} = 0.192$ and $T = 650K$)

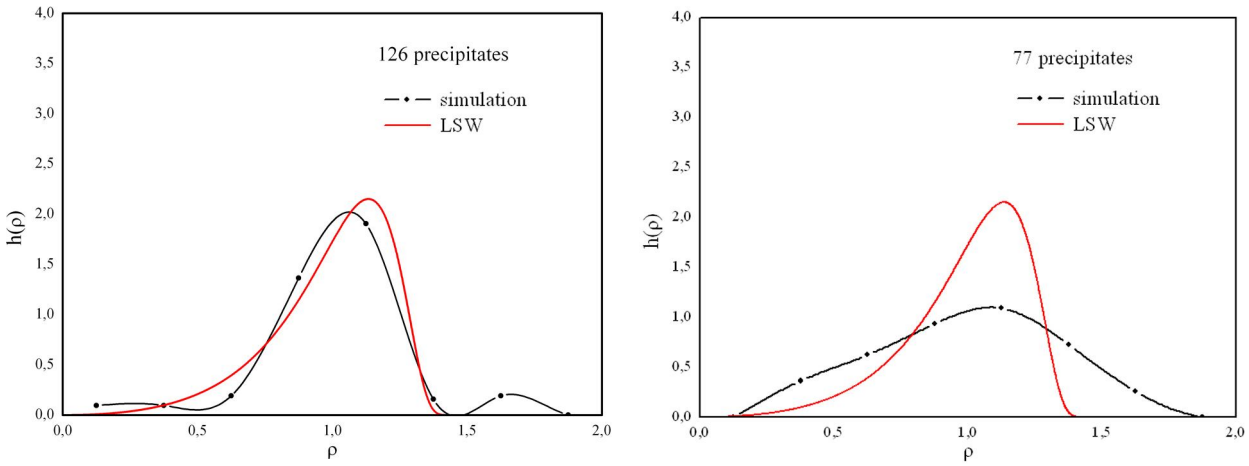

(a) (b)

Figure 4.2.17. The size distribution function for $c_{Fe} = 0.192$ and $T = 650K$:

(a) $t^* = 0.4$ (a.u.)**; (b)** $t^* = 4$ (a.u.)

As seen from Fig. 4.2.17, the size distribution of precipitates varies with time. At $t^* = 0.4$ (a.u.) (the volume fraction ≈ 0.1) it almost coincides with the theoretical one. At that time the distribution is symmetrical. Then the width of the distribution becomes larger as the volume fraction increases and the curve is not symmetrical anymore. The center of the distribution also does not correspond to the theoretical LSW curve. These discrepancies can be explained by the limitations used in LSW theory and the low volume fraction, in particular.

Comparing these results to the section *A* it is visible that magnetism influences the stability of the ordered $L1_2$ phase, in case of absence of magnetic interactions, the ordered phase completely disappear. Thus, the important role of magnetic interactions is justified.

C. Simulations of the precipitation kinetics in Ni-Fe alloys for different concentrations

We have also done the simulation with different concentration of the matrix – going from $c_{Fe} = 0.192$ closer to the disordered phase ($c_{Fe} = 0.185$) and to the ordered phase ($c_{Fe} = 0.205$), where the chemical long-range order parameter appears for both paramagnetic and magnetic states.

For the first case, the disappearance of the ordered nuclei was faster than for $c_{Fe} = 0.192$. In spite of small magnetization values for this concentration, the magnetic interactions increased the driving force of the phase transformation. The ordered phase dissolves in the matrix at very early times and already at $t^* = 0.04$ (a.u.) it completely disappears.

For the second case of $c_{Fe} = 0.205$, two types of simulations were performed. At this concentration in the paramagnetic state the chemical long range order already exists and it is interesting to see how in this case the magnetic interactions will influence the morphology of microstructure.

	w_{total} (**r**), (meV)
1	52.57129
2	-18.1899
3	12.57007
4	8.453229

Table 4.2.10. Total interaction parameters, w_{total}(r), for c_{Fe} = 0.205

For calculation of the total interaction parameters we have used $\sigma_{Fe} = 0.62716354$ and $\sigma_{Ni} = 0.327129$.

For both chemical (Table 4.2.8) and magnetic interactions (Table 4.2.10) obtained results correspond to the expected growth and coarsening of precipitates (Fig. 4.2.18). The simulation was held until $t^* \approx 7$ (a.u.).

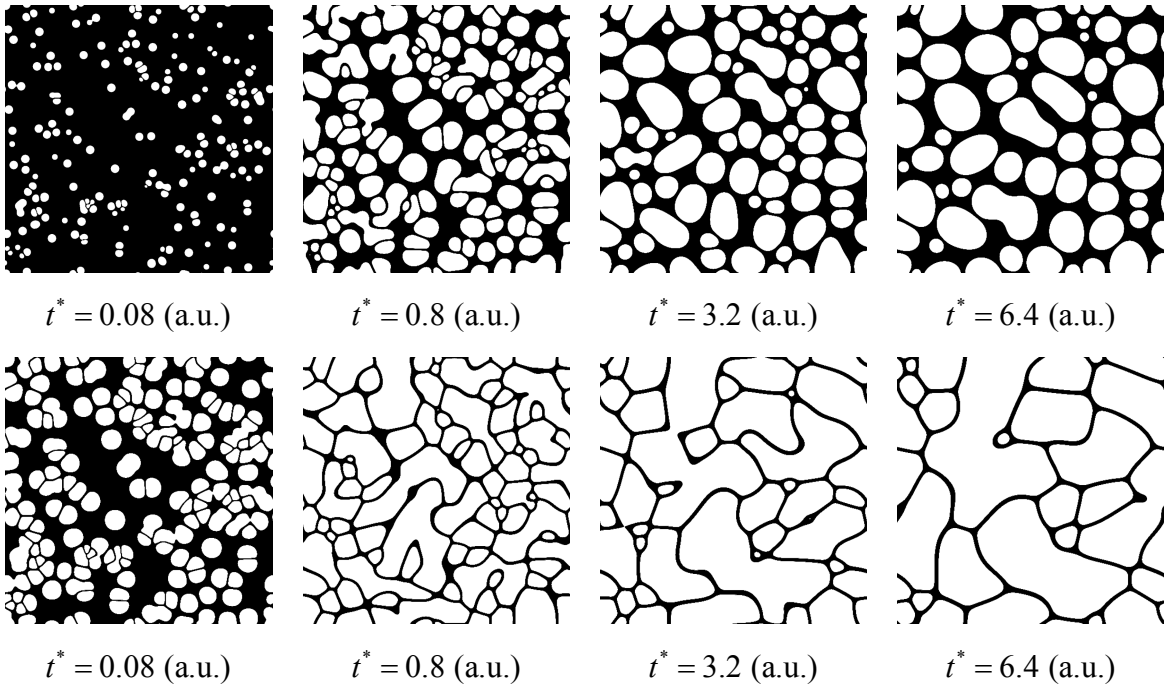

Figure 4.2.18. Microstructure evolution at different time t^* for c_{Fe} = 0.205 and T = 650K:

(a) Without magnetic interactions ($J_{\alpha-\beta} = 0$)

(b) With magnetic interactions

When magnetic interactions are ignored, the initial nuclei grow and coarsen forming the spherical precipitates (Fig. 4.2.18a) with the average precipitates radius at the final time ≈ 10 nm. At the same time when magnetic interactions are included, the precipitates grow till the size of the ordered domains separated by the antiphase boundaries (Fig. 4.2.18b). This can be explained by the decreasing of the coarsening rate without magnetic interactions. It was also previously shown that the real physical time corresponding to the simulation in this case is also delayed. The volume fraction of the ordered precipitates as well as the driving force of phase transformation is also larger when magnetic interactions are considered.

It is also possible to compare these results with the previous section *B* ($c_{Fe} = 0.192$). In Fig. 4.2.19 the comparison of the time evolution of the cube of the mean radius and the volume fraction is given.

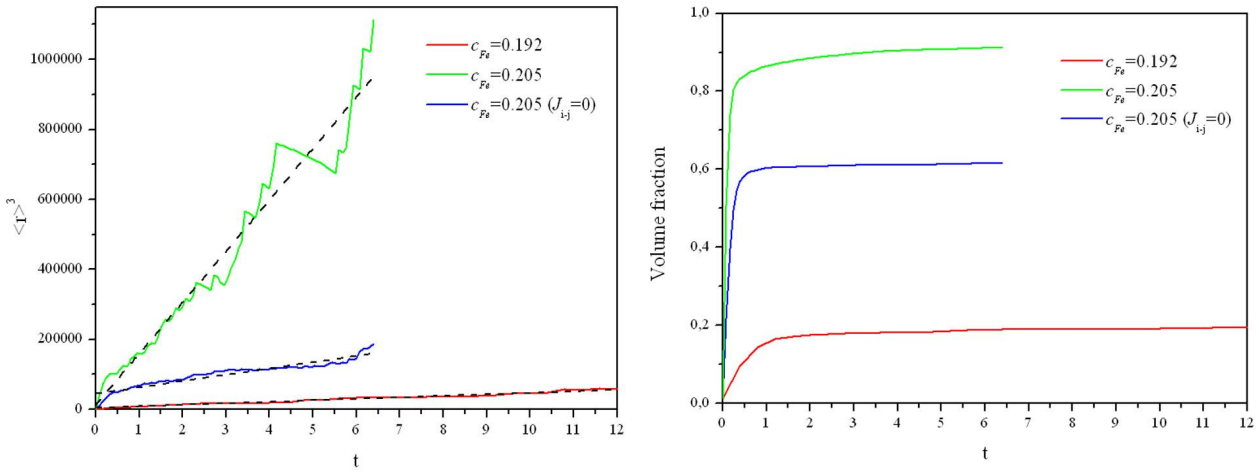

(a) (b)

Figure 4.2.19. Comparison of the statistical data at $T = 650K$:
(a) The cube of the average radius and its linear fit (black dashed line)
(b) The volume fraction of the ordered phase

As can be seen from the figure, for simulation with $c_{Fe} = 0.205$, the coarsening stage starts early and the rate of coarsening can be approximately estimated as $k = 17965.6$ for the paramagnetic case, and $k = 146670.8$ for the ferromagnetic one. From Fig. 4.2.19a it is seen that increasing the concentration results in the increase of the coarsening rate. It has also increased when magnetic interactions were included in the simulation. The volume fraction of the ordered phase also influences the coarsening rate, i.e. as the volume fraction increases, the coarsening rate also increases. The volume fraction (Fig. 4.2.19b) is also influenced by the initial matrix concentration from one side, and by the magnetic interactions from the other. With a concentration increase, the volume fraction has increased almost by a factor 4 (from 0.2 for

c_{Fe} = 0.192 to 0.9 for c_{Fe} = 0.205). Considering the magnetic interactions also has increased its value from 0.6 to 0.9 (for c_{Fe} = 0.205 in the paramagnetic and ferromagnetic states, respectively).

4.2.3.3 Simulations at 716*K*

As it was previously mentioned we are interested in the kinetics at this temperature because the phase coexistence interval is very close to the stoichiometric concentration. Notably, as it can be seen from the isothermal section of the free energy (Fig. 4.2.20a), the concentration of disordered phase is approximately 0.22 and of ordered phase is 0.26. Comparing to the experimental phase diagram (Fig. 4.2.9) this interval is too wide. From the comparison of free energies of paramagnetic ordered and magnetic ordered systems, it is again seen that magnetism induces lowering of the free energy and therefore, again, it should stabilize the ordered structure as in the previous case for $T = 650K$. The plots of the equilibrium chemical and magnetic order parameters (Fig. 4.2.20b) are similar to the previously discussed (Fig. 4.2.10b).

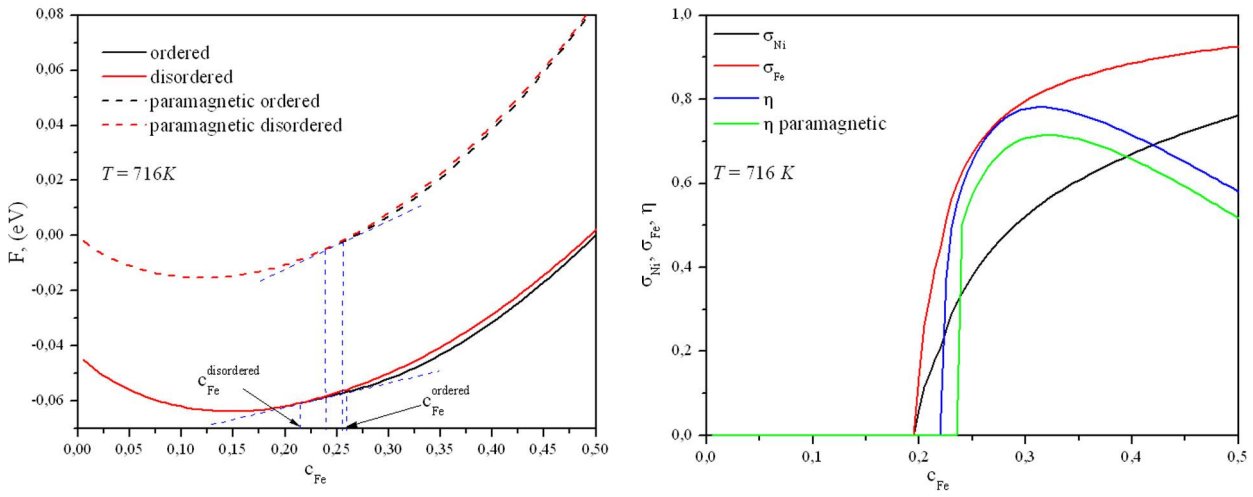

(a) (b)

Figure 4.2.20. Isothermal section at $T = 716K$ of:

(a) Free energy

(b) Equilibrium long-range order parameters

A. Simulation of the precipitation kinetics in Ni-Fe without magnetic interactions

The interaction parameters in this case correspond to the paramagnetic data and were taken from Table. 4.2.8. From the concentration interval $c_{Fe} \in [0.22; 0.26]$ we have chosen a concentration $c_{Fe} = 0.23$. Starting with the same initial conditions as for previous section 4.2.3.2*A*, the disappearance of the ordered phase is observed at $t^* = 0.06$ (a.u.). Thus, the

simulation was held only until $t^* = 0.08$ (a.u.). The microstructure evolution is presented in Fig. 4.2.21.

(a) (b) (c)

Figure 4.2.21. Microstructure evolution for c_{Fe} = 0.23 at T = 716K when $J_{\alpha-\beta} = 0$ at time:

(a) $t^* = 0$ (a.u.)**; (b)** $t^* = 0.01$ (a.u.)**; (c)** $t^* = 0.02$ (a.u.)

Obtained results are consistent with the previously shown for $c_{Fe} = 0.192$. The ordered phase disappears quite fast and, therefore, it is not stable due to the interactions and high temperature. The time variation of the volume fraction (Fig. 4.2.22) represents the same features as for $c_{Fe} = 0.192$ (Fig. 4.2.12).

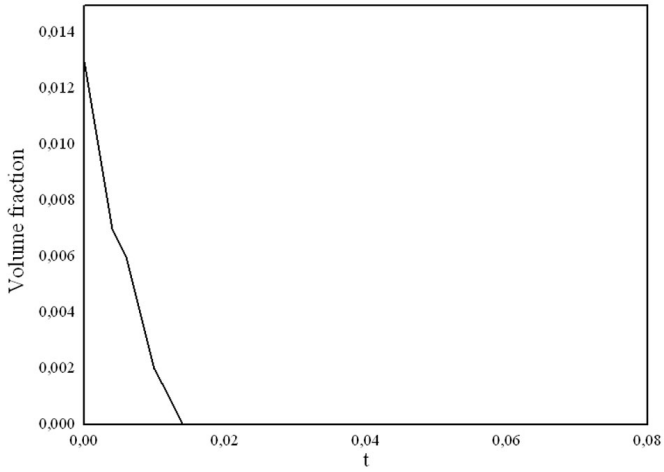

Figure 4.2.22. The time evolution of the volume fraction of the ordered phase

(for c_{Fe} = 0.23 at T = 716K when $J_{\alpha-\beta} = 0$)

At the beginning of evolution the number of nuclei decreases very fast and only few of them begin to grow, then the process continues the same way until all nuclei will be dissolved. The volume fraction tends to zero already at $t^* = 0.014$ (a.u.) and confirms total disappearance of the ordered phase at very early time.

In Fig. 4.2.23 the size distribution of ordered nuclei is compared with the theoretical LSW distribution (Eq. 3.33). The center and the width of distribution do not agree with the

theoretical curve. As the volume fraction decreases, the width becomes narrower and symmetrical. At this concentration the shift of the center of distribution is more pronounced than for $c_{Fe} = 0.192$.

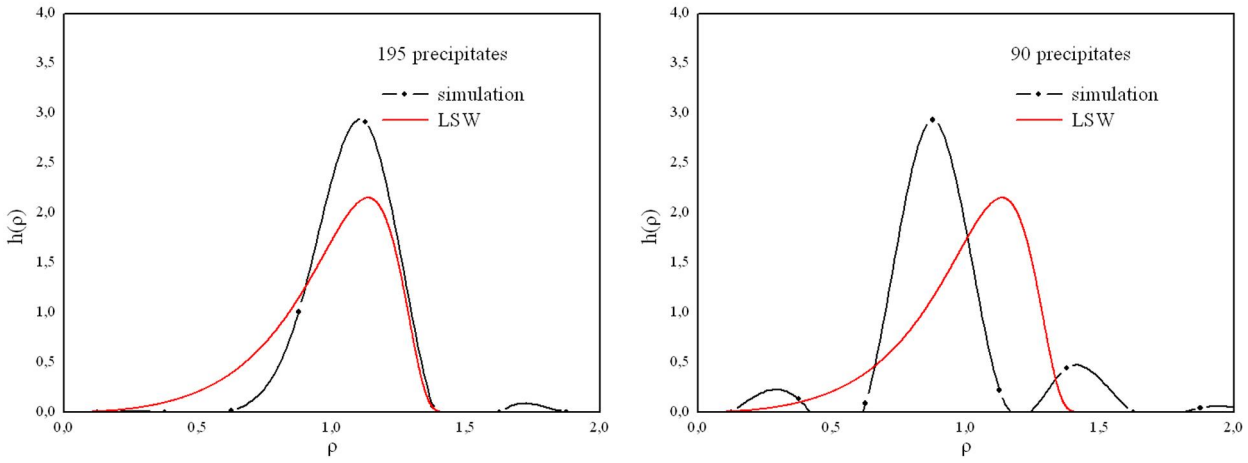

(a) (b)

Figure 4.2.23. The size distribution function for $c_{Fe} = 0.23$ and $T = 716K$ at time:

(a) $t^* = 0$ (a.u.)**; (b)** $t^* = 0.012$ (a.u.)

B. Simulation of the precipitation kinetics in Ni-Fe with magnetic interactions

Following the same way as in section 4.2.3.2*B* the total interaction parameters, $w_{total}(\mathbf{r})$, were calculated using Eq. 4.2.9. Obtained parameters are given in Table 4.2.11.

	w_{total} (**r**), (meV)
1	53.76043
2	-16.6812
3	12.46971
4	8.187753

Table 4.2.11. Total interaction parameters, $w_{total}(\mathbf{r})$, for $c_{Fe} = 0.23$

For calculation of the presented interaction parameters we have used $\sigma_{Fe} = 0.56248371$ and $\sigma_{Ni} = 0.28819062$.

In Fig. 4.2.24 the microstructure evolution at different time, t^*, of simulation is presented.

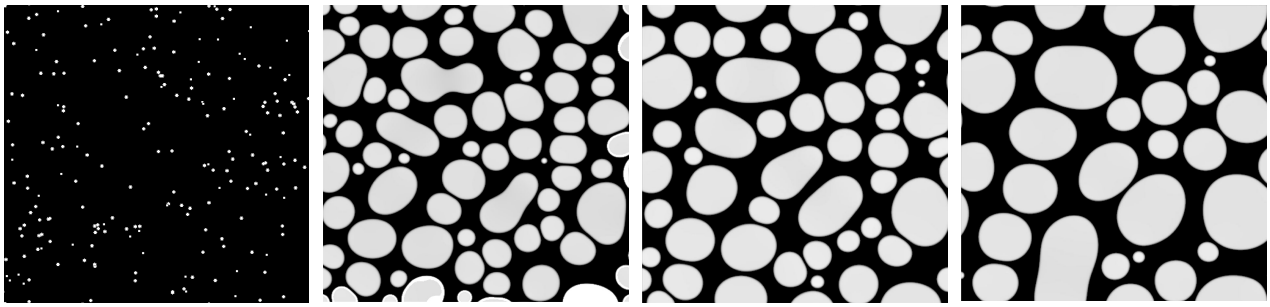

(a) (b) (c) (d)

Figure 4.2.24. Microstructure evolution for $c_{Fe} = 0.23$ at $T = 716K$ at time:

(a) $t^* = 0$ (a.u.)**; (b)** $t^* = 4$ (a.u.)**; (c)** $t^* = 8$ (a.u.)**; (d)** $t^* = 16$ (a.u.)

During the ageing the ordered nuclei became stable, grew in size and then the coarsening stage started (at $t^* \approx 1$ (a.u.)). The average size of the precipitate at the end of simulation is approximately 13.5 nm, which is twice larger than in case of $c_{Fe} = 0.192$ at $T = 650K$. As was mentioned earlier, the stabilization of the ordered phase is observed when magnetic interactions are included in the simulation. Consequently, they play an important role in the kinetic processes and are necessary for the reliable description of the studied system due to the interplay between chemical and magnetic order in Ni_3Fe alloys. In Fig. 4.2.25 the cube of the average radius of the precipitates and the time evolution of the volume fraction of the ordered phase are presented. These curves were obtained after averaging over 2 simulations with different initial nuclei sizes ($r = 5$ and $r = 7$).

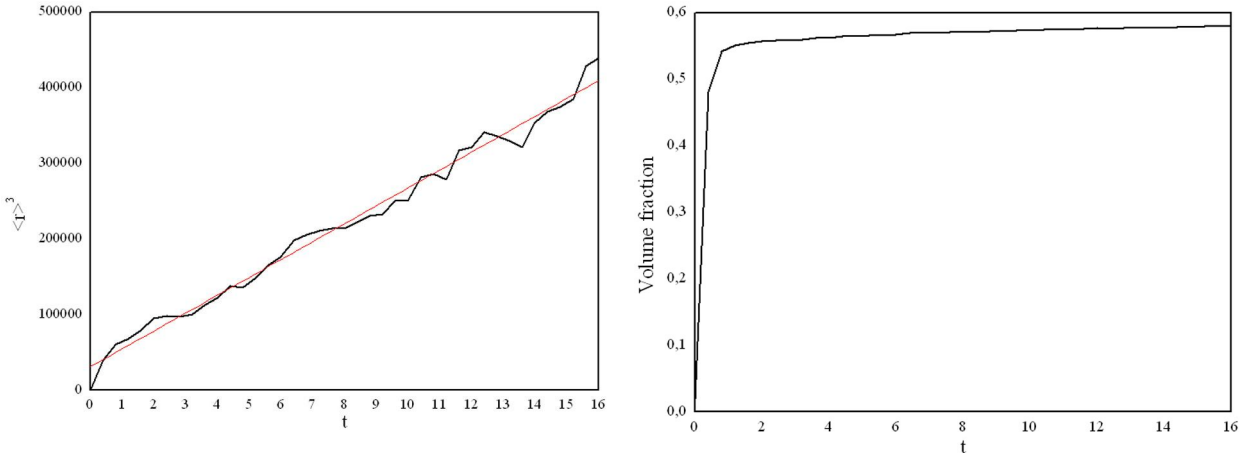

(a) (b)

Figure 4.2.25. The statistical characteristics for simulation for $c_{Fe} = 0.23$ at $T = 716K$:

(a) The cube of the average radius (black line) and its linear fit (red line)

(b) The volume fraction of the ordered phase

The cube of the average radius of the precipitates can be approximated by a linear time dependence (Fig. 4.2.25a), which is consistent with the previous result from section 4.2.3.1*B* and Eq. 3.33. The coarsening rate can be estimated in arbitrary units as $k = 23655.3$. The volume fraction (Fig. 4.2.25b) tends to the equilibrium value 0.6. However, it has not reached its equilibrium value and the concentration of ordered precipitates (≈ 0.24) is not equal to the equilibrium concentration of the ordered phase (0.26). Therefore, further ageing time is desirable to obtain an equilibrium system. However, already at this concentration and temperature, the coarsening rate and the volume fraction has significantly increased in comparison with the results from the previous simulation at $T = 650K$. The size distribution of the ordered precipitates is given in Fig. 4.2.26.

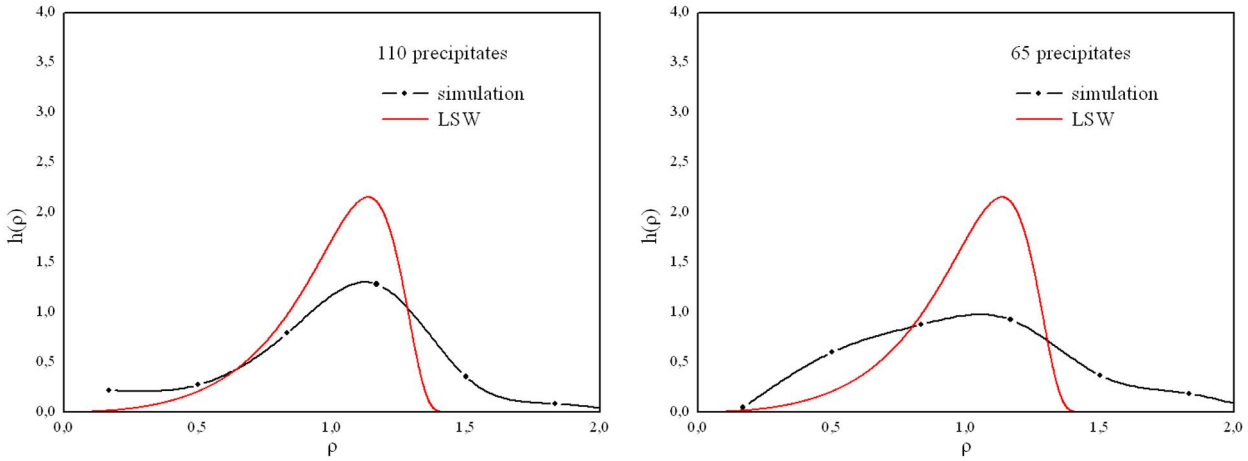

(a) (b)

Figure 4.2.26. The size distribution function for $c_{Fe} = 0.23$ and $T = 716K$ at time:
(a) $t^* = 0.4$ (a.u.)**;** **(b)** $t^* = 4$ (a.u.)**;**

As seen from Fig. 4.2.26, the size distribution changes its shape with time. The width of the simulated distribution is wider in comparison with LSW curve. The center of the distribution seems to lie very close to the theoretically predicted. But due to the limitations of LSW theory it is hard to compare these two distributions. As was mentioned earlier, Lifshitz-Slyozov and Wagner assumed very low fraction of precipitates but for presented simulation it is not negligible anymore. The form of the size distribution is very similar to that obtained in previous section 4.2.3.2*B*.

C. Simulation of the precipitation kinetics in Ni-Fe alloy for different concentrations

As in the previous section, it was interesting to check the microstructure evolution with other Fe-concentration from the co-existence interval. For $c_{Fe} = 0.225$, which is close to the

concentration of the disordered phase, the kinetics is similar to the case without magnetic interactions. The same result was obtained for $c_{Fe} = 0.185$ at $T = 650K$ and is due to the small magnetization values which make total interaction parameters, $w_{total}(\mathbf{r})$, very close to paramagnetic ones, $w_{prm}(\mathbf{r})$. In this case the ordered phase disappears at $t^* \approx 1$ (a.u.).

When matrix concentration, $c_{Fe} = 0.24$, is closer to the equilibrium ordered phase, the nuclei of the ordered phase follow the growth and coarsening stages. As was mentioned in section 4.2.3.2*C*, the magnetic interactions influence the behavior of the system.

	w_{total} (**r**), (meV)
1	52.70558
2	-18.1526
3	12.58581
4	8.444071

Table 4.2.12. Total interaction parameters, $w_{total}(\mathbf{r})$, for $c_{Fe} = 0.24$

For calculation of the total interaction parameters we have used $\sigma_{Fe} = 0.62614201$ and $\sigma_{Ni} = 0.33936110$. In Fig. 4.2.27 the obtained results are presented for two types of simulations, with and without magnetic interactions. The simulation was held until $t^* \approx 7$ (a.u.).

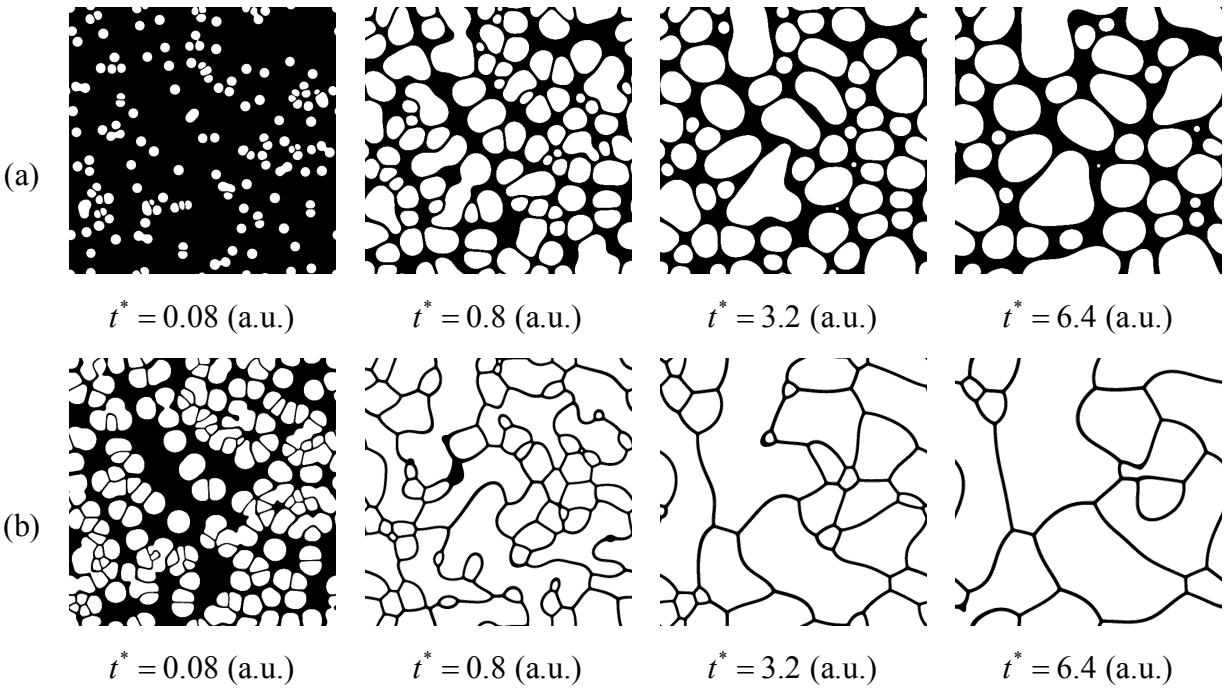

Figure 4.2.27. Microstructure evolution at different time *t* for $c_{Fe} = 0.24$ and $T = 716K$:
(a) Without magnetic interactions ($J_{i\text{-}j} = 0$)
(b) With magnetic interactions

Obtained results confirm our previous statement that magnetic interactions intensify the ordering processes and increase the soluble fraction of the ordered phase. Therefore, large ordered domains are formed earlier than in the paramagnetic state. When magnetic interactions are ignored, at the end of the simulation the large precipitates (with average radius at final time ≈12 nm) were obtained rather than the expected ordered domains.

As in section 4.2.3.2*C*, it is interesting to compare the statistical data for $c_{Fe} = 0.23$ and $c_{Fe} = 0.24$ (Fig. 4.2.28). As expected, the increase of concentration results in the increase of the coarsening rate which is equal to $k = 251021.6$ when magnetic interactions are taken into account and is $k = 39014.9$ when they are ignored. Thus, the coarsening reactions are faster at larger concentrations.

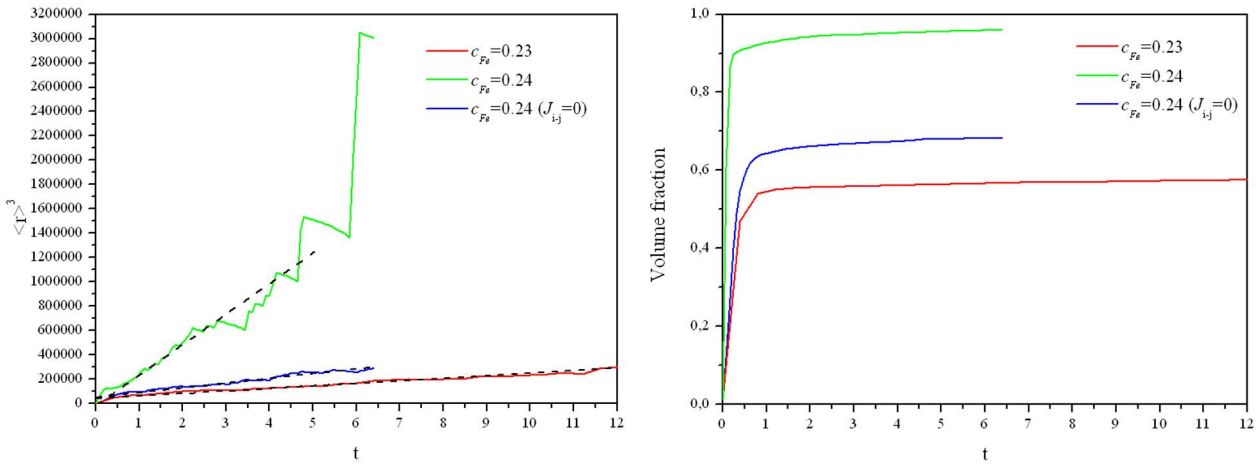

(a) (b)

Figure 4.2.28. Comparison of the statistical data at *T* = 716*K*:

(a) The cube of the average radius and its linear fit (black dashed line)

(b) The volume fraction of the ordered phase

The volume fraction has also increased with the concentration. As seen from Fig. 4.2.28b it has reached 0.96 at $c_{Fe} = 0.24$. Magnetic interactions also influence the volume fraction of the ordered phase (it tends to 0.7 when magnetic interactions are not considered).

4.2.3.4. Conclusions

The results of the performed kinetics simulation at both temperatures (650*K* and 716*K*) are in good agreement with each other and qualitatively reproduce the kinetics in Ni-Fe alloys.

From the results of our simulations it follows that including magnetic interactions has a great influence on the kinetic properties of the system. The rate of coarsening and the volume fraction increases when magnetic interactions are taken into account. It was also outlined that it can influence the morphology of microstructure by accelerating the coarsening rate

(Table 4.2.13), i.e. at the same evolution time large ordered domains will form instead of precipitates with a spherical shape.

***T*, (*K*)**	***magnetism***	c_{Fe}	***k*, (a.u.)**	***volume fraction***
650	-	0.192	-	0
	+		4380.5	0.2
	-	0.205	17965.6	0.6
	+		146670.8	0.9
716	-	0.23	-	0
	+		23655.3	0.58
	-	0.24	39014.9	0.7
	+		251021.6	0.96

Table 4.2.13. Comparison of the coarsening rate and the volume fraction for presented kinetic simulations

The extensive comparison of the obtained simulation results with experiments is unfortunately impossible due to the lack of such data. As was estimated in section 4.2.2, the real ageing time to obtain simulated microstructure at such low temperatures is scarcely possible (the unit simulation time corresponds to 10^7 and 10^5 hours in real time for 650*K* and 716*K*, respectively). Such alloys need very long thermal treatment in order to obtain a perfect ordered $L1_2$ structure. Thus, in experimental works the results correspond probably to the metastable structures and according to the measurements of the long-range order parameter – it just approaches equilibrium ordered value [12]. That is why the theoretical investigations of such alloys are of great interest.

From the kinetic simulations at the stoichiometric concentration $c_{Fe} = 0.25$ we have obtained structure with very large ordered domains (Fig. 4.2.29) separated by the antiphase boundaries. As previously was explained, the ordered domains appear in different orientations due to the possible four translation variants for the $L1_2$ structure. In MC simulations we have also obtained similar feature (Fig. 4.1.15a) considering only NN interactions. In this case the contribution from the interface energy was absent. When we have extended interactions till NNN – it seemed that the opposite situation has arisen and the antiphase boundaries have disappeared due to the minimization of energy. It should be also mentioned that obtained final configuration

in MC simulaions corresponds to the equilibrium state of the system. The microstructure given in Fig. 4.2.29 represents the non-equilibrium configuration and it is logical to assume that after longer ageing times the small domains will disappear and the system will consist only of large antiphase domains.

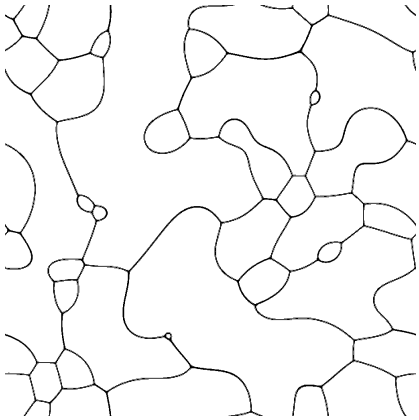

Figure 4.2.29. Microstructure at $t^* = 1.6$ (a.u.) for $c_{Fe} = 0.25$ at $T = 716K$

According to the literature data for $c_{Fe} \approx 0.27$ [130] such domains are indeed seen after long ageing time (Fig. 4.2.30).

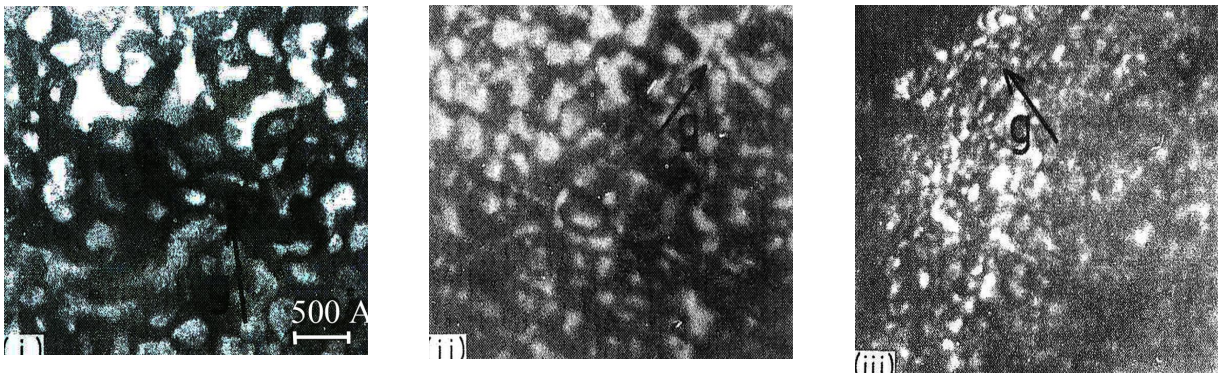

(a) (b) (c)

Figure 4.2.30. Electron micrographs illustrating domain boundaries in $Ni_{73}Fe_{27}$ alloy [130]:

(a) Annealed for 1070 hours at $T = 770K$

(b) Annealed 1700 hours at $T = 758K$

(c) Annealed for 1700 hours at $T = 733K$

It is seen that ordered domains are separated by the disordered phase and these results are consistent with our simulations.

In the previous study we were not interested in the initial mechanism of the ordering and as the order-disorder transition temperature is of the 1st order we assumed and employed the nucleation mechanism and, at the beginning of the simulation, the nuclei of the ordered phase

were embedded into the disordered matrix. Therefore, the growth and coarsening stages followed this process. The growth stage for all simulations was fast.

We should also mention the importance of choice of the interaction parameters. As in our simulations we have chosen constant values of both paramagnetic and magnetic interactions and ignored their variation with concentration and temperature, we do not expect that our results will repeat exactly experimental ones (Fig. 4.2.7). However, the main features of the system close to the stoichiometry, and the expected influence of the magnetism is well reproduced.

General conclusion and perspectives

In the present work we have discussed the mutual influence of magnetic and chemical ordering in $Ni_{1-x}Fe_x$ alloys (x is the concentration of Fe, c_{Fe}) and its effect on the thermodynamics and the kinetics of the systems. As was previously mentioned, at low temperature, these alloys undergo magnetic and atomic ordering. As the temperature decreases, a ferromagnetic order appears firstly, then an order disorder phase transition from a fcc chemically disordered state to a $L1_2$-type ordered state takes place. The investigation of such alloys is quite complicated in view of the necessity to consider both spin and atomic subsystems simultaneously. Two approaches (Monte Carlo and mean-field) have been employed to investigation of the thermodynamic properties of Ni-Fe alloys and the Önsager microscopic diffusion equation was used to study kinetics. Our simulations show that, in spite of some simplifications, these two models permit to capture quite well many features observed in Ni-rich $Ni_{1-x}Fe_x$ alloys.

Let us mention the most important results obtained by means of Monte Carlo simulations:

- When magnetic($J^{\alpha\beta}$) and chemical ($V^{\alpha\beta}$) interactions are considered simultaneously, the increase of both Curie and Kurnakov transition temperatures with respect to the case with only one type of interaction is observed. From one side, the short-range atomic order above T_K increases the Curie temperature and from the other side the antiferromagnetic interaction between nearest neighbour atoms leads to a rise in T_K in such ferromagnetic materials (from 630K to 800K for $Ni_{75}Fe_{25}$). The Curie temperature of chemically ordered phase is higher than the Curie temperature of chemically disordered phase. This behavior agrees with experimental data.
- The chemical ordering at T_K is also responsible for creating singularities in the magnetic quantities. There is a jump in the magnetization and the magnetic energy curves at T_K and consequently, a δ-peak in the zero-field susceptibility and the magnetic specific heat appears.
- The application of an external magnetic field, B, which aligns the magnetic moments, induces atomic rearrangements due to the antiferromagnetic Fe-Fe coupling and promotes the increase of the order-disorder transition temperature.
- Including chemical interactions for next-nearest neighbors softens the order-disorder phase transition.

- Our model is able to reproduce quite well the experimental phase diagram around the 25% at. Fe concentration. The deviations from the experimental data for other concentrations are attributed to some restrictions such as constant interactions and constant magnetic moments of atoms. Although our simulations have been performed only in the vicinity of the stoichiometric concentration, our results seem to confirm the asymmetry of the concentration dependence of the order-disorder transition temperature (the peak is at 26% at. Ni). The magnetic transition line is also well reproduced.

From the mean-field theory we have obtained both thermodynamic and kinetic descriptions of the system. The main results can be summarized as following:

- The interaction parameters obtained from the first-principles calculations have been used. These parameters predict the oscillating character of the Fe-Fe magnetic interaction and ferromagnetic nearest neighbor Fe-Fe interaction. However, using these parameters with a mean field approach allows qualitatively reproduce the miscibility gap on the phase diagram, where the fcc disordered phase coexist with the ordered $L1_2$ phase.
- The comparison of the obtained thermodynamic data with the Monte Carlo results has shown similar behavior of order parameters. In particular, the order of both transitions and the jump in the magnetization are well reproduced. The difference between the Curie and the Kurnakov temperatures has been found smaller using mean field calculations than Monte Carlo simulations.
- The microstructural evolution for different concentrations has been simulated. The growth and the coarsening of $L1_2$ precipitates have been reproduced.
- The kinetic analysis indicates a cubic law for the precipitate average radius in agreement with the LSW theory. It was shown that magnetic interaction increases the coarsening rate.
- Our simulations evidence that during kinetics the magnetic interactions stabilize the $L1_2$ nuclei and increase the driving force of the order-disorder phase transformation.

Following this work, the *perspectives* on this subject are:

- To include the concentration dependencies of the interaction parameters (chemical and magnetic) and of the atomic magnetic moments in Monte Carlo and mean-field simulations.
- To take into account more coordination shells for the interaction parameters.
- To include the variation of the magnetization during the ordering process in the Önsager microscopic diffusion equation.

- To combine kinetic Monte Carlo simulations and simulations using the Önsager equation, i.e. to simulate the nucleation stage by Monte Carlo and to use the obtained configuration with $L1_2$ nuclei as an initial configuration for the simulations based on the Önsager equation.
- Since our simulations have shown that an external applied field stabilizes the $L1_2$ structure (Monte Carlo simulations), and consequently should increase the kinetics rate (Önsager equation based simulations), it would be very interesting to check the speeding-up of the kinetic process experimentally under an external applied field. Consequently, the applied field should favor the achieving of equilibrium ordered state.

Appendix

5.1. Calculation of interaction parameters within 2 coordination shells

The exchange parameters are defined using KCM formula (Eq. 4.1.3) and experimental data. The polynomial dependence can be derived. For the stoichiometric concentration we obtain:

$$\begin{aligned}\tilde{w}_{prm}(\mathbf{k}_X, c_{Fe}=0.25) &= -0.414 + 0.25\cdot 0.450 = -0.3015 \text{ [eV]}\\ \tilde{w}_{prm}(\mathbf{k}_\Gamma, c_{Fe}=0.25) &= 0.855 + 0.25\cdot(-2.177) + 0.25^2\cdot 2.087 = 0.4411875 \text{ [eV]}\end{aligned} \tag{5.1.1}$$

Including in (Eq. 3.22) terms for 1st and 2nd neighbors, the respective ordering energies are:

$$\begin{aligned}\tilde{w}_{prm}(\mathbf{k}_X, c_{Fe}=0.25) &= -4w_1 + 6w_2 = -0.3015 \text{ [eV]}\\ \tilde{w}_{prm}(\mathbf{k}_\Gamma, c_{Fe}=0.25) &= 12w_1 + 6w_2 = 0.4411875 \text{ [eV]}\end{aligned} \tag{5.1.2}$$

And real-space ordering energies w_1 and w_2 will be respectively:

$$\begin{aligned} w_1^{MFT} &= 46.4 \text{ [meV]}\\ w_2^{MFT} &= -19.305 \text{ [meV]}\end{aligned} \quad \Rightarrow \quad \begin{aligned}\frac{w_1^{MFT}}{k_B} &= 538.64K\\ \frac{w_2^{MFT}}{k_B} &= -224.02K\end{aligned} \tag{5.1.3}$$

These values are used to fit interaction parameters $V_1^{\alpha\beta}$ given by Dang *et al.* [40]. Ordering energy defined by $V_1^{\alpha\beta}$ from Ref. [40] is:

$$\frac{w_1^{MC}}{k_B} = \frac{2V_1^{Ni-Fe} - (V_1^{Fe-Fe} + V_1^{Ni-Ni})}{k_B} = 1410K \quad \Rightarrow \quad w_1^{MC} = 121.5 \text{ [meV]}$$

From Eq. 5.1.2 it is possible to estimate the value of ordering energy if only nearest neighbors are considered: $w_1^{MFT} = \frac{0.3015}{4} = 75.375$ [meV]. Using the ratio between MC and MFT values of w_1 ($\frac{w_1^{MC}}{w_1^{MFT}} = 1.612$) we obtain:

$$\tilde{w}_{prm}^{MC}(\mathbf{k}_X, c_{Fe}=0.25) = -4w_1^{MC} + 6w_2^{MC} = 1.612\cdot 0.3015 = 0.486 \text{ [eV]},$$

and keeping the ratio: $\frac{w_1^{MFT}}{w_2^{MFT}} = -2.40445 = \frac{w_1^{MC}}{w_2^{MC}}$ we will obtain new ordering energies for Monte Carlo simulations:

$$\begin{aligned} w_1^{MC} &= 74.826 \text{ [meV]}\\ w_2^{MFT} &= -31.12 \text{ [meV]}\end{aligned} \quad \Rightarrow \quad \begin{aligned}\frac{w_1^{MC}}{k_B} &= 868.29K\\ \frac{w_2^{MFT}}{k_B} &= -361.12K\end{aligned} \tag{5.1.4}$$

It is possible now to proceed with definition of pair-wise energetic parameters $V_{r=\{1,2\}}^{\alpha\beta}$. More intuitive way to define pair-wise interactions is to deduce them from those of

Dang *et al.* [40] but applying obtained above results. Thus, using (Eq. 5.1.4) it is possible to define: $\frac{w_1^{MC[27]}}{w_1^{MC}} = \frac{1410}{868.29} = 1.62388$. This ratio is used to obtain new $V_1^{\alpha\beta}$:

$$\frac{V_1^{Fe-Fe}}{k_B} = \frac{8400}{1.62388} = 5172.79K \; ; \quad \frac{V_1^{Ni-Fe}}{k_B} = \frac{9200}{1.62388} = 5665.44K \; ; \quad \frac{V_1^{Ni-Ni}}{k_B} = \frac{8590}{1.62388} = 5289.795K \tag{5.1.5a}$$

To define $V_2^{\alpha\beta}$ we kept the ratio $\frac{w_1^{MFT}}{w_2^{MFT}} = -2.40445 = \frac{w_1^{MC}}{w_2^{MC}}$ between each respective pair-wise parameter and obtained:

$$\frac{V_2^{Fe-Fe}}{k_B} = \frac{V_1^{Fe-Fe}}{-2.40445} = -2151.353K \; ; \quad \frac{V_2^{Ni-Fe}}{k_B} = \frac{V_1^{Ni-Fe}}{-2.40445} = -2356.244K \; ; \quad \frac{V_2^{Ni-Ni}}{k_B} = \frac{V_1^{Ni-Ni}}{-2.40445} = -2200.015K \tag{5.1.5b}$$

5.2. Derivation of mean-field formulae

5.2.1. Magnetic entropy

In the section 3.4 the approach of molecular field has been introduced. In the framework of this approximation it is possible to obtain an expression for the magnetic entropy for an arbitrary spin **S**. According to the (Eq. 3.12) magnetic field which acts on the crystal can be written in a following form:

$$\mathbf{H} = \mathbf{H}_{ext} + \mathbf{H}_{mol} = \mathbf{H}_{ext} + q \cdot \sigma \, ,$$

where q – is the molecular field constant; σ – is the magnetization.

In the absence of external magnetic field ($\mathbf{H}_{ext} = 0$) this expression will be simplified to:

$$\mathbf{H} = \mathbf{H}_{mol} = q \cdot \sigma \, .$$

The free energy functional (Eq. 3.1) can be also defined using the definition of a statistical sum:

$$F = -k_B T \ln Z$$

As we are interested in the magnetic ordering, the statistical sum Z represents all possible spins configurations and can be written as:

$$Z=\sum_{m_1=-\mathbf{S}}^{\mathbf{S}}\ldots\sum_{m_N=-\mathbf{S}}^{\mathbf{S}}\exp\left(\frac{M\mathbf{H}}{k_BT}\right)=\left\{\begin{array}{l}M=g\mu B\sum_{i=1}^{N}m_i\\ M-\text{total magnetic moment}\\ m_i-\text{magnetic quantum number}\\ \quad\text{of the i-th particle}\\ N-\text{ is the total number of particles}\end{array}\right\}=$$

$$=\prod_{i=1}^{N}\left(\sum_{m_i=-\mathbf{S}}^{\mathbf{S}}\exp\left(\frac{g\mu_B m_i}{k_BT}\mathbf{H}\right)\right)=\left[\frac{sh\left(\frac{g\mu_B(2\mathbf{S}+1)}{2k_BT}\mathbf{H}\right)}{sh\left(\frac{g\mu_B}{2k_BT}\mathbf{H}\right)}\right]^N$$

The following property has been used for the derivation of this formula:

$$\sum_{k=-n}^{n}x^k=x^{-n}\sum_{l=0}^{2n}x^l=\frac{\left(x^{2n+1}-1\right)}{x^n\left(x-1\right)}=\frac{x^{n+\frac{1}{2}}-x^{-n-\frac{1}{2}}}{x^{\frac{1}{2}}-x^{-\frac{1}{2}}};$$

$$sh(x)=\frac{\exp(x)-\exp(-x)}{2}$$

As statistical sum is defined, we proceed to the free energy:

$$F=-k_BT\ln Z=-Nk_BT\ln\left(\frac{sh\left(\frac{g\mu_B(2\mathbf{S}+1)}{2k_BT}\mathbf{H}\right)}{sh\left(\frac{g\mu_B}{2k_BT}\mathbf{H}\right)}\right)=$$

$$=-Nk_BT\left[\ln\left(sh\left(\frac{g\mu_B(2\mathbf{S}+1)}{2k_BT}\mathbf{H}\right)\right)-\ln\left(sh\left(\frac{g\mu_B}{2k_BT}\mathbf{H}\right)\right)\right]$$

The entropy is defined then as a 1st derivative of free energy F:

$$S=-\frac{\partial F}{\partial T}=-\frac{\partial}{\partial T}\left\{-Nk_BT\left[\ln\left(sh\left(\frac{g\mu_B(2\mathbf{S}+1)}{2k_BT}\mathbf{H}\right)\right)-\ln\left(sh\left(\frac{g\mu_B}{2k_BT}\mathbf{H}\right)\right)\right]\right\}=$$

$$=-\left\{-Nk_B\left[\ln\left(sh\left(\frac{g\mu_B(2\mathbf{S}+1)}{2k_BT}\mathbf{H}\right)\right)-\ln\left(sh\left(\frac{g\mu_B}{2k_BT}\mathbf{H}\right)\right)\right]\right\}+\left(-Nk_BT\right)\times$$

$$\times\left\{\frac{ch\left(\frac{g\mu_B(2\mathbf{S}+1)}{2k_BT}\mathbf{H}\right)}{sh\left(\frac{g\mu_B(2\mathbf{S}+1)}{2k_BT}\mathbf{H}\right)}\frac{g\mu_B(2\mathbf{S}+1)}{2k_B}\mathbf{H}\left(-\frac{1}{T^2}\right)-\frac{ch\left(\frac{g\mu_B}{2k_BT}\mathbf{H}\right)}{sh\left(\frac{g\mu_B}{2k_BT}\mathbf{H}\right)}\frac{g\mu_B}{2k_B}\mathbf{H}\left(-\frac{1}{T^2}\right)\right\}=$$

$$=Nk_B\left[\ln\left(sh\left(\frac{g\mu_B(2\mathbf{S}+1)}{2k_BT}\mathbf{H}\right)\right)-\ln\left(sh\left(\frac{g\mu_B}{2k_BT}\mathbf{H}\right)\right)\right]-$$

$$-Nk_B\left\{\frac{g\mu_B}{2k_BT}\mathbf{H}\left((2\mathbf{S}+1)coth\left(\frac{g\mu_B(2\mathbf{S}+1)}{2k_BT}\mathbf{H}\right)-coth\left(\frac{g\mu_B}{2k_BT}\mathbf{H}\right)\right)\right\}=$$

$$=\left\{\begin{array}{l}B_{\mathbf{J}}(x)=\left(1+\frac{1}{2\mathbf{J}}\right)coth\left(\left(1+\frac{1}{2\mathbf{J}}\right)x\right)-\frac{1}{2\mathbf{J}}coth\left(\frac{1}{2\mathbf{J}}x\right)\\ y=\frac{\mathbf{S}g\mu_B}{k_BT}\mathbf{H}=\frac{\mathbf{S}g\mu_B}{k_BT}(q\cdot\sigma)\end{array}\right\}=$$

$$=Nk_B\left[\ln\left(sh\left(\frac{(2\mathbf{S}+1)y}{2\mathbf{S}}\right)\right)-\ln\left(sh\left(\frac{y}{2\mathbf{S}}\right)\right)-yB_{\mathbf{S}}(y)\right]$$

We should mention that for numerical calculation of magnetic entropy, its expression can be simplified in order to avoid zero-values of logarithm's argument. The following should be done:

$$\ln\left(sh\left(\frac{(2\mathbf{S}+1)y}{2\mathbf{S}}\right)\right)-\ln\left(sh\left(\frac{y}{2\mathbf{S}}\right)\right)=\ln\left(\frac{sh\left(\frac{(2\mathbf{S}+1)y}{2\mathbf{S}}\right)}{sh\left(\frac{y}{2\mathbf{S}}\right)}\right)$$

It can be seen that the argument can be written in a following form:

$$\left\{\begin{array}{l}\frac{y}{2\mathbf{S}}=x\\(2S+1)=A=const\end{array}\right.\quad\Rightarrow\quad\ln\left(\frac{sh\left(\frac{(2\mathbf{S}+1)y}{2\mathbf{S}}\right)}{sh\left(\frac{y}{2\mathbf{S}}\right)}\right)=\ln\left(\frac{sh(Ax)}{sh(x)}\right)$$

Using the definition of hyperbolic sinus we will be able to further simplify this expression:

$$\frac{sh(Ax)}{sh(x)}=\frac{\mathrm{e}^{Ax}-\mathrm{e}^{-Ax}}{\mathrm{e}^{x}-\mathrm{e}^{-x}}=\left\{a^n-b^n=(a^n-b^n)(a^{(n-1)}+\mathrm{a}^{(n-2)}b+\ldots+ba^{(n-2)}+b^{(A-1)})\right\}=$$

$$=\mathrm{e}^{(A-1)x}+\mathrm{e}^{(A-2)x}\mathrm{e}^{-x}+\ldots+\mathrm{e}^{x}\mathrm{e}^{-(A-2)x}+\mathrm{e}^{-(A-1)x}=\left\{\begin{array}{l}2\sum_{i=1}^{A/2}ch\left((2i-1)x\right),\ \text{if A - is even number}\\2\sum_{i=1}^{(A-1)/2}ch(2ix)+1,\ \text{if A - is odd number}\end{array}\right.$$

So, we obtain following:

$$\ln\left(\frac{sh\left(\frac{(2\mathbf{S}+1)y}{2\mathbf{S}}\right)}{sh\left(\frac{y}{2\mathbf{S}}\right)}\right)=\ln\left(\psi\left(\frac{y}{2\mathbf{S}}\right)\right),$$

where $\psi\left(\frac{y}{2S}\right)=\left\{\begin{array}{l}2\sum_{i=1}^{A/2}ch\left((2i-1)\frac{y}{2S}\right),\ \text{if A=(2S+1) - is even number}\\2\sum_{i=1}^{(A-1)/2}ch\left(2i\frac{y}{2S}\right)+1,\ \text{if A=(2S+1) - is odd number}\end{array}\right.$

5.2.2. Free energy of a system with 2 magnetic species

Free energy functional is defined as (Eq. 3.1.):

$$F = U - TS$$

When system comprises both magnetic and chemical subsystems, the internal energy and entropy can be written as:

$$U = \langle H_{tot} \rangle = \langle H_{chem} + H_{magn} \rangle = U_{chem} + U_{magn}$$
$$S = S_{chem} + S_{magn}$$

For final derivation of free energy, we separate chemical and magnetic parts, respectively. These expressions were also previously shown in Refs. [50-51].

I. Internal energy, *U*.

1) <u>chemical internal energy, U_{chem}</u>.

To define an internal energy, we should start with the Hamiltonian representation. For chemical subsystem, the Hamiltonian was given in (Eq. 3.4):

$$\mathscr{H}_{chem} = \frac{1}{2}\sum_{\mathrm{r,r'}}\sum_{\alpha,\beta} V_{\alpha\beta}(\mathbf{r}-\mathbf{r}')c_{\alpha}(\mathbf{r})c_{\beta}(\mathbf{r}'),$$

where (α, β) represent the type of atom; $V_{\alpha\beta}(\mathbf{r}\text{-}\mathbf{r}')$ are the chemical interaction parameters, $c_{\alpha}(\mathbf{r})$ ($c_{\beta}(\mathbf{r}')$)-represents the occupation of a site $\mathbf{r}$ ($\mathbf{r}'$) by an atom of type α (β) and is defined as:

$$c_{\alpha}(\mathbf{r}) = \begin{cases} 1, \text{ if site } (\mathbf{r}) \text{ is occupied by } \alpha\text{-atom} \\ 0, \text{ otherwise} \end{cases}$$

This Hamiltonian can be simplified to:

$$\mathscr{H}_{chem} = \frac{1}{2}\sum_{\mathrm{r,r'}}\{V_{\alpha\alpha}(\mathbf{r}-\mathbf{r}')c_{\alpha}(\mathbf{r})c_{\alpha}(\mathbf{r}') + V_{\alpha\beta}(\mathbf{r}-\mathbf{r}')c_{\alpha}(\mathbf{r})c_{\beta}(\mathbf{r}') +$$
$$+ V_{\beta\alpha}(\mathbf{r}-\mathbf{r}')c_{\beta}(\mathbf{r})c_{\alpha}(\mathbf{r}') + V_{\beta\beta}(\mathbf{r}-\mathbf{r}')c_{\beta}(\mathbf{r})c_{\beta}(\mathbf{r}')\} =$$
$$= \left\{ \begin{array}{c} V_{\alpha\beta}(\mathbf{r}-\mathbf{r}') = V_{\beta\alpha}(\mathbf{r}-\mathbf{r}') \\ c_{\beta}(\mathbf{r}) = 1 - c_{\alpha}(\mathbf{r}); \quad c_{\alpha} = c \end{array} \right\} =$$

$$= \frac{1}{2}\sum_{\mathbf{r},\mathbf{r}'}\{V_{\alpha\alpha}(\mathbf{r}-\mathbf{r}')c(\mathbf{r})c(\mathbf{r}') + V_{\beta\beta}(\mathbf{r}-\mathbf{r}')(1-c(\mathbf{r}))(1-c(\mathbf{r}')) +$$

$$+V_{\alpha\beta}(\mathbf{r}-\mathbf{r}')\big((1-c(\mathbf{r}))c(\mathbf{r}') + c(\mathbf{r})(1-c(\mathbf{r}'))\big)\} =$$

$$= \frac{1}{2}\sum_{\mathbf{r},\mathbf{r}'}\{c(\mathbf{r})c(\mathbf{r}')\left[V_{\alpha\alpha}(\mathbf{r}-\mathbf{r}') + V_{\beta\beta}(\mathbf{r}-\mathbf{r}') - 2V_{\alpha\beta}(\mathbf{r}-\mathbf{r}')\right] +$$

$$+V_{\alpha\beta}(\mathbf{r}-\mathbf{r}')\big(c(\mathbf{r})+c(\mathbf{r}')\big) + V_{\beta\beta}(\mathbf{r}-\mathbf{r}')(1-(c(\mathbf{r})+c(\mathbf{r}'))\} =$$

$$= \left\{W^{chem}(\mathbf{r}-\mathbf{r}') = V_{\alpha\alpha}(\mathbf{r}-\mathbf{r}') + V_{\beta\beta}(\mathbf{r}-\mathbf{r}') - 2V_{\alpha\beta}(\mathbf{r}-\mathbf{r}')\right\} =$$

$$= \frac{1}{2}\sum_{\mathbf{r},\mathbf{r}'}\{W^{chem}(\mathbf{r}-\mathbf{r}')c(\mathbf{r})c(\mathbf{r}') + V_{\alpha\beta}(\mathbf{r}-\mathbf{r}')\big(c(\mathbf{r})+c(\mathbf{r}')\big) +$$

$$+V_{\beta\beta}(\mathbf{r}-\mathbf{r}')(1-(c(\mathbf{r})+c(\mathbf{r}'))\} =$$

$$= \frac{1}{2}\sum_{\mathbf{r},\mathbf{r}'}W^{chem}(\mathbf{r}-\mathbf{r}')c(\mathbf{r})c(\mathbf{r}') + \frac{1}{2}\sum_{\mathbf{r},\mathbf{r}'}V_{\alpha\beta}(\mathbf{r}-\mathbf{r}')c(\mathbf{r}) + \frac{1}{2}\sum_{\mathbf{r},\mathbf{r}'}V_{\alpha\beta}(\mathbf{r}-\mathbf{r}')c(\mathbf{r}') +$$

$$+\frac{1}{2}\sum_{\mathbf{r},\mathbf{r}'}V_{\beta\beta}(\mathbf{r}-\mathbf{r}') - \frac{1}{2}\sum_{\mathbf{r},\mathbf{r}'}V_{\beta\beta}(\mathbf{r}-\mathbf{r}')c(\mathbf{r}) - \frac{1}{2}\sum_{\mathbf{r},\mathbf{r}'}V_{\beta\beta}(\mathbf{r}-\mathbf{r}')c(\mathbf{r}') =$$

$$= \left\{\begin{array}{l}\sum_{\mathbf{r},\mathbf{r}'}V_{\beta\beta}(\mathbf{r}-\mathbf{r}') = \sum_{\mathbf{r}}\Phi_{\beta\beta}(\mathbf{r})\exp(-i\mathbf{k}\cdot\mathbf{r})\big|_{\mathbf{k}=0} = \Phi_{\beta\beta}(\mathbf{0}) \\ \sum_{\mathbf{r}}c(\mathbf{r}) = \{c(\mathbf{r}) = c_{\alpha}(\mathbf{r})\} = N_{\alpha}\end{array}\right\} =$$

$$= \frac{1}{2}\sum_{\mathbf{r},\mathbf{r}'}W^{chem}(\mathbf{r}-\mathbf{r}')c(\mathbf{r})c(\mathbf{r}') + \frac{1}{2}\Phi_{\beta\beta}(\mathbf{0}) + \frac{N_{\alpha}}{2}\left[\Phi_{\alpha\beta}(\mathbf{0}) + \Phi_{\alpha\beta}(\mathbf{0}) - \Phi_{\beta\beta}(\mathbf{0}) - \Phi_{\beta\beta}(\mathbf{0})\right] =$$

$$= \frac{1}{2}\sum_{\mathbf{r},\mathbf{r}'}W^{chem}(\mathbf{r}-\mathbf{r}')c(\mathbf{r})c(\mathbf{r}') + \frac{1}{2}\Phi_{\beta\beta}(\mathbf{0}) + N_{\alpha}\left[\Phi_{\alpha\beta}(\mathbf{0}) - \Phi_{\beta\beta}(\mathbf{0})\right] = \quad ,$$

$$= \left\{\frac{1}{2}\Phi_{\beta\beta}(\mathbf{0}) + N_{\alpha}\left[\Phi_{\alpha\beta}(\mathbf{0}) - \Phi_{\beta\beta}(\mathbf{0})\right] = const = U^{0}_{chem}\right\} =$$

$$= \frac{1}{2}\sum_{\mathbf{r},\mathbf{r}'}W^{chem}(\mathbf{r}-\mathbf{r}')c(\mathbf{r})c(\mathbf{r}') + U^{0}_{chem}$$

where $W^{chem}(\mathbf{r}-\mathbf{r}')$ is the *ordering* ('*mixing*') energy, previously defined in (Eq. 3.10). The constant term U^{0}_{chem} can be taken as an origin of a new coordinate system, so we can rewrite:

$$\mathscr{H}_{chem} = \frac{1}{2}\sum_{\mathbf{r},\mathbf{r}'}W^{chem}(\mathbf{r}-\mathbf{r}')c(\mathbf{r})c(\mathbf{r}')$$

To obtain internal energy we average the Hamiltonian over all atomic configurations. In the framework of mean-field we have: $\langle c(\mathbf{r})c(\mathbf{r}')\rangle = \langle c(\mathbf{r})\rangle\langle c(\mathbf{r}')\rangle = p(\mathbf{r})p(\mathbf{r}')$. Using the static concentration wave approach (section 3.6) it is possible to define these probabilities (Eq. 3.19). As for the studied case of Ni_3Fe alloy the ordered structure corresponds to the $L1_2$-type, the probability $p(\mathbf{r})$ is defined as:

$$p(\mathbf{r}) = c + \frac{\eta}{4}\left(\mathrm{e}^{i2\pi\mathbf{a}_1^*\cdot\mathbf{r}} + \mathrm{e}^{i2\pi\mathbf{a}_2^*\cdot\mathbf{r}} + \mathrm{e}^{i2\pi\mathbf{a}_3^*\cdot\mathbf{r}}\right) = c + \frac{\eta}{4}\mathrm{e}^{i\mathbf{k}\cdot\mathbf{r}},$$

where η is the chemical long-range order parameter. So, chemical internal energy will have a following form:

$$U_{chem} = \left\langle \mathscr{H}_{chem} \right\rangle = \left\langle \frac{1}{2}\sum_{\mathrm{r},\mathrm{r}'} W^{chem}(\mathbf{r}-\mathbf{r}')c(\mathbf{r})c(\mathbf{r}') \right\rangle = \frac{1}{2}\sum_{\mathrm{r},\mathrm{r}'} W^{chem}(\mathbf{r}-\mathbf{r}')\left\langle c(\mathbf{r})c(\mathbf{r}')\right\rangle =$$

$$= \frac{1}{2}\sum_{\mathrm{r},\mathrm{r}'} W^{chem}(\mathbf{r}-\mathbf{r}')\left\langle c(\mathbf{r})\right\rangle\left\langle c(\mathbf{r}')\right\rangle = \frac{1}{2}\sum_{\mathrm{r},\mathrm{r}'} W^{chem}(\mathbf{r}-\mathbf{r}')p(\mathbf{r})p(\mathbf{r}') =$$

$$= \frac{1}{2}\sum_{\mathrm{r},\mathrm{r}'} W^{chem}(\mathbf{r}-\mathbf{r}')\left[c^2 + \frac{\eta}{4}c\,\mathrm{e}^{i\mathbf{k}\cdot\mathbf{r}} + \frac{\eta}{4}c\,\mathrm{e}^{i\mathbf{k}\cdot\mathbf{r}'} + \frac{\eta^2}{16}\mathrm{e}^{i\mathbf{k}\cdot\mathbf{r}}\,\mathrm{e}^{i\mathbf{k}\cdot\mathbf{r}'}\right] =$$

$$= \frac{1}{2}\sum_{\mathrm{r},\mathrm{r}'} W^{chem}(\mathbf{r}-\mathbf{r}')c^2 + \frac{\eta}{8}\sum_{\mathrm{r},\mathrm{r}'} W^{chem}(\mathbf{r}-\mathbf{r}')c\,\mathrm{e}^{i\mathbf{k}\cdot\mathbf{r}} + \frac{\eta}{8}\sum_{\mathrm{r},\mathrm{r}'} W^{chem}(\mathbf{r}-\mathbf{r}')c\,\mathrm{e}^{i\mathbf{k}\cdot\mathbf{r}'} +$$

$$+ \frac{1}{2}\sum_{\mathrm{r},\mathrm{r}'} W^{chem}(\mathbf{r}-\mathbf{r}')\frac{\eta^2}{16}\mathrm{e}^{i\mathbf{k}\cdot\mathbf{r}}\,\mathrm{e}^{i\mathbf{k}\cdot\mathbf{r}'} = \left\{\begin{array}{l} \sum_{\mathrm{r},\mathrm{r}'} W^{chem}(\mathbf{r}-\mathbf{r}')\,\mathrm{e}^{i\mathbf{k}\cdot\mathbf{r}} \to 0 \\ \mathbf{k} = (k_x, k_y, k_z) = 2\pi(h\mathbf{a}_1^* + k\mathbf{a}_2^* + l\mathbf{a}_3^*) \\ \sum_{\mathrm{r},\mathrm{r}'} W^{chem}(\mathbf{r}-\mathbf{r}')\,\mathrm{e}^{i\mathbf{k}\cdot\mathbf{r}}\,\mathrm{e}^{i\mathbf{k}\cdot\mathbf{r}'} = N\tilde{W}^{chem}(\mathbf{k}) \end{array}\right\} =$$

$$= \frac{N}{2}\left[c^2\tilde{W}^{chem}(\mathbf{0}) + \frac{3}{16}\eta^2\tilde{W}^{chem}(\mathbf{k})\right]$$

2) <u>magnetic internal energy, U_{magn}</u>.

Magnetic Hamiltonian can be written in the following form:

$$\mathscr{H}_{magn} = \frac{1}{2}\sum_{\mathrm{r},\mathrm{r}'}\sum_{\alpha,\beta} J_{\alpha\beta}(\mathbf{r}-\mathbf{r}')c_\alpha(\mathbf{r})c_\beta(\mathbf{r}')s_\alpha(\mathbf{r})s_\beta(\mathbf{r}'),$$

where (α, β) represent the type of atom; $J_{\alpha\beta}(\mathbf{r}\text{-}\mathbf{r}')$ are the magnetic exchange interaction parameters, $c_\alpha(\mathbf{r})$ ($c_\beta(\mathbf{r}')$)-represents the occupation of a site $\mathbf{r}$ ($\mathbf{r}'$) by an atom of type α (β) and spins of each atom is represented by spin variable $s_\alpha(\mathbf{r})$ ($s_\beta(\mathbf{r}')$).

We can rewrite this Hamiltonian as:

$$\mathscr{H}_{magn} = \frac{1}{2}\sum_{\mathrm{r},\mathrm{r}'}\{J_{\alpha\alpha}(\mathbf{r}-\mathbf{r}')c_\alpha(\mathbf{r})c_\alpha(\mathbf{r}')s_\alpha(\mathbf{r})s_\alpha(\mathbf{r}') + J_{\alpha\beta}(\mathbf{r}-\mathbf{r}')c_\alpha(\mathbf{r})c_\beta(\mathbf{r}')s_\alpha(\mathbf{r})s_\beta(\mathbf{r}') +$$

$$+ J_{\beta\alpha}(\mathbf{r}-\mathbf{r}')c_\beta(\mathbf{r})c_\alpha(\mathbf{r}')s_\beta(\mathbf{r})s_\alpha(\mathbf{r}') + J_{\beta\beta}(\mathbf{r}-\mathbf{r}')c_\beta(\mathbf{r})c_\beta(\mathbf{r}')s_\beta(\mathbf{r})s_\beta(\mathbf{r}')\} =$$

$$= \left\{\begin{array}{l} J_{\alpha\beta}(\mathbf{r}-\mathbf{r}') = J_{\beta\alpha}(\mathbf{r}-\mathbf{r}') \\ c_\beta(\mathbf{r}) = 1 - c_\alpha(\mathbf{r}); \qquad c_\alpha(\mathbf{r}) = c \end{array}\right\} =$$

$$= \frac{1}{2}\sum_{\mathbf{r},\mathbf{r}'}\{J_{\alpha\alpha}(\mathbf{r}-\mathbf{r}')c(\mathbf{r})c(\mathbf{r}')s_\alpha(\mathbf{r})s_\alpha(\mathbf{r}') + J_{\beta\beta}(\mathbf{r}-\mathbf{r}')(1-c(\mathbf{r}))(1-c(\mathbf{r}'))s_\beta(\mathbf{r})s_\beta(\mathbf{r}') +$$

$$+J_{\alpha\beta}(\mathbf{r}-\mathbf{r}')\Big((1-c(\mathbf{r}))c(\mathbf{r}')s_\beta(\mathbf{r})s_\alpha(\mathbf{r}') + c(\mathbf{r})(1-c(\mathbf{r}'))s_\alpha(\mathbf{r})s_\beta(\mathbf{r}')\Big)\} =$$

$$= \frac{1}{2}\sum_{\mathbf{r},\mathbf{r}'}\{c(\mathbf{r})c(\mathbf{r}')[J_{\alpha\alpha}(\mathbf{r}-\mathbf{r}')s_\alpha(\mathbf{r})s_\alpha(\mathbf{r}') + J_{\beta\beta}(\mathbf{r}-\mathbf{r}')s_\beta(\mathbf{r})s_\beta(\mathbf{r}') -$$

$$-J_{\alpha\beta}(\mathbf{r}-\mathbf{r}')((s_\alpha(\mathbf{r})s_\beta(\mathbf{r}') + s_\beta(\mathbf{r})s_\alpha(\mathbf{r}'))] + J_{\alpha\beta}(\mathbf{r}-\mathbf{r}')\Big(c(\mathbf{r})s_\alpha(\mathbf{r})s_\beta(\mathbf{r}') + c(\mathbf{r}')s_\beta(\mathbf{r})s_\alpha(\mathbf{r}')\Big) +$$

$$+J_{\beta\beta}(\mathbf{r}-\mathbf{r}')(1-(c(\mathbf{r})+c(\mathbf{r}'))s_\beta(\mathbf{r})s_\beta(\mathbf{r}')\}$$

Magnetic internal energy is obtained after averaging the Hamiltonian over all spin configurations. Using the molecular mean-field approach, we have $\langle s_\alpha(\mathbf{r})\rangle = \sigma_\alpha s_\alpha$ and $\langle s_\alpha(\mathbf{r})s_\beta(\mathbf{r}')\rangle = \langle s_\alpha(\mathbf{r})\rangle\langle s_\beta(\mathbf{r}')\rangle = \sigma_\alpha\sigma_\beta s_\alpha s_\beta$, where σ_α (σ_β) – is the reduced magnetization of α (β) sublattice. So, using mean-field and SCW approaches we will obtain:

$$U_{magn} = \langle \mathscr{H}_{magn}\rangle = \frac{1}{2}\sum_{\mathbf{r},\mathbf{r}'}\Big\{\langle c(\mathbf{r})c(\mathbf{r}')\rangle[J_{\alpha\alpha}(\mathbf{r}-\mathbf{r}')\langle s_\alpha(\mathbf{r})s_\alpha(\mathbf{r}')\rangle + J_{\beta\beta}(\mathbf{r}-\mathbf{r}')\langle s_\beta(\mathbf{r})s_\beta(\mathbf{r}')\rangle -$$

$$-J_{\alpha\beta}(\mathbf{r}-\mathbf{r}')((\langle s_\alpha(\mathbf{r})s_\beta(\mathbf{r}')\rangle + \langle s_\beta(\mathbf{r})s_\alpha(\mathbf{r}')\rangle)] + J_{\beta\beta}(\mathbf{r}-\mathbf{r}')(1-(\langle c(\mathbf{r})\rangle + \langle c(\mathbf{r}')\rangle)\langle s_\beta(\mathbf{r})s_\beta(\mathbf{r}')\rangle +$$

$$+J_{\alpha\beta}(\mathbf{r}-\mathbf{r}')\Big(\langle c(\mathbf{r})\rangle\langle s_\alpha(\mathbf{r})s_\beta(\mathbf{r}')\rangle + \langle c(\mathbf{r}')\rangle\langle s_\beta(\mathbf{r})s_\alpha(\mathbf{r}')\rangle\Big)\Big\} =$$

$$= \frac{1}{2}\sum_{\mathbf{r},\mathbf{r}'}\Big\{p(\mathbf{r})p(\mathbf{r}')[J_{\alpha\alpha}(\mathbf{r}-\mathbf{r}')\sigma_\alpha^2 s_\alpha^2 + J_{\beta\beta}(\mathbf{r}-\mathbf{r}')\sigma_\beta^2 s_\beta^2 - 2J_{\alpha\beta}(\mathbf{r}-\mathbf{r}')\sigma_\alpha\sigma_\beta s_\alpha s_\beta] +$$

$$+J_{\alpha\beta}(\mathbf{r}-\mathbf{r}')\sigma_\alpha\sigma_\beta s_\alpha s_\beta\big(p(\mathbf{r})+p(\mathbf{r}')\big) + J_{\beta\beta}(\mathbf{r}-\mathbf{r}')\sigma_\beta^2 s_\beta^2(1-(p(\mathbf{r})+p(\mathbf{r}'))\Big\} =$$

$$= \frac{1}{2}\sum_{\mathbf{r},\mathbf{r}'}\Big\{\Big(J_{\alpha\alpha}(\mathbf{r}-\mathbf{r}')\sigma_\alpha^2 s_\alpha^2 + J_{\beta\beta}(\mathbf{r}-\mathbf{r}')\sigma_\beta^2 s_\beta^2 - 2J_{\alpha\beta}(\mathbf{r}-\mathbf{r}')\sigma_\alpha\sigma_\beta s_\alpha s_\beta\Big)[c^2 + \frac{\eta}{4}c\,e^{i\mathbf{k}\cdot\mathbf{r}} +$$

$$+\frac{\eta}{4}c\,e^{i\mathbf{k}\cdot\mathbf{r}'} + \frac{\eta^2}{16}e^{i\mathbf{k}\cdot\mathbf{r}}e^{i\mathbf{k}\cdot\mathbf{r}'}] + J_{\alpha\beta}(\mathbf{r}-\mathbf{r}')\sigma_\alpha\sigma_\beta s_\alpha s_\beta\left(2c + \frac{\eta}{4}e^{i\mathbf{k}\cdot\mathbf{r}} + \frac{\eta}{4}e^{i\mathbf{k}\cdot\mathbf{r}'}\right) +$$

$$+J_{\beta\beta}(\mathbf{r}-\mathbf{r}')\sigma_\beta^2 s_\beta^2\left(1-\left(2c + \frac{\eta}{4}e^{i\mathbf{k}\cdot\mathbf{r}} + \frac{\eta}{4}e^{i\mathbf{k}\cdot\mathbf{r}'}\right)\right)\Big\} = \frac{1}{2}\sum_{\mathbf{r},\mathbf{r}'}\Big(J_{\alpha\alpha}(\mathbf{r}-\mathbf{r}')\sigma_\alpha^2 s_\alpha^2 +$$

$$+J_{\beta\beta}(\mathbf{r}-\mathbf{r}')\sigma_\beta^2 s_\beta^2 - 2J_{\alpha\beta}(\mathbf{r}-\mathbf{r}')\sigma_\alpha\sigma_\beta s_\alpha s_\beta\Big)\frac{\eta^2}{16}e^{i\mathbf{k}\cdot\mathbf{r}}e^{i\mathbf{k}\cdot\mathbf{r}'} +$$

$$+\frac{1}{2}\sum_{\mathbf{r},\mathbf{r}'}\Big\{J_{\alpha\alpha}(\mathbf{r}-\mathbf{r}')\sigma_\alpha^2 s_\alpha^2 c^2 + J_{\beta\beta}(\mathbf{r}-\mathbf{r}')\sigma_\beta^2 s_\beta^2 c^2 - 2J_{\alpha\beta}(\mathbf{r}-\mathbf{r}')\sigma_\alpha\sigma_\beta s_\alpha s_\beta c^2 +$$

$$+J_{\alpha\alpha}(\mathbf{r}-\mathbf{r}')\sigma_\alpha^2 s_\alpha^2\frac{\eta}{4}c\,e^{i\mathbf{k}\cdot\mathbf{r}} + J_{\beta\beta}(\mathbf{r}-\mathbf{r}')\sigma_\beta^2 s_\beta^2\frac{\eta}{4}c\,e^{i\mathbf{k}\cdot\mathbf{r}} - 2J_{\alpha\beta}(\mathbf{r}-\mathbf{r}')\sigma_\alpha\sigma_\beta s_\alpha s_\beta\frac{\eta}{4}c\,e^{i\mathbf{k}\cdot\mathbf{r}} +$$

$$+J_{\alpha\alpha}(\mathbf{r}-\mathbf{r}')\sigma_\alpha^2 s_\alpha^2\frac{\eta}{4}c\,e^{i\mathbf{k}\cdot\mathbf{r}'} + J_{\beta\beta}(\mathbf{r}-\mathbf{r}')\sigma_\beta^2 s_\beta^2\frac{\eta}{4}c\,e^{i\mathbf{k}\cdot\mathbf{r}'} - 2J_{\alpha\beta}(\mathbf{r}-\mathbf{r}')\sigma_\alpha\sigma_\beta s_\alpha s_\beta\frac{\eta}{4}c\,e^{i\mathbf{k}\cdot\mathbf{r}'} +$$

$$+J_{\beta\beta}(\mathbf{r}-\mathbf{r}')\sigma_\beta^2 s_\beta^2\left(1-\left(2c + \frac{\eta}{4}e^{i\mathbf{k}\cdot\mathbf{r}} + \frac{\eta}{4}e^{i\mathbf{k}\cdot\mathbf{r}'}\right)\right) + J_{\alpha\beta}(\mathbf{r}-\mathbf{r}')\sigma_\alpha\sigma_\beta s_\alpha s_\beta\left(2c + \frac{\eta}{4}e^{i\mathbf{k}\cdot\mathbf{r}} + \frac{\eta}{4}e^{i\mathbf{k}\cdot\mathbf{r}'}\right)\Big\} =$$

$$= \left\{ W^{magn}(\mathbf{r}-\mathbf{r}') = J_{\alpha\alpha}(\mathbf{r}-\mathbf{r}')\sigma_\alpha^2 s_\alpha^2 + J_{\beta\beta}(\mathbf{r}-\mathbf{r}')\sigma_\beta^2 s_\beta^2 - 2J_{\alpha\beta}(\mathbf{r}-\mathbf{r}')\sigma_\alpha\sigma_\beta s_\alpha s_\beta \right\} =$$

$$= \frac{1}{2}\{\sum_{\mathrm{r},\mathrm{r}'} W^{magn}(\mathbf{r}-\mathbf{r}')\frac{\eta^2}{16}e^{i\mathbf{k}\cdot\mathbf{r}}\,e^{i\mathbf{k}\cdot\mathbf{r}'} + \sum_{\mathrm{r},\mathrm{r}'}\{J_{\alpha\beta}(\mathbf{r}-\mathbf{r}')\sigma_\alpha\sigma_\beta s_\alpha s_\beta(-2c^2+2c+\frac{\eta}{4}e^{i\mathbf{k}\cdot\mathbf{r}}+\frac{\eta}{4}e^{i\mathbf{k}\cdot\mathbf{r}'}-$$

$$-2\frac{\eta}{4}c\,e^{i\mathbf{k}\cdot\mathbf{r}}-2\frac{\eta}{4}c\,e^{i\mathbf{k}\cdot\mathbf{r}'}) + J_{\alpha\alpha}(\mathbf{r}-\mathbf{r}')\sigma_\alpha^2 s_\alpha^2(c^2+\frac{\eta}{4}c\,e^{i\mathbf{k}\cdot\mathbf{r}}+\frac{\eta}{4}c\,e^{i\mathbf{k}\cdot\mathbf{r}'}) + J_{\beta\beta}(\mathbf{r}-\mathbf{r}')\sigma_\beta^2 s_\beta^2(c^2+$$

$$+\frac{\eta}{4}c\,e^{i\mathbf{k}\cdot\mathbf{r}}+\frac{\eta}{4}c\,e^{i\mathbf{k}\cdot\mathbf{r}'}+1-(2c+\frac{\eta}{4}e^{i\mathbf{k}\cdot\mathbf{r}}+\frac{\eta}{4}e^{i\mathbf{k}\cdot\mathbf{r}'}))\}\} = \frac{1}{2}\{\sum_{\mathrm{r},\mathrm{r}'} W^{magn}(\mathbf{r}-\mathbf{r}')\frac{\eta^2}{16}e^{i\mathbf{k}\cdot\mathbf{r}}\,e^{i\mathbf{k}\cdot\mathbf{r}'} +$$

$$+\sum_{\mathrm{r},\mathrm{r}'}\{J_{\alpha\alpha}(\mathbf{r}-\mathbf{r}')\sigma_\alpha^2 s_\alpha^2 c^2 + J_{\beta\beta}(\mathbf{r}-\mathbf{r}')\sigma_\beta^2 s_\beta^2(1-c)^2 + 2J_{\alpha\beta}(\mathbf{r}-\mathbf{r}')\sigma_\alpha\sigma_\beta s_\alpha s_\beta c(1-c) +$$

$$+J_{\alpha\alpha}(\mathbf{r}-\mathbf{r}')\sigma_\alpha^2 s_\alpha^2(\frac{\eta}{4}e^{i\mathbf{k}\cdot\mathbf{r}}+\frac{\eta}{4}e^{i\mathbf{k}\cdot\mathbf{r}'})c + J_{\beta\beta}(\mathbf{r}-\mathbf{r}')\sigma_\beta^2 s_\beta^2(\frac{\eta}{4}e^{i\mathbf{k}\cdot\mathbf{r}}+\frac{\eta}{4}e^{i\mathbf{k}\cdot\mathbf{r}'})(c-1) +$$

$$+J_{\alpha\beta}(\mathbf{r}-\mathbf{r}')\sigma_\alpha\sigma_\beta s_\alpha s_\beta(\frac{\eta}{4}e^{i\mathbf{k}\cdot\mathbf{r}}+\frac{\eta}{4}e^{i\mathbf{k}\cdot\mathbf{r}'})(1-2c)\}\} = \frac{1}{2}\{\sum_{\mathrm{r},\mathrm{r}'} W^{magn}(\mathbf{r}-\mathbf{r}')\frac{\eta^2}{16}e^{i\mathbf{k}\cdot\mathbf{r}}\,e^{i\mathbf{k}\cdot\mathbf{r}'} +$$

$$+\sum_{\mathrm{r},\mathrm{r}'}\{J_{\alpha\alpha}(\mathbf{r}-\mathbf{r}')\sigma_\alpha^2 s_\alpha^2 c^2 + J_{\beta\beta}(\mathbf{r}-\mathbf{r}')\sigma_\beta^2 s_\beta^2(1-c)^2 + 2J_{\alpha\beta}(\mathbf{r}-\mathbf{r}')\sigma_\alpha\sigma_\beta s_\alpha s_\beta c(1-c)\} +$$

$$+\sum_{\mathrm{r},\mathrm{r}'}(\frac{\eta}{4}e^{i\mathbf{k}\cdot\mathbf{r}}+\frac{\eta}{4}e^{i\mathbf{k}\cdot\mathbf{r}'})\left[W^{magn}(\mathbf{r}-\mathbf{r}')c - J_{\beta\beta}(\mathbf{r}-\mathbf{r}')\sigma_\beta^2 s_\beta^2 + J_{\alpha\beta}(\mathbf{r}-\mathbf{r}')\sigma_\alpha\sigma_\beta s_\alpha s_\beta\right]\} =$$

$$= \frac{N}{2}\left[\tilde{W}^{magn}(\mathbf{k})\frac{3}{16}\eta^2 + \tilde{J}_{\alpha\alpha}(\mathbf{0})\sigma_\alpha^2 s_\alpha^2 c^2 + \tilde{J}_{\beta\beta}(\mathbf{0})\sigma_\beta^2 s_\beta^2(1-c)^2 + 2\tilde{J}_{\alpha\beta}(\mathbf{0})\sigma_\alpha\sigma_\beta s_\alpha s_\beta c(1-c)\right]$$

II. Entropy, *S*.

1) Chemical entropy, S_{chem}:

For the system with 2 different kinds of atoms α and β, statistics gives following definition of entropy:

$$S_{chem} = k_B \ln\Omega = k_B \ln\left(\frac{N!}{N_\alpha! N_\beta!}\right) = \left\{\begin{matrix} N_\alpha + N_\beta = N \\ \ln(f!) \simeq f\ln f - f \end{matrix}\right\} = k_B(N\ln N - N_\alpha \ln N_\alpha -$$

$$-N_\beta \ln N_\beta - N + N_\alpha + N_\beta) = k_B((N_\alpha + N_\beta)\ln N - N_\alpha \ln N_\alpha - N_\beta \ln N_\beta) =$$

$$= -Nk_B\left(\frac{N_\alpha}{N}\ln\frac{N_\alpha}{N} + \frac{N_\beta}{N}\ln\frac{N_\beta}{N}\right) = \left\{\begin{matrix} \frac{N_i}{N} = p_i, \;\; i = (\alpha,\beta) \\ p_\alpha + p_\beta = 1 \end{matrix}\right\} =$$

$$= -Nk_B\left(p_\alpha \ln p_\alpha + (1-p_\alpha)\ln(1-p_\alpha)\right)$$

And therefore for a crystal where each site **r** can be characterized by a probability $p(\mathbf{r})$, we have:

$$S_{chem} = -Nk_B\sum_{\mathbf{r}}\left(p_\alpha(\mathbf{r})\ln p_\alpha(\mathbf{r}) + (1-p_\alpha(\mathbf{r}))\ln(1-p_\alpha(\mathbf{r}))\right)$$

Using SCW approach we obtain:

$$p = p_\alpha = c + \frac{\eta}{4} e^{i\mathbf{k}\cdot\mathbf{r}} \rightarrow \begin{cases} p_1 = c + \frac{3}{4}\eta \\ p_2 = c - \frac{1}{4}\eta \end{cases}$$

$$S_{chem} = -\frac{Nk_B}{4}\left(\begin{array}{l}\left(c+\frac{3}{4}\eta\right)\ln\left(c+\frac{3}{4}\eta\right)+\left(1-c-\frac{3}{4}\eta\right)\ln\left(1-c-\frac{3}{4}\eta\right)+ \\ +3\left(c-\frac{\eta}{4}\right)\ln\left(c-\frac{\eta}{4}\right)+\left(1-c+\frac{\eta}{4}\right)\ln\left(1-c+\frac{\eta}{4}\right)\end{array}\right)$$

2) Magnetic entropy, S_{magn}:

The expression for magnetic entropy was previously obtained in the section 5.2.1. When system has magnetic atoms of 2 kinds, like Fe and Ni, the entropy will be defined as a sum:

$$S_{magn} = S_\alpha + S_\beta = \left\{\begin{array}{l}\alpha(\beta) = Fe(Ni) \\ N = N_\alpha + N_\beta \\ c = c_\alpha\end{array}\right\} = Nk_B\{c[\ln\left(sh\left(\frac{(2s_\alpha+1)y_\alpha(\sigma_{\alpha,\beta})}{2s_\alpha}\right)\right) - \ln\left(sh\left(\frac{y_\alpha(\sigma_{\alpha,\beta})}{2s_\alpha}\right)\right) -$$
$$-y_\alpha(\sigma_{\alpha,\beta})B_{s_\alpha}(y_\alpha(\sigma_{\alpha,\beta}))] + (1-c)[\ln\left(sh\left(\frac{(2s_\beta+1)y_\beta(\sigma_{\beta,\alpha})}{2s_\beta}\right)\right) - \ln\left(sh\left(\frac{y_\beta(\sigma_{\beta,\alpha})}{2s_\beta}\right)\right) -$$
$$-y_\beta(\sigma_{\beta,\alpha})B_{s_\beta}(y_\beta(\sigma_{\beta,\alpha}))]\}$$

III. Final configurational free energy, F:

$$\frac{F}{N} = \frac{1}{2}\Big[c^2\tilde{W}^{chem}(\mathbf{0}) + \tilde{J}_{\alpha\alpha}(\mathbf{0})\sigma_\alpha^2 s_\alpha^2 c^2 + \tilde{J}_{\beta\beta}(\mathbf{0})\sigma_\beta^2 s_\beta^2 (1-c)^2 + 2\tilde{J}_{\alpha\beta}(\mathbf{0})\sigma_\alpha\sigma_\beta s_\alpha s_\beta c(1-c) +$$
$$+\frac{3}{16}\eta^2\left(\tilde{W}^{chem}(\mathbf{k}) + \tilde{J}_{\alpha\alpha}(\mathbf{k})\sigma_\alpha^2 s_\alpha^2 + \tilde{J}_{\beta\beta}(\mathbf{k})\sigma_\beta^2 s_\beta^2 - 2\tilde{J}_{\alpha\beta}(\mathbf{k})\sigma_\alpha\sigma_\beta s_\alpha s_\beta\right)\Big] +$$
$$+\frac{k_B T}{4}\left(\begin{array}{l}\left(c+\frac{3}{4}\eta\right)\ln\left(c+\frac{3}{4}\eta\right)+\left(1-c-\frac{3}{4}\eta\right)\ln\left(1-c-\frac{3}{4}\eta\right)+ \\ +3\left(c-\frac{\eta}{4}\right)\ln\left(c-\frac{\eta}{4}\right)+\left(1-c+\frac{\eta}{4}\right)\ln\left(1-c+\frac{\eta}{4}\right)\end{array}\right) -$$
$$-Nk_B T\left\{c\left[\ln\left(sh\left(\frac{(2s_\alpha+1)y_\alpha(\sigma_{\alpha,\beta})}{2s_\alpha}\right)\right) - \ln\left(sh\left(\frac{y_\alpha(\sigma_{\alpha,\beta})}{2s_\alpha}\right)\right) - y_\alpha(\sigma_{\alpha,\beta})B_{s_\alpha}(y_\alpha(\sigma_{\alpha,\beta}))\right] +\right.$$
$$\left.+(1-c)\left[\ln\left(sh\left(\frac{(2s_\beta+1)y_\beta(\sigma_{\beta,\alpha})}{2s_\beta}\right)\right) - \ln\left(sh\left(\frac{y_\beta(\sigma_{\beta,\alpha})}{2s_\beta}\right)\right) - y_\beta(\sigma_{\beta,\alpha})B_{s_\beta}(y_\beta(\sigma_{\beta,\alpha}))\right]\right\}$$

5.2.3. Definition of equilibrium thermodynamic quantities

To define equilibrium values of thermodynamic parameters, it is necessary to differentiate the presented free energy, i.e. to find derivatives $\frac{\partial F}{\partial \eta}$; $\frac{\partial F}{\partial \sigma_\alpha}$; $\frac{\partial F}{\partial \sigma_\beta}$, and set them equal to 0:

$$\frac{\partial (F/N)}{\partial \eta} = \frac{1}{2}\cdot 2\cdot \frac{3}{16}\eta\left[\tilde{W}^{chem}(\mathbf{k}) + \tilde{J}_{\alpha\alpha}(\mathbf{k})\sigma_\alpha^2 s_\alpha^2 + \tilde{J}_{\beta\beta}(\mathbf{k})\sigma_\beta^2 s_\beta^2 + 2\tilde{J}_{\alpha\beta}(\mathbf{k})\sigma_\alpha\sigma_\beta s_\alpha s_\beta\right] +$$

$$+\frac{k_B T}{4}\left\{3\cdot\left(-\frac{1}{4}\right)\ln(c-\frac{\eta}{4}) + 3\cdot\left(-\frac{1}{4}\right)\frac{c-\frac{\eta}{4}}{c-\frac{\eta}{4}} + \frac{3}{4}\ln(1-c+\frac{\eta}{4}) + 3\cdot\frac{1}{4}\frac{1-c+\frac{\eta}{4}}{1-c+\frac{\eta}{4}} + \right.$$

$$\left. +\frac{3}{4}\ln(c+\frac{3}{4}\eta) + \frac{3}{4}\frac{c+\frac{3}{4}\eta}{c+\frac{3}{4}\eta} + \left(-\frac{3}{4}\right)\ln(1-c-\frac{3}{4}\eta) + \left(-\frac{3}{4}\right)\frac{1-c-\frac{3}{4}\eta}{1-c-\frac{3}{4}\eta}\right\} =$$

$$= \frac{3}{16}\left\{\eta\left[\tilde{W}^{chem}(\mathbf{k}) + \tilde{J}_{\alpha\alpha}(\mathbf{k})\sigma_\alpha^2 s_\alpha^2 + \tilde{J}_{\beta\beta}(\mathbf{k})\sigma_\beta^2 s_\beta^2 + 2\tilde{J}_{\alpha\beta}(\mathbf{k})\sigma_\alpha\sigma_\beta s_\alpha s_\beta\right] - k_B T\ln\frac{(c-\frac{\eta}{4})(1-c-\frac{3}{4}\eta)}{(c+\frac{3}{4}\eta)(1-c+\frac{\eta}{4})}\right\}$$

From the condition $\frac{\partial F}{\partial \eta} = 0$,we have:

$$\ln\frac{(c-\frac{\eta}{4})(1-c-\frac{3}{4}\eta)}{(c+\frac{3}{4}\eta)(1-c+\frac{\eta}{4})} = \frac{\eta}{k_B T}\left[\tilde{W}^{chem}(\mathbf{k}) + \tilde{J}_{\alpha\alpha}(\mathbf{k})\sigma_\alpha^2 s_\alpha^2 + \tilde{J}_{\beta\beta}(\mathbf{k})\sigma_\beta^2 s_\beta^2 + 2\tilde{J}_{\alpha\beta}(\mathbf{k})\sigma_\alpha\sigma_\beta s_\alpha s_\beta\right]$$

Before derivation of $\frac{\partial F}{\partial \sigma_\alpha}$ and $\frac{\partial F}{\partial \sigma_\beta}$, it will be useful to find a derivative of magnetic entropy:

$$\frac{\partial S}{\partial \sigma} = \frac{\partial}{\partial \sigma}\left\{Nk_B\left[\ln\left(sh\left(\frac{(2\mathbf{S}+1)y}{2\mathbf{S}}\right)\right) - \ln\left(sh\left(\frac{y}{2\mathbf{S}}\right)\right) - yB_{\mathbf{S}}(y)\right]\right\} = Nk_B\left\{\frac{1}{sh\left(\frac{(2\mathbf{S}+1)y}{2\mathbf{S}}\right)}\times\right.$$

$$\left.\times ch\left(\frac{(2\mathbf{S}+1)y}{2\mathbf{S}}\right)\cdot\frac{\partial y}{\partial \sigma}\cdot\frac{(2\mathbf{S}+1)}{2\mathbf{S}} - \frac{1}{sh\left(\frac{y}{2\mathbf{S}}\right)}\cdot ch\left(\frac{y}{2\mathbf{S}}\right)\cdot\frac{\partial y}{\partial \sigma}\cdot\frac{1}{2\mathbf{S}} - \frac{\partial y}{\partial \sigma}B_{\mathbf{S}}(y) - y\frac{\partial B_{\mathbf{S}}(y)}{\partial \sigma}\right\} =$$

$$= \left\{y = \frac{\mathbf{S}g\mu_B}{k_B T}(q\cdot\sigma) \Rightarrow \frac{\partial y}{\partial \sigma} = \frac{\mathbf{S}g\mu_B q}{k_B T}\right\} = Nk_B\left\{\frac{(2\mathbf{S}+1)}{2\mathbf{S}}\cdot\frac{\mathbf{S}g\mu_B q}{k_B T}\cdot coth\left(\frac{(2\mathbf{S}+1)y}{2\mathbf{S}}\right) - \right.$$

$$\left. -\frac{1}{2\mathbf{S}}\cdot\frac{\mathbf{S}g\mu_B q}{k_B T}\cdot coth\left(\frac{1y}{2\mathbf{S}}\right) - \frac{\mathbf{S}g\mu_B q}{k_B T}B_{\mathbf{S}}(y) - y\frac{\partial B_{\mathbf{S}}(y)}{\partial \sigma}\right\} =$$

$$= \left\{ B_{\mathbf{J}}(x) = \left(1+\frac{1}{2\mathbf{J}}\right) coth\left(\left(1+\frac{1}{2\mathbf{J}}\right)x\right) - \frac{1}{2\mathbf{J}} coth\left(\frac{1}{2\mathbf{J}}x\right)\right\} =$$

$$= -Nk_B y \frac{\partial B_{\mathbf{S}}(y)}{\partial \sigma} = -Nk_B \frac{\mathbf{S}g\mu_B}{k_B T}(q\cdot\sigma)\frac{\partial B_{\mathbf{S}}(y)}{\partial \sigma} = -\frac{N\mathbf{S}g\mu_B(q\cdot\sigma)}{T}\cdot\frac{\partial B_{\mathbf{S}}(y)}{\partial \sigma}$$

According to the molecular field, the reduced magnetization, $\sigma = \frac{\mathbf{M}}{M_{Sat}}$, can be defined using (Eq. 3.13):

$$\mathbf{M} = g\mu_B \mathbf{J} B_J\left(\frac{\mathbf{J}g\mu_B}{k_B T}(\mathbf{H}_{ext} + q\cdot\mathbf{M})\right) = M_{Sat} B_J(x) \Rightarrow \sigma = \frac{g\mu_B \mathbf{J} B_J\left(\frac{\mathbf{J}g\mu_B}{k_B T}\mathbf{H}\right)}{M_{Sat}} = B_J\left(\frac{M_{Sat}}{k_B T}\mathbf{H}\right)$$

Hence we have: $\frac{\partial S}{\partial \sigma} = -\frac{N\mathbf{S}g\mu_B(q\cdot\sigma)}{T}\cdot\frac{\partial B_{\mathbf{S}}(y)}{\partial \sigma} = -N\frac{M_{sat}(q\cdot\sigma)}{T}$

With this simplified expression it is easy to obtain:

$$\frac{\partial(F/N)}{\partial \sigma_\alpha} = \frac{1}{2}\left[2\tilde{J}_{\alpha\alpha}(\mathbf{0})\sigma_\alpha s_\alpha^2 c^2 + 2\tilde{J}_{\alpha\beta}(\mathbf{0})\sigma_\beta s_\alpha s_\beta c(1-c) + \frac{3}{16}\eta^2\left[2\tilde{J}_{\alpha\alpha}(\mathbf{k})\sigma_\alpha s_\alpha^2 - 2\tilde{J}_{\alpha\beta}(\mathbf{k})\sigma_\beta s_\alpha s_\beta\right]\right] -$$

$$-Tc\left(-\frac{M_{sat}(q\cdot\sigma_\alpha)}{T}\right)$$

As $\frac{\partial(F/N)}{\partial \sigma_\alpha} = 0$, we have:

$$M_{sat}(q\cdot\sigma_\alpha) = -\frac{1}{c}\left(\tilde{J}_{\alpha\alpha}(\mathbf{0})\sigma_\alpha s_\alpha^2 c^2 + \tilde{J}_{\alpha\beta}(\mathbf{0})\sigma_\beta s_\alpha s_\beta c(1-c) + \frac{3}{16}\eta^2\left[\tilde{J}_{\alpha\alpha}(\mathbf{k})\sigma_\alpha s_\alpha^2 - \tilde{J}_{\alpha\beta}(\mathbf{k})\sigma_\beta s_\alpha s_\beta\right]\right)$$

And using previously shown definition of σ we obtain:

$$\sigma_\alpha = B_{\mathbf{S}_\alpha}\left(-\frac{1}{k_B Tc}\left(\begin{array}{l}\tilde{J}_{\alpha\alpha}(\mathbf{0})\sigma_\alpha s_\alpha^2 c^2 + \tilde{J}_{\alpha\beta}(\mathbf{0})\sigma_\beta s_\alpha s_\beta c(1-c) + \\ +\frac{3}{16}\eta^2\left[\tilde{J}_{\alpha\alpha}(\mathbf{k})\sigma_\alpha s_\alpha^2 - \tilde{J}_{\alpha\beta}(\mathbf{k})\sigma_\beta s_\alpha s_\beta\right]\end{array}\right)\right)$$

and, respectively:

$$\sigma_\beta = B_{\mathbf{S}_\alpha}\left(-\frac{1}{k_B T(1-c)}\left(\begin{array}{l}\tilde{J}_{\beta\beta}(\mathbf{0})\sigma_\beta s_\beta^2 (1-c)^2 + \tilde{J}_{\alpha\beta}(\mathbf{0})\sigma_\alpha s_\alpha s_\beta c(1-c) + \\ +\frac{3}{16}\eta^2\left[\tilde{J}_{\beta\beta}(\mathbf{k})\sigma_\beta s_\beta^2 - \tilde{J}_{\alpha\beta}(\mathbf{k})\sigma_\alpha s_\alpha s_\beta\right]\end{array}\right)\right)$$

5.3. The algorithm of solution of the Önsager-type equation

The integration of the Önsager equation for binary alloy (Eq. 3.39) was performed using the explicit Euler scheme in the reciprocal space (Eq. 3.40). The algorithm is following:

Input parameters:

- The "mixing" energies w_i (i = 1..4) and thermal energy $k_B T$
- The concentration of the matrix c, number of nuclei and their radius
- Equilibrium concentration of ordered and disordered phase
- The time step (Δt) and simulation time
- The size of the simulation box (nx, ny)

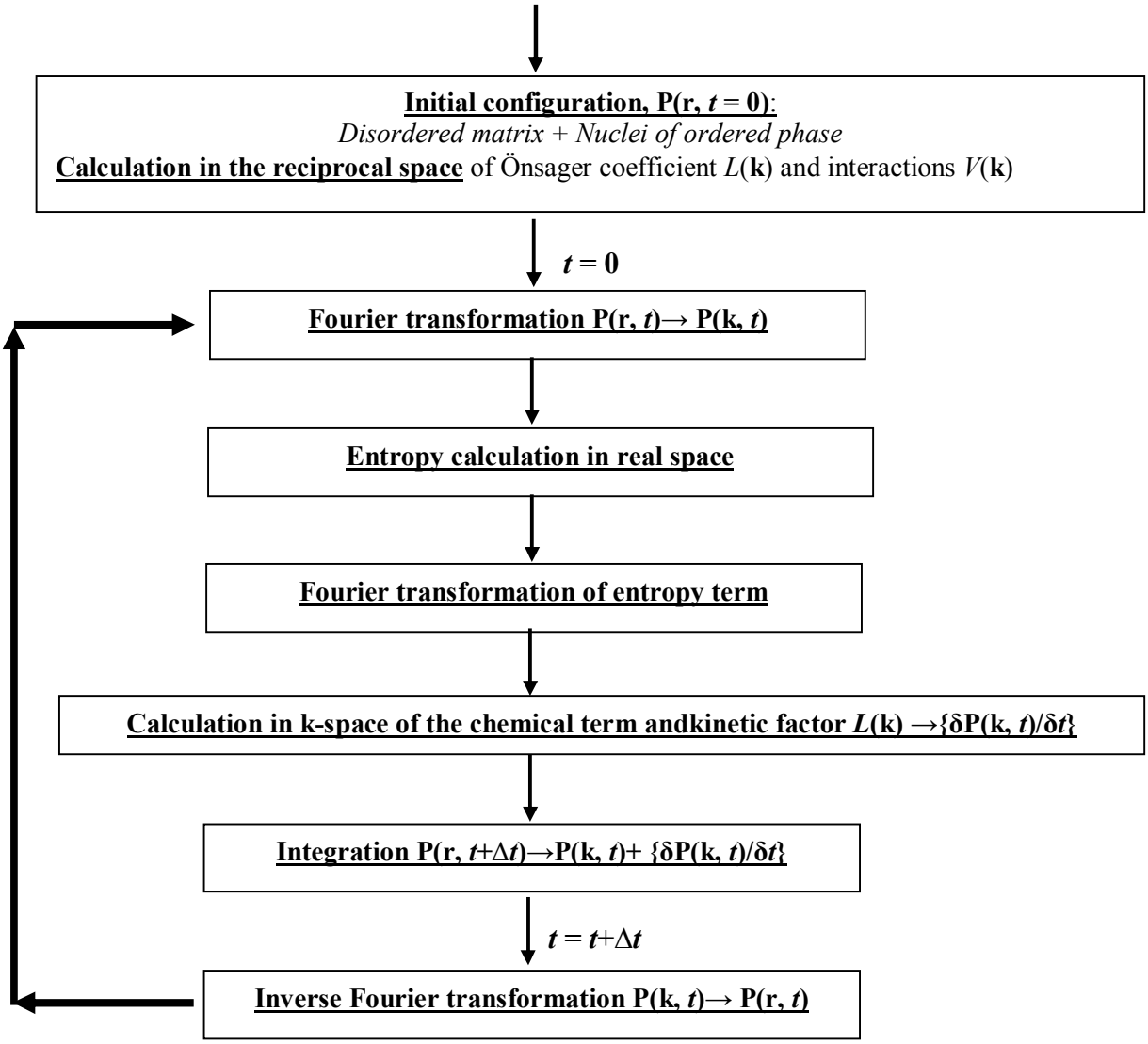

Bibliography

1. Binary alloys Phase Diagrams, Vol.1, American Society for Metals, Metals park, CA, 1996
2. G. Béranger, F. Duffault, J. Morlet, J. F. Tiers, "Les alliages de Fer et de Nickel. Cent ans après le découverte de l'Invar...", Lavoisier: Tec&Doc, Paris, (1996)
3. Enciclopedic dictionary on solid state physics, in 2 parts, Naukova Dumka, Kiev, 1998, in 2 parts, (in Russian)
4. E. P. Wohlfarth (ed.), "Ferromagnetic materials: a handbook on the properties of magnetically ordered substances", Vol. 1, North-Holland Publishing Company, (1980)
5. S. V. Vonsovskii, "Magnetism", Nauka, Moscow, 1971, (in Russian);
   English analog: S. V. Vonsovskii, "Magnetism", Wiley, New-York, 1974
6. D. C. Mattis, "The theory of magnetism", Springer series in solid-state sciences ; v,17, v.55, Springer-Verlag, Berlin - New York, 1981
7. N. Ashkroft, N. Mermin, "Solid state physics", 1975, (in Russian)
8. C. Kittel, "Introduction to solid state physics", 3rd Ed., John Wiley&Sons, New York, 1966
9. R. M. Bozorth, "Magnetism", Rev. Mod. Phys. 19, 29 (1947)
10. . M. Bozorth, "The Permalloy problem", Rev. Mod, Phys. 25, 42 (1953)
11. A. T. English, G. Y. Chin, "Metallurgy and magnetic properties control in Permalloy", J. Appl. Phys. 38, 1183 (1967)
12. R. J. Wakelin, E. L. Yates, "A study of the order-disorder transformation in Iron-Nickel alloys in the region $FeNi_3$", Proc. Phys. Soc. Lond. B 66, 221 (1953)
13. T. G. Kollie, C. R. Brooks, "The heat capacity of Ni_3Fe:experimental data from 300 to 1670 K", Phys. Stat. Sol. (a) 19, 545 (1973)
14. J. Orehotsky, J. B. Sousa, M. F. Pinheiro, "Critical behavior in Ni_3Fe and Ni_3Mn", J. Appl. Phys 53, 7939 (1982)
15. X. Jiang, G. E. Ice, C. J. Sparks, L. Robertson, P. Zsćhack, "Local atomic order and individual pair displacements of $Fe_{46.5}Ni_{53.5}$ and $Fe_{22.5}Ni_{77.5}$ from diffuse x-ray scattering studies", Phys. Rev. B 54, 3211 (1996)
16. G. Ice, C. J. Sparks, A. Habenschuss, "Anomalous x-ray scattering measurement of near-neighbor individual pair displacements and chemical order in $Fe_{22.5}Ni_{77.5}$", Phys. Rev. Lett. 68, 863 (1992)

17. H. Ferjani, F. Bley, Y. Calvayrac, “Ordering and domain coarsening kinetics in substituted permalloys”, Journal de physique, Colloque C7, suppl. 12, C7 (1977)
18. S. Lefebvre, F. Bley, M. Fayard, M. Roth, “Neutron diffuse scattering investigation of different states of order in $^{62}Ni_{0.765}Fe_{0.235}$”, Acta. Metall. 29, 749 (1981)
19. S. Lefebvre, F. Bley, M. Bessiere, M. Fayard, M. Roth, J. B. Cohen, “Short-range order in Ni_3Fe”,Acta Cryst. A36, 1 (1980)
20. F. Bley, Z. Amilius, S. Lefebvre, “Wave vector dependent kinetics of short-range ordering in $^{62}Ni_{0.765}Fe_{0.235}$ studied by neutron diffuse scattering”, Acta Metall. 36, 1643 (1988)
21. C. G. Shull, M. K. Wilkinson, “Neutron diffraction studies of the magnetic structure of alloys of transition elements”, Phys. Rev. 97, 304 (1955)
22. J. W. Drijver, F. van der Woude, S. Radelaar, “Order-disorder transition in Ni_3Fe studied by Mössbauer spectroscopy”, Phys. Rev. Lett. 34, 1026 (1975)
23. J. W. Drijver, F. van der Woude, S. Radelaar, “Mössbauer study of atomic order in Ni_3Fe. I.Determination of the long-range order parameter”, Phys. Rev. B 16, 985 (1977)
24. C. E. Johnson, M. S. Ridout, T. E. Cranshaw, “The Mössbauer effect in Iron alloys”, Proc. Phys. Soc. 81, 1079 (1963)
25. T. E. Cranshaw, “The electronic and magnetic structure of ordered Ni_3Fe studied by Mössbauer spectroscopy”, J. Phys F 17, 967 (1987)
26. J. K. Van Deen, F. Van der Woude, “Phase diagram of the order-disorder transition in Ni_3Fe”, Acta Metallurgica 29, 1255 (1981)
27. J. B. Staunton, D. D. Johnson, B. L. Gyorffy, “Interaction between magnetic and compositional order in Ni-rich Ni_cFe_{1-c} alloys”, J. Appl. Phys. 61, 3693 (1987)
28. J. B. Staunton, D. D. Johnson, B. L. Gyorffy, C. J. Walden, “Magnetic and compositional order in transition metal alloys”, Phil. Mag. B 61, 773 (1990)
29. T. Nautiyal, S. Auluck, “Electronic structure and Fermi surface of Ni_3Fe”, Phys. Rev. B 47, 1726 (1993)
30. Y. Mishin, M. J. Mehl, D. A. Papaconstantopoulos, “Phase stability in the Fe-Ni system: Investigation by first-principles calculations and atomistic simulations”, Acta Mater. 53, 4029 (2005)
31. H.-P. Cheng, D. E. Ellis, “First-principles potentials in modeling structure and thermodynamics of Fe-Ni alloys”, Phys. Rev. B 39, 12469 (1989)
32. M Schröter, H. Ebert, H. Akai, P. Entel, E. Hoffmann, G. G. Reddy, “First-principles investigations of atomic disorder effects on magnetic and structural instabilities in transtition metal alloys”, Phys. Rev. B 52, 188 (1995)

33. P. Yu, X. F. Jin, J. Kudrnovský, D. S. Wang, P. Bruno, "Curie temperatures of f.c.c. and b.c.c. nickel and permalloy: Supercell and Green's function methods", Phys. Rev B 77, 054431 (2008)
34. J. Kudrnovský, V. Drchal, P. Bruno, "Magnetic properties of f.c.c. Ni-based transition metal alloys", Phys. Rev B 77, 224422 (2008)
35. Y. Chen, S. Iwata, T. Mohri, "First-principles calculation of phase equilibria and phase separation of the Fe-Ni alloy system", Rare metals 25, 437 (2006)
36. P. James, O. Eriksson, B. Johansson, I. A. Abrikosov, "Calculated magnetic properties of binary alloys between Fe, Co, Ni and Cu", Phys. Rev. B 59, 419 (1999)
37. A. V. Ruban, M. I. Katsnelson, W. Olovsson, S. I. Simak, A. I. Abrikosov, "Origin of magnetic frustrations in Fe-Ni Invar alloys", Phys. Rev. B 71, 054402 (2005)
38. A. V. Ruban, S. Khmelevskyi, P. Mohn, B. Johansson, "Magnetic state, magnetovolume effects, and atomic order in $Fe_{65}Ni_{35}$ Invar alloy: A first principles study", Phys. Rev. B 76, 014420 (2007)
39. I. A. Abrikosov, A. E. Kissavos, F. Liot, B. Alling, S. I. Simak, O. Peil, A. V. Ruban, "Competition between magnetic structures in the Fe rich fcc FeNi alloys", Phys. Rev. B 76, 014434 (2007)
40. M.-Z. Dang, D. G. Rancourt, "Simultaneous magnetic and chemical order-disorder phenomena in Fe_3Ni, FeNi and $FeNi_3$", Phys. Rev. B 53, 2291 (1996)
41. M.-Z. Dang, M. Dubé, D. G. Rancourt, "Local moment magnetism of f.c.c. Fe-Ni alloys. II. Ising approximation Monte-Carlo", J. Magn. Magn. Mater. 147, 133 (1995)
42. M. Dubé, P. R. L. Heron, D. G. Rancourt, "Local moment magnetism of f.c.c. Fe-Ni alloys. II. Cluster-method mean-field theory", J. Magn. Magn. Mater. 147, 122 (1995)
43. D. G. Rancourt, M. Dubé, P. R. L. Heron, "General method for applying mean-field theory to disordered magnetic alloys", J. Magn. Magn. Mater. 125, 39 (1993)
44. M. B. Taylor, B. L. Gyorffy, C. J. Walden, "Magnetic and compositional order in nickel-rich Ni_cFe_{1-c} alloys", J. Phys.: Condens. Matter 3, 1575 (1991)
45. M. B. Taylor, B. L. Gyorffy, "Monte-Carlo simulations of an f.c.c. Ni_cFe_{1-c} alloy with vector magnetic freedom", J. Magn. Magn. Mater. 104-107, 877 (1992)
46. F. Livet, "Linearized inverse Monte-Carlo method applied to Ni_3Fe", Acta Metall. 35, 2915 (1987)
47. P. J. Lawrence, P. L. Rossiter, "Chemical and magnetic interactions in f.c.c. Fe-Ni alloys using the cluster-variation method", J. Phys. F: Met. Phys. 16, 543 (1986)
48. T. Horiuchi, M. Igarashi, F. Abe, T. Mohri, "Phenomenological calculation of phase-equilibria in the Fe-Ni system", Calphad 26, 591 (2002)

49. P. Cenedese, A. Marty, Y. Calvayrac, “Calculation of phase diagrams for the order-disorder transition in the binary system Ni-Fe and Ni-Al”, J. Phys. France 50, 2193 (1989)
50. V. A, Tatarenko, T. M. Radchenko, V. M. Nadutov, “Parameters of interatomic interactions in substitutional alloy of f.c.c. Ni-Fe on the basis of experimental data on magnetic characteristics and equilibrium values of intensities of radiation diffuse scattering”, Metallofiz. Noveishie Tekhnol. 25, 1303 (2003), (in Ukrainian)
51. V. A. Tatarenko, T. M. Radchenko, “The application of the diffuse scattering to the calculation of phase diagrams of f.c.c. substitutional alloys”, Intermetallics 11, 1319 (2003)
52. L. Billiard, P. Villemain, A. Chamberod, “Short-range and long-range order in ferromagnetic binary alloys”, J. Phys. C: Solid State Phys. 11, 2815 (1978)
53. R. A. Tahir-Kheli, T. Kawasaki, “Simultaneous occurrence of magnetic and spatial long-range order in binary alloys”, J. Phys. C: Solid State Phys. 10, 2207 (1977)
54. J. W. Cable, E. O. Wollan, “Magnetic-moment distribution in NiFe and AuFe alloys”, Phys. Rev. B 7, 2005 (1973)
55. G. G. E. Low, M. F. Collins, “Magnetic moment distribution in dilute Nickel alloys”, J. Apply. Phys. 34, 1195 (1963)
56. R. A. Reck, “Local magnetic moment and g′ in Fe-Ni alloys”, Phys. Rev. B 9, 2381 (1974)
57. J. Crangle, G. C. Hallam, “The magnetization of face-centered cubic and body-centered cubic iron+nickel alloys”, Proc. Phys. Soc. Lond. A272, 119 (1963)
58. A. P. Miodownik, “Physics and application of Invar alloys” (ed. H. Sato et al.), Honda Memorial Series on Material Science (Tokyo: Maruzen Company, Ltd.: 1978), No. 3, chapt. 12, p. 288
59. E. I. Kondorsky, V. L. Sedov, “Antiferromagnetism of Iron in face-centered crystalline lattice and the causes of anomalies in Invar physical properties”, J. Apply. Phys. 31, 331S (1960)
60. S. C. Abrahams, L. Guttman, J. S. Kasper, “Neutron diffraction determination of antiferromagnetism in face-centered-cubic (γ) iron”, Phys. Rev. 127, 2052 (1962)
61. C. S. Wang, B. M. Klein, H. Krakauer, “Theory of magnetic and structural ordering in iron”, Phys. Rev. Lett. 54, 1852 (1985)
62. F. J. Pinski, J. Staunton, B. L. Gyorffy, D. D. Johnson, G. M. Stocks, “Ferromagnetism versus antiferromagnetism in face-centered-cubic iron”, Phys. Rev. Lett. 56, 2096 (1986)

63. D. I. Uzunov, "Introduction to the theory of critical phenomena: mean-field, fluctuations and renormalization", World Scientific, 1993
64. A. Z. Menshikov, E. E. Yurchikov, "Curie temperature of f.c.c. iron-nickel alloys", Izvestiya Acad. Nauk USSR, Fiz. Series. 36, 1463 (1972), (in Russian)
65. J. G. Dash, B. D. Dunlap, D. G. Howard, "Internal field of Fe^{57} in Nickel from 22 K to the Curie point", Phys. Rev. 141, 376 (1966)
66. G. F. Bolling, A. Arrott, R. H. Richman, "A Study of Curie Temperatures and the Effect of Carbon in Face-Centred Cubic Iron-Nickel Alloys", phys. stat. sol. (b) 26, 743 (1968)
67. H. Asano, "Magnetism of γ Fe-Ni Invar Alloys with Low Nickel Concentration", J. Phys. Soc. Jpn 27, 542 (1969)
68. K. P. Belov, "Magnetic transformations", Fizmatgiz, Moscow, 1959, (in Russian)
69. R. M. Bozorth, J. G. Walker, "Magnetic crystal anisotropy and magnetostriction of Iron-Nickel aloys", Phys. Rev. 89, 624 (1953)
70. K. Chen, A. M. Ferrenberg, D. P. Landau, "Static critical behavior of three-dimensional classical Heisenberg models: a high resolution Monte Carlo study", Phys. Rev B 48, 3249 (1993)
71. M. P. Nightingale, H. W. J. Blöte, "Monte Carlo calculation of free energy, critical point, and surface critical behavior of three-dimensional Heisenberg ferromagnets", Phys. Rev. Lett. 60, 1562 (1988)
72. M. Ferer, A. Hamid-Aidinejad, "Three-dimensional Heisenberg ferromagnet: a series investigation", Phys. Rev. B 34, 6481 (1986)
73. D. W. Heermann, "Computer simulation methods", Springer-Verlag, Berlin, 1990
74. K. Binder, D. Landau, "A guide to Monte-Carlo simulations in statistical physics", Cambridge University Press, 2000
75. P. K. MacKeown, "Stochastic simulations in physics", Springer-Verlag, Singapore (1997)
76. B. Diu, C. Guttmann, D. Lederer, B. Roulet, "Physique Statistique", Hermann, Paris, 1989
77. L. D. Landau, E. M. Lifshitz, "Statistical physics", 2nd Ed., Nauka, Moscow, 1964, (in Russian)
78. R. Kubo, "Statistical mechanics", Nauka, Moscow, 1967 (in Russian)
79. N. Metropolis, A. Rosenbluth, M. Rosenbluth, A. Teller, "Equation of state calculations by fast computing machines", J. Chem. Phys. 21, 1087 (1953)
80. S. Kirkpatrick, C. D. Gelatt, Jr., M. P. Vecchi, "Optimization by simulated annealing", Science 220, 671 (1983)

81. S. Kirkpatrick, “Optimization by simulated annealing: quantitative studies”, J. Stat. Phys. 34, 975 (1984)
82. A. M. Ferrenberg, D. P. Landau, K. Binder, “Statistical and systematic errors in Monte Carlo sampling”, J. Stat. Phys. 63, 867 (1991)
83. M. S. S. Challa, D. P. Landau, K. Binder, “Finite-size effects at temperature-driven first-order transitions”, Phys. Rev. B 34, 1841 (1986)
84. S. Chen, A. Ferrenberg, D. P. Landau, “Monte Carlo simulation of the transitions in a two-dimensional random-bond Potts model”, Phys. Rev. E 52, 1377 (1995)
85. McKenzie, C. Domb, D.L. Hunter, “Extended high-temperature series for the classical Heisenberg model in three dimensions”, J. Phys A 15, 3899 (1982)
86. D. Ledue, D. P. Landau, J. Teillet, “Static critical behavior of the ferromagnetic Ising model on the quasiperiodic octagonal tiling”, Phys. Rev. B 51, 12523 (1995)
87. D. Ledue, D. P. Landau, “Quasiperiodic fluctuation effect on a first-order phase transition: A Monte Carlo investigation”, Phys. Rev. B 63, 054425 (2001)
88. A. A. Smirnov, “Molecular-kinetic theory of metals”, Nauka, Moscow, 1966 (in Russian)
89. A. A. Smirnov, “Generalized theory of ordering of alloys”, Naukova Dumka, Kyiv, 1986, (in Russian)
90. F. C. Nix, W. Schockley, “Order-disorder transformations in alloys”, Rev. Mod. Phys. 10, 1, 1938
91. A. G. Khachaturyan, “Theory of structural Transformations in solids”, Dover, New York, 2008
92. A. G. Khachaturyan, “Ordering in substitutional and interstitial solid solutions”, Progr. Mat. Sci. 22, 1 (1978)
93. J. G. Kirkwood, “Order and disorder in binary solutions”, J. Chem. Phys. 6, 70 (1938)
94. R. Kikuchi, “A theory of cooperative phenomena”, Phys. Rev. 81, 988 (1951)
95. R. Kikuchi, “Superposition approximation and natural iteration calculation in cluster variation method”, J. Chem. Phys. 60, 1071 (1974)
96. J. M. Cowley, “An approximate theory of order and disorder in alloys”, Phys. Rev. 77, 669 (1950)
97. J. M. Cowley, “Short- and long-range order parameters in disordered solutions”, Phys. Rev. 120, 1648 (1960)
98. B. Dünweg, K. Binder, “Model calculations of magnetic alloys on the body-centered-cubic lattices”, Phys. Rev. B 36, 6935 (1987)
99. K. Binder, “Ordering of face-centered-cubic lattice with nearest-neighbor interaction”, Phys. Rev. Lett. 45, 811 (1980)

100. P. C. Gehlen, J. B. Cohen, “Computer simulation of structure associated with local order in alloys”, Phys. Rev. 139, A844 (1965)

101. D. de Fontaine, “***K***-space symmetry rules for order-disorder reactions”, Acta Metallurgica 23, 553 (1975)

102. J. L. Morán-López, L. M. Falicov, “Ferromagnetism and spatial long-range order in binary alloys”, J. Phys. C: Sol. St. Phys. 13, 1715 (1980)

103. F. Mejiá-Lira, J. Urías, J. L. Morán-López, “Order-disorder transformations in ferromagnetic binary alloys”, Phys. Rev. B 24, 5270(1981)

104. J. Urías, J. L. Morán-López, “Phase separation in binary alloys with one magnetic component”, Phys. Rev. B 26, 2669(1982)

105. S. V. Semenovskaya, “The application of X-Ray diffuse scattering to the calculation of the Fe-Al equilibrium diagram”, phys. stat. sol. (b) 64, 291 (1974)

106. J. M. Sanchez, D. de Fontaine, “Ordering in f.c.c. lattices with first- and second-neighbor interactions”, Phys. Rev. B 21, 216 (1980)

107. J. M. Sanchez, D. de Fontaine, “Ising model phase-diagram calculations in the f.c.c. lattice with first- and second-neighbor interactions”, Phys. Rev. B 25, 1759 (1982)

108. J. M. Sanchez, C. H. Lin, “Modeling of magnetic and chemical ordering in binary alloys”, Phys. Rev. B 30, 1448 (1984)

109. W. Ostwald, Z. Phys. Chem. 37, 385 (1901)

110. L. Ratke, P. W. Voorhees, “Growth and Coarsening. Ripening in material processing”, Springer, (2002)

111. I. M. Lifshitz, V. V. Slyozov, “The kinetics of precipitation from supersaturated solid solutions”, J. Phys. Chem. Sol. 19, 35 (1961)

112. C. Wagner, Z. Electrochem. 65, 581 (1961)

113. S. Ferry, Ph. D. Thesis, (2007), defended at University of Rouen, Unpublished

114. A. Baldan, “Progress in Ostwald ripening theories and their applications to nickel-base superalloys”, J. Mater. Sci. 37, 2171 (2002)

115. H. Sato, R. Kikuchi, “Kinetics of order-disorder transformations in alloys”, Acta Metall. 24, 797 (1976)

116. K. Gschwend, H. Sato, R, Kikuchi, “Kinetics of order-disorder transformations in alloys. II”, J. Chem. Phys. 69, 5006 (1978)

117. K. Gschwend, H. Sato, R, Kikuchi, H. Iwasaki, H. Maniwa, “Kinetics of order-disorder transformations in alloys. III”, J. Chem. Phys. 71, 2844 (1979)

118. A. J. Ardell, R. b. Nicholson, “The coarsening of γ′ in Ni-Al alloys”, J. Phys. Chem. Sol. 27, 1793 (1966)

119. L.-Q. Chen, A. G. Khachaturyan, "Computer simulation of structural transformation during precipitation of an ordered intermetalic phase", Acta Metall. Mater. 39, 2533 (1991)

120. L.-Q. Chen, "Thermodynamics and kinetics of order-disorder processes derived from the cluster-activation method and microscopic diffusion theory", Phys. Rev. B 49, 3791 (1994)

121. R. Poduri, L.-Q. Chen, "Computer simulation of the kinetics of order-disorder and phase separation during precipitation of δ′ (Al_3Li) in Al-Li alloys", Acta Mater. 45, 245 (1997)

122. R. Poduri, L.-Q. Chen, "Computer simulation of atomic ordering and compositional clustering in the pseudobinary Ni_3Al-Ni_3V system", Acta Mater. 46, 1719 (1998)

123. R. Poduri, L.-Q. Chen, "Computer simulation of morphological evolution and coarsening of δ′ (Al_3Li) precipitates in Al-Li alloys", Acta Mater. 46, 3915 (1998)

124. Y. Le Bouar, A. G. Khachaturyan, "Mechanism and modelling of saw-tooth structure formation in the $L1_2$-$L1_0$ two-phase system", Acta Mater. 48, 1705 (2000)

125. H. Zapolsky, C. Pareige, L. Marteau, D. Blavette, L. Q. Chen, "Atome probe analyses and mean-field numerical simulation of the ternary phase diagrams in Ni-Al-V", Calphad 25, 125 (2001)

126. H. Zapolsky, S. Ferry, X. Sauvage, D. Blavette, L.Q. Chen, "Kinetics of cubic to tetragonal transformation in Ni-V-X alloys", (accepted in Phil. Mag.)

127. private communication with I. A. Abrikosov and M. Ekholm

128. Numerical recipes in Fortran

129. B. Millon, J. Růžhičková, J. Velíšek, J. Vřeštál, "Diffusion processes in the Fe-Ni system", Mater. Sci. En. 50, 43 (1981)

130. D. G. Morris, G. T. Brown, R. C. Piller, R. E. Smallman, "Ordering and domain growth in Ni_3Fe", Acta Metallurgica 24, 21 (1976)

131. R. J. Taunt, B. Ralph, "The mechanism of ordering in Ni_3Fe: Modular ordering", Phys. Stat. Sol. A 24, 207 (1974)

132. E. Lima Jr., V. Drago, "Influence of chemical disorder on the magnetic behavior and phase diagram of the Fe_xNi_{1-x} system", J. Magn. Magn. Mater. 280, 251 (2004)

133. M. A. Krivoglaz, "Theory of X-ray and thermal neutron scattering by real crystals", Plenum Press Inc., New York, 1969

134. P. C. Clapp, S. C. Moss, "Correlation functions of disordered alloys. I", Phys. Rev. 142, 418 (1966);

P. C. Clapp, S. C. Moss, “Correlation functions of disordered alloys. II”, Phys. Rev. 171, 754 (1968);

S. C. Moss, P. C. Clapp, “Correlation functions of disordered alloys. III”, Phys. Rev. 171, 764 (1968)

135. F. Brouers, A. V. Vedyaev, “On the magnetic properties of substitutional disordered ferromagnets”, Sol. St. Commun. 9, 1521 (1971)

136. J. B. Müller, J. Hesse, “A model for magnetic abnormalies of FeNi Invar alloys. I. Macroscopic Magnetic Properties”, Z. Phys. B-Cond. Mat. 54, 35 (1983)

137. A. V. Ruban, I. A. Abrikosov, “Configurational thermodynamics of alloys from first-principles: effective cluster interactions”, Rep. Prog. Phys. 71, 046501 (2008)

Résumé et abstract

Titre: Modélisation atomique de l'évolution microstructurale dans les alliages Ni-Fe: corrélation entre les propriétés magnétiques et structurales

Résumé

Les alliages Fe-Ni sont largement utilisés en raison de leurs propriétés intéressantes fondamentales découlant de la coexistence de l'orde chimique et l'ordre magnétique. L'objectif de ce travail était de comprendre l'influence mutuelle de ces deux mises en ordre sur les propriétés thermodynamiques d'équilibre et la cinétique dans les alliages Permalloy (Ni_3Fe). A partir de simulations Monte Carlo et de type Champ Moyen, nous avons mis en évidence l'effet des interactions magnétiques sur la température de transition ordre/désordre et réciproquement, l'influence des interactions chimiques sur la température de Curie. La cinétique de précipitation a été étudiée à partir de l'équation de microdiffusion d'Onsager en utilisant les paramètres déduits de calculs *ab-initio*. Ces simulations ont montré l'influence des interactions magnétiques sur la formation des particules $L1_2$ stable. Les deux types de simulations, thermodynamique et cinétique, ont donc confirmé l'importance de prendre en compte simultanément les interactions magnétiques et chimiques. Les résultats obtenus concordent bien avec les données expérimentales disponibles.

Mots-clés: alliages Fe-Ni, simulation Monte Carlo, matériaux magnétiques doux, approximation de Champ Moyen, transformation de phase ordre/désordre, simulation d'Onsager, température de Curie, cinétique de précipitation

Title: Atomic modeling of the microstructure evolution in Ni-Fe alloys: correlation between magnetic and structural properties

Abstract

Fe-Ni alloys are widely used due to their interesting fundamental properties which arise from the coexistence of the chemical and magnetic order. The aim of this work was to understand the mutual influence of these two types of ordering on the thermodynamic and kinetic processes in Permalloys (Ni_3Fe). From Monte Carlo and Mean Field simulations the effect of the magnetic interactions on the order/disorder transition temperature has been observed, and reciprocally the influence of the chemical interactions on the Curie temperature. The kinetics of the precipitation has been studied by means of the Onsager microdiffusion equation using parameters extracted from *ab-initio* calculations. These simulations have evidenced the influence of the magnetic interactions on the formation of the stable $L1_2$ particles. Both thermodynamic and kinetic investigations have confirmed the importance of taking into account simultaneously both magnetic and chemical interactions. The obtained results agree well with the available experimental data.

Keywords: Fe-Ni alloys, Monte Carlo simulation, soft magnetic materials, Mean field approximation, order/disorder phase transformation, Onsager simulation, Curie temperature, precipitation kinetics